January 2015

experimental investigation of a reacting transverse jet in a high pressure oscillating vitiated crossflow

Christopher Allen Fugger
Purdue University

Graduate School Form 30
Updated 1/15/2015

PURDUE UNIVERSITY
GRADUATE SCHOOL
Thesis/Dissertation Acceptance

This is to certify that the thesis/dissertation prepared

By Christopher Allen Fugger

Entitled

EXPERIMENTAL INVESTIGATION OF A TRANSVERSE REACTING JET IN A HIGH PRESSURE OSCILLATING VITIATED CROSSFLOW

For the degree of Doctor of Philosophy

Is approved by the final examining committee:

William E. Anderson
Chair

Robert P. Lucht

Steve Heister

Enrique Portillo Bilbao

To the best of my knowledge and as understood by the student in the Thesis/Dissertation Agreement, Publication Delay, and Certification Disclaimer (Graduate School Form 32), this thesis/dissertation adheres to the provisions of Purdue University's "Policy of Integrity in Research" and the use of copyright material.

Approved by Major Professor(s): William E. Anderson

Approved by: Weinong Chen 7/7/2015

Head of the Departmental Graduate Program Date

EXPERIMENTAL INVESTIGATION OF A REACTING TRANSVERSE JET IN A HIGH PRESSURE OSCILLATING VITIATED CROSSFLOW

A Dissertation

Submitted to the Faculty

of

Purdue University

by

Christopher A. Fugger

In Partial Fulfillment of the

Requirements for the Degree

of

Doctor of Philosophy

August 2015

Purdue University

West Lafayette, Indiana

ACKNOWLEDGMENTS

I would like to thank my adviser Professor William Anderson for the many research opportunities that he has given me through graduate school as well as his guidance in my research. I would also like to thank Professor Robert Lucht, Professor Steve Heister, and Dr. Enrique Portillo-Bilbao for their guidance and advisement in my research. I'm also thankful to Scott Meyer for all of his technical support, and Robert McGuire for teaching me the nuisances of machining.

I'm especially indebted to Rohan Gejji for spending long hours in the lab helping with test article setup and testing. I would also like to thank Pratikash Panda, Heather Wiest, Andrew Pratt, Robert Zhang, Mike Bedard, Brandon Kan, Mario Roa, Zach Hallum, Jared Neal, and many other lab colleagues with the additional help they provided in my test cell activities. I would also like to thank Cheng Huang for sharing his Dynamic Mode Decomposition code, and Pratikash Panda for working with me on the vector post-processing codes. I also want to thank Dr. Yen Matsutomi and Dr. Yu Matsutomi for their involvement and helpfulness in the lab early on in graduate school.

TABLE OF CONTENTS

Page

LIST OF TABLES

LIST OF FIGURES

Figure Page

Figure Page

NOMENCLATURE

JICF	Jet in crossflow
RJICF	Reacting jet in crossflow
LES	Large eddy simulation
CFD	Computational fluid dynamics
POD	Proper orthogonal decomposition
DMD	Dynamic mode decomposition
CVP	Counter rotating vortex pair
NG	Natural gas
Re	Reynolds number
PLIF	Planar laser induced fluorescence
PIV	Particle image velocimetry
CEA	Chemical equilibrium with applications
PSD	Power spectral density estimate
FOV	Field of view
J	Jet to crossflow momentum flux ratio
St	Strouhal number
R	Jet to crossflow velocity ratio
S	Jet to crossflow density ratio
2L	1st longitudinal combustor acoustic mode
4L	2nd longitudinal combustor acoustic mode
p	pressure
u	velocity
$\bar{()}$	Mean component, e.g. $\bar{u}$ is the mean velocity
$()'$	Fluctuating component about the mean, e.g. p' is the pressure fluctuation and $p' = p - \bar{p}$

$()_j$	Jet value, e.g. $\bar{u}_j$ is the mean jet velocity
$()_{cf}$	Crossflow value, e.g. u'_{cf} is the fluctuating component of the crossflow velocity
f	Frequency
T	Period
D_j	5.8 mm jet orifice exit diameter

ABSTRACT

Fugger, Christopher A. Ph.D., Purdue University, August 2015. Experimental Investigation of a Reacting Transverse Jet in a High Pressure Oscillating Vitiated Crossflow. Major Professor: William E. Anderson.

Staged combustion is one design approach in a gas turbine engine to reduce pollutant emission levels. In axially staged combustion, portions of the air and fuel are injected downstream of a lean premixed low NOx primary combustion zone. The gas residence time at elevated temperatures is decreased resulting in lower thermal NOx, and the reduced oxygen and high temperature vitiated primary zone flow further help to reduce pollutant emissions and quickly complete combustion.

One implementation of axially staged combustion is transverse fuel jet injection. An important consideration for staged combustion systems, though, is how the primary and secondary combustion zones can couple through the acoustic resonances of the chamber. These couplings can lead to additional source terms that pump energy into the resonant acoustic field and help sustain the high-amplitude combustor pressure oscillations. An understanding of these couplings is important so that it may be possible to design a secondary combustion system that provides inherent damping to the combustor system.

To systematically characterize the coupling of a reacting jet in unsteady crossflow in detail, the effects of an an unsteady pressure flowfield and an unsteady velocity flowfield are separately investigated. An optically accessible resonant combustion chamber was designed and built as part of this work to generate a standing wave unsteady vitiated crossflow at a chamber pressure of 0.9 MPa. The location of transverse jet injection corresponds to one of two locations, where one location is the pressure node and the other location the pressure anti-node of the resonant chamber acoustic mode. The injection location is optically accessible, and the dynamic inter-

actions between the transverse jet flow and the 1st and 2nd axial combustor modes are measured using 10 kHz OH-PLIF and 2D PIV.

This document analyzes five test cases: two non-reacting jet cases and three reacting jet cases. All cases correspond to jet injection near a pressure node of the 1st axial combustor mode, where the dominant flowfield fluctuations are a time-varying crossflow velocity. For the non-reacting jets, the nominal jet-to-crossflow momentum flux ratio is 19. For the reacting jets, the nominal jet-to-crossflow momentum flux ratio is 6. Two cross sectional planes parallel to the jet injection wall are investigated: 1 and 2.7 jet diameters from the jet injection wall.

The combustor crossflow high frequency wall mounted pressure data is given for each test case. The velocity and OH-PLIF data is presented as instantaneous snapshots, time and phase averaged flowfields, modal decompositions using Proper Orthogonal Decomposition and Dynamic Mode Decomposition, and a jet cycle analysis relative to the crossflow acoustic cycle.

Analysis of the five test cases shows that the jet cross sectional velocity and OH-PLIF dynamics display a multitude of dynamics. These are often organized into shear layer dynamics and wake dynamics, but are not mutually exclusive. For large unsteady crossflow velocity oscillations at the 1st axial combustor mode, both dynamics show strong organization at the unsteady crossflow frequency. Deciphering these dynamics is complicated by the fact that the ostensible jet response to the time-varying crossflow is a time-varying jet penetration. This drives the jet toward and away from the jet injection wall. These motions are perpendicular to the laser sheet and creates significant out-of-plane motions.

The amplitude of crossflow unsteadiness appears to play a role in the sharpness of the wake dynamics. For the non-reacting cases, the wake dynamics are strong and dominant spectral features in the flowfield. For the reacting cases, the wake dynamics are spectrally distinct in the lower amplitude crossflow unsteadiness case, but a large unsteady amplitude crossflow appears to suppress the spectral bands in the frequency range corresponding to wake vortex dynamics.

1. Introduction

1.1 Motivation

The requirement of compliance with emissions regulations for high efficiency gas turbines drives the development of novel combustor technologies. Combustion temperatures continue to increase for base load operation while the NOx, CO and unburned hydrocarbon emissions must go down. In recent years, the focus of gas turbine development has been increasingly placed on operational flexibility. This flexibility is needed to meet the requirements from the grid to compensate for fluctuations in energy production that result from renewables. The need to increase the operational envelope for gas turbine combustion systems is accompanied by the necessity to mitigate thermoacoustically induced combustion instabilities and minimize pollutant emissions.

Thermoacoustic combustion instability is a positive coupling between the combustor resonant acoustics and heat release oscillations. Pressure fluctuations in the combustion chamber induces fluctuations in the air and/or fuel reactants. This drives heat release oscillations either through equivalence ratio or thermal power oscillations. Combustion dynamics present a significant risk for manufacturers of lean-burning low-emission combustors. It is difficult to reproduce instabilities reliably in model combustors, and they are expensive to manage in full scale engine testing, where they can result in flame flashback, non-uniform turbine inlet conditions, increased part wear or complete part failure, increased pollutant production, lowered power output, or a decreased operating range [1]. It is a very complex problem, and accurate and detailed computations are needed to understand it [2, 3]. However, before these models can be used confidently they need to be tested against measurements from well-designed experiments.

Staged combustion is one design approach to reduce pollutant emission levels. In axially staged combustion, portions of the air and fuel are injected downstream of a lean premixed low NOx primary combustion zone to bring the gas to its final temperature. The gas residence time at elevated temperatures is decreased resulting in lower thermal NOx [2]. Additionally, the reduced oxygen and high temperature vitiated primary zone flow further help to reduce pollutant emissions and quickly complete combustion. The lowest emission combustor will optimize the multiple reactions zones over the entire engine operating range.

One implementation of axially staged combustion is transverse fuel jet injection. It is a natural and attractive mixing scheme for compact combustors as well as low-emissions staged combustion devices [4]. NOx reduction strategies using transverse fuel jets report reduced emissions under certain operating conditions [5, 6]. An important consideration for staged combustion systems, though, is how the primary and secondary combustion zones can couple through the acoustic resonances of the chamber. These couplings can lead to additional source terms that feed energy into the resonant acoustic field and help sustain the high-amplitude combustor pressure oscillations. The Rayleigh integral is used to capture the combustion-acoustic coupling and provide a measure of energy input or extraction from the acoustic field [7]. For a reacting transverse jet, the classical Rayleigh integral, equation 1.1, is the product of unsteady jet heat release $q'(x,t)$ and unsteady flowfield pressure $p'(x,t)$, where the integration is performed over one acoustic cycle [8]. A negative (positive) integral acts as a sink (source) term on the oscillating pressure field, i.e. provides acoustic damping (driving). An understanding of these couplings is important so that it may be possible to design a secondary combustion system that provides inherent damping to the combustor system.

$$\int_x \int_0^T p'(x,t) q'(x,t) dt dx \tag{1.1}$$

Of particular interest is the coupling between the hydrodynamic modes of the transverse jet and the oscillating crossflow. The formation, evolution and manip-

ulation of the jet vorticity is intimately linked to the jet penetration and mixing processes [4]. Optimal jet fluid excitation time scales have been reported for forced jets in a steady crossflow and described in terms of a universal time scale of vortex formation [9]. The range of reported jet response sensitivities to forcing amplitude, frequency and the temporal mode shape of the forcing are believed connected with the global stability characteristics of the jet hydrodynamics. For example, under critical jet-to-crossflow momentum flux ratio values the jet becomes self-excitable, exhibiting large scale oscillation modes that resist any significant response to external forcing regardless of the frequency or amplitude [4, 10]. For a reacting flow, this has implications on the heat release response from outside forcing. A globally unstable jet flame requires relatively larger forcing amplitudes before the heat release locks into the forcing frequency instead of the natural hydrodynamic mode, and even then the heat release dynamics tend to shift back toward the natural modes further along the jet [11].

To systematically characterize the coupling of a jet in unsteady crossflow in detail, the effects of an an unsteady pressure flowfield and an unsteady velocity flowfield are separately investigated. A resonant chamber is used to create an acoustic standing wave that is superimposed on a mean flow. This is the unsteady crossflow. The location of jet injection corresponds to one of two locations, where one location is the pressure node and the other location the pressure anti-node of the resonant chamber acoustic mode. The injection location is optically accessible, and the dynamic interactions between the transverse jet flow and the 1st and 2nd axial combustor modes are measured using 10 kHz OH PLIF and 2D PIV. Figure 1.1 shows the dump combustor and jet injection location.

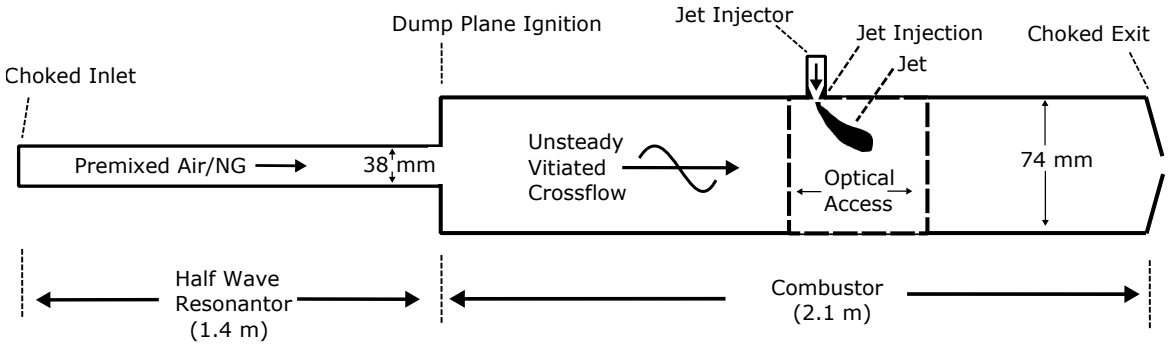

Figure 1.1.. Schematic of the optically accessible unsteady transverse jet test rig. The wavelength of the dominant combustor frequency is driven by the length from the dump plane to the chamber exit nozzle. Varying the combustor operating conditions varies the resonant chamber acoustic amplitudes. The transverse jet is injected at discrete locations in the chamber.

1.2 Document Overview

The objectives of the document and a background of transverse jets are first given. The design and operation of a resonant dump combustor for generating an unsteady vitiated crossflow at elevated operating conditions is also described. The choice of dominant resonant chamber acoustics is driven by the dump combustor length and operating conditions. For the transverse jet, a polynomial contoured injector is used with a preheated H_2/N_2 jet mixture. The injector dimensions and mixture gas temperature were carefully chosen to strategically avoid overlap of the natural injector resonances with either the dominant chamber crossflow acoustics or the jet hydrodynamics.

The document presents a focused set of 10 kHz PIV and OH-PLIF results from a larger gathered data set on non-reacting and reacting jets in unsteady crossflows for transverse jet injection near the pressure node and anti-node of the 1st and 2nd axial combustor modes. The focus for this document is on transverse jet injection at the pressure node of the 1st axial combustor mode. At this injection location, the

dominant crossflow unsteadiness is a time varying crossflow velocity about the mean. Five test cases are analyzed: two non-reacting jet cases and three reacting jet cases. The jet cross sections interrogated are parallel to the jet injection wall and bisect the jet core and jet wake.

For the non-reacting H_2/N_2 jet in a heated air crossflow, the jet is not ignited. The interrogation planes analyzed are at $Z/D = 1.0$ and 2.7, where Z is the transverse distance from the jet injection wall and D is the 5.8 mm jet orifice exit diameter. For the non-reacting operating conditions, the jet-to-crossflow momentum flux ratio is 19. The resonant crossflow chamber acoustics are not excited, however the crossflow contains low amplitude and multi-spectral unsteadiness within 0.5 kPa.

The time average velocity for planes $Z/D = 1$ and 2.7 display characteristic JICF features. These include a high velocity jet shear layer and a low velocity jet wake. The time average velocity structures grow in size further away from the jet injection wall consistent with a jet bending into the crossflow and crossflow fluid entrainment. The jet dynamics are extracted by performing a proper orthogonal decomposition (POD) and dynamic mode decomposition (DMD) on the velocity field. The POD and DMD modal decompositions at both cross sectional planes shows organized and strong wake dynamics manifested as vortex structure initiation, growth, convection and dissipation. The vortex structure frequencies correspond to well reported JICF wake Strouhal numbers.

For a reacting H_2/N_2 jet in an unsteady vitiated crossflow, the interrogation planes analyzed are at a distance of Z/D=1.0 and 2.7 from the jet injection wall. For the reacting operating conditions, the resultant jet-to-crossflow momentum flux ratio is 6. At the plane $Z/D = 1$, two reacting cases are compared for the same crossflow and jet operating conditions. The first contained low amplitude and multi-spectral crossflow unsteadiness below 5 kPa. The second contained coherent fluctuating crossflow pressure amplitudes up to 15 kPa at the 1st axial combustor mode. At the plane Z/D=2.7, one reacting case was analyzed with a crossflow fluctuating pressure amplitude up to 14 kPa at the 1st axial combustor mode.

At the plane $Z/D = 1$, the low and high amplitude crossflow cases for the reacting jet showed similar time average velocity and OH-PLIF structures. A phase average of the high amplitude crossflow case shows a jet shear layer locked into the crossflow velocity oscillations: the jet shear layer velocity increased with an increase in crossflow velocity, and decreased with a decrease in crossflow velocity. Similarly, the extracted OH-PLIF reaction front is observed to lengthen with an increase in crossflow velocity and decrease with a decreasing crossflow velocity, but with a small phase delay relative to the jet shear layer velocity pulsations. A POD and DMD analysis shows that for the lower amplitude unsteady crossflow amplitude case at the plane $Z/D = 1$, there is an increase in the spectral sharpness and strength for frequencies around 1 kHz to 1.3 kHz. This frequency range corresponds to JICF wake dynamic Strouhal numbers (based on the mean crossflow velocity) reported under non-reacting and reacting conditions. The dominance of the velocity wake frequencies in all of the reacting test cases is not as great, however, as for the non-reacting jet cases considered.

The document then provides a summary of the work followed by the major conclusions. These conclusions include: (i) two dimensional laser diagnostic measurements on a reacting unsteady jet provides relevant, but restrictive information on the jet-crossflow coupling, (ii) for the non-reacting jet cases, the time average velocity field is highly symmetric and the low velocity jet wake dynamics show distinct and strong spectral peaks at frequencies corresponding to Strouhal numbers consistent with unsteady JICF wake dynamics reported in literature, (iii) at a distance of 1 and 2.7 jet diameters from the jet injection wall, the amplitude of the crossflow unsteadiness has a clear influence on the jet velocity and OH-PLIF dynamics. For the larger amplitude unsteady crossflow case at Z/D=1 and unsteady case at Z/D=2.7, the jet velocity and reaction front lock into the crossflow acoustic frequency. The jet shear layer is in phase with the crossflow velocity. The reaction front near to the Y/D=0 centerline shows a small phase shift with the crossflow velocity. (iv) Lastly, the amplitude of crossflow unsteadiness appears to play a role in the sharpness of the wake dynamics as determined by a POD and DMD on the velocity and OH-PLIF fields.

For the non-reacting cases, the wake dynamics are strong and dominant spectral features in the flowfield. For the reacting cases, the larger unsteady amplitude crossflow appears to suppress the spectral sharpness in the frequency range corresponding to wake Strouhal numbers.

1.3 Objectives

Combustion dynamics prediction and control is a challenge in low-emission high-power GT engines. The transverse fuel jet is a candidate injection technology in axially staged combustion systems investigating lowered emissions and higher power output. It is important to understand how these fuel jets might couple with an unsteady flowfield generated from the combustion dynamics of the primary zone burners. The objective of this research is to experimentally investigate the structure and dynamics of a reacting transverse jet injected into an acoustically oscillating vitiated crossflow at elevated operating conditions representative of the engine environment. The objective is divided into three parts.

1. Engineering design, build, test, and qualify an optically accessible high pressure combustion experiment for combustion dynamic studies on injecting transverse fuel jets into acoustically oscillatory vitiated crossflows. Central to this is a simple design for numerical modeling efforts undertaken by other research groups.

2. Perform high-speed OH-PLIF and PIV on the transverse jet flame to measure the structure and dynamic coupling with the unsteady crossflow. Central to this is the production of high-quality and high spatial and temporal resolution validation data sets for numerical simulations.

3. Isolate and characterize the dominant jet flame in oscillating crossflow coupling mechanisms. An analysis tool set is created for this.

2. Background

2.1 Jet in Crossflow

A jet injected transversely into a cross flow, i.e. the jet in cross flow (JICF), is an extensively examined canonical flowfield due in part to its relevance to a variety of mixing systems [4]. For example, dilution air JICF are used for combustor and turbine gas inlet thermal management [4,12], and air and fuel JICF are used to control levels of pollutants such as NOx and CO principally by controlling the combustor mixture ratios [5, 6]. The JICF is also found in smoke stack plume dispersion and as fuel injectors for aerospace engines, e.g. scramjets.

Its wide application is typically associated with its excellent mixing characteristics as compared to a simple coflow or free jet and is thus amenable to smaller compact aerospace combustors [4]. Mixing is typically synonymous with the rich and complex vortical systems which enhance the entrainment of cross flow fluid into the jet. Figure 2.1 shows a schematic of the the transverse jet, where four dominant vortical structures are shown.

Beginning upstream of the jet, the horseshoe vortices arise from the crossflow boundary layer separation from an adverse pressure gradient leading up to the jet. These vortices are observed to wrap around the jet base and display stationary oscillating structures that extend downstream into the jet near wake region [14]. The jet wake region begins immediately downstream of the jet orifice. On the downstream and lateral sides of the jet, the wake vortices, or tornado vortices, result ultimately from the obstruction of the jet as seen to the incoming crossflow. As the crossflow fluid accelerates around the jet, an adverse wall pressure gradient is created with subsequent crossflow boundary layer separation events alternating on the sides of the jet [13]. This results in periodic eruptions of vortical structures (with axes closely

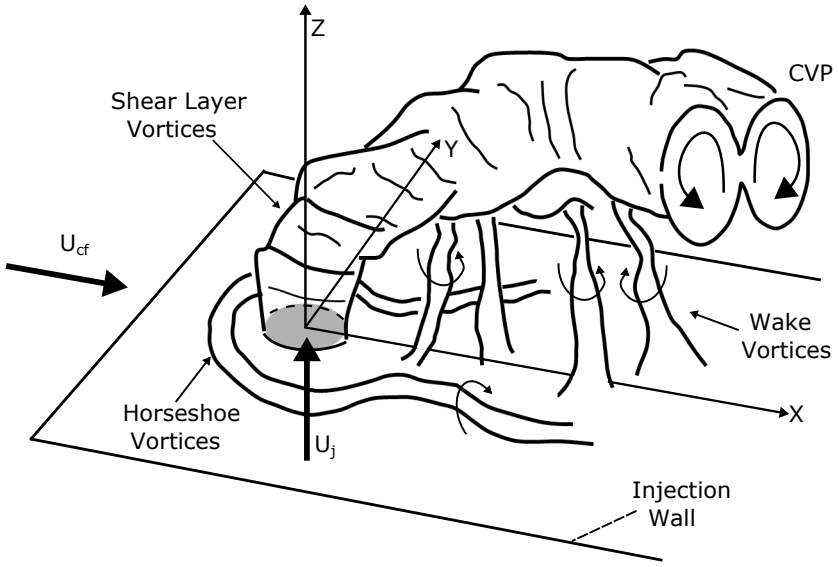

Figure 2.1.. Schematic of the transverse jet, introduced flush with respect to the injection wall. Adapted from [13].

aligned perpendicular to the wall) that are attached on one end to the wall boundary layer and entrained on the other end by the jet. The close oscillatory time scales of the wake and horseshoe vortices and the close spatial proximity to one another is suggested to be an influence in observed phase locked synchronous behavior in which the wake unsteadiness locks into the horseshoe vortex fundamental or subharmonic frequency [14].

The third major flow feature, the counter rotating vortex pair (CVP), dominates the jet cross section and is typically associated with the increased overall JICF mixing efficiency. The CVP is believed to be generated and/or sustained by the reorientation of the shear layer vortices by the cross flow and/or the vorticity generation through the jet windward and leeward pressure differences [15–17]. The shear layer vortices, at a much smaller time scale compared to the wake or horseshow structures, are the result of a Kelvin-Helmholtz instability of the transverse jet shear layer separating at the jet orifice [10]. Due to their association with the CVP and thus the overall mixing efficiency, they have been the focus of many studies over the past few decades [4].

Recent direct numerical simulation of a non reacting transverse jet showed that after a few jet diameters, most of the jet crossflow entrainment occurs on the downstream side of the jet [15]. This suggests the wake vortices may also play a role in the JICF mixing.

Typically in characterizing the JICF, the operating conditions are represented nondimensionally. The most common is the jet to crossflow momentum flux ratio

$$J = \frac{\rho_j u_j^2}{\rho_{cf} u_{cf}^2} \tag{2.1}$$

the jet to crossflow velocity ratio,

$$R = \frac{u_j}{u_{cf}} \tag{2.2}$$

the jet to crossflow density ratio,

$$S = \frac{\rho_j}{\rho_{cf}} \tag{2.3}$$

and the jet and crossflow Reynolds numbers

$$Re_j = \frac{u_j D}{\nu_j} \ , \ Re_{cf} = \frac{u_{cf} D}{\nu_{cf}} \tag{2.4}$$

where the subscript j denotes the jet, cf denotes the crossflow, and D is the jet orifice exit diameter. Flowfield JICF quantities often scale with these parameters. Employing characteristic length scales such as RD, R^2D, or JD the transverse jet centerline velocity trajectory (i.e. penetration into the crossflow) and concentration decay of the jet fluid (i.e. a measure of mixing) follow fairly closely a power law scaling. For example, the differences in mixing between the JICF and the free jet are most pronounced in the jet nearfield region ($X/D < 7$ from Figure 2.1), with a concentration decay power law exponent increase of nearly 30% for the JICF [18]. Characteristic time scales of the vortical structures are often represented by a Strouhal number

$$St_j = \frac{fD}{u_j}, \quad St_{cf} = \frac{fD}{u_{cf}} \tag{2.5}$$

where the scaling velocity depends on the apparent origin of the structure. Structures scaling with the jet velocity (and the typically relatively small jet diameters) then exhibit much higher St than hydrodynamics associated with the crossflow impulse. For example, St_cf associated with the jet wake over a large range of operating conditions usually lie within $0.1 < St_{cf} < 0.15$ [13, 19], whereas St_j for the shear layer rollup can be an order of magnitude larger. A compilation of the nominal JICF time scales is presented later combined with the relevant acoustic time scales of the experimental apparatus.

The forced transverse jet in a steady crossflow has been investigated for its potential in mixing and penetration enhancement and in understanding the physics of the jet in an unsteady environment. This approach aims to control the vorticity generation and breakdown integral to the entrainment and mixing mechanisms. There are two main types of active control forcing: (1) temporal excitation of the transverse jet fluid originating in the jet feed system [4, 9, 20–22] and (2) a time varying unsteady crossflow to explore the unsteady physics [8, 23–26] or as a control mechanism for combustion instabilities [8]. Active forcing originating in the jet has been the focus of most studies on forced JICF exploring the association of the jet shear layer instabilities with the CVP initiation, evolution and mixing. It's also a more practical solution in real devices where it would otherwise be inefficient to actuate changes in the much larger crossflow massflux to realize gains. Additionally, devices often require relatively steady influx conditions, something which an unsteady crossflow doesn't provide.

For the forced jet in a steady crossflow, the temporal excitation of the jet fluid seeks to generate time varying jet orifice exit flowfield properties. This is most often done using two experimental methods. Fast actuation valve assemblies modulate a portion of the jet fluid with the ability to produce sinusoidal [20] and square wave [22] jet exit fluctuations. More commonly, loudspeakers also produce sinusoidal and square wave excitation, but over a much larger frequency and tunability range [21, 27–29]. The specific conditions over which enhanced mixing, jet penetration or vortex structure

manipulation occur vary rather widely across the different sets of experiments. These differences have been attributed to the behavior of the JICF under different operating conditions and different hydrodynamic responses [4, 9, 30].

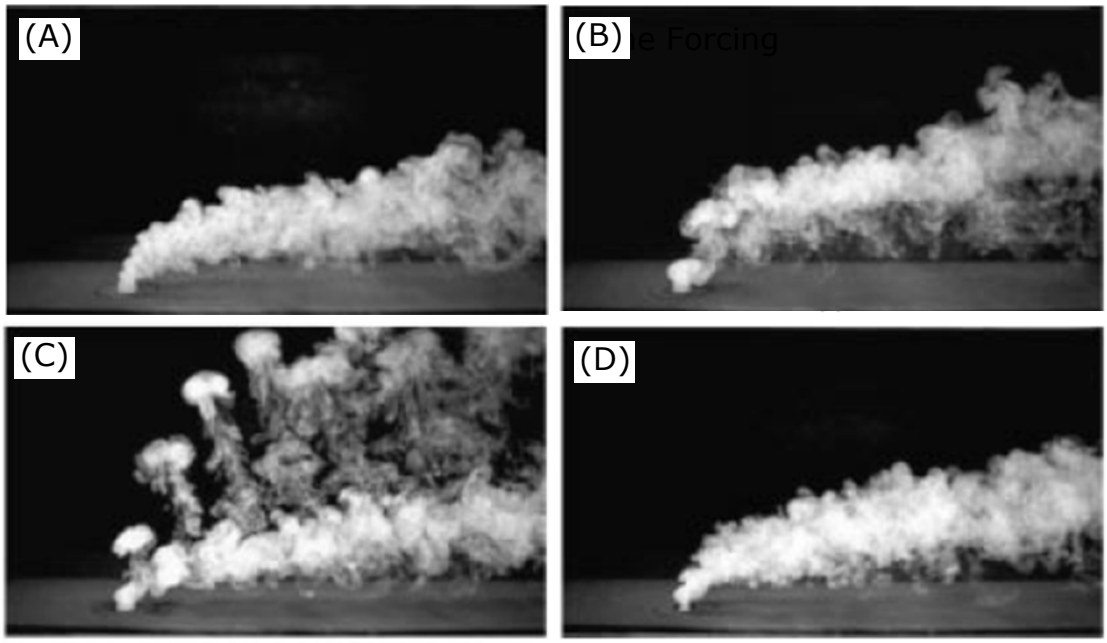

Figure 2.2.. Smoke visualization of the R = 2.58 jet for $u'_{j,RMS}/\overline{u}_{cf} = 1.4$. Re_j=1500. (A) Unforced. (B) Sine wave forcing at f= 1/3 the preferred f. (C) Square wave forcing with duty cycle of 15% at f= 1/4 the preferred f. (D) Square wave forcing at duty cycle 62% and at f = the preferred f. The preferred f=220 Hz is the unforced jet nearfield shear layer rollup frequency. Images taken from [27].

Figure 2.2 highlights the differences in jet behavior for an $R = 2.58$ operating condition. For the isodensity air jet at low R ($\approx< 3$), the jet displays minimal response under both low and high amplitude sinusoidal forcing regardless of the frequency [27]. This is not observed for higher R jets [20]. Square wave excitation (as opposed to sinusoidal) of the low R jet, however, has a profound effect on the jet under low and high amplitude forcing. Square wave excitation modulates both the forcing frequency f and duty cycle α, where the duty cycle is defined as the ratio of the velocity

fluctuation pulsation width τ to the period of the square wave excitation $T = 1/f$. Significantly increased penetration and spreading (defined as the optimal) occur for square wave duty cycles corresponding to specific pulse widths at subharmonics (see Figure 2.2) and nonsubharmonics of the natural (i.e. unforced) shear layer vortex shedding frequency [9,27]. These optimal τ are explained in terms of a universal time scale for vortex formation since these cases coincide with visible and deeply penetrating vortex rings [9]. The formation of these ring structures can be nondimensionalized with a parameter L/D, where L is a stroke length and D the jet exit diameter. For square wave pulsing, L is defined by τ multiplied by the peak to peak jet exit velocity fluctuation amplitude. Over a range of frequencies, the optimal cases were observed to fall into $L/D = 1.7 - 2$ and $3.2 - 4.2$ [9]. However, for long duty cycle forcing (e.g. sinusoidal forcing) of fully pulsed jets, strong near field interaction among the vortical structures results in a quasi steady behaving jet [30].

The hydrodynamic stability characteristics of the jet helps to clarify some of the reported JICF behavior. Notably, low R gas jets appear insensitive to sinusoidal excitation regardless of frequency or amplitude [27], while isodensity R>3.2 jets exhibit clear sensitivity to low level forcing [31]. These differences are attributed to whether the jet is convectively or globally unstable. A flow is absolutely unstable if, after an initial perturbation "push", the disturbance energy grows in time at all spatial locations (upstream and downstream) [32]. A globally unstable jet exhibits self-excited limit cycle bulk oscillations that cause the jet to be relatively insensitive to external forcing. If the disturbance energy is convected away faster than it is produced, it's referred to as a convective instability. A convective instability will act as an amplifier that spatially amplifies select initial disturbances in the downstream direction only and returns to the unperturbed steady state once the external push is removed. A convective instability is a time damped mode. For a reacting flow, the flow regime has implications on the heat release response from external disturbances (e.g. forcing). An absolutely unstable jet flame requires relatively larger forcing amplitudes before the heat release locks into the forcing frequency instead of the natural hydrodynamic

mode, and even then the heat release dynamics tend to shift back toward the natural modes further along the jet [11]. On the other hand, a convectively unstable flow is susceptible to the combustion instability phenomena.

For the transverse jet in a time-varying (unsteady) crossflow (JIUCF), a less extensive description of the flowfield is available. To the authors knowledge, there are only six known studies on this topic, two of which are for a reacting jet. In one study, a low density non reacting jet was subjected to a time-varying ambient air monotone crossflow [23]. The unsteady sinusoidal crossflow was generated by a rotating butterfly valve far upstream of the jet test section. Schlieren imaging showed the jet flapping at the crossflow frequency and a decreased instantaneous penetration and transverse spreading relative to a steady crossflow case with identical instantaneous flowfield properties.

In another experimental study, a technique was developed to physically translate the jet orifice back and forth in a steady crossflow, effectively mimicking a JIUCF [24]. The translations were sinusoidal. Figure 2.3 shows results from twelve cases varying the magnitude of crossflow fluctuation $u'_{cf}/\overline{u}'_{cf}$ and the oscillation frequency, defined as a Strouhal number $St_{cf} = fD/\overline{u}'_{cf}$. Under all cases, the unsteady crossflow organizes the jet fluid in successive large scale coherent structures formed during the low-speed phase of the crossflow cycle when the instantaneous J is large. These large clouds are connected to one another by counter rotating vortex bridges formed during the high-speed phase of the cycle when the jet penetration is lowest. The size, spacing and penetration of these structures depends on the parameters $u'_{cf}/\overline{u}'_{cf}$ and the St_{cf}. Instantaneously and in a time-average, all cases considered resulted in better dilution of the jet fluid as compared to the steady JICF case, and the time averaged jet spread was largest for higher $u'_{cf}/\overline{u}'_{cf}$ and lower St_{cf}.

It's interesting to note that in the LES study of a steady turbulent JICF, part of the enhanced JICF entrainment mechanism was attributed to the jet actively engulfing crossflow fluid on the windward side [33]. Figure 2.4 shows this. Vortical rollup on the windward and leeward jet edges eventually collide and interact, opening

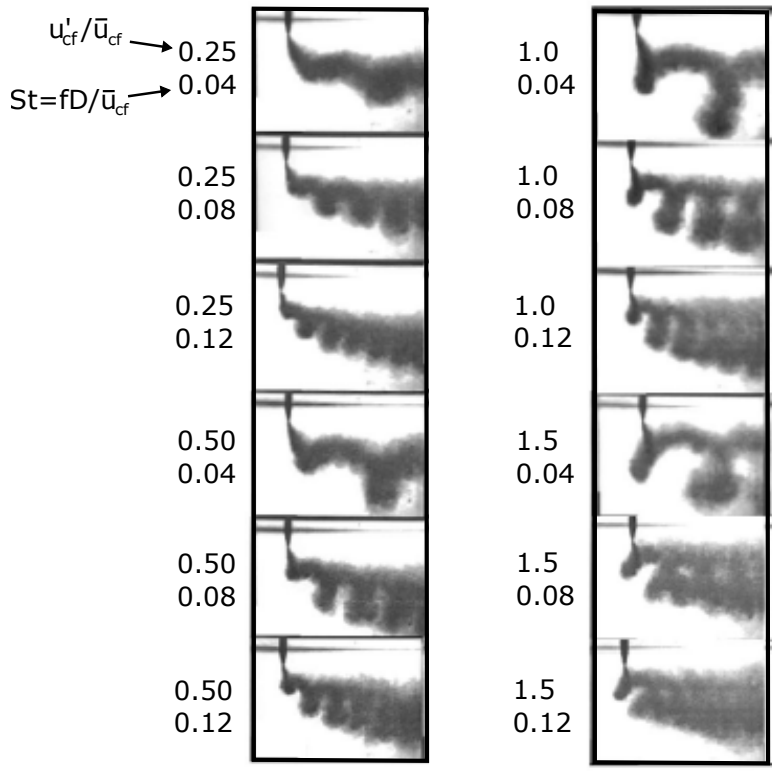

Figure 2.3.. Phase averaged jet behavior under varying unsteady crossflow amplitude and Strouhal number. Twelve cases are shown and to the left of each two numbers are shown. The first is $u'_{cf}/\overline{u}'_{cf}$ and the second is the Strouhal number $St_{cf} = fD/\overline{u}_{cf}$. Images taken from [24].

gaps on the windward edge where large pockets of crossflow fluid are engulfed (marked by arrows). The similarity with the successive large scale structures for the JIUCF in Figure 2.3 suggests the unsteady crossflow enhances mixing by driving the creation of these pockets at the crossflow frequency.

The JIUCF has also been studied computationally, more recently with the LES technique [8,25,26]. Simulations of a non-reacting R=4 jet in a sinusoidally oscillating crossflow were performed for crossflow forcing amplitudes of $0.10 < u'_{cf}/\overline{u}_{cf} < 0.50$ at frequencies $0.06 < St_j = fd_j/u_j < 0.16$ [25]. Low level forcing (10%) was reported to have minimal impact on the jet penetration, evolution, structure and dynamics. At moderate (20%) to high forcing (50%) all of these were affected. The conclusions

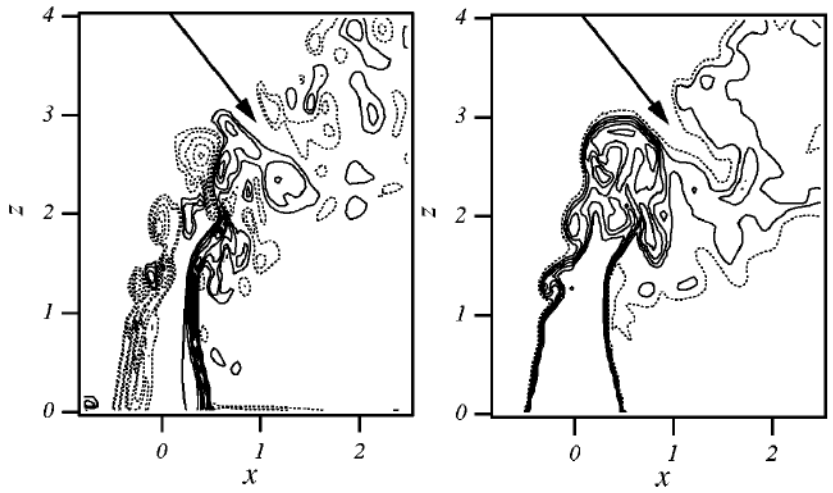

Figure 2.4.. Contours of instantaneous spanwise vorticity (left) and scalar concentration (right) on the JICF centerplane. Arrows highlight active crossflow entrainment regions. Images taken from [33].

of the study were: (i) jet flapping at the forcing frequency was present under all forcing levels and the flapping amplitude increased with an increase in forcing, (ii) the steady JICF shear layer vortex rollup became suppressed with increased forcing, (iii) monotonic jet plume breakup with increasing forcing amplitude, (iv) a reduced jet trajectory, but increased plume transverse spread for moderate to high forcing and (v) CVP modulation under high forcing, coincident with transverse elongation and spanwise compression of the jet plume and resulting in a spatial increase, but temporal decrease in mixing efficiency.

Another LES study investigated the coupling mechanism between a reacting jet and an acoustically unsteady crossflow. One objective was to understand the physics of an experimentally observed stability trend wherein an unsteady dump combustor generated and sustained an acoustically oscillating crossflow, i.e. a combustion instability, and a reacting jet injected near the 1st axial combustor pressure anti-node in certain cases caused the chamber pressure oscillations to decrease. The experiments

were run on the test rig described in this thesis as part of a related study performed by the author, which is not detailed in this document.

A major conclusion of the study was that from a minor volume change of the jet feed system plenum, the reacting jet moved from contributing system damping (through unsteady heat release according to the Rayleigh criterion, see Equation 1.1) to system driving. This was explained in terms of a jet impedance change due to the change in manifold volume. For the jet located at the pressure anti-node, flowfield pressure fluctuations drove jet heat release oscillations predominantly by two mechanisms: mass flow rate and equivalence ratio oscillations. The change in impedance shifted the phase of the jet heat release oscillations relative to the crossflow pressure fluctuations.

2.2 Dump Combustors

A dump combustor is used to generate and sustain the acoustically oscillating vitiated crossflow at discrete frequencies. The transverse fuel jet is injected perpendicularly at discrete locations in the combustor, resulting in a reacting transverse fuel jet in a vitiated oscillatory crossflow. The advantage of using a dump combustor is its operability at elevated temperatures and pressures conditions while providing an acoustically unsteady environment.

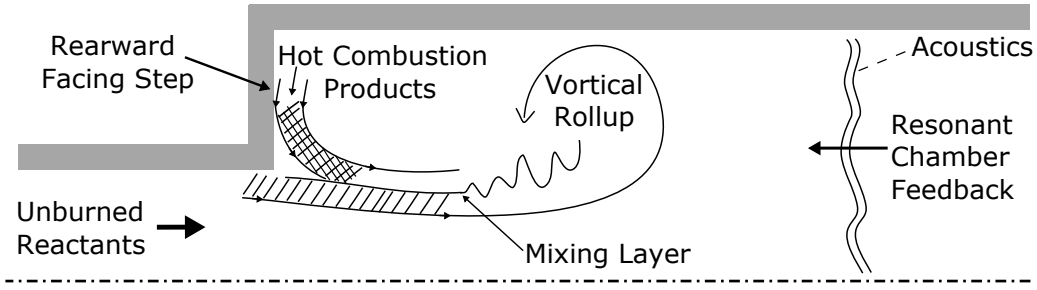

Figure 2.5.. Dump combustor flowfield. Adapted from [34].

Figure 2.5 is a representation of the flow in a rearward facing step dump combustor. The dump combustor achieves flameholding with a recirculation zone created by the sudden flow area expansion. The flowfield behind the step consists of a turbulent, reacting, reattaching mixing layer [35, 36] in which the recirculation region provides a continuous source of ignition due to the trapping of hot combustion products. Under certain geometrical and flow conditions, large scale coherent vortical structures develop at a resonant frequency of the chamber system. This is often colloquially regarded as a combustion instability if the result is resonant pressure oscillations.

The mechanism for the combustion instability is widely supported to be a function of flame vortex interactions downstream of the step in a positive feedback loop with the resonant chamber acoustics. Flame-vortex interactions cause unsteady heat release, which in turn drive the acoustic field [34,37,38]. The Rayleigh integral provides a measure of these interactions, where a positive coupling between the flowfield p and q adds energy into the acoustic flowfield. Achieving a positive closed feedback loop fundamentally relies on the appropriate phase relationship between the kinematic flowfield and the unsteady heat release.

For axial flow dump combustors with a large axial length relative to the hydraulic diameter, the resonant acoustic modes are dominantly longitudinal in nature. For a low subsonic mean flow with low amplitude acoustic oscillations, these modes resemble a standing wave oscillation superimposed on the mean flow. This has been successfully approximated as a 1D flow problem with dominant wavelength satisfying the combustion chamber length [36, 39]. The closed inlet and exhaust of a pressure vessel (e.g., choked orifice plate or converging choked nozzle) are approximated as acoustically closed, i.e. a pressure anti-node. A closed inlet and closed outlet sets the 1D fundamental wavelength to be twice the chamber length.

Bluff body, swirl and dump stabilized unstable combustors have demonstrated a wide range of excited frequencies and amplitudes by varying geometry and operating conditions. Tuned resonances of the inlet feed system can become excited due to unsteady combustion [36, 40] and can similarly drive resonant modes of the chamber

sections downstream of the dump plane [39]. Changes in the propellant mixture equivalence ratios, oxidizer-fuel choices and temperature also affect the driven excitation frequency and amplitude [41, 42].

3. Experimental System and Methods

3.1 Test Facility

The experiment is designed to robustly handle a range of operating conditions, such as preheat temperatures, chamber pressures, mass flowrates and mixtures of gases, to accommodate parametric investigations of the jet and crossflow conditions.

The forced transverse jet combustion rig is located in the Purdue University Maurice Zucrow High Pressure Laboratory. The experiment consists of multiple independently regulated and controlled gaseous flow circuits: natural gas and air for the dump combustor; nitrogen, hydrogen, natural gas, or air for the transverse jet; and nitrogen purge flows for fuel lines on both the jet and dump combustor. Figure A.1 shows a plumbing and instrumentation diagram (P&ID) of the test facility and rig. For documentation, Appendix B includes additional schematics and pictures of the hardware, test rig and optical diagnostic setup.

A natural gas fired heat exchanger provides heated non vitiated air up to 800 K at 40 bar at a flow rate up to 4 kg/s. An on-site air plant provides 0.45 kg/s of air with a 150 bar storage pressure. A secondary electric heat exchanger provides heated nitrogen or heated non vitiated air up to 40 bar at 0.25 kg/s and 900 K. On site nitrogen is available at 400 bar with a storage capability of 9000 kg and a liquid nitrogen boiloff pumped for larger continuous consumption needs. Natural gas is compressed and stored on site at 2400 bar and the composition of the gas is provided by the Panhandle Eastern Pipe Line Company for the Tuscola East segment. Hydrogen is sourced from high pressure gas cylinders at a purity of 99.8%.

To reduce pressure losses, all gas flow lines were sized to keep the fluid velocity below 30 m/s. The massflow rate of the every gas, propellant and nitrogen purges, entering the combustor is calculated. Mass flow rates of gases are controlled using the

sonic venturi, an upstream thermocouple temperature measurement and a computer controlled electronic regulator to set the pressure upstream of the venturi. For nitrogen purges, the upstream venturi pressure is set with a manually loaded regulator.

The mass flow rate is then calculated from:

$$\dot{m} = C_d A_t Y_{CR} F_{TP} P_u \sqrt{\frac{1}{R T_u^\circ}} \tag{3.1}$$

$$Y_{CR} = \left[\frac{\gamma}{Z} \left(\frac{2}{\gamma + 1} \right)^{\frac{\gamma+1}{\gamma-1}} \right]^{\frac{1}{2}} \tag{3.2}$$

$$F_{TP} = \frac{P^\circ}{P} = \left[1 - \frac{\gamma \beta^4}{2} \left(\frac{2}{\gamma + 1} \right)^{\frac{\gamma+1}{\gamma-1}} \right]^{-1} \tag{3.3}$$

Where C_d is the discharge coefficient of the venturi, R is the gas constant, A_t is venturi throat area, Y_{cr} is the critical flow function, F_{tp} is the factor correcting static pressure to total (stagnation) pressure, gamma is the ratio of specific heats, Z is the compressibility factor, and β is the ratio of the throat diameter to the upstream flow diameter. This expression is an approximation appropriate when β <0.5, which is the case for all plumbing here.

All venturis are of an ASME MFC-7M toroidal sonic venture type and, assuming turbulent flow, the discharge coefficient is:

$$C_d = 0.99354 - \frac{1.525}{Re_d^{0.5}} \tag{3.4}$$

Which has an uncertainty of +/-1%.

The specific heat ratio for mass flow rate calculation depends on the state of the gas, e.g. whether the gas is a mixture of constituents (e.g. Natural Gas) or if the gas has been preheated. For all gases except NG, the specific heat ratio and compressibility factor are calculated from the NIST database REFPROP using as input the measured temperature and pressure upstream of the venturi.

Table 3.1. Major Natural Gas Species Sandia National Lab Chemkin Coefficients and Hydrogen Chemkin Coefficients [$\frac{kcal}{molK}$]

Species	A1	A2	A3	A4	A5
Methane	3.871	-4.248×10^{-3}	2.454×10^{-5}	-2.178×10^{-8}	6.301×10^{-12}
Ethane	1.043	1.893×10^{-2}	-3.119×10^{-6}	-2.774×10^{-9}	7.586×10^{-13}
Propane	0.200	3.233×10^{-2}	-1.177×10^{-5}	1.511×10^{-9}	-7.737×10^{-13}
I-Butane	-1.535	5.526×10^{-3}	-4.056×10^{-4}	1.968×10^{-8}	-5.226×10^{-12}
N-Butane	-1.228	5.042×10^{-2}	-2.842×10^{-5}	9.297×10^{-9}	-2.265×10^{-12}
Pentane	-2.275	7.068×10^{-2}	-5.166×10^{-5}	2.332×10^{-8}	-5.728×10^{-12}
Nitrogen	3.696	-1.298×10^{-3}	2.464×10^{-6}	-9.380×10^{-10}	-3.703×10^{-14}
Carbon Dioxide	1.996	1.170×10^{-2}	-1.427×10^{-5}	1.03×10^{-8}	-3.197×10^{-12}
Hydrogen	0.358	-0.622×10^{-3}	0.152×10^{-5}	-0.164×10^{-8}	0.737×10^{-12}

Determining the flowrate for NG requires knowledge of the constituents. The mole fractions of the NG constituents are provided by the NG supplier via their daily updated website [43]. The procedure for calculating the specific heat and compressibility factor of NG is taken from [44] and is repeated here for completeness. The heat capacity for each species is calculated from a polynomial curvefit using the Chemkin Thermodynamics database (see Table 3.1) to obtain the coefficients

$$\frac{C_{pi}}{R_u} = A_1 + A_2 T_{measured} + A_3 T^2_{measured} + A_4 T^3_{measured} + A_5 T^4_{measured} \tag{3.5}$$

Since the velocities of the gas are designed to be lower than 30 m/s (M<0.3), the gas temperature directly upstream of the venturi is used in Equation 3.5. The average specific heat ratio for the NG was 1.33. After calculating the heat capacity for each species, the heat capacity is multiplied by the mole fraction of each species. The compressibility factor is determined by first calculating the reduced temperature (T_R) and pressure (P_R):

$$P_R = \frac{P}{P_{CR}} \ , \ T_R = \frac{T}{T_{CR}} \tag{3.6}$$

where P_{CR} and T_{CR} are the critical pressure and temperature, respectively. For the following calculations, the temperature and pressure upstream of the venturi are used. The compressibility factor for the NG is determined through the Standing-Katz chart [45]. In the Dranchuk & Abou-Kassem method, the compressibility factor can be calculated from [46]:

$$Z = \left[A_1 + \frac{A_2}{T_{pr}} + \frac{A_3}{T_{pr}^3} + \frac{A_4}{T_{pr}^4} + \frac{A_5}{T_{pr}^5}\right]\rho_r + \left[A_6 + \frac{A_7}{T_{pr}} + \frac{A_8}{T_{pr}^2}\right]\rho_r^2 - A_9\left[\frac{A_7}{T_{pr}} + \frac{A_8}{T_{pr}^2}\right]\rho_r^5 + \frac{A_{10}}{T_{pr}^3}\left[1 + A_{11}\rho_{pr}^2\right]\rho_{pr}^2 e^{-A_{11}\rho_{pr}^2} + 1 \tag{3.7}$$

where ρ_{pr} is the reduced density and is given by:

$$\rho_{pr} = \frac{0.27 P_{pr}}{Z T_{pr}} \tag{3.8}$$

The terms P_{pr} and T_{pr} are pseudo-reduced pressure and temperature, respectively,

$$P_{pr} = \frac{P}{P_{pc}} \quad T_{pr} = \frac{T}{T_{pc}} \tag{3.9}$$

where P_{pc} and T_{pc} are the pseudo-critical pressure and temperature, respectively. The pseudo-critical pressure and temperature are calculated using [47]:

$$P_{pc} = \sum_{i=1}^{k} x_i P_{pi} \quad T_{pc} = \sum_{i=1}^{k} x_i T_{ci} \tag{3.10}$$

where P_{ci} and T_{ci} are the critical pressure and temperature for the constituent i of the NG, respectively, k is the number of constituents, and x_i is the mole fraction of the constituent i. The values for the critical pressure and critical temperature for typical NG compositions can be found in [47].

The coefficients A_1 through A_{11} in Equation 3.7 were determined by fitting the Standing-Katz chart [48]. The coefficients are shown in Table 3.2. Equations 3.7 and

Table 3.2. Coeffcients of Dranchuk & Abou-Kassem method

$A_1 = 0.3265$	$A_2 = -1.0700$	$A_3 = -0.5339$	$A_4 = 0.01569$
$A_5 = -0.05165$	$A_6 = 0.5475$	$A_7 = -0.7361$	$A_8 = 0.1844$
$A_9 = 0.1056$	$A_{10} = 0.6134$	$A_{11} = 0.7210$	

3.8 are implicit and are solved iteratively. Plugging Equation 3.8 into Equation 3.7 yields:

$$f(\rho_r) = [A_1 + \frac{A_2}{T_{pr}} + \frac{A_3}{T_{pr}^3} + \frac{A_4}{T_{pr}^4} + \frac{A_5}{T_{pr}^5}]\rho_r + [A_6 + \frac{A_7}{T_{pr}} + \frac{A_8}{T_{pr}^2}]\rho_r^2 - A_9[\frac{A_7}{T_{pr}} + \frac{A_8}{T_{pr}^2}]\rho_r^5 + \frac{A_{10}}{T_{pr}^3}(1 + A_{11}\rho_r^2)\rho_r^2 e^{-A_{11}\rho_r^2} + 1 - \frac{0.27P_{pr}}{T_{pr}\rho_r} \quad (3.11)$$

where the roots can found using the Newton-Raphson method. Once ρ_r is determined, the compressibility factor is calculated from Equation 3.8. The compressibility factor calculated using this method has an average error of 0.59% and is applicable over the ranges [48]:

$$0.2 < P_{pr} < 30 \ , \ 1.0 < T_{pr} < 3.0 \quad (3.12)$$

For the test conditions presented, the compressibility factor for the NG falls within the range of 0.85 to 0.99.

Control and low frequency data acquisition at 100 Hz is performed using a labview 2012 virtual instrument (VI) program. Pressure measurements for mass flow rate calculation and system health monitoring are made using Druck PMP 1260 transducers with 0.25% full scale accuracy. Temperature measurements are made using Omega grounded type-K thermocouples with 0.75% error and are rated up to 1523 K. Analog input of pressure and temperature are signal conditioned using, respectively, and read in with the ADC PCI-6052E. Analog output and digital output control are provided by NI PCI 6733 cards and NI PCI-6534, respectively.

3.2 Mass Flow Uncertainty Analysis

To calculate the error or uncertainty in the mass flow rates, the errors in each of the components in the massflow calculation equation are combined using the root-sum-square method. The relative uncertainty of the gaseous mass flow rate is

$$\left(\frac{\triangle \dot{m}}{\dot{m}}\right)^2 = \left(\frac{\triangle C_d}{C_d}\right)^2 + \left(\frac{\triangle D_t}{D_t}\right)^2 + \left(\frac{\triangle P_u}{P_u}\right)^2 + \frac{1}{4}\left(\frac{\triangle Z}{ZY_{cr}}\right)^2 + \frac{1}{4}\left(\frac{\triangle T_u^o}{T_u^o}\right)^2 \quad (3.13)$$

where $\triangle$ denotes the error or uncertainty in the quantity, D_t is the venturi throat diameter, and $\frac{\triangle \dot{m}}{\dot{m}}$ is the relative uncertainty in the mass flow rate. The nominal machining diameter tolerance for the venturis is $\pm$ 0.0127 mm for venturi diamaters greater than 2.54 mm and $\pm$ 0.00635 mm otherwise. The relative uncertainty of the air and nitrogen mass flow rates was $\pm$1.1%, and the relative uncertainty of the hydrogen mass flow rate was also $\pm$1.1%. The largest contribution to the mass flow uncertainty is the discharge coefficient uncertainty. The relative uncertainty of the natural gas mass flow rate was $\pm$2.3%, where a bulk of this uncertainty is derived from the uncertainty in the natural gas composition.

3.3 Dump Combustor Assembly

Figure 3.1 shows the transverse jet model combustor. It consists of two main components: a dump combustor that generates the oscillating crossflow, and transverse jet downstream in an optically accessible test section that allows visualization of the reacting flowfield around the jet. The dump combustor burns a premixed, preheated air and fuel mixture. Preheated non-vitiated air is premixed with the NG fuel in the main premixer. The NG is issued into the premixer using a fuel peg, which is a small sealed quarter inch stainless steel tube with four 1.3 mm (0.05) diameter holes: two pointing into and two pointing perpendicular to the incoming air flow. Four cylindrical bluff bodies in the premixer arranged in an alternating pattern of horizontal and vertical orientations enhance the mixing of the air and fuel.

A choked orifice plate follows the premixer to minimize acoustic coherence with the combustor resonant acoustics to ensure a constant chamber inlet mass flow rate. The orifice plate contains 9 square edge orifices (arranged in a 3 by 3 square grid) with an orifice diameter of 4.4 mm and a length to diameter ratio 5.75. A constant area half-wave resonator of the combustor section serves as the combustor inlet. The premixed flow is ignited by a spark about 0.08 m downstream of the dump plane. Combustion is stabilized at the dump plane rearward facing step due to the recirculation zone created by the sudden flow expansion. The combustor has a constant cross sectional area of 0.006 m^2. It is terminated with a linearly converging choked nozzle that provides a nominal mean chamber pressure of 0.9 MPa.

The dump combustor and half-wave resonator inlet are assembled from smaller length module test sections, where the lengths of both can be discretely and independently varied by either removing or adding module test sections. The modular test sections are fabricated using structural steel square tube welded to ANSI pipe flanges. The half-wave resonator is made using 50.8 mm OD square tube sections with 6.4 mm wall thickness. The dump combustor (not including the optical test section) is made using 101.6 mm OD square tube sections with 12.7 mm wall thickness. Spiral wound gaskets are used for sealing between the pipe flanges. One module test section is replaced with an optically accessible test section, and its axial location can be discretely varied in the dump combustor. The optical test section houses the transverse jet injector. Figure 3.1 shows the transverse jet injection location 1.11 m downstream of the dump plane. Figure B.1 shows an assembly configuration with the transverse jet injection location 1.68 m downstream of the dump plane.

Figure 3.2 and 3.3 shows a transverse and streamwise cross sectional schematic diagram, respectively, of the optical test section, where three of the four walls contain machined fused quartz windows. The windows are 125 mm by 72 mm in the streamwise and spanwise direction, respectively, and sit flush with the inner flow path. High-temperature graphoil is used as a gasket for sealing between the cube and windows and has not been found to significantly degrade due to the vitiated combus-

tor environment. The fourth optical test section wall contains a generically designed port feature for multi-purpose use. It accommodates both wall flush mounted and extended nozzle transverse jet injection. The optical design permits direct line-of-sight with a wall flush mounted jet orifice and good optical access upstream and downstream of the jet. A 76 mm length transition duct directly precedes the optical test section and reduces the inside corner radii of the structural square tubing down to the small radii of the optical test section. The cross sectional area along the length of the transition section is fixed to minimize adverse pressure gradient effects. A rectangular optical section design allows for the use of flat windows and permits line-of-sight viewing of the injection wall.

Pressure and temperature instrumentation ports are located throughout the experiment. The 100 Hz low frequency data system instrumentation provide system health monitoring and mean flow properties. Both instrumentation mate with stainless steel fittings welded directly to the experiment. Low frequency pressure transducers (LP) are connected using an approximately 120 mm length 6 mm stainless steel tube mated to the fitting. This standoff reduced the transducer heat load. Thermocouples (TC) are connected using Swagelok fittings and are inserted into the flowpath to varying degrees based on the need and location. Inside the dump combustor, the thermocouples protrude approximately 6 mm into the flow. The high frequency pressure transducer ports are custom made from stainless steel round bar and welded to the experiment, except for the optical test section where the port is machined directly into the body of the test article. The locations of LP, TC and the high frequency pressure transducers (P) on the experiment are shown in each rig assembly schematic. For example, Figure 3.1 shows the location of the combustor instrumentation. More high frequency instrumentation ports exist than are used for the work herein. The HF pressure ports that are used herein are appended with a number, e.g. P1 is the transducer closest to the combustion chamber exit nozzle. For a given test, a total of ten HF pressure transducers are recorded. The remaining transducer locations not utilized are plugged.

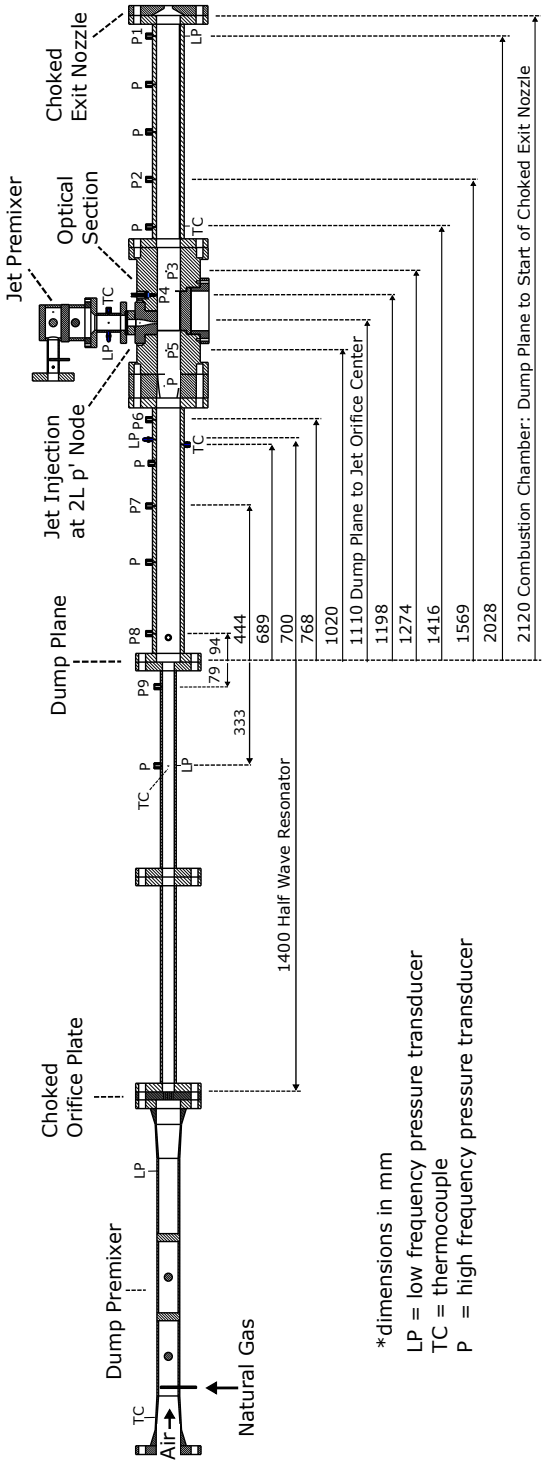

Figure 3.1.. Unsteady transverse jet rig. The transverse jet injection location here is 1.11 m downstream of the dump plane. High frequency pressure locations with installed transducers for this work are appended with a number, e.g. P1.

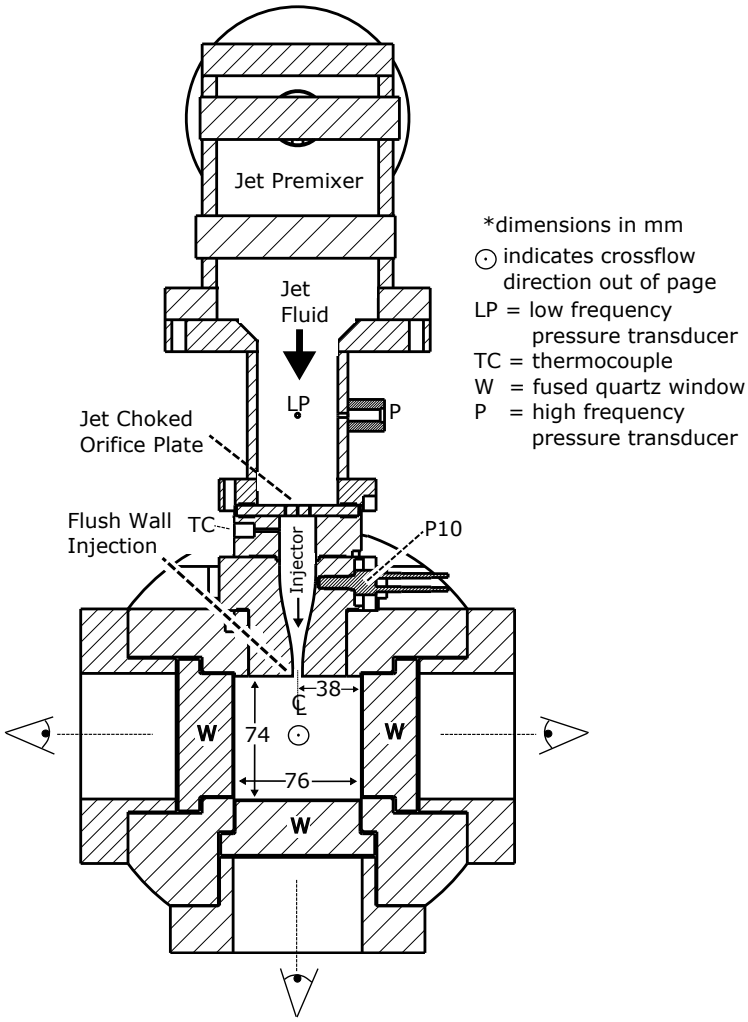

Figure 3.2.. Transverse cross sectional schematic of the optically accessible test section.

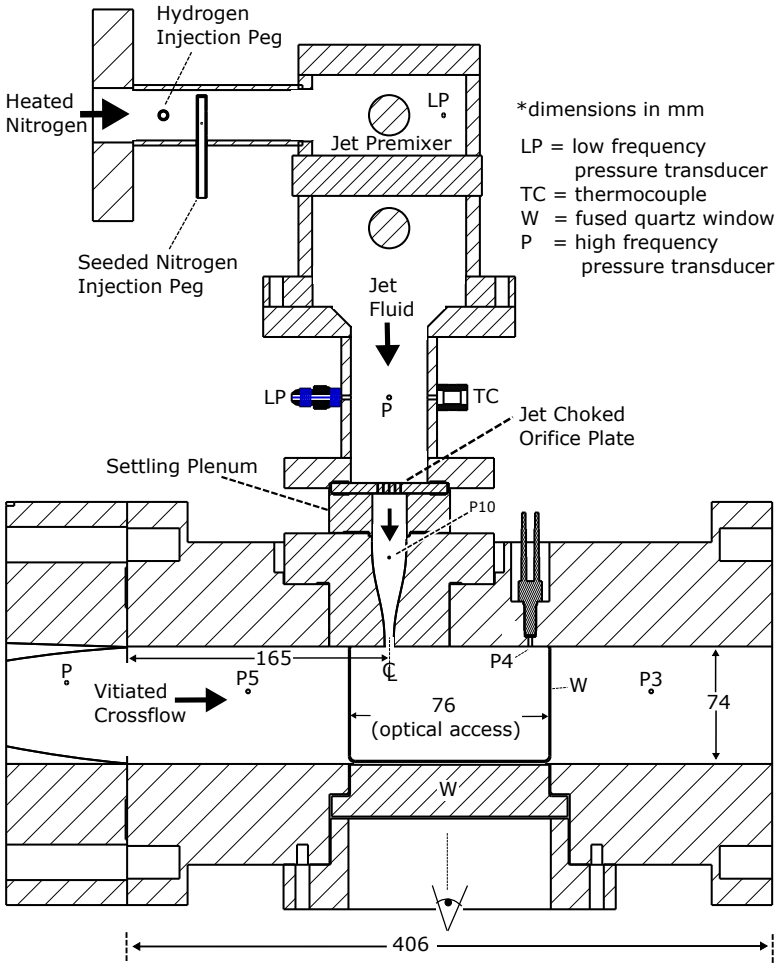

Figure 3.3.. Streamwise cross sectional schematic of the optically accessible test section.

3.4 Transverse Jet Assembly

The transverse jet injector is designed for specific acoustic properties to control its coupling with the rig acoustics and JICF hydrodynamics. To minimize injector feed system coupling, the injector inlet is choked and the volume of the injector is reduced. Reducing the injector volume in this way serves to increase the natural injector bulk mode frequency away from the relatively low frequency combustor $2L$ and $4L$. Section 3.5.2 details the injector acoustic design considerations relative to the time scales of the test rig and jet hydrodynamics.

The injector assembly consists of a premixing chamber, a choke plate, a settling plenum and the jet nozzle. Figure 3.4 shows a schematic diagram of the transverse jet injector. The transverse jet fluid is a premixed preheated 60/40 mixture (by moles) of hydrogen and nitrogen, respectively. Three separately controlled and metered propellant lines feed the premixing chamber (see Figure 3.3): a primary nitrogen circuit, a hydrogen circuit and a secondary nitrogen circuit. The secondary nitrogen circuit flow at ambient temperature is routed through a pressurized fluidized bed TiO_2 seeding vessel for the PIV diagnostic. A sonic venturi downstream of the seeding vessel, but upstream of the premixer meters this flow. The primary nitrogen circuit is routed through an electric heater and the gas temperature is varied to achieve the necessary injector 60/40 H_2/N_2 mixture temperature. The heated N_2 circuit sonic venturi is downstream of the heater and upstream of the premixer. The hydrogen sonic venturi is located directly upstream of the premixer. Mixing is achieved in the premixing chamber with multiple bluff bodies and a long residence.

An orifice plate with an array of evenly spaced 0.04 mm holes provides a large pressure drop ($\triangle P/P = 0.56$) between the premixing chamber and the injector body. This ensures that the mass flow rate from the premixing chamber is constant and independent of any pressure oscillations occurring inside the jet nozzle. The orifice jets mix out in a discretely variable length circular settling plenum of constant diameter that matches the starting diameter of the injector nozzle contour. The discretely

A	Plenum Reservoir Diameter	48 mm
B	Settling Plenum Diameter	21.7 mm
C	Settling Plenum Length	30 mm
D_j	Exit Orifice Diameter	5.8 mm
E	Nozzle Contour Length	66 mm

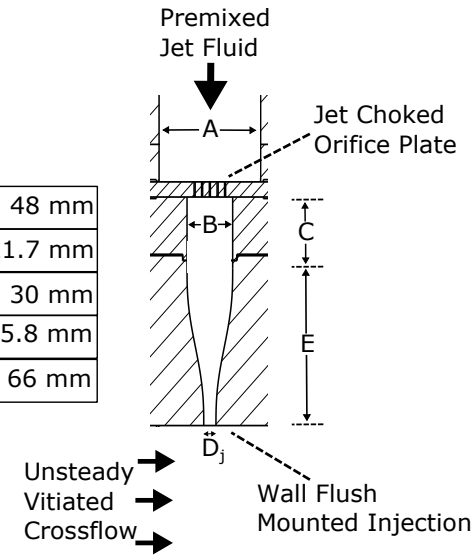

Figure 3.4.. Transverse jet injector consisting of a choked orifice plate, settling plenum, and a contoured converging nozzle. The overall length and volume were designed to avoid overlap of the natural injector resonances with either the dominant crossflow acoustics or jet hydrodynamics.

variable length settling plenum is designed as a tuning parameter to adjust the resonant characteristics of the injector, and for this study was fixed at a length of 30 mm. The circular jet nozzle has a fifth order polynomial contraction contour, a 5.8 mm diameter orifice exit, an inlet to jet exit contour area ratio of 14, and a contour length of 66 mm. Equation 3.14 gives the polynomial diameter nozzle contraction contour $Diameter(\epsilon)$ as a function of the distance leading up to the jet orifice exit.

$$Diameter(\epsilon) = D_j + \frac{10(B-D_j)}{E^3}\epsilon^3 - \frac{15(B-D_j)}{E^4}\epsilon^4 + \frac{6(B-D_j)}{E^5}\epsilon^5 \ , \ 0 \leq \epsilon \leq E \tag{3.14}$$

The injector contour profile design methodology was provided by Dr. Ann Karagozian of UCLA. The nozzle contraction contour is an academic JICF style injector used in other subsonic transverse jet research groups under non-reacting and reacting conditions and is associated with a top hat velocity profile at the jet exit with a relatively

small jet momentum thickness [10, 27, 49]. For the wall flush mounted 5.8 mm exit diameter jet nozzle herein, the optical access afforded is 24.9 mm upstream and 101 mm downstream of the jet orifice exit centerline. The upstream edge of the jet orifice is 163 mm downstream of the start of the cube test section.

Ignition of the transverse fuel jet relies on the hot vitiated crossflow. A separate igniter for the jet is not provided. For test cases with only a preheated air crossflow, the transverse jet therefore is a non-reacting jet in crossflow.

3.5 Rig Acoustics

To spatially and temporally measure the unsteady acoustic pressure, the experiment is highly instrumented with HF pressure transducers (Kulite models EWCT-212M-10BARA and WCT-212M-70BARA) to spatially and temporally characterize the non-reacting and reacting gas unsteady flowfield. The HF pressure transducers are recorded on a separate 16 channel high-speed data system (DSPcon DataFlex 1000A, Control Module S/N 104024 and Analog Module S/N 105933) sampling at 180 kHz per channel. The dump combustor longitudinal resonant acoustics are under 2 kHz and are resolved with high temporal resolution for the 90 kHz Nyquist data system sampling rate.

Synchronization between the HF data system and the low frequency data system is achieved with a square wave TTL pulse simultaneously sent to both data systems. For tests with optical measurements, 10-12 HF data channels are dedicated to recording HF pressure transducer data and the remaining channels reserved for recording camera triggers and camera exposures. During data post-processing, these signals are used to temporally align the HF pressure data and the recorded optical data for a direct comparison between the unsteady acoustic flowfield and the transverse jet LIF and PIV data.

For HF pressure behavior, three locations are focused on: P1, P5, and P10. These locations at a minimum provide enough information to describe the crossflow funda-

mental acoustic behavior for comparing with the optical diagnostic data. The location P1 is in the crossflow and directly upstream of the combustion chamber exit nozzle. This location is close to the chamber $2L$ p' anti-node and provides a good measure of the $2L$ p' modeshape amplitude. It also provides a good measure of most chamber acoustics p' modeshape amplitudes since it's directly upstream of the exit nozzle (solid boundary). The location P5 is in the crossflow and directly upstream of the jet injection location. The location P10 is inside the injector. Figure 3.1 shows the locations of P1 and P5 in the chamber.

3.5.1 Dump Combustor

The half-wave inlet half-wave combustor provides dominant longitudinal resonant acoustics in the combustor at the 2L (near 200 Hz) and its harmonics 4L (near 400 Hz) and 6L (near 600 Hz). The pressure oscillation amplitudes and dominant modes are manipulated by discretely varying the combustor geometry, e.g. inlet resonator length, and the combustor inlet operating conditions: the preheated air temperature and the equivalence ratio.

Figure 3.5 shows representative spectral behavior of the dump combustor exciting the 2L, 4L and 6L resonant chamber modes, each corresponding to a different operating condition. These cases were taken from tests with both the dump combustor and the injected transverse fuel reacting. Since the combustor is naturally self-excited thermo-acoustically, a power spectrum of pressure typically contains peaks located at many of the combustor longitudinal modes, regardless of the operating condition. For a test, the geometry and operating condition is strategically chosen to isolate the target crossflow oscillation amplitude and frequency with minimal interference from other modes near the jet injection location.

Figure 3.5 also shows unfiltered high frequency pressure over the time slices corresponding to spectra in Figure 3.5 (A) and (C) highlighting the temporal evolution for a single dominant frequency or for codominant crossflow frequencies. Peak-to-

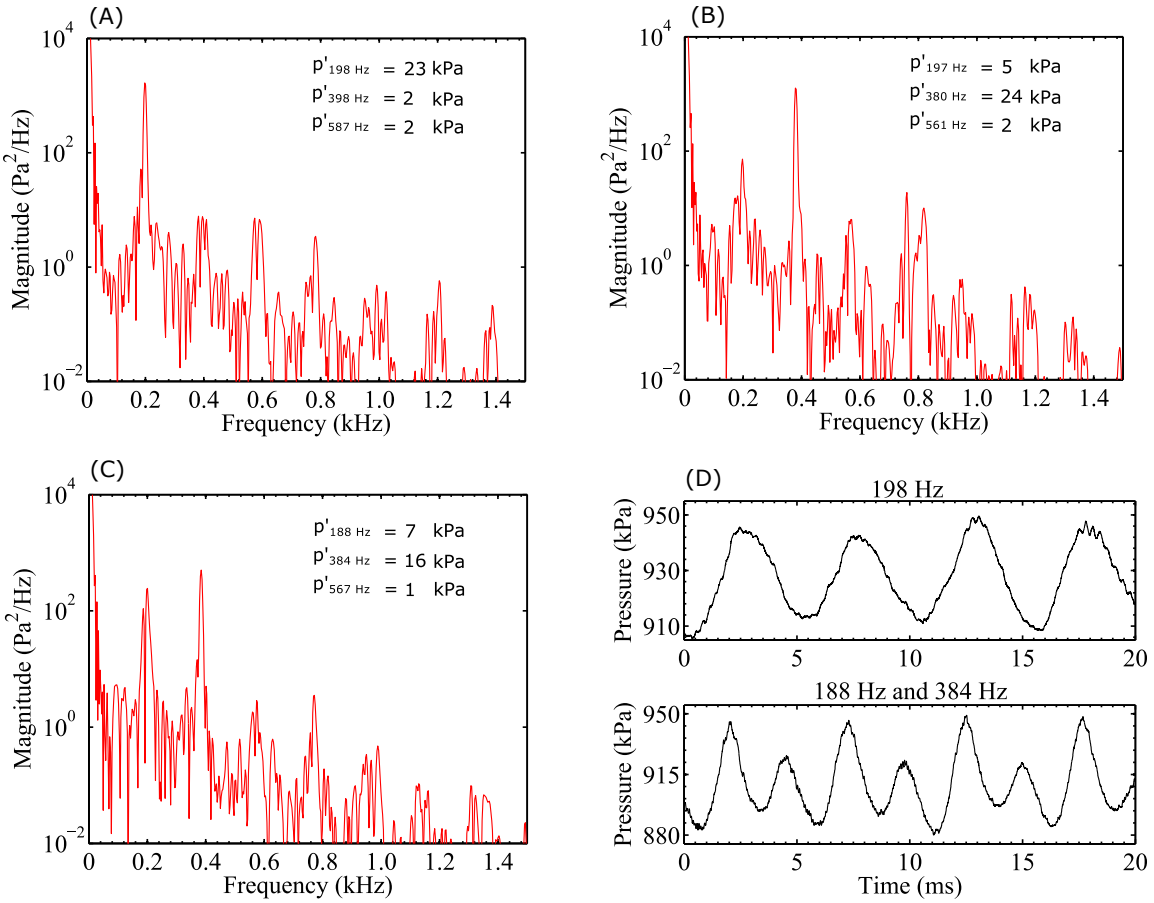

Figure 3.5.. Pressure PSD from different hot-fire tests showing excitation of the crossflow $2L$ (A), $4L$ (B), and $2L$-$4L$ combination (C). Time traces of the raw pressure are shown in (D) for a single dominant crossflow frequency (top: $2L$ 198 Hz) and a case where the $2L$ (198 Hz) and $4L$ (384 Hz) are both active (bottom).

peak pressure oscillation amplitudes (peak to trough) of the 2L, 4L and 6L have been repeatedly measured in this combustor up to 20% of the 0.9 MPa mean chamber pressure for certain operating conditions. At these high amplitudes, the resonant acoustics are highly nonlinear and resemble steep fronted traveling waves. Typically, though, tests are selected where the peak-to-peak amplitudes are between 1-8% of the mean chamber pressure, both for practical relevance to real devices and to ensure the transverse jet flame phenomenon is not dominantly a blowoff-reignition cycle due

to higher amplitude crossflow pertubations. At the 1%-8% amplitudes, the chamber acoustic behavior is temporally relatively linear, which is observed by noting the sinusoidal resemblance in the raw pressure traces at a fixed combustor location.

The lower amplitude chamber acoustics are also relatively spatially linear. Figure 3.6 shows representative instantaneous and averaged pressure spatial mode shapes for the 2L, 4L and 6L acoustic modes downstream of the dump plane for test cases where both the dump plane and transverse jet are reacting. A sinusoid highlights the similarity with a linearized acoustic. Starting at the combustor dump plane, the top plots show one pressure node and two anti-nodes out of phase relative to one another by one half of a period T/2; this is the 2L mode of the dump combustor and inlet resonator combination. Starting at the dump plane, the 4L mode contains two nodes and three anti-nodes, and the 6L mode contains three nodes and four anti-nodes.

To separately measure the jet coupling due to a surrounding flowfield pressure anti-node and pressure node, the transverse jet is injected either at a location 1.11 m or 1.68 m downstream from the dump plane. The location 1.11 m is close to the 2L pressure node and 4L pressure anti-node, and the location 1.68 m is close to the 2L pressure anti-node and the 4L pressure node. These are indicated by vertical dotted lines in Figure 3.6. By varying the combustor operating conditions, either a pressure node or anti-node is generated surrounding the jet injection location.

Figure 3.7 gives a qualitative description of one cycle of the combustion chamber $2L$ mode for jet injection at the 1.11 m location. First, define the pressure oscillation amplitude p' by $p = \overline{p} + p'$, where p is the actual instantaneous pressure and $\overline{p}$ is the time-average pressure. Similarly, define the velocity oscillation amplitude u'_{cf} by $u_{cf} = \overline{u}_{cf} + u'_{cf}$, where u_{cf} is the actual instantaneous crossflow velocity and $\overline{u}_{cf}$ is the time-average crossflow velocity.

The start of the cycle at 0^o is defined as a high pressure ($p' > 0$) at the chamber exit nozzle and a low pressure at the dump plane ($p' < 0$). The crossflow velocity at the point of jet injection is momentarily at its mean value. Between 0^o and 90^o the chamber exit pressure decreases and the crossflow velocity fluctuation u'_{cf} becomes

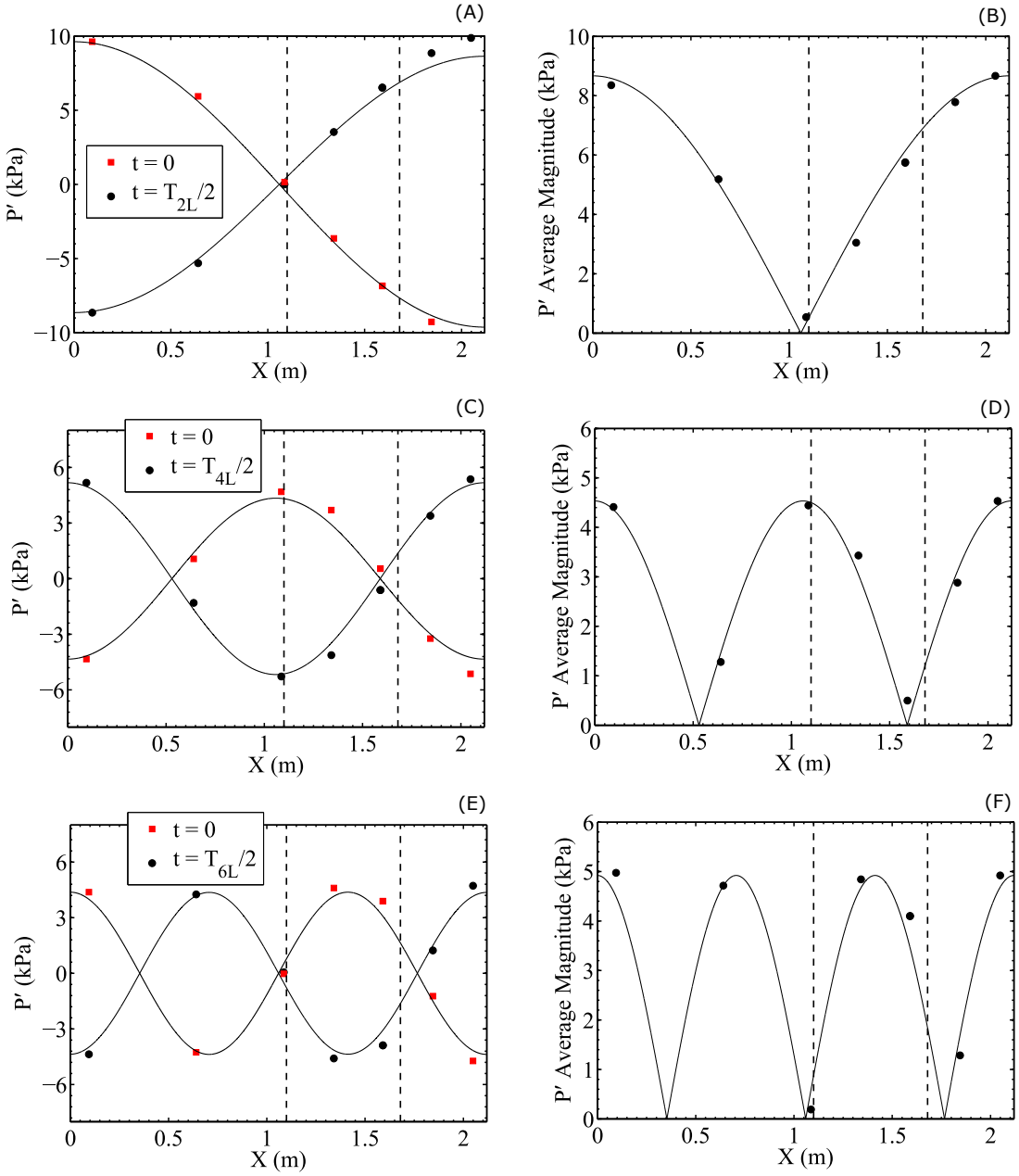

Figure 3.6.. Combustion chamber acoustic pressure mode shapes. Instantaneous snapshot is shown for the $2L$ (A), $4L$ (C), and $6L$ (E). A time averaged mode shape magnitude is shown for the $2L$ (B), $4L$ (D), and $6L$ (F). Data points represent pressure locations. The two jet locations are indicated by vertical dotted lines. X=0 is the dump plane.

negative causing the actual crossflow velocity at the jet to decrease below its mean value. At 90^o, $|-u'_{cf}|$ is largest and the crossflow is at the lowest speed for the cycle at the jet. Between 90^o and 180^o, the chamber exit pressure continues decreasing and the crossflow velocity begins increasing again. At 180^o, $u'_{cf} = 0$ and $u_{cf} = \overline{u}_{cf}$. Between 180^o and 270^o, the chamber exit pressure starts increasing from its minimum value, and the crossflow at the jet location is accelerating toward its maximum cycle speed, which happens at 270^o. As the chamber exit pressure stops increasing, the cycle is complete.

3.5.2 Jet Injector and Problem Time Scales

The transverse jet injector is designed to have a small volume with a choked inlet to minimize injector coupling with the crossflow acoustics. The injector nozzle cavity has unavoidable natural acoustic resonances that are a function of the geometry, gas properties, and boundary conditions. Exciting these frequencies can lead to biasing the displayed JICF dynamics. In conjunction with an FEA analysis, the injector geometry and gas properties are chosen to avoid significant overlap of the injector natural resonances with the unsteady crossflow frequencies and the JICF hydrodynamics.

Time scales of the crossflow acoustics, injector cavity resonances, and reported JICF vortex structures were considered. Table 3.3 gives a compilation of time scales as frequencies f nondimesionalized as a Strouhal number, equation 3.15, where either the mean jet or mean crossflow velocity is used, $\overline{u}_j$ and $\overline{u}_{cf}$, respectively, and D is the jet orifice exit diameter. For each reported St, Table 3.3 indicates the reported Reynolds number for the jet and crossflow, Re_j and Re_{cf}, respectively, and the jet-to-crossflow momentum flux ratio J.

$$St_j = \frac{fD}{\overline{u}_j}, \quad St_{cf} = \frac{fD}{\overline{u}_{cf}} \tag{3.15}$$

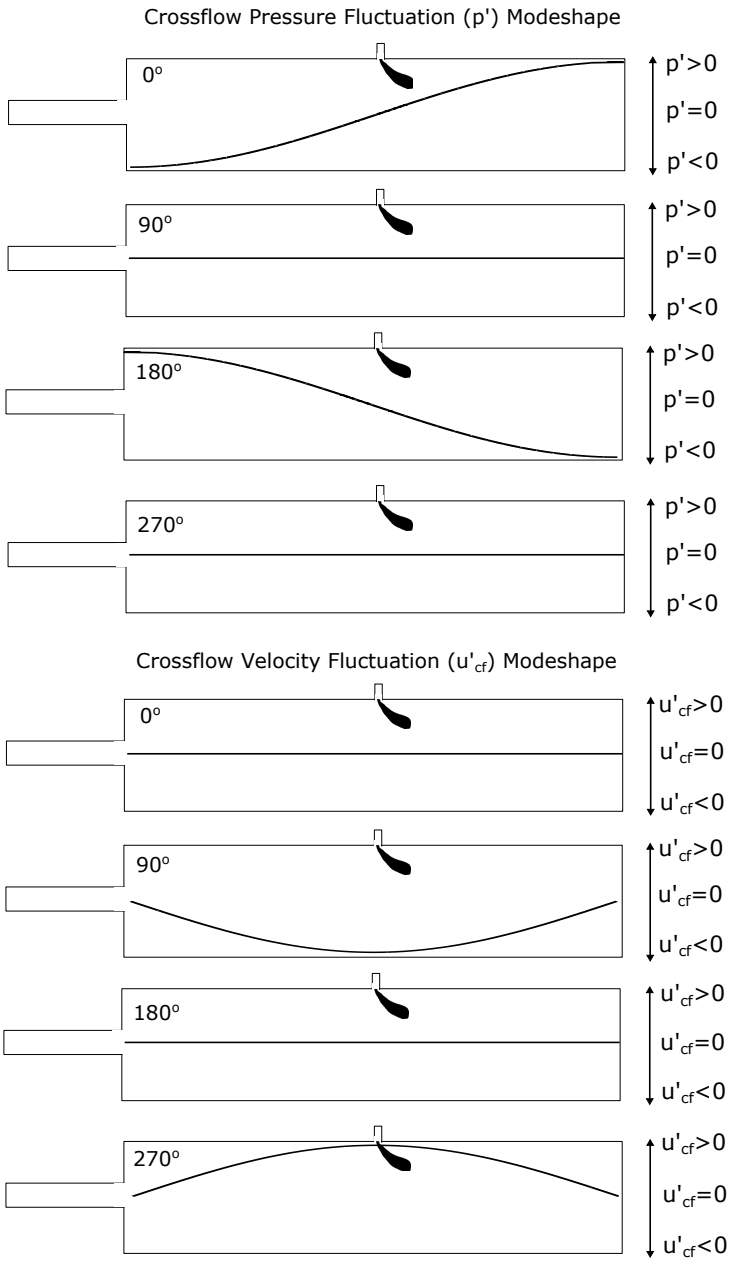

Figure 3.7.. Qualitative description of one acoustic cycle in the combustion chamber for the pressure oscillation (top four) and the velocity oscillation (bottom four). Four phases of the cycle are shown: 0^o, 90^o, 180^o, and 270^o. The transverse jet is drawn in only for reference.

For the present work, the dominant crossflow frequencies are the 2L ($\approx$ 200 Hz) and 4L ($\approx$ 400 Hz). For the vitiated crossflow and reacting jet case, the nominal $\overline{u}_j$

and $\overline{u}_{cf}$ are 80 m/s and 50 m/s, respectively. For the $2L$ frequency, this results in $St_j = 0.015$ based on the jet velocity and $St_{cf} = 0.023$ based on the crossflow velocity. This calculated nominal jet to crossflow velocity ratio is R = 1.5, density ratio S = 2.4, and momentum flux ratio $J = 6$.

The cyclical unsteady structures of the transverse jet include the jet upstream shear layer rollup and pairing, global jet flapping, horseshoe vortices, and wake (or tornado) vortices. Thorough studies of reported frequencies traditionally are performed on the non-reacting and often low Re flows, however these values are still reported in Table 3.3. For the jet in unsteady crossflow, simulations of both non reacting and reacting jets display shear layer St_j numbers in the range of 0.7-0.8.

Most evident in Table 3.3 are the time scale differences between the crossflow frequencies and the transverse jet dynamics. For example, the period of the combustor $2L$ is an order of magnitude lower than the jet shear layer structures. The closest jet hydrodynamics to the frequencies of the oscillating crossflow herein are the wake vortices, which do display a reduced organization near the nominal R and J of this study [13]. Therefore, since the jet hydrodynamic time scales are much lower than the oscillating crossflow time scale, the natural jet dynamics are not expected a priori to display a direct and significant coupling with the unsteady crossflow acoustics.

An FEA analysis using COMSOL was performed on the injector to strategically design the injector natural resonance to avoid overlap with either the dominant crossflow acoustics or the jet hydrodynamics. The injector geometry in Figure 3.4 and the jet H_2/N_2 mixture gas temperature were parametrically varied. For the calculation, the flow was assumed static (zero mean flow), the jet choked orifice plate was modeled as a closed inlet (pressure anti-node), the orifice exit as an open outlet (pressure node), and the side walls a hard boundary. A mesh sensitivity study was performed using the COMSOL mesh resolution options. The results were found to be insensitive to the COMSOL provided mesh options.

The chosen injector geometry is shown in Figure 3.4 for a 60/40 H_2/N_2 jet (by moles) at a mixture temperature of 365 K. This results in an FEA computed bulk

resonance of 670 Hz. The 670 Hz frequency lies directly between the low amplitude combustor 6L and 8L, and below the jet wake frequencies. To verify the validity of the FEA calculation, power spectra of the injector pressure measurements and jet flame images were analyzed. Spectral results from both sources occasionally display an approximately 660-680 Hz frequency. However, when present this frequency displays orders of magnitude lower power in both spectra and is close to the apparent noise floor.

With the injector design constrained, additional time scales can be defined. One time scale is the travel time τ_i for a parcel of fluid moving from the injector inlet (the jet choked orifice plate) to the jet orifice exit D_j. Treating the nozzle as a quasi-$1D$ flow with simple area change, the velocity through the jet injector from mass conservation results in

$$u_j(\epsilon) = \begin{cases} \frac{u_j(0)D_j^2}{Diameter(\epsilon)^2} & 0 \leq \epsilon \leq E. \\ \frac{u_j(0)D_j^2}{Diameter(E)^2} & \epsilon > E. \end{cases} \tag{3.16}$$

where $u_j(0) = 80m/s$ according to the notation in Figure 3.4, and the density ρ_j in the injector is assumed constant under a low Mach number flow approximation. Integrating the inverse of velocity $u_j(\epsilon)^{-1}$ relative to ϵ results in the travel time $\tau_i =$ 10.8 ms. Using τ_i as the period T_i for the fluid parcel travel event, a corresponding frequency f_i is defined by $f_i = 1/T_i = 93$ Hz. This frequency is given as a Strouhal number St_j and St_{cf} in Table 3.3 using either the nominal jet or crossflow velocity, respectively.

Additionally, an injector acoustic time scale τ_a is defined. The jet mixture sound speed a_j=586 m/s at the nominal conditions is used for a velocity scale and the $1D$ injector length is the length scale $L_i = C + E = 96\ mm$, where the dimensions C and E are defined in Figure 3.4. This results in a one way travel time $\tau_a = L_i/a_j$ =0.16 ms. The relatively low mean injector velocity flow is assumed negligible. The time it takes for the acoustic disturbance to propagate from the jet orifice exit to the jet choked orifice plate and back, $2\tau_a$, has a period T_a=0.32 ms and a corresponding

frequency $f_a = 1/T_a = 3125$ Hz. This frequency is given as a Strouhal number St_j and St_{cf} in Table 3.3 using either the nominal jet or crossflow velocity, respectively.

Lastly, a crossflow time scale τ_{cf} is defined. Consider fluid parcel travel times outside of the jet injector in the crossflow. Using the jet diameter D_j as a length scale for a crossflow fluid parcel traveling with a velocity scale of 50 m/s, $\tau_{cf} = 0.12$ ms. Using τ_{cf} as the period T_{cf} for the fluid parcel travel event, a corresponding frequency f is defined $f_{cf} = 1/T_{cf} = 8621$ Hz. This frequency is given as a Strouhal number St_j and St_{cf} in Table 3.3 using either the nominal jet or crossflow velocity, respectively.

3.5.3 Pressure Instrumentation Ports

The HF pressure measurements provide spatial-temporal behavior of the vitiated and non-vitiated unsteady flowfield and are correlated with the optical imaging of the transverse jet. To ensure that the measured spatial-temporal trends in unsteady pressure are accurately captured, an uncertainty is placed on the measurement of the unsteady pressure amplitude and phase. The methodology considers specifically the design of the instrumentation port under relatively large pressure amplitudes. This section outlines the uncertainty estimation approach.

The HF transducers are wall mounted in recessed cavities for improved survivability. The natural acoustic behavior of the recessed cavity is carefully considered and tuned by design to minimize acoustic interference in measuring either the true amplitude or phase for a range of frequencies. A Helmholtz style instrumentation port design is used due to the ease of fabrication and minimized hot gas flow into the cavity. This reduces the transducer heat load which is particularly severe during the relatively long duration hot fires. Figure 3.8 shows the port design.

Adopting a lumped acoustic approach, the port is modeled with a spring-mass-dashpot system analogy. The cavity gas provides the stiffness, the orifice gas provides the mass and the dissipative losses are provided by thermal, viscous, radiation and

Table 3.3. Time scales and Strouhal numbers of the jet in crossflow

	Re_j (Re_{cf})	J	St_j	St_{cf}
Combustor 2L ($\approx$ 200 Hz)	90000 (47000)	6	0.015	0.023
Combustor 4L ($\approx$ 400 Hz)	90000 (47000)	6	0.029	0.046
Injector Resonance 671 Hz	90000 (47000)	6	0.049	0.078
Injector $2\tau_a = 0.32$ ms			0.23	0.36
Injector $\tau_i = 10.2$ ms			0.007	0.01
Crossflow $\tau_{cf} = 0.12$ ms			0.625	1.0
Wake Vortices [13]	8000-40000 (11400)	4-16		0.12-0.16
Shear Layer Vortices [10]	3000	4-16	0.4-1.5	
Shear Layer Vortices (Unsteady Crossflow) [8, 25]		4,6	0.7,0.8	
Horseshoe Vortex System [14]	2500 (5000)	4		0.1-0.3
Jet Flapping [25]	13000	4	0.1	0.4
Cylinder in a Crossflow [50]	(50000)	4		0.2

turbulence mechanisms. This results in a well known inhomogeneous second order differential equation for the orifice mass displacement of a Helmholtz resonator [51]. The resultant linear and lossless undamped (natural) resonant frequency of the port is

$$f_o = \frac{c_o}{2\pi}\sqrt{\frac{A}{L'V}} \tag{3.17}$$

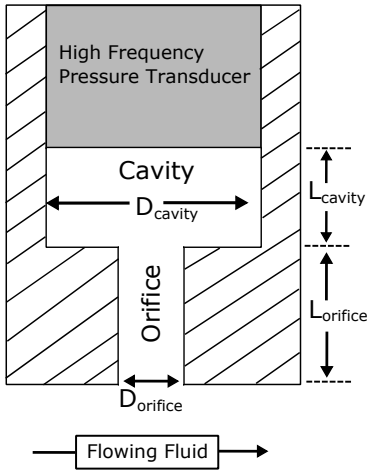

Figure 3.8.. High frequency pressure instrumentation port design.

where c_o is the linear sound speed, A is the area of the port orifice, V is the cavity volume and L' is the effective port orifice mass length equal to the actual port orifice length L and a correction factor accounting for lumped mass.

To account for higher amplitude acoustic nonlinearity, the linear and lossless differential equation is modified. The stiffness factor (i.e. restoring force in the analogy) accounts for the change in density as a function of change in pressure. A parameter of nonlinearity, B/A (defined in Figure 3.18), is defined by keeping terms through the quadratic in a Taylor expansion of pressure to density [52]. This results in equation 3.18, where the term in brackets accounts for changes in the linearly derived speed of sound under elevated acoustic pressure amplitudes. The second term in the brackets in equation 3.18 therefore dictates the degree to which p' deviates from linear assumptions. In the small pressure amplitude approximation $N \approx 1$.

$$p' = \rho' c_o^2[N] = \rho' c_o^2[1+\frac{1}{2}\frac{B}{A}(\frac{\rho'}{\rho_o})] = \rho' c_o^2[1+\frac{1}{2}\frac{B}{A}(\frac{p'}{p_o})^{\frac{1}{\gamma}}] = \rho' c_o^2[1+\frac{1}{2}(\gamma-1)(\frac{p'}{p_o})^{\frac{1}{\gamma}}] \quad (3.18)$$

Solving the modified inhomogeneous differential equation, the ratio between the acoustic pressure inside the cavity p'_c to the acoustic pressure at the orifice inlet p' is shown by equation 3.19. Here, R is the impedance total specific resistance (thermal,

viscous, radiation, turbulent), X is the impedance specific reactance, and f is the oscillatory p' frequency at the orifice entrance.

$$\frac{p'_c}{p'} = N(\frac{-\rho_o c_o^2 A}{2\pi f V})\frac{2\pi f \rho_o L'(1 - N\frac{f_o^2}{f^2}) + iR}{[2\pi f \rho_o L'(1 - N\frac{f_o^2}{f^2})]^2 + R^2} = N(\frac{-\rho_o c_o^2 A}{2\pi f V})\frac{X + iR}{X^2 + R^2} \tag{3.19}$$

Two points from equation 3.19 are immediately apparent. First, the phase angle between p'_c and p' depends on the relative magnitude of R to X, i.e. a relatively large R can introduce a measured phase shift. Secondly, the port will amplify the magnitude of p' for frequencies approaching the port natural resonance, resulting in the pressure instrumentation measuring a modulated amplitude.

As $p^{'}$ increases, though, the dominant impedance mechanisms shift. The incipient turbulent dissipation begins dominating the thermo-viscous-radiation losses in R [53, 54]. The total resistance takes on significant growth from its small amplitude (i.e. linear) approximation [53]. For elevated pressure combustion stability studies, it's not uncommon to encounter large relative pressure amplitudes [39].

It is inherently challenging to analytically predict turbulent dissipation losses across a range of acoustic amplitudes. Therefore, nonlinear impedance values are extrapolated from Helmholtz cavities driven over a range of $p'/\overline{p}$ levels. The total resistance R is written as

$$R = R_r + R_i = \left[\frac{2\pi\rho A f_o^2}{c_o}\right] + 4(\epsilon_l + \epsilon_{NL} + (l/D))\sqrt{\nu\rho\pi f} \tag{3.20}$$

where R_r is the radiation resistance, R_i is the viscous resistance, ϵ_l is a resistance factor depending on the port orifice surface quality, ϵ_{NL} is a nonlinear correction term, and ν is the dynamic viscosity. The reactance X is given as

$$X = 2\pi f \rho L'(1 - (f_o^2/f^2)) \tag{3.21}$$

The value of R will increase as p' increases. For sound pressure levels between 75 dB and 150 dB, the ratio of the total resistance R (includes the nonlinearity) to

the linear resistance R_{lin} is shown in Figure 3.9 for a Helmholtz resonator. For this thesis, the peak-to-peak pressure amplitudes considered are at most approximately 25 kPa, where $\overline{P} \approx 950$ kPa and $p'/\overline{p} = 2.6\%$. This results in a projected $R_{total}/R_{lin} \approx 15$.

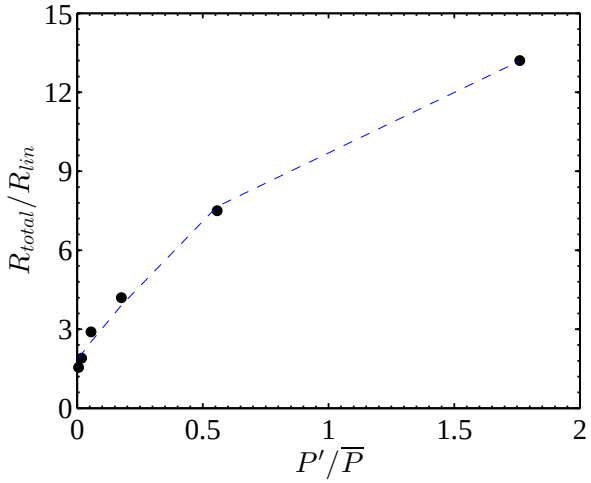

Figure 3.9.. Nonlinear resistance for a Helmholtz cavity driven at varying pressure amplitudes P', where $\overline{P}$ is 101 kPa. Data points adapted from [53]. The dotted curve is a second order polynomial fit evaluated at the data points.

For most locations in the combustion chamber, the chamber wall sets the port orifice length. $L_{orifice} = 13$ mm. The orifice diameter $D_{orifice} = 2$ mm. The cavity dimensions are approximately $D_{cavity} = 7$ mm and $L_{cavity} = 1$ mm. A few ports on the test rig are different. For example, the injector port is significantly smaller so as to create a $f_o > 10kHz$. In all cases, however, an analysis is performed to place an uncertainty on the measurement with known port geometry.

Figure 3.10 shows the amplitude and phase of equation 3.19 for two different port gas temperatures. Both are plotted against $100f/f_o$ which is the the frequency of oscillation f at the entrance to the orifice relative to the port Helmholtz frequency f_{oc}. Here, f_{oc} is the port Helmholtz frequency corrected for non negligible acoustic amplitudes (solution of the modified differential equation). Air is assumed for both

cases. Since the answer is temperature dependent, tests were performed with an exposed junction thermocouple inside a pressure port to determine the actual port gas temperature. Tests revealed a temperature of $\approx$ 100 K lower than the flowing heated air crossflow temperature for heated air crossflow test cases. For reacting crossflow test cases, the thermocouple measured upwards of $1150K$. Two temperatures are then compared 700 K and 1150 K. The frequencies of interest in the combustor are the $2L$ ($\approx$ 200 Hz) and $4L$ ($\approx$ 400 Hz). A 200 Hz frequency results in at most a 0.25 kPa difference between p'_c and p' and a phase difference of 0.25^o. A 400 Hz frequency results in at most a 0.5 kPa difference between p'_c and p' and a phase difference of 0.6^o. Note that at large frequencies, e.g. 3500 kHz, relatively small acoustic fluctuations can be significantly artificially amplified inside the port. On a pressure PSD, these high kilohertz frequencies manifest then as sharp peaks. These will be identified later in the discussion of results.

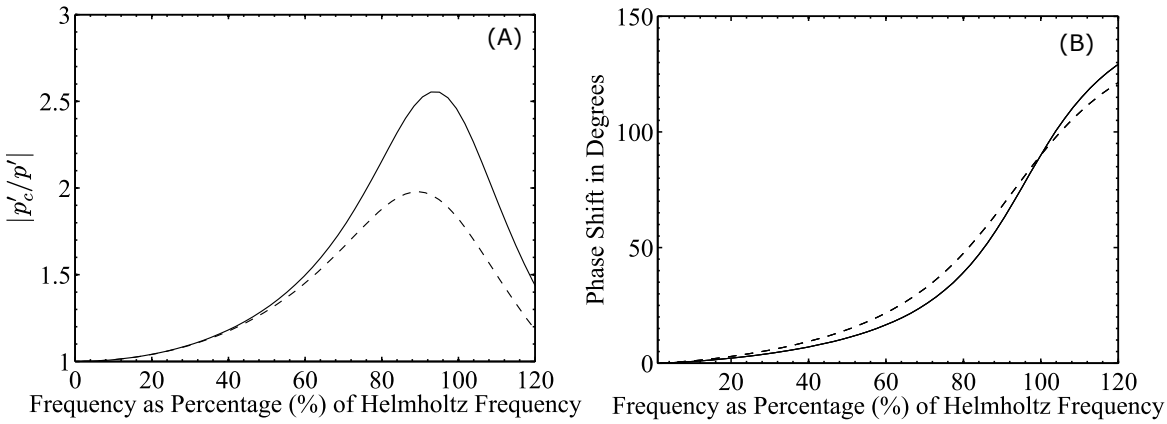

Figure 3.10.. Instrumentation port uncertainty estimation. (A) The amplitude of equation 3.19. (B) The phase of equation 3.19. Both x-axes are the frequency f relative to the Helmholtx port frequency f_o. Two port gas temperatures are compared and the gas is assumed to be air. Solid line is 700 K and dotted line is 1150 K.

3.6 Optical Diagnostic Setup

The optically accessible combustor test section is designed to afford increased visualization and interrogation of the reacting jet flowfield from multiple directions. Two optical measurement techniques were performed for this work, OH-PLIF and PIV. Planar laser induced fluorescence of the hydroxide radical (OH-PLIF) is used to identify and characterize the reaction zones and burned gas region. Time resolved two dimensional PIV is performed simultaneously with OH-PLIF to visualize jet flame-flowfield interactions. Figure 3.11 shows the layout of the simultaneous OH-PLIF and PIV system. Figure 3.12 shows the optical arrangement surrounding the optically accessible test section. The subsequent discussion will detail the optical setup.

For the OH-PLIF measurements, a frequency doubled (532 nm) Nd:YAG laser (Edgewave IS200-2-L) was used to pump a tunable dye laser (Sirah Credo) operating with the dye Rhodamine 590 dissolved in ethanol. The 566.4 nm output beam was frequency doubled to 283.2 nm and tuned to the Q1(8) transition of OH in the v"=0,v'=1 vibrational band of the $A^2\Sigma - X^2\Pi$ system. The average laser pulse energy at 10 kHz was generally 6 - 6.5 W. A reference leg is used to continuously monitor the dye laser power output and wavelength, where an uncoated window directs a small amount of the total dye laser output through a Bunsen flame and the generated bunsen LIF signal is collected with a photomultiplier tube and monitored on an oscilloscope. The laser sheet was formed using two cylindrical lenses (f = -25 mm and f = 300 mm) resulting in a 50 mm collimated sheet height, and a third cylindrical lens (f = 750 mm) to focus the sheet thickness to approximately a FWHM of 500 μm. The OH fluorescence was collected perpendicular to the laser sheet using a UV sensitive lens (Cerco Sodern Type 2178, f = 100 mm focal length, f/2.8), high speed image intensifier (LaVision HS-IRO), and a high speed CMOS camera (Phantom v411). To suppress background radiation, an optical band pass filter (Semrock 320/40) was placed in front of the UV lens and a 100 ns intensifier gate width was used. At the 10

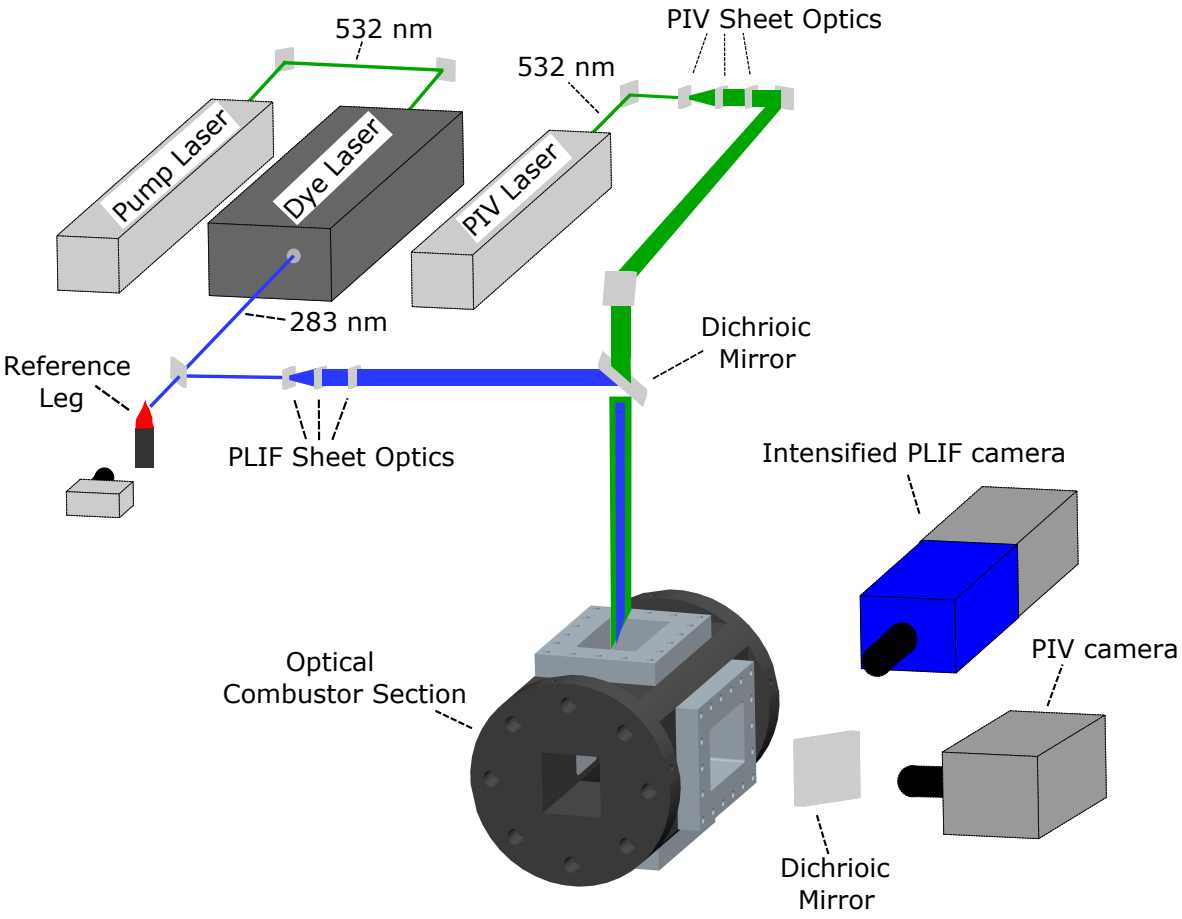

Figure 3.11.. Layout of the simultaneous 10 kHz PIV and OH-PLIF system.

kHz repetition rate, the CMOS camera array size of 640 x 584 was recorded, resulting in a raw image resolution of 93 $\mu m/pixel$.

For the PIV measurements, a dual cavity Nd:Yag laser (Edgewave IS811-DE) outputting 532 nm at 10 kHz and 1.7 mJ/pulse was used to illuminate seeded tracer particles. The laser sheet was formed using two cylindrical lenses (f = -25 mm and f = 300 mm) resulting in a 50 mm collimated sheet height, and a third cylindrical lens (f = 1000 mm) to focus the sheet to approximately a FWHM of 600 μm. Titanium dioxide tracers particles (250 nm nominal diameter) are seeded into the tertiary nitrogen flow using a fluidized bed seeding vessel. The flow into the fluidized bed is controlled using

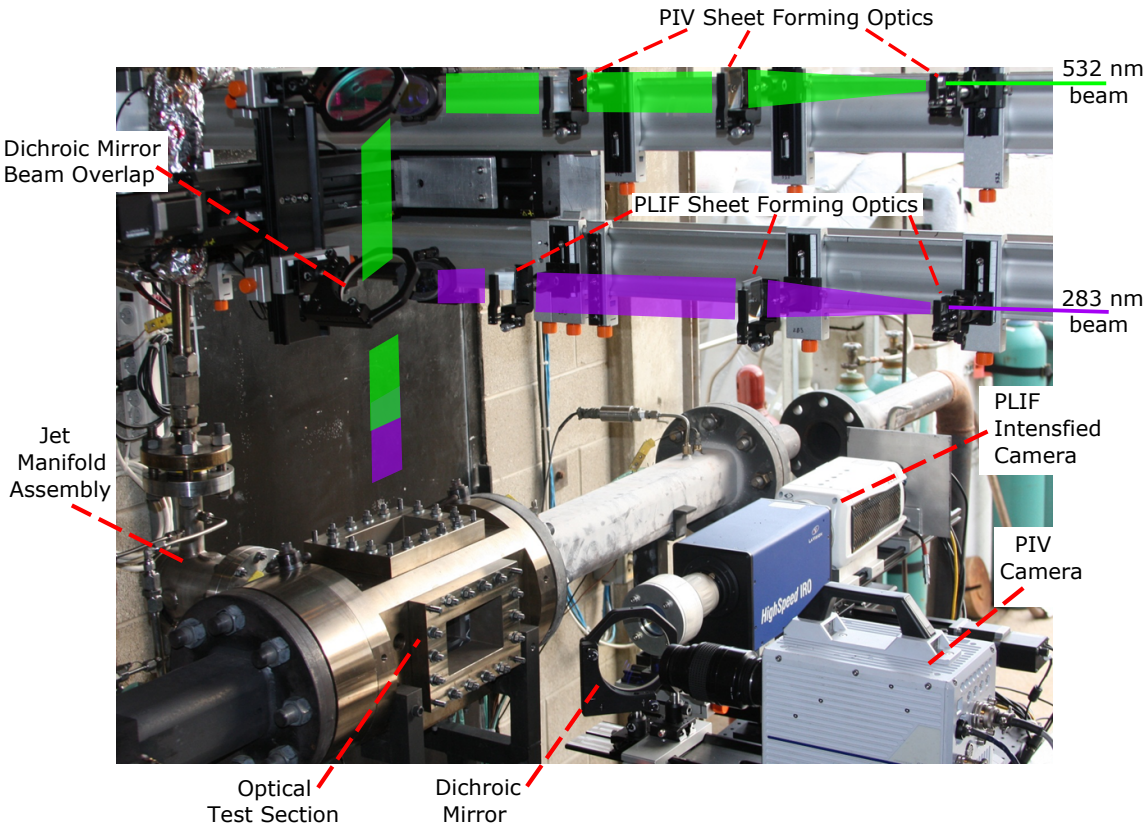

Figure 3.12.. Simultaneous PIV and OH-PLIF laser diagnostic setup surrounding the optically accessible combustor test section. The paths of the 532 nm PIV beam (green) and the 283 nm PLIF beam (purple) are drawn in. For this configuration, the two laser sheets are overlapped before entering through the top window. The camera systems image through the side window.

an electrically controlled three way needle valve and flows through a sintered glass plate in which the TiO_2 rests on the opposite side, where the flow is then seeded. The resultant 532 nm scattered signal is collected perpendicular to the laser sheet using a f=105 mm lens (f/2.8) and a high speed CMOS camera (Photron FASTCAM SA4 Model 500K-M2). An optical band pass filter (3 nm FWHM centered on 532 nm) was placed in front of the lens to suppress background radiation. At the 10 kHz repetition rate, the CMOS camera array size of 512 x 352 was recorded, resulting in a raw particle image resolution of 83 $\mu m/pixel$.

The OH-PLIF and PIV measurements are converted from raw pixels to engineering units using a dot target calibration procedure. The calibration is performed using a LaVision Type 5 dot target and the LaVision Davis calibration software. The raw scattered PIV images are preprocessed in Davis using a sliding 4x4 kernel for particle intensity normalization. This corrects for spatial intensity variation, partially due to laser sheet non uniformity and inhomogeneous particle diameter. A custom developed algorithmic mask is then applied to the images to exclude regions in the field of view with minimal seeding density. This was necessary since only the jet fluid was seeded with TiO_2 and regions with predominately crossflow fluid contain low seeding density. Vector fields were then computed from the resultant particle images spatial cross correlation using the multi-pass adaptive window offset algorithm in the LaVision Davis 8.2.0 software package. Results presented here were processed using a final window size of 16 x 16 pixels with 50% overlap. The resultant spatial vector resolution was 1.33 mm with resultant vector spacing of 0.67 mm. A local 3x3 median filter was applied to identify spurious vectors beyond a specified threshold and replaced with an interpolated vector.

A ridged tiered optical rail structure is mounted over the optical combustor test section to accommodate the multiple simultaneous laser diagnostics. Adjacent breadboards accommodate additional optics and camera systems. All final turning mirrors are placed on 2-axis translational stages and utilized between tests to vary the flowfield interrogation region. Similarly, all camera systems are mounted on 2-axis translational stages and travel accordingly as interrogation region changes to preserve camera focus. For the simultaneous PIV and OH PLIF imaging, a dichroic mirror with high transmission for 532 nm and high reflectivity for 283 nm is used to overlap the two laser sheets before entering the optical test section. Both laser sheets enter through the same window in this configuration. A dichroic mirror with high reflection for 310 nm and high transmission for 532 nm is used to split the OH fluorescence and PIV scattered signal while maintaining perpendicular viewing angles.

Both cameras image the same dot target allowing the PLIF and PIV coordinate axes to be spatially overlapped during data post processing. Test day calibrations are performed for both the OH-PLIF and PIV systems. For PIV, smoke calibrations are performed and lens focus adjusted to ensure a good focus on the laser sheet. For OH-PLIF, a set of brightfield images are recorded using a uniformly illuminated light source mounted to the front of the lens. The brightfield images are used to correct for spatial non-uniformity in the intensifier-camera response for test conditions intensifier settings and applied during data post processing. Background images with and without the PLIF sheet blocked for the non reacting jet in vitiated and heated air crossflows were taken. To correct for any laser sheet non-uniformity, e.g. regions of the sheet with increased UV intensity, acetone PLIF was performed. However, the variation in the non-uniformity across a single set of images and throughout the test day required a shot to shot correction procedure, which is described later.

Synchronization of the camera and laser timing was controlled using a pulse generator (Quantum Composer 9520) as the master clock source. The PLIF 283 nm pulse is temporally centered between the two 532 nm PIV pulses. For PIV, the pulse separation time dt is $5\,\mu s$, which was optimized to the measurement dynamic range. Laser timing was verified with an oscilloscope and photodiode. Frame straddling was also verified with the PIV 532 nm beams. Camera frame triggers, exposures, IRO firing, and the start of an image sequence are all recorded on the high-speed data system.

3.7 Rig Operation

The dump combustor transverse jet test rig is not a continuously combusting test rig. Reacting flow hot-fire tests are performed over a short duration, nominally 15-30 s. This significantly reduces the cost of design and manufacturing of a model combustor since active cooling of hot combustor parts is unnecessary for short durations.

Also, between tests while the experiment is cooling down, the large gigabyte sized image sets are downloaded from the cameras.

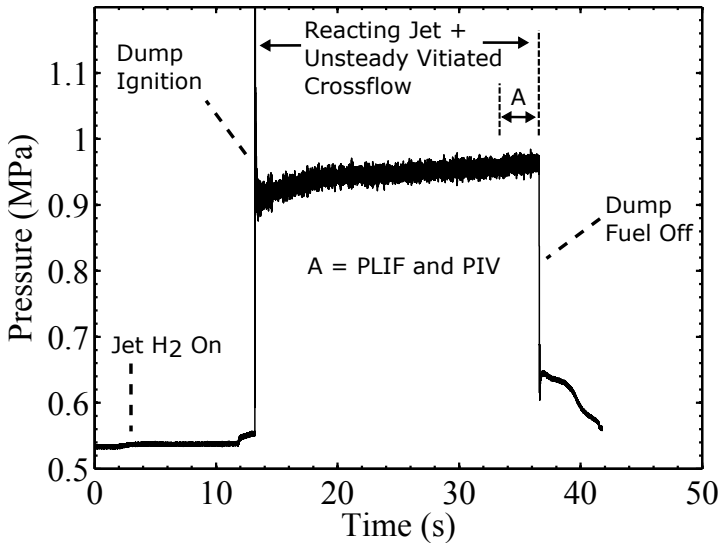

Figure 3.13.. Combustor chamber pressure representative of the unsteady transverse jet test rig.

Figure 3.13 shows a representative test sequence for optical imaging of the reacting 60/40 H_2/N_2 transverse jet injected into the unsteady crossflow. At 0 s preheated air at the set test condition (massflow and temperature) flows through the rig, preheating the combustor to the heated air temperature. During this time, the transverse jet fluid consists only of the nitrogen at the set test condition. At 2 s, the transverse jet hydrogen run valve is actuated and all jet feed line and manifold pressures are allowed to become steady before crossflow ignition occurs. At 10 s the dump plane igniter is turned on and at 12 s the dump combustor fuel natural gas run valve is actuated. Once dump combustor ignition is confirmed (14 s), the igniter is turned off and the crossflow and transverse jet fuel run valves are left open for an additional 18 s to ensure chamber pressure and temperatures steady off. Around 22 s, a portion of the jet tertiary nitrogen is routed through the T_iO_2 particle seeder. At 33 s, the camera systems are triggered and images are recorded of the reacting transverse jet

in an unsteady crossflow. Once the imaging is complete, the dump combustor fuel run valve is closed (36 s) followed by the closing of the jet hydrogen run valve. At this time, the combustor continues to flow preheated air in the crossflow, and the targeted nitrogen flow rate through the jet.

Alternative testing sequences have also been performed in separate passive combustion instability control investigations on this test rig. In these cases, the time of transverse jet fuel arrival lags the dump combustor ignition. This approach is to first generate and sustain a longitudinally unstable dump combustor with a defined limit cycle amplitude and frequency. Afterwards, the transverse jet fuel is introduced to the jet resulting in, instantaneously, a reacting jet in unsteady crossflow. The dump combustor instability behavior (as measured by high frequency pressure measurements) before, during, and after the transverse jet fuel arrival are correlated to determine any effect a secondary injection source (i.e. additional heat input from the jet) might have on the resonant chamber acoustics.

4. Introduction to Results

4.1 Complete Testing Campaign

A focused set of results from a larger gathered data set on non-reacting and reacting jets in unsteady crossflows are presented for detailed analysis. A laser diagnostic testing campaign over a six month period resulted in simultaneous 10 kHz PIV and OH-PLIF measurements of the jet at an injection location 1.11 m from the dump plane (near the 2L p' node and 4L p' anti-node) and 10 kHz OH-PLIF at an injection location 1.68 m from the dump plane (near the 2L p' anti-node and 4L p' node). Velocity measurements were not performed at the 1.68 m injection location. Table 4.1 summarizes all of the configurations investigated. Configurations 1 and 2 are the focus of the analysis and described below.

First, a schematic diagram of the FOV and defined coordinate system is shown in Figure 4.1. The jet orifice exit is flush-mounted on the injection wall. All PIV and OH-PLIF measurements are made on the jet XY cross sectional planes at discrete Z locations, where Z is perpendicular to the jet injection wall. The jet injection wall is defined as Z = 0. The XY cross sectional planes are parallel to the injection wall. The axes X and Y are parallel and perpendicular, respectively, to the crossflow streamwise direction, and the jet orifice exit center is defined as $(X, Y) = (0, 0)$. For the XY cross section, planes investigated are Z/D = 1.0, 1.9, 2.7, 3.6, 4.4, 5.3, and 6.2. All coordinates are normalized with the jet orifice exit diameter D = 5.8 mm. Both laser sheets propagate in the $-Y$ direction.

For configurations 1 and 4, a 60/40 H_2/N_2 jet is injected into the unsteady vitiated crossflow at a nominal J = 6. This is the reacting jet-reacting unsteady crossflow condition. For the non reacting jet, two cases were considered. For the first case, configuration 2, the same 60/40 H_2/N_2 jet (same jet massflow, mixture composition

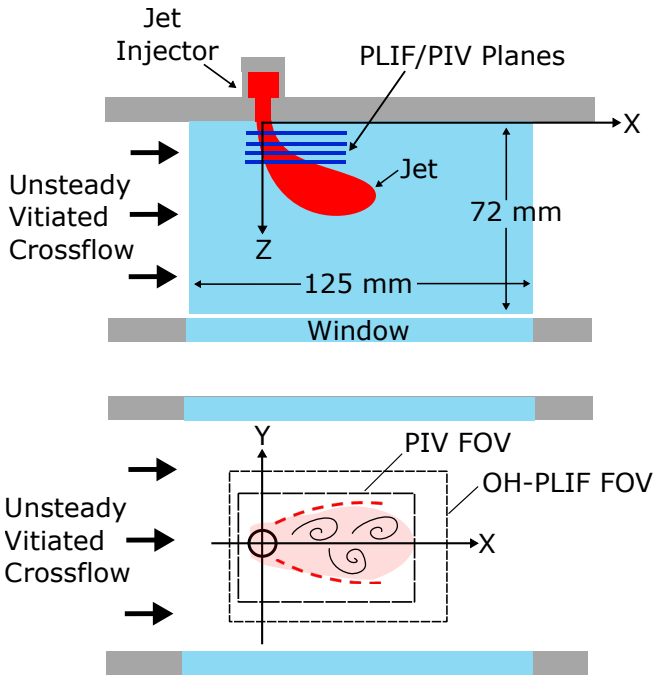

Figure 4.1.. Schematic diagram of jet coordinate system and the cross sectional interrogation planes

and mixture temperature) issues into an air crossflow (no NG added) at the same crossflow target flowrate and preheat temperature as in the vitiated crossflow cases. The jet is not ignited. For the second case, configurations 3 and 5, the vitiated crossflow operating conditions are the same as in configurations 1 and 4, but the jet hydrogen is omitted while holding the jet nitrogen operating conditions (i.e. $\dot{m}$ and preheat temperature) the same as to configuration 2. Jet injection for configurations 1, 2, and 3 is 1.11 m from the dump plane. Configuration 5 and 6 at a jet injection location of 1.68 m from the dump plane only include OH-PLIF data. For all configuration except 2, at a given Z/D location, separate hot fire tests are performed to change the dominant crossflow acoustic frequency to either the 2L or 4L. Since the experiment operates in short combustion duration bursts and due to limited on-board camera storage, the interrogation plane Z/D is varied between tests. Thus each configuration includes data at multiple Z/D planes. Also, since the method of producing

an oscillatory crossflow depends on a reacting dump combustor, configuration 2 is nominally considered a steady crossflow reference case.

Table 4.1. Non-reacting and reacting jet configurations tested

	Jet Location 1.11 m		Jet Location 1.68 m	
	H_2/N_2 Jet	N_2 Jet	H_2/N_2 Jet	N_2 Jet
	(Config 1)	(Config 3)	(Config 4)	(Config 5)
Vitiated Crossflow	PIV	PIV	OH-PLIF	OH-PLIF
(Dump Plane Reacting)	OH PLIF	OH-PLIF		
	(Config 2)			
Heated Air Crossflow	PIV			
(Dump Plane Non-Reacting)	OH PLIF			

4.2 Test Cases for Detailed Analysis

Table 4.2 shows the operating conditions of the test cases focused on herein for detailed analysis. Table 4.2 quantities are time-averaged values taken over the short duration OH-PLIF and PIV measurements. For the non-vitiated crossflow cases, the crossflow temperature T_{cf} is measured with a thermocouple inserted approximately 12 mm into the crossflow upstream of the jet on the wall opposite the injector. For the vitiated crossflow cases, a direct measurement of crossflow temperature downstream of the dump plane and upstream of the jet is not available. For this, the dump combustor post flame gas properties are determined by performing a rocket problem type calculation using the NASA thermochemistry code Chemical Equilibrium with Applications (CEA) [55]. The preheated and premixed air-natural gas mixture temperature in the inlet resonator to the dump plane is used for the initial temperature. Since the natural gas contains a mixture of hydrocarbons, the fuel composition is approximated using the top 5 species by mole as provided by the Panhandle Eastern

Pipe Line company [43]. The adiabatic flame temperature for the given equivalence ratio is listed as T_{cf}. Note that this is in actuality only a reference state since the actual crossflow temperature does not realize this temperature due to thermal losses (especially since the combustor is not lined with a thermal barrier coating). The pressure listed is the dump combustor mean chamber pressure and is an average of both low frequency pressure transducers in the combustion chamber. The jet mixture temperature T_j is measured directly upstream of the choked jet orifice plate.

The tabulated momentum flux ratio J and velocity ratio R were calculated as follows. Substituting the mass flow relation for the jet $\dot{m}_j = \rho_j u_j A_j$ and the crossflow $\dot{m}_{cf} = \rho_{cf} u_{cf} A_{cf}$ into the momentum flux ratio J definition results in

$$J = \frac{\rho_j u_j^2}{\rho_{cf} u_{cf}^2} = \frac{\rho_{cf} \left(\frac{\dot{m}_j}{A_j}\right)^2}{\rho_j \left(\frac{\dot{m}_{cf}}{A_{cf}}\right)^2} \tag{4.1}$$

where A_j is the jet orifice exit area and A_{cf} is the crossflow area. The jet mixture composition density ρ_j is calculated using the NIST database REFPROP using as inputs T_j and the mean combustion chamber pressure [56]. The crossflow density ρ_{cf} is provided by CEA at the input mean chamber pressure and adiabatic flame temperature conditions. Note that the ideal gas law could have been used in this case for density with little error. The velocity ratio R is then calculated from known quantities

$$R = \frac{u_j}{u_{cf}} = \frac{\left(\frac{\dot{m}_j}{\rho_j A_j}\right)}{\left(\frac{\dot{m}_{cf}}{\rho_{cf} A_{cf}}\right)} \tag{4.2}$$

The Reynolds number for the jet and crosflow are $Re_j = u_j D_j / \nu_j$ and $Re_j = u_{cf} D_H / \nu_{cf}$, respectively, where $D_H = 4A_{cf}/P_{cf}$ is the hydraulic diameter of the crossflow and P_{cf} is the crossflow perimeter. The kinematic viscosity ν for the jet and heated air crossflows is calculated using REFPROP and the procedure above. The kinematic viscosity of the vitiated crossflow is a CEA output along with T_{ad}.

Table 4.2. Operating conditions of the five test cases presented for detailed analysis.

	case 1	case 2	case 3	case 4	case 5
Configuration	2	2	1	1	1
Plane Z/D	1.0	2.7	1.0	1.0	2.7
Crossflow Conditions					
$\dot{m}_{AIR}$ (kg/s)	0.39	0.40	0.41	0.41	0.40
Equivalence Ratio ϕ_{cf}	-	-	0.66	0.66	0.67
T_{cf} (K)	666	664	2029	2030	2038
Pressure (kPa)	518	522	945	956	925
Re_{cf}	158382	160596	77068	77032	74397
u_{cf} (m/s)	25.9	26.0	45.8	45.7	46.0
Jet Conditions					
H_2 (g/s)	0.67	0.67	0.68	0.68	0.67
N_2 (g/s)	6.41	6.45	6.46	6.46	6.48
H_2/N_2 Mole Fraction Ratio	60/40	59/41	59/41	59/41	59/41
Mixture T_j (K)	367	375	361	361	362
u_j (m/s)	127	129	68.1	67.9	70.5
Re_j	86883	85997	88324	88312	88292
JICF Parameters					
Momentum Flux Ratio J	18.9	19.0	5.6	5.6	5.9
Density Ratio S	0.8	0.8	2.5	2.5	2.5

For the different cases of the non-reacting and reacting jet, the velocity measurements at a given Z/D location are not directly comparable. This is due presumably to differing jet penetrations for the vitiated and heated air cases on account of differences in their momentum flux ratios for fixed jet conditions. It is well known that the JICF

penetration scales with J. Using the ideal gas law for the jet density $P_j = \rho_j R_j T_j$ and the crossflow density $P_{cf} = \rho_{cf} R_{cf} T_{cf}$, equation 4.1 becomes

$$J = \frac{\left(\frac{\dot{m}_j}{A_j}\right)^2 R_j T_j P_j^{-1}}{\left(\frac{\dot{m}_{cf}}{A_{cf}}\right)^2 R_{cf} T_{cf} P_{cf}^{-1}} \tag{4.3}$$

Defining $J_{config1}$ and $J_{config2}$ for the vitiated and heated air 60/40 H_2/N_2 jet cases, respectively, the ratio of the two is

$$\frac{J_{config1}}{J_{config2}} = \frac{\left[\frac{\left(\frac{\dot{m}_j}{A_j}\right)^2 R_j T_j P_j^{-1}}{\left(\frac{\dot{m}_{cf}}{A_{cf}}\right)^2 R_{cf} T_{cf} P_{cf}^{-1}}\right]_{config1}}{\left[\frac{\left(\frac{\dot{m}_j}{A_j}\right)^2 R_j T_j P_j^{-1}}{\left(\frac{\dot{m}_{cf}}{A_{cf}}\right)^2 R_{cf} T_{cf} P_{cf}^{-1}}\right]_{config2}} \tag{4.4}$$

The jet conditions $\dot{m}_j$, R_j, A_j, and T_j are fixed for configurations 1 and 2. For the crossflow, the massflow rate for configurations 1 and 2 are approximately the same since the fuel flowrate in the reacting case is much smaller than the fixed air flowrate $\dot{m}_{cf}$. Thus, the crossflow conditions $\dot{m}_{cf}$, A_{cf}, R_{cf} are fixed for configurations 1 and 2. Also, assuming R_{cf} is approximately the same for both, and that $(P_j = P_{cf})_{config1}$, $(P_j = P_{cf})_{config2}$, equation 4.4 reduces to a function of the ratio of crossflow temperatures

$$\frac{J_{config1}}{J_{config2}} = \frac{T_{cfconfig2}}{T_{cfconfig1}} \tag{4.5}$$

At the nominal inlet preheat condition 650 K for the dump combustor air-NG mixture at $\phi = 0.66$, the equilibrium adiabatic flame is $\approx$ 2000 K. Chamber thermal losses reduce the actual crossflow temperature at the jet. The thermocouple measurement inserted $\approx$ 12 mm into the crossflow upstream of the jet on the wall opposite the injector measures a crossflow temperature of $\approx$ 1600 K at this condition, which is the maximum rating for this thermocouple. This can be considered a reasonable lower bounds and the adiabatic flame temperature an upper bound. An estimated range

for the change in jet penetration for the vitiated versus the non-vitiated crossflow cases for the same jet conditions is

$$0.3 \leq \frac{J_{config1}}{J_{config2}} \leq 0.4 \tag{4.6}$$

For the nominal $J_{config1}$=6, the lower (upper) bounds raises $J_{config2}$ to 15 (20). Therefore, with such an increase in jet penetration for the non-reacting case, velocity data at a given Z/D cross sectional location will capture different points in the spatio-temporal evolution of the jet.

For the N_2 jet in a vitiated crossflow, $J_{config3}$, the penetration difference can be similarly estimated. Using equation 4.4, the ratio of $J_{config3}$ to $J_{config1}$ can be reduced to

$$\frac{J_{config1}}{J_{config3}} = \frac{\left[\dot{m}_j^2 R_j T_j\right]_{H_2/N_2}}{\left[\dot{m}_j^2 R_j T_j\right]_{N_2}} \tag{4.7}$$

where the crossflow terms fall out since they are approximately the same for config 1 and config 3, and the pressure terms cancel due to $(P_j = Pcf)_{config1}$ and $(P_j = Pcf)_{config3}$. For the nominal jet nitrogen flowrate of 6.5 g/s and a 60/40 mole fraction of H_2/N_2, the squared ratio of $\dot{m}_{j,H_2/N_2}$ to $\dot{m}_{j,N_2}$ is approximately 1.2. The gas constants are $R_{N_2} = 297\ J/kgK$ and $R_{H_2/N_2} = 670\ J/kgK$. Since the nitrogen temperature is unchanged for all configurations and the hydrogen is not preheated, $T_{j,H_2/N_2}$ is lower than T_{j,N_2}. For a nominal $T_{j,H_2/N_2} = 367K$, T_{j,N_2} is $\approx 400K$ which accounts for the unheated seeded nitrogen circuit, which can vary between $\approx$ 40-55% of the jet total nitrogen for good jet seeding density. This results in $\frac{J_{config1}}{J_{config3}} \approx 2.9$, which for the nominal $J_{config1} = 6$, results in a $J_{config3} = 2.1$ jet with reduced penetration.

4.3 Plotting Method

The processed OH-PLIF and PIV data will be presented as time-averaged, phase-averaged, and instantaneous fields. Additionally, results from two modal decom-

position techniques is presented: Proper Orthogonal Decomposition and Dynamic Mode Decomposition. The time-average and modal decomposition results are typically calculated using 1000 sequential simultaneously recorded PIV and OH-PLIF measurements unless otherwise noted. To investigate the dependence of the results on the number of images, a comparison is made for configuration 2 in Table 4.1 in section 4.4.

For the PIV data, the two-component vector fields are plotted with a false colored contour background that represents a computed vector or scalar quantity. For clarity, a reduced number of vectors is displayed on the plots, specifically 32 vectors in both the X and Y direction. This results in a displayed vector spacing of 1.33 mm. Note that this is half the actual vector spacing. For velocity results that are not DMD or POD, in-plane velocity vectors are scaled so that a velocity of u_j=70 m/s corresponds to a vector length of $0.4D_j$. The DMD and POD velocity vector scaling is specified on a case by case basis. Coordinates for the OH-PLIF and PIV images are normalized with the jet orifice exit diameter $D = D_j = 5.8$ mm. The PIV results are plotted with axes extending beyond the PIV FOV, and equal to the axes of the OH-PLIF results. The fixed axes scaling facilitates a smoother comparison between the two measurements. It's noted that the actual OH-PLIF FOV is greater than that which is presented, but is reduced to cover the region the jet flame predominantly occupies.

Before data reduction of the PLIF measurements, the raw PLIF measurements are first corrected for distortion and scaled to engineering units. Next, a bright-field normalization is performed to correct for spatial non-uniformity in the intensifier-camera response. To correct for laser sheet non-uniformity, e.g. regions of the sheet with increased UV intensity, acetone PLIF was performed. However, the variation in the non-uniformity across a sequential set of images and across sets on a given test day required a shot to shot and case by case correction procedure. For this, two techniques were developed, one of which will be demonstrated here. To demonstrate the procedure, the time-average of a set of OH-PLIF measurements displaying strong sheet intensity variation is shown in Figure 4.2 (A). The crossflow is from left to right

and the laser sheet propagates in the $-Y$ direction. Two features of this flow are apparent: the vitiated crossflow background and the sheet profile variation in X/D. A key interest in the OH-PLIF images is the extraction of the assumed reaction front as defined by the larger OH gradients signifying super-equilibrium concentrations of OH. As the laser sheet propagates in the $-Y$ direction toward the jet flame, the surrounding vitiated crossflow LIF contributes a relatively significant background. This presents a challenge for gradient based edge finding techniques in reliably locating the jet flame front. Moreover, a non-uniform sheet intensity profile adds further difficulty by biasing regions with low OH signal with artificially large gradients. It's important to identify and correct these features since these regions may not in fact contain super-equilibrium OH signal, but rather mostly OH signal of the hot temperature products [57].

The sheet non-uniformity in Figure 4.2 (A) is observed predominantly in the streamwise X/D crossflow direction. The true FOV for PLIF extends up to $Y/D = 4$. For $-1 < X/D < 7$, it's observed that the instantaneous OH-PLIF jet flame structures do not extend beyond $Y/D = 3.5$ in the jet nearfield regions studied. Therefore, the vitiated crossflow LIF in the region $-1 < X/D < 7$ and $Y/D > 3.5$ can be used as a measure of the sheet non-uniformity. For the region $-1 < X/D < 7$ and $3.5 < Y/D < 3.7$, the LIF signal is averaged in Y/D for each discrete X/D pixel column. This is the raw mean LIF signal shown in 4.2 (B). A moving average filter is applied to the raw mean for smoothing, shown as 'filtered' in Figure 4.2 (B). Note that the sheet profile is indeed strong in the region near $X/D = 3$ as compared to $X/D = 0$ or $X/D >$4.5. Replicating the 1D filtered sheet profile in the Y/D direction produces the 2D filtered intensity profile in Figure 4.2 (C). Normalization of Figure 4.2 (A) by Figure 4.2 (C) by right array division results in a sheet corrected OH-PLIF field. Figure 4.2 (D) shows a scaled sheet corrected field, where an average of the low intensity jet fluid directly downstream of the jet was set as the grayscale minimum to accentuate the jet edges. Qualitatively, the edges of the jet flame relative to the vitiated crossflow signal are accentuated by the correction procedure (Figure 4.2 (D)

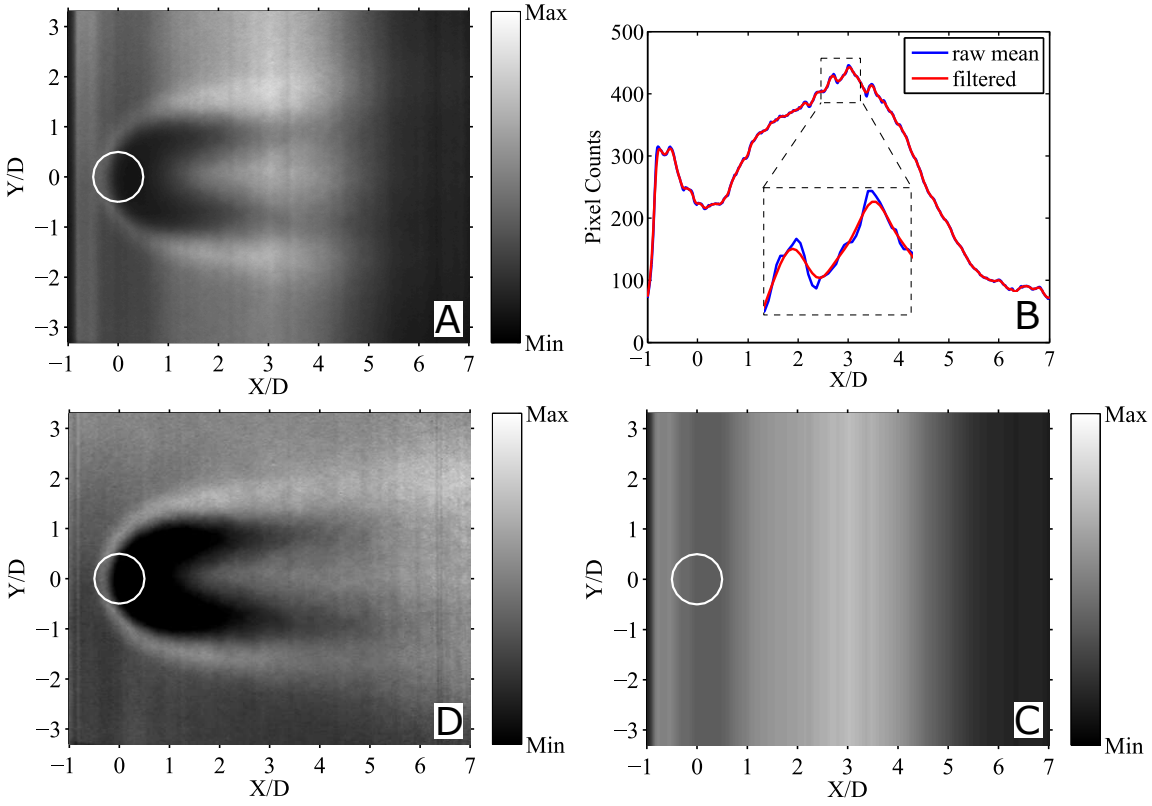

Figure 4.2.. Sheet intensity normalization for OH-PLIF measurements. (A) Raw OH-PLIF mean. (B) Streamwise 1D sheet intensity profile. (C) Spatial sheet intensity profile. (D) Image (A) corrected for the sheet intensity nonuniformity. Images shown are for Z/D=1.

relative to Figure 4.2 (A)) and the jet upstream reaction front near $X/D = 0$ is made clear.

To reiterate, the objective of the OH-PLIF measurements are in the extraction of the flame front. Therefore, reliable and robust preprocessing of the measurement fields is important. It's found that the procedure in Figure 4.2 performs optimally in half of the instances. In some time series of instantaneous OH-PLIF measurements, a frequency space based sheet intensity correction performs better. For this, two dimensional image filtering in the frequency domain was performed. A 2D FFT of each image identifies the dominant spatial frequencies associated with the axial intensity variation, which are then removed by convolution in the frequency domain with an

ideal filter removing those frequencies. The frequencies are typically straightforward to identify since the wavelengths associated with intensity variation are on the order of the size of the FOV. The resulting corrected OH-PLIF measurement shows a more uniform X/D spatial intensity variation. The frequency space filtering procedure and the procedure of Figure 4.2 are both used herein to preprocess the OH-PLIF measurements prior to extraction of the flame front. Note also that minor sheet absorption is observed as the sheet propagates in the $-Y$ direction through the FOV. Although this is generally small enough to not warrant much consideration in extracting a flame edge, the frequency based correction procedure is apt to handle this correction.

An algorithm was developed to extract the jet flame surface topography from the above corrected OH-PLIF measurements. The algorithm is a gradient based edge detection method based on previously published techniques for identifying, qualifying and extracting the flame edge from the OH signal gradient [57,58]. A robust algorithm was necessary to distinguish between the high background OH due to the vitiated crossflow and jet flame products. It's noted that the derived flame surface is not a direct measure of the reaction rate and that the actual reaction rate will vary along the surface due to non-homogeneous local equivalence ratio, strain rate, and local preheating due to hot gas recirculation [57]. Nonetheless, with the simultaneously recorded PIV measurements, the derived flame surface topography will be used to characterize flow-flame interactions at the larger resolvable scales.

For the instantaneous OH-PLIF measurements corrected for distortion, pixel response non-uniformity, background, and sheet intensity variation, an image processing anisotropic diffusion filter is applied. This filter is chosen for its ability to reduce image noise while preserving edges. Once applied, a user defined threshhold identifies the predominantly jet fluid region, and a spatial gradient of the field is generated. Gradients above a defined threshold and corresponding to the jet fluid locations are binarized. A morphological thinning procedure of the binarized field produces sets of pixel wide curves. These are assumed to be the flame front curves demarcated by the relatively sharp OH gradient very near the flame front. The binarized thinned

flame front field is then filtered to remove spurious lengths below a threshold. The curves correspond to definable X and Y coordinates and thus the flame front can be mathematically treated and compared with the velocity field. It's noted that the multiply defined thresholds in this procedure can produce varied results on a case by case basis. Each sequence of OH-PLIF measurements requires separate tuning of the threshold parameters.

Ten high frequency pressure transducers in the combustion chamber and injector are recorded and analyzed. For high frequency pressure behavior, three locations are focused on: P1, P5, and P10. These locations at a minimum provide enough information to describe the crossflow $2L$ behavior for comparing with the optical diagnostic data. The location P1 is in the crossflow and directly upstream of the combustion chamber exit nozzle. This location is close to the chamber $2L$ p' anti-node and provides a good measure of the $2L$ p' modeshape amplitude. It also provides a good measure of most chamber acoustics p' modeshape amplitudes since it's directly upstream of the exit nozzle. The location P5 is in the crossflow and directly upstream of the jet injection location. The location P10 is inside the injector.

Except for vector generation, all data post processing is performed using Matlab. Bandpass filtering of pressure data is performed with a second order Butterworth filter made using the Matlab function butter and implemented using the filtfilt function. Power spectral density estimates (PSD) are calculated using the Matlab periodogram function with a Hann window.

4.4 Resolution in Space and Time

The ability to resolve the the spatial-temporal development of the flowfield enables the capturing of the dynamic coupling between the jet and crossflow. There is a limit, however, of allowable space-time resolution set by the measurement technique, hardware, and the data post processing. The fact that such a limit exists restricts the

processes that can be studied with high fidelity and care must be taken to consider the allowable scope.

Planar OH-PLIF and PIV are applied to a decreased field of view surrounding the jet orifice exit in order to increase the spatial measurement resolution. The reduced FOV affords visualization mostly of the jet nearfield ($-3 < Y/D < 3$ and $-1 < Y/D < 6$). For OH-PLIF, the raw image resolution of 93 $\mu m/pixel$ results in 62 pixels spanning a jet diameter distance $D_j = 5.8$ mm. As the jet structures convect away from the jet exit, structure pairing and crossflow entertainment tend the structures to larger sizes in the nearfield before eventually breaking down further downstream. These processes need to be considered in space and time relative to the measurement system.

Temporally, the 10 kHz repetition rate is sufficient for capturing the time scales of the unsteady crossflow acoustics at $\approx$ 200 Hz (2L acoustic mode) and $\approx$ 400 Hz (4L acoustic mode). Figure 4.3 shows the temporal measurement resolution relative to a crossflow cycle of the 2L and 4L modes. For a 200 Hz and 400 Hz cycle, there are 50 and 25 instantaneous flowfield measurements, respectively. The jet hydrodynamic time scales, however, are not necessarily expected a priori to be captured with high fidelity in time since the largest time scales should occur with frequencies anywhere in the range 500-3 kHz, and the smallest time scales well above the 5 kHz Nyquist cutoff. For example, initial shear layer rollup is expected to occur anywhere between 5-15 kHz (see Table 3.3).

Spatially, the 10 kHz repetition rate is more problematic for certain flowfield velocity scales. Consider $u_{cf} = 50$ m/s. Over the 10 kHz imaging measurement interval of 0.1 ms, a fluid parcel travels 5 mm, or in terms of the jet diameter $0.86D_j$. For $u_j = 80$ m/s, a fluid parcel travels $1.37D_j$. Attempting to resolve the evolution of the fine scale flame front dynamics (e.g. local flame stretching and extinction) anywhere near the jet shear layer where the velocities are quite high is difficult at this measurement repetition rate and high Reynolds number flow. On the other hand, relatively robust tracking should be possible of the evolution of the larger scale

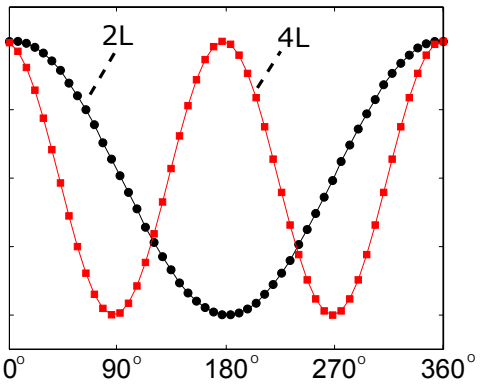

Figure 4.3.. 10 kHz imaging resolution (data points) relative to the cross-flow 2L and 4L acoustic cycle (curves). The x-axes in degrees corresponds to the 2L cycle.

coherent structures scaling with D_j. However, this is exacerbated by out of plane motions making planar based measurements more difficult to correctly interpret.

For PIV, the raw scattered measurement spatial resolution 83 $\mu m/pixel$ is less useful since vector generation results from application of larger sized interrogation windows for the cross-correlation. In this case, the 16 x 16 interrogation window results in a spatial vector resolution of 1.33 mm with resultant vector spacing of 0.67 mm for the 50% window overlap. This corresponds to 8 vectors spanning the jet diameter. The vector resolution effectively results in a spatial filtering of the true velocity field with a loss in resolution for length scales below the window interrogation size. With the resulting coarse conditionally sampled velocity field, the determination of differential quantities in the velocity gradient tensor such as vorticity and strain results not only in a reduced spatial resolution, but possibly large bias uncertainties in certain regions of the flow.

Finally, since only the jet fluid was seeded with TiO_2, regions with predominately crossflow fluid contain low to zero seeding density. This results in velocity biasing in the mean calculated flowfields near the jet-crossflow interface. At a given cross sectional plane, infrequent vector generation in some regions of the flowfield occur due

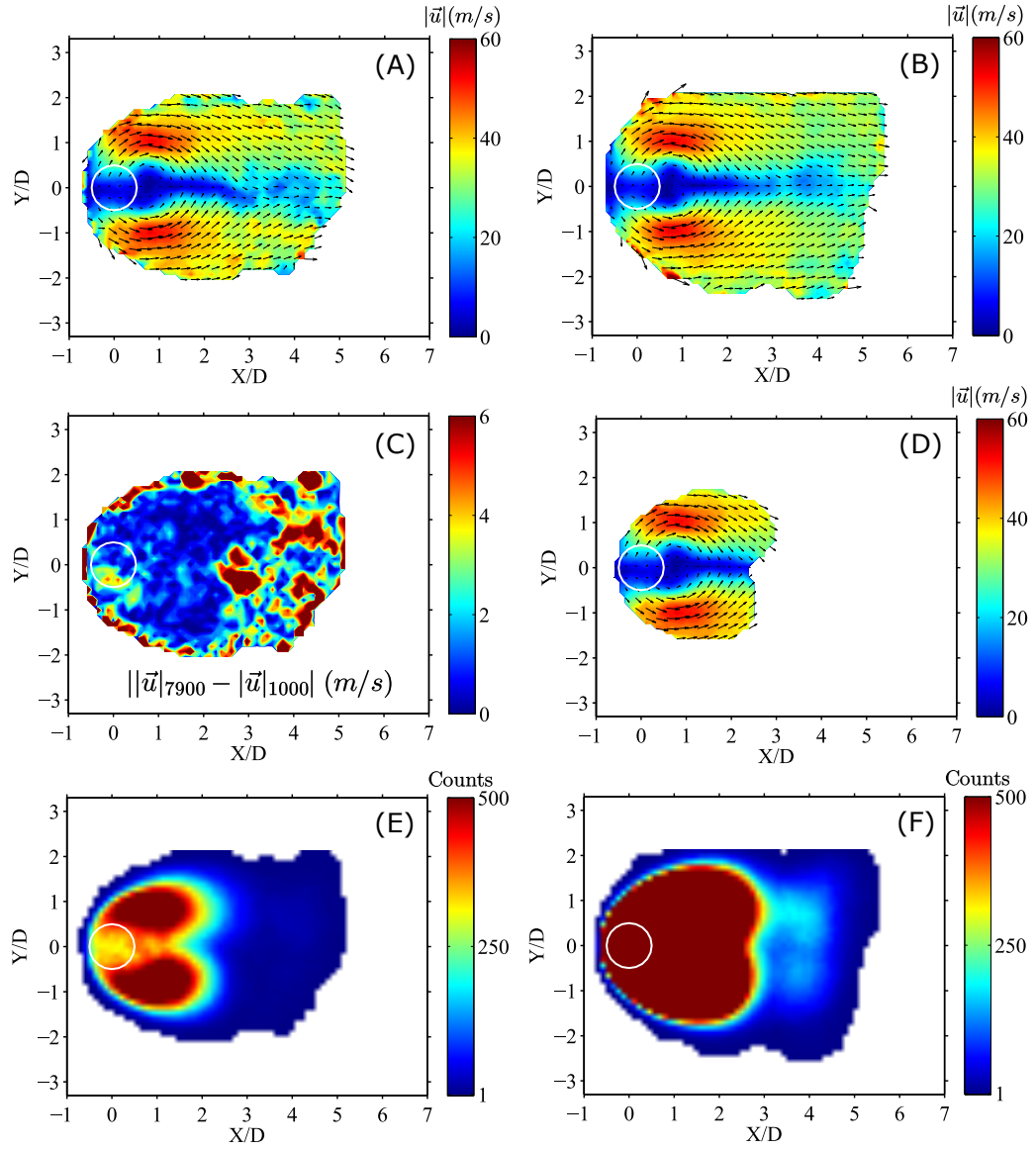

Figure 4.4.. Time averaged velocity of JICF. (A) $|\vec{u}|$ time average of 1000 frames. (B) $|\vec{u}|$ time average of 7940 frames. (C) $|\vec{u}|$ difference between (B) and (A). (D) $|\vec{u}|$ time average of 1000 frames after applying 5% vector cutoff criteria. (E) Spatial vector counts for 1000 frame sequence. (F) Spatial vector counts for 7940 frame sequence.

to random turbulent fluctuations convecting small pockets of seed away from the bulk of the jet. Also, jet flapping in and out of the cross sectional plane which separates random pockets of seed from the bulk of the in plane jet fluid. Results presented

using a discrete number of images must be carefully interpreted. To characterize this, an analysis was performed to locate and quantify these regions. A comparison is made for the mean vector field of configuration 2 in Table 4.1 to investigate the misinterpretation of the processed results on the quantity of input calculable vectors. This case was chosen since it is observed as the most extreme case among the analyzed cases in the possible misinterpretation of the flow.

Figure 4.4 shows the mean velocity magnitude calculated using 1000 images (A) and 7940 images (B). Good qualitative agreement is observed for $|\vec{u}|$ closer to the jet exit $X/D < 3$ and away from the outermost vectors bordering the predominantly crossflow fluid (blank space). A closer look at the spatial differences is shown in Figure 4.4 (C) by looking at the absolute difference of $|\vec{u}|$ based on 1000 images, $|\vec{u}|_{1000}$, and based on 7940 images, $|\vec{u}|_{7940}$. Coherent small differences are only observed within a few jet diameters of the orifice exit. Along the jet-crossflow interface and further downstream ($X/D > 3$) the differences become quite large and sporadic. These differences can be attributed in part to the calculable local vector count. Figure 4.4 (E) and (F) shows a spatial map of the vector count at each spatial location for the 1000 and 7940 image sequence, respectively. The vector count is the number of times a vector is calculated at each location over the respective image sequence. Notice that for the 1000 image mean, the vector count past $\approx 2D$ from the jet orifice decreases significantly. This is because the jet in general does not occupy these downstream locations for the configuration 2 operating conditions. The best agreement in the mean $|\vec{u}|$ is observed in the regions qualitatively containing vector counts of at least 50. Therefore, to minimize misinterpretation of presented image results, a 5% vector count threshold is applied. For processing a 1000 image sequence, the 5% threshold results in locations with less 50 vectors to not be included in the mean and phase averaged presented images.

5. Non-Reacting H_2/N_2 Jet in a Heated Air Crossflow at Plane Z/D = 1.0

The flowfield is now described for the non-reacting H_2/N_2 jet in heated air crossflow. This is case 1 in Table 4.2. The cross sectional plane is $Z/D = 1.0$. At this plane, the raw PIV scattering measurements show the jet fluid concentrated close to the jet orifice in what will be shown to be a small wake region. For the non-reacting operating conditions, J=18.9 and thus much of the jet still contains a large out of plane motion (momentum) at $Z/D = 1.0$. Because of the intermittent and small region of vector generation directly behind the jet, a larger sample size of 0.5 s is used to characterize the time-average and the wake dynamics. This corresponds to 5000 instantaneous calculated PIV vector fields.

Figure 5.1 shows the crossflow and injector pressure behavior over this time. The pressure traces shown for P1, P5 and P10 are bandpass filtered between 20 Hz and 2000 Hz to show the dominant trend and to remove the pressure measurement port broadband noise. The locations P1 and P5 have a low fluctuating component typically within ±0.5 kPa between 20 Hz to 2 kHz, which is characteristic of the heated air crossflow conditions. The injector pressure P10 shows relatively larger amplitudes, but appear more random and do not contain strong acoustic coherence at any one frequency. A PSD of P5 and P10 for the 0.5 s duration shows a broad spectrum of small amplitude peaks across the 5 kHz range. Such broad low amplitude spectral behavior is typical for this naturally self-excitable dump combustor under non-reacting conditions.

Notable in the spectrum of P1 and P5 are broad peaks centered around 2.7 kHz and 3.2 kHz, respectively. This is the pressure measurement port broadband noise and is quantified in section 3.5.3. Briefly, these are the broadband Helmholtz reso-

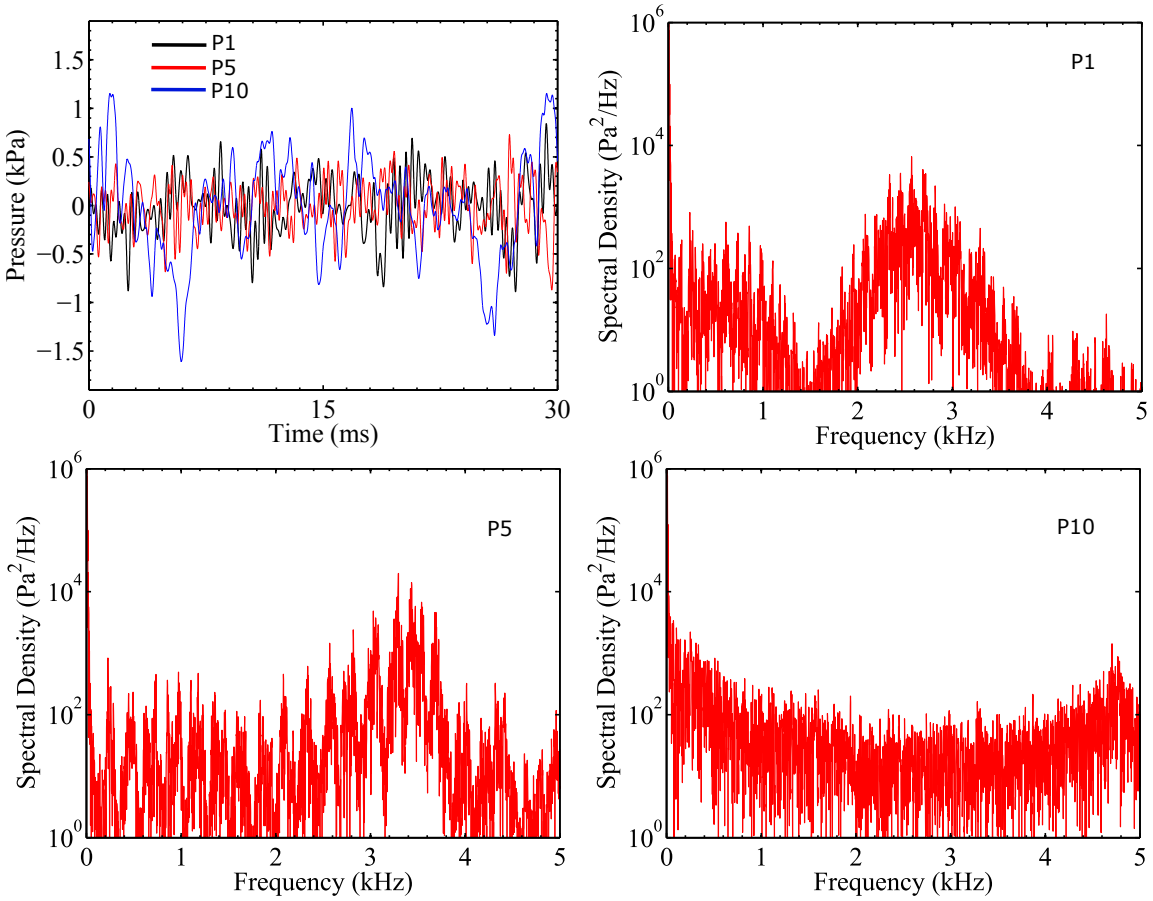

Figure 5.1.. Pressure trace over 30 ms bandpass filtered between 20 Hz and 2000 Hz. Shown also are the PSDs calculated from the raw pressure (not bandpass filtered) for P1, P5, and P10.

nances f_H of the pressure instrumentation ports. An estimation of f_H using equation 3.17, the port geometry and the heated air crossflow temperature for a sounds speed estimation results in $f_H \approx 4$ kHz. The P10 PSD supports this since it does not show a broad peak between 3-5 kHz. The injector fluid properties are different from that of the crossflow, and the injector port is designed for a $f_H \approx 15$ kHz to minimize measurement inaccuracy with the expected lower time scales of the JICF hydrodynamics.

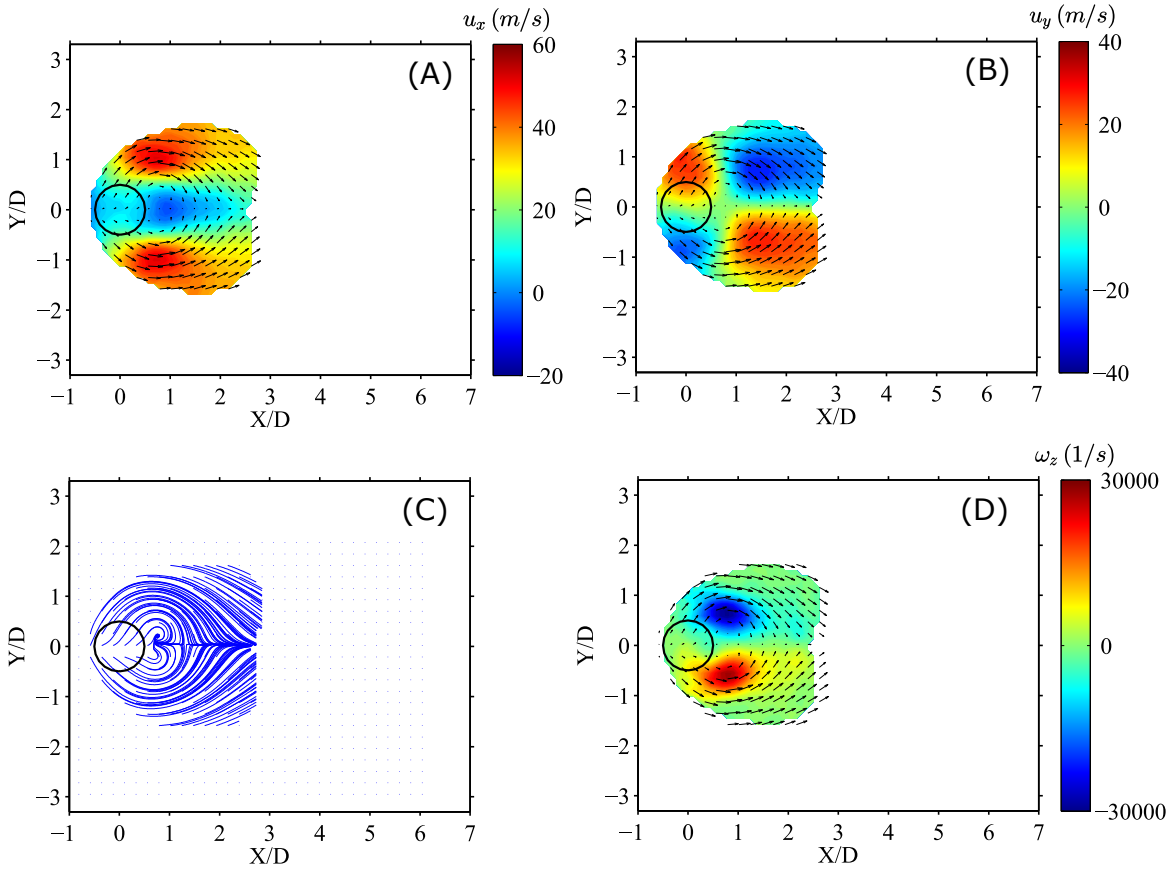

Figure 5.2.. Time average velocity field for H_2/N_2 jet in heated hir crossflow at plane Z/D = 1.0. (A) u_x, (B) u_y, (C) streamlines, (D) ω_z. The jet orifice exit is shown as a thick black circle centered on $(X/D, Y/D) = (0, 0)$.

Figure 5.2 shows the time-averaged vector field with a false colored contour background for the x-velocity component u_x, the y-velocity component u_y, the out-of-plane z component of vorticity $\omega_z = \left(\frac{\partial u_y}{\partial x} - \frac{\partial u_x}{\partial y}\right)\vec{e}_z$, and the mean computed streamlines. The flowfield is characterized by a small low velocity wake region directly downstream of the jet encompassed by a higher velocity shear layer beginning laterally on either side of the orifice. The apparent X/D axial contraction of the shear layer and wake is due to the bulk of the jet still carrying a large out of plane motion at the plane Z/D=1 and for the large J value. It's clearest with u_y that the flow is moving out-

ward near X/D=0 and strongly curling inward after X/D=1. A strong wake region is developed directly behind the jet orifice with a pair of counter rotating vortex structures. This wake region exists as a consequence of the jet acting as a flow obstruction to the incoming crossflow. Also note the symmetry about Y/D=0. Conversely, the instantaneous flowfields are highly asymmetric showing a strongly fluctuating wake and shear layer.

A POD analysis is performed to identify, sort and characterize the large scale coherent structures of the velocity field. The POD is implemented using the method of snapshots originally developed by Sirovich [59] and is implemented following identically the method of snapshots on vector fields [60]. Since the POD procedure herein follows [60] and the mathematical basis well established, only a brief description is given. Each sequential vector field is treated as a snapshot of the flow. The POD result is the expansion of the fluctuating part of a snapshot as

$$u^n = \sum_{i=1}^{N} a_i^n \phi^i \tag{5.1}$$

where u^n is a single matrix containing all of a single snapshots data, N is the total number of snapshots, ϕ^i are the proper orthonormal modes (i.e. the POD modes), and a_i^n are the POD temporal coefficients. The POD modes, or spatial modes, are constructed by using as a basis the eigenvectors of an eigenvalue problem of the autocovariance matrix $U^T U$ created by the full N snapshot data set $U = [u^1 u^2 ... u^N]$. The POD temporal coefficients are then derived by projecting the raw snapshot data onto the POD modes. The aim is to decompose the original spatial-temporal data set as a finite series of POD spatial modes that best approximate the original data. The total amount of kinetic energy of the velocity fluctuations associated with a spatial POD mode is proportional to its eigenvalue magnitude [60]. Therefore, by ordering the eigenvalues in decreasing order of magnitude, a reconstruction can be made with the most energetic modes, thereby creating a reduced order finite approximation of an otherwise highly turbulent velocity time series. The most characteristic coherent structures in the flowfield are identified in this manner as the largest eigenvalues and

used to identify the dominant jet dynamics. The POD performed here is done on the fluctuating velocity field, i.e. the mean is subtracted before the POD.

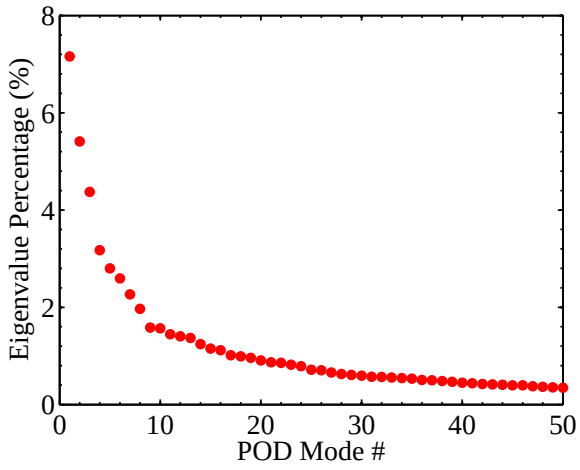

Figure 5.3.. POD eigenvalue relative percentages for first 50 POD modes. The plane is Z/D=1. 5000 images were used for the POD.

For the POD modes presented herein, the percentage shown is the eigenvalue magnitude relative to a summation of eigenvalue magnitudes. This is proportional to the total energy of velocity fluctuations associated with that mode. The presented POD spatial modes are also normalized unless otherwise noted and thus the vector lengths (and corresponding vector calculated background) for the POD modes do not have meaningful significance in engineering units per se until combined with the temporal coefficients in the reconstruction of the snapshots. However, the spatial variation across a normalized mode holds significance in so far that it shows the variance across the mode. Additionally, the normalized modes corresponding to the largest eigenvalues capture the dominant large scale dynamic structures of the jet. Finally, for the POD analysis, the 5% vector cutoff threshold is not applied to the presentation of the results as it was for the time averaged results since it is understood that the most descriptive features of the flowfield as determined by the most energetic modes will sort these low quantity calculable vector energies accordingly.

Figure 5.3 shows the energy as a percentage of the first 50 POD eigenvalues λ_i, where i refers to the POD mode number. The first POD mode contains 7.2% of the total energy of velocity fluctuations while POD modes 2 and 3 contain 5.4% and 4.4%, respectively. The first ten modes combined contain a total of 38% of the energy and the remaining modes make up instantaneous turbulent variations of the flow patterns. Spectral analysis is performed on the POD temporal coefficients to identify the frequency content associated with the spatial mode. Figure 5.3 shows a PSD of the first five modes temporal coefficients, where mode 1 is plotted twice with different axes. First note that in all modes, a large portion of the spectral energy is concentrated below 1 kHz. POD mode 1 contains several well defined peaks in this range, most notable for a wide band centered near 481 Hz. POD mode 3 shows a frequency near this at 490 Hz. POD modes 1-4 contain relatively minor kHz frequency peaks, though these are more difficult to distinguish in these spectra. These spectra must be interpreted with caution, however. A careful inspection of each of the identified POD frequencies shows that each is within $\pm$ 40 Hz of a frequency peak in the crossflow pressure spectra.

The first five POD spatial modes (normalized) are shown in Figure 5.5. Each POD mode vector field is plotted three times overlaid on the false colored background for u_x (left column), u_y (middle column), and ω_z (right column). POD modes 1, 2, and 3 clearly show in-plane vortical flow structures in the region of the jet. POD mode 1 containing the largest percentage of energy contains a clockwise rotating vortex structure located directly downstream of the jet orifice and centered at $(X/D, Y/D)$=(1.25,0). Multiplying mode 1 by a negative coefficient changes the direction of rotation. Mode 3 resembles a version of mode 1 contracted back toward the jet orifice with the vortex centered at $(X/D, Y/D)$=(0.5,0). The two modes indicate nearly the same structure with a spatial phase shift. Two modes with a phase shift are necessary to track moving structures. Multiplying mode 2 by a negative coefficient shows that this mode bears a resemblance with the location of the higher velocity jet shear layer in the time averaged velocity, a kidney shaped structure. Within the

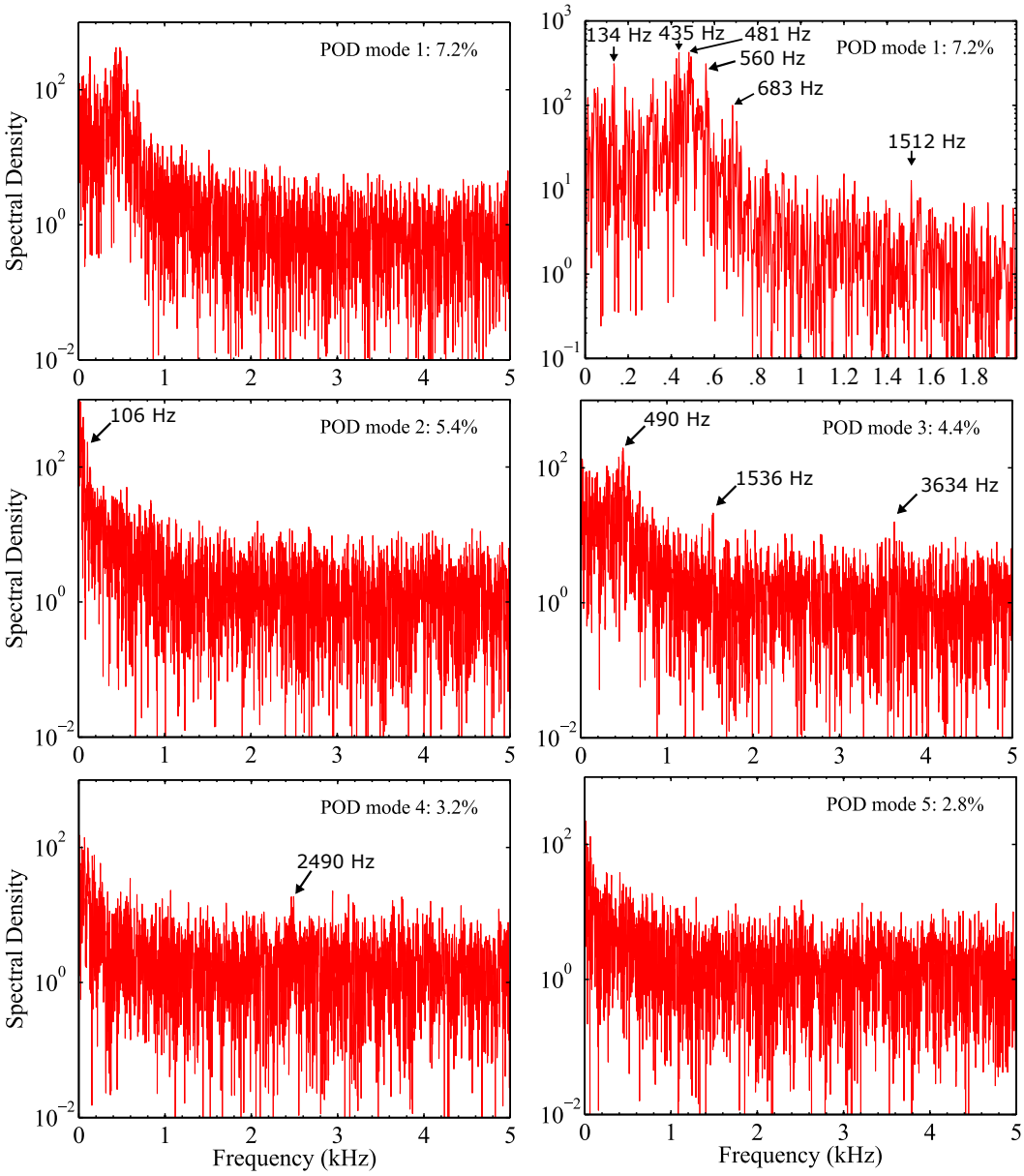

Figure 5.4.. PSD of the POD temporal coefficients. Dominant frequencies are highlighted within each POD mode.

kidney structure of mode 2, ω_z shows a pair of counter rotating vortex structures located at $(X/D, Y/D)$=(1,$\pm$0.5). Mode 4 resembles an asymmetric version of mode 3, and mode 5 resembles a combination of mode 2 and mode 4.

The time averaged velocity shows a symmetric wake surrounded by the higher velocity jet shear layers. The field as a whole is contracted near to the jet orifice for the high J value. The time averaged field contrasts with observations of the instantaneous velocity fields, where instead a highly asymmetric and dynamic wake region exists. The first few POD modes capture the largest and most coherent dynamic structures. Notably, alternating structures which begin near to the jet lateral edges, gradually extend away from the orifice while also rolling in toward the Y/D=0 centerline, and eventually a decaying contraction giving rise to the start of another event but instead on the other side of the jet. This process of extension in Y/D and waving in X/D is not a static process. It requires multiple POD modes to track the movement. A reconstruction using the POD modes 1-3 shows this general behavior and also shows the movement of the vortex structure centered on the centerline Y/D moving back and forth between X/D=0.5 and 1.25. There is a considerable amount of cycle to cycle variation in the instantaneous fields, and thus no one POD mode contains a significant amount of energy. The modes 4, 5 and beyond then represent irregularities in the dynamic wake cycle, due to the influence of turbulence on the velocity fluctuations and the broad band spectral acoustics present in the crossflow.

At this plane $Z/D = 1$, the POD spectral content describes the jet wake as the dominant flowfield feature. Consider the accumulation of energy in the spectral band centered around 481 Hz in POD mode 1 or 490 Hz in POD mode 3. The 481 Hz frequency in terms of a Strouhal number is $St_{cf} = (481Hz)D_j/(26m/s) = 0.11$. This Strouhal number agrees well with reported JICF wake dynamics. This also agrees with the POD spatial mode shapes describing oscillatory motions directly behind the jet orifice in the jet wake. Therefore, this suggests that these dynamics are actually the jet wake hydrodynamics.

There is an additional frequency at 134 Hz in POD mode 1. Assuming a steady velocity through the jet injector, integration of the jet injector velocity from the jet choked orifice plate to the jet orifice exit results in a travel time of 6.8 ms for a parcel

of fluid. Treating this as a period, a frequency of 147 Hz results (1/6.8 ms). This suggests that the 134 Hz frequency may be a consequence of the injector geometry.

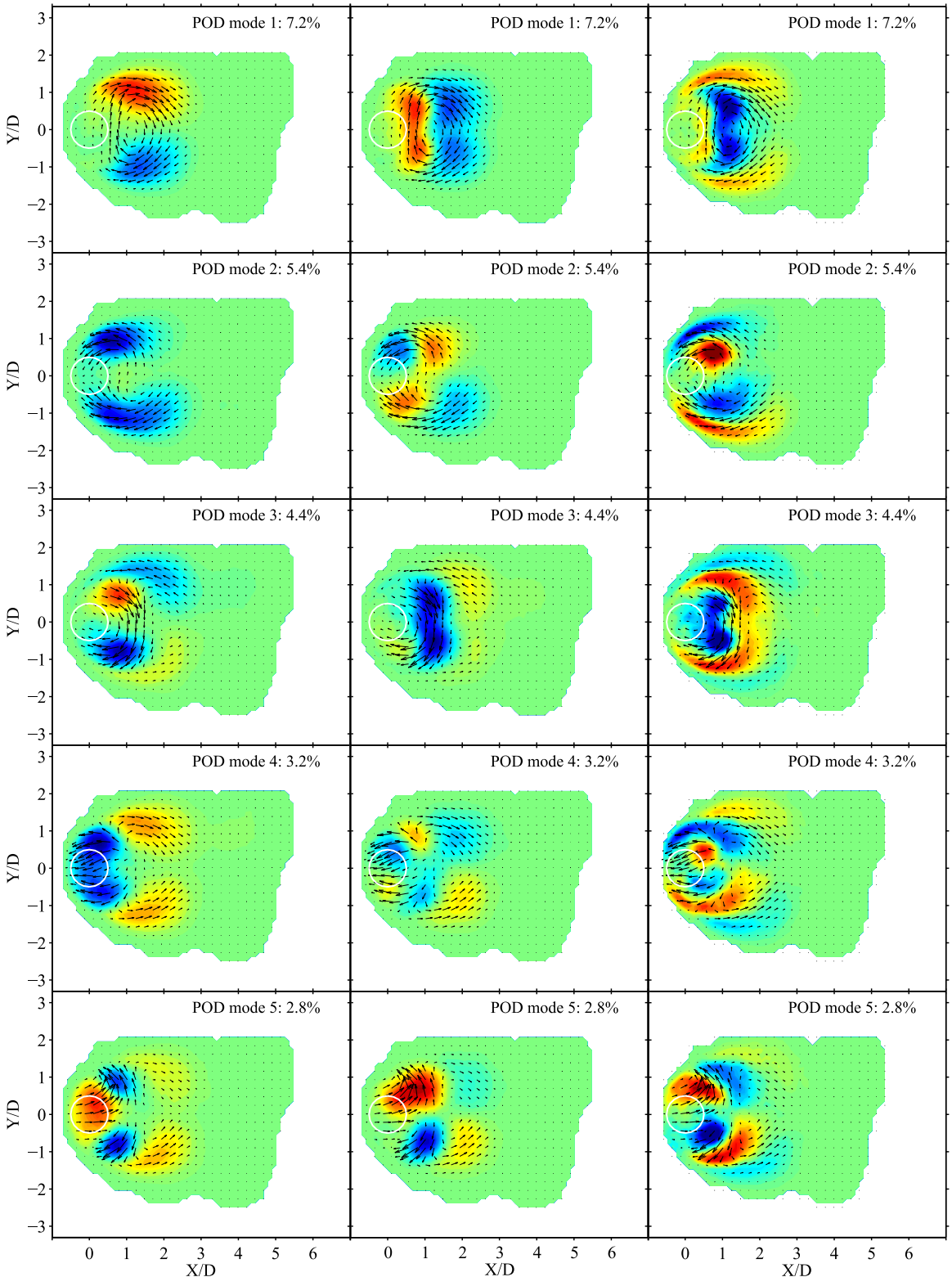

Figure 5.5.. Normalized spatial POD modes 1-5 showing u_x (left), u_y (middle) and ω_z (right).

6. Non-Reacting H_2/N_2 Jet in a Heated Air Crossflow at Plane Z/D = 2.7

The flowfield is now described for the non-reacting H_2/N_2 jet in heated air crossflow at the cross sectional plane $Z/D = 2.7$. This is case 2 in Table 4.2. At this plane, the raw PIV scattering measurements show the jet fluid continuously occupying most of the PIV FOV. A 0.1 s duration of data is presented corresponding to 1000 instantaneous calculated PIV vector fields. Figure 6.1 shows the crossflow and injector pressure behavior over this time. A PSD of P1, P5, and P10 for the 0.1 s duration shows multiple small amplitude peaks across the 5 kHz spectrum, most notably for P1 and P5, from the self excited dump combustor. Similar pressure measurement port broadband noise is evident in P1 and P5, but not P10. Therefore, the presented pressure traces are bandpass filtered between 20 Hz and 2000 Hz to show the general trend and remove the port bias. Similar to the previous non-reacting data, the locations P1 and P5 have a low fluctuating component typically within ±0.5 kPa which is characteristic of the heated air crossflow conditions. The injector pressure P10 shows relatively larger amplitudes, but does not contain strong acoustic coherence at any one frequency.

Figure 6.2 shows the time-averaged velocity quantities u_x, u_y, ω_z, and streamlines. The flowfield is characterized by an elongated low velocity wake region beginning around $X/D = 1.25$ encompassed by a higher velocity jet shear layer. This was also observed at the plane Z/D=1, except the shear layer quickly curled in toward the centerline Y/D=0 behind the jet orifice. Here at $Z/D = 2.7$, the low velocity wake coincides with a bubble in the streamlines centered at $(X/D, Y/D)$=(2.5,0). Also, the extension of the wake to X/D=6 and the larger shear layer suggests the jet at this plane is beginning to bend into the crossflow. This is supported by the

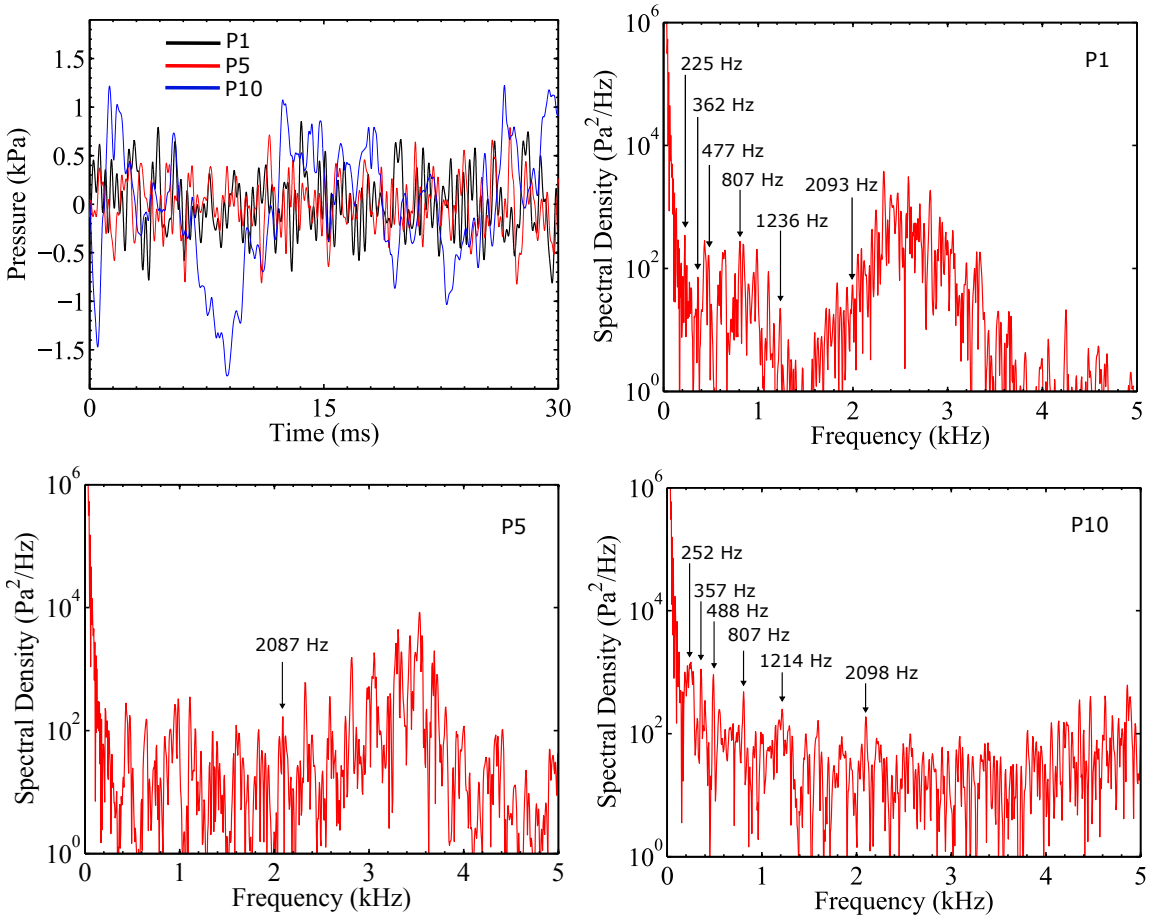

Figure 6.1.. Pressure trace over 30 ms bandpass filtered between 20 Hz and 2000 Hz. Shown also are the PSDs calculated from the raw pressure (not bandpass filtered) for P1, P5, and P10.

time-averaged results at the plane Z/D=1 where it was observed that the jet fluid was concentrated near the jet orifice. Also note the time average symmetry about Y/D=0, which was also observed at the plane Z/D=1. The instantaneous flowfields are highly asymmetric and turbulent. Compared to the plane Z/D=1, the mean counter rotating ω_z vortex structures have significantly increased in size (by a factor of two), but are at least a factor of two weaker.

A POD analysis of the 0.1 s duration is performed. First, Figure 6.3 shows the spectral behavior of the first 6 POD temporal coefficients. For each POD mode, some

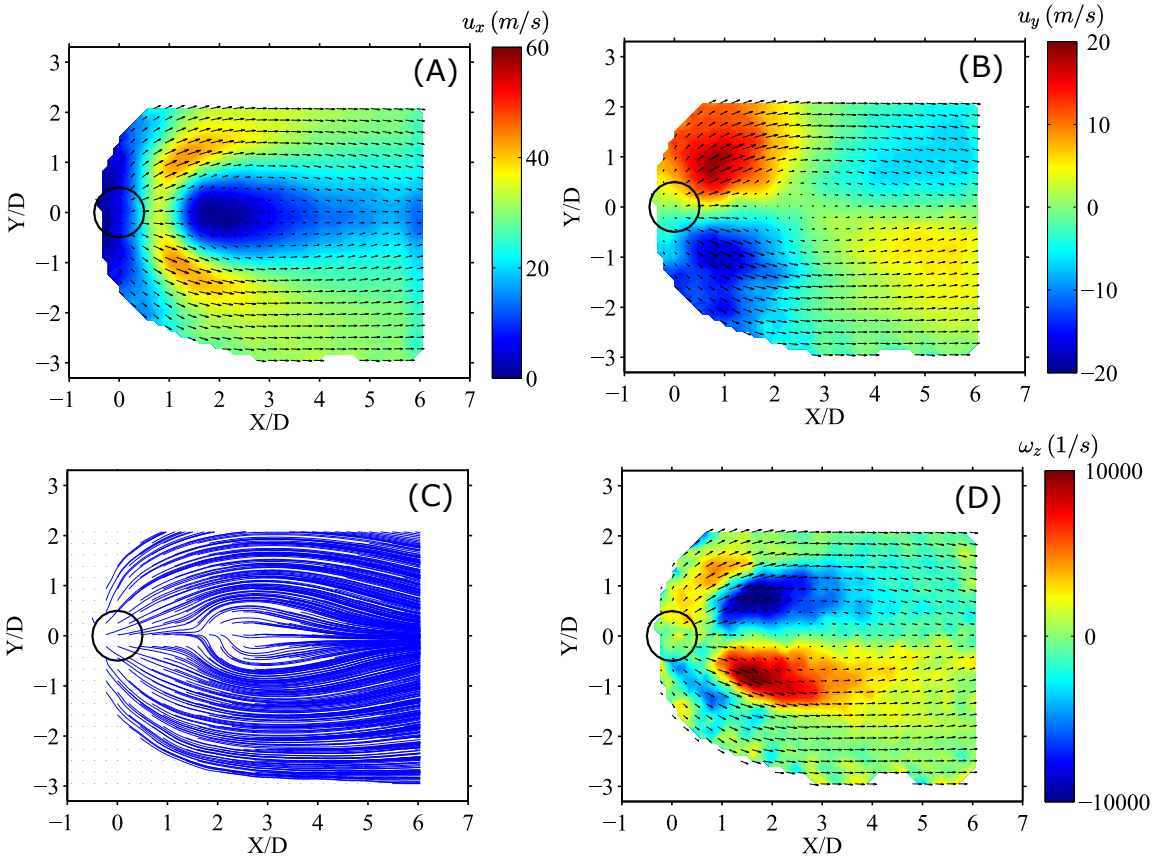

Figure 6.2.. Mean velocity field for H_2/N_2 jet in heated air crossflow at plane Z/D = 2.7. (A) u_x, (B) u_y, (C) streamlines, (D) ω_z.

of the dominant spectral peaks are highlighted. First note the energy distribution for the first six POD modes. POD mode 1 and mode 2 contain just 3.6% and 2.2%, respectively, whereas at the plane Z/D=1, POD mode 1 and mode 2 contain 7.2% and 5.4%, respectively. At the plane Z/D=1, the only feature was the wake dynamics, whereas at the plane Z/D=2.7, the time average shows a larger wake and jet shear layer region. Most notable for mode 1 is an energetic peak at 400 Hz and sharp peak at 2129 Hz. A strong 400 Hz frequency is also observed in mode 3. Similar to plane Z/D=1, these spectra must be interpreted with caution. A careful inspection of each of the identified POD frequencies shows that each is within ± 50 Hz of a frequency peak in the crossflow pressure spectra. The pressure spectra, however, does not show

a power preference for the band 400 Hz - 500 Hz relative to other frequency bands, while the POD spectra at both planes show broad energetic peaks over this range. Briefly consider the characteristic wake frequencies of the JICF. These are typically reported as $St_{cf} = fD_j/\overline{u}_{cf}$, and for non reacting and reacting JICF generally vary between 0.1 and 0.15 [13,19]. In our case, $\overline{u}_{cf}$ is $\approx$ 25 m/s resulting in a St_{cf} between 450 Hz and 670 Hz. The POD mode 4 and 6 contains a 615 Hz and 566 Hz peak, respectively. Also, the 400 Hz band of mode 1 and mode 3 contains peaks between 450 Hz and 500 Hz. To continue this discussion, it's instructive to inspect the spatial mode shapes for these modes.

The first five POD spatial modes (normalized) are shown in Figure 6.7. Each POD mode vector field is plotted three times overlaid on the false colored background for u_x (left column), u_y (middle column), and ω_z (right column). POD modes 1-5 clearly show in-plane vortical flow structures in the region of the jet. POD mode 1 containing the largest percentage of energy contains a counter clockwise rotating vortex structure located directly downstream of the jet orifice and centered at $(X/D, Y/D)$=(2,0). Multiplying mode 1 by a negative coefficient changes the direction of rotation. Mode 5 resembles a version of mode 1 extended away from the jet orifice with a vortex centered at $(X/D, Y/D)$=(3.5,0). The two modes indicate nearly the same structure with a spatial phase shift. Multiple modes with phase shifts are necessary to track moving vortex structures. Mode 3 contains multiple oppositely rotating vortex structures centered on Y/D=0 at $X/D = 0.75$, 2.75, and 5.25. Mode 2 shows a significant streamwise velocity component directly behind the jet orifice with corresponding counter rotating vortex structures located at $(X/D, Y/D)$=(1,$\pm$1).

At this plane Z/D=2.7, the time average velocity shows an elongated narrow wake region, surrounding high velocity jet shear layer, and a pair of counter rotating vorticity structures beginning directly downstream of the jet orifice. The time averaged field contrasts with observations of the instantaneous velocity fields, where instead a highly asymmetric and dynamic wake and shear layer exist. The first few POD modes represent the largest and most coherent dynamics. In addition to the central

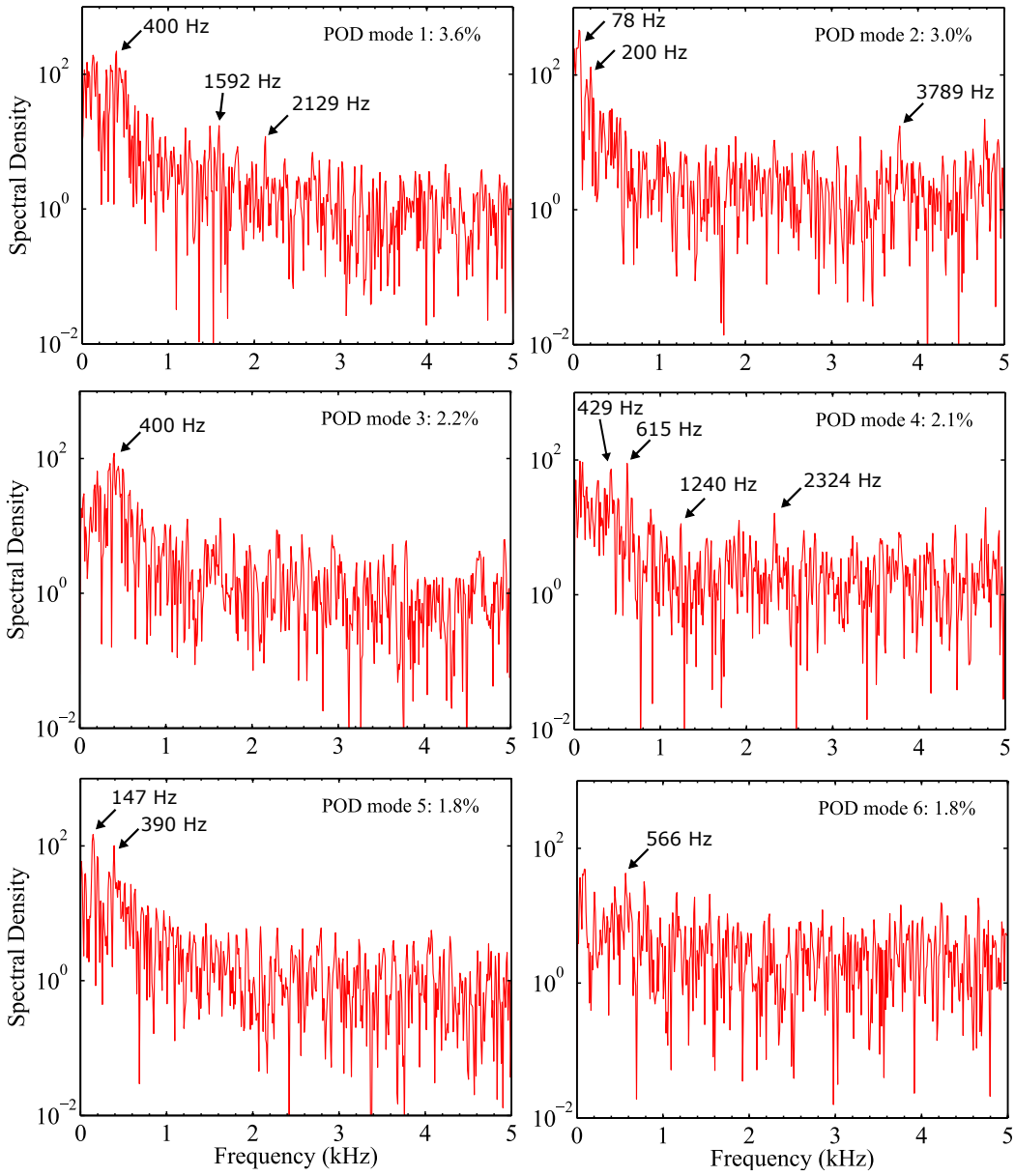

Figure 6.3.. PSD of the POD temporal coefficients. Dominant frequencies are highlighted within each POD mode.

vortex structure, POD mode 1 captures alternating high velocity events on the jet shear layer. Comparing with the instantaneous velocity fields, bursts of high velocity in the shear layer start near to the jet orifice around Y/D=0. In some instances, this initial burst resembles the region directly behind the jet orifice in mode 2. In other

instances, the high velocity region also follows the extending jet shear layer. Mode 1 captures this. The similarity of the remaining modes and the lower energy for mode 1 and 2 indicate that there is a considerable amount of cycle to cycle variation in the instantaneous fields, and thus no one POD mode contains a significant amount of energy. Also, these processes are not static and require multiple POD modes to track the movement. The other modes then also represent irregularities in the cycle, due to the influence of turbulence on the velocity fluctuations and the broad band spectral acoustics present in the crossflow.

When compared to the plane Z/D =1, the POD mode 1 at planes Z/D =1 and Z/D =2.7 are remarkably similar. Both planes POD mode 1 shows vortex structures centered on Y/D=0 in the low velocity wake region. Modes 3 and 5 for plane Z/D =2.7 also show Y/D=0 centered structures indicating the different POD modes capture the convection and diffusion of these structures. Unlike plane Z/D =1, a POD reconstruction using modes 1-5 for plane Z/D =2.7 contains many instances where 2-4 vortex structures are simultaneously present. The lack of observation of this many structures at the plane Z/D =1 is likely due to the small wake size and the corresponding PIV spatial resolution.

The multi-frequency content of a given POD mode and the correlation across modes indicates physical processes are spread out across many POD modes. A single POD mode contains information from different processes. A DMD analysis of the velocity field is performed to complement the POD. DMD is a modal decomposition technique, like POD, that takes an ensemble of data, in this case a series of instantaneous flowfield snapshots, and reduces it to orthogonal modes approximating the original dynamic dataset. Whereas POD focuses on minimizing the error between the decomposed modes and the original dataset, DMD decomposes the dataset in terms of temporal evolution, where each DMD eigenmode corresponds to a single frequency [61,62]. In the case of POD, a single POD mode often contains multiple frequencies, confusing the determination of mechanistic processes when comparing POD modes. The utility of DMD in extracting dynamics as a function of frequency is re-

alized when complex coupling phenomena involving multiple physical processes (e.g. acoustics, heat release, and hydrodynamics) can be viewed as individual modes [63].

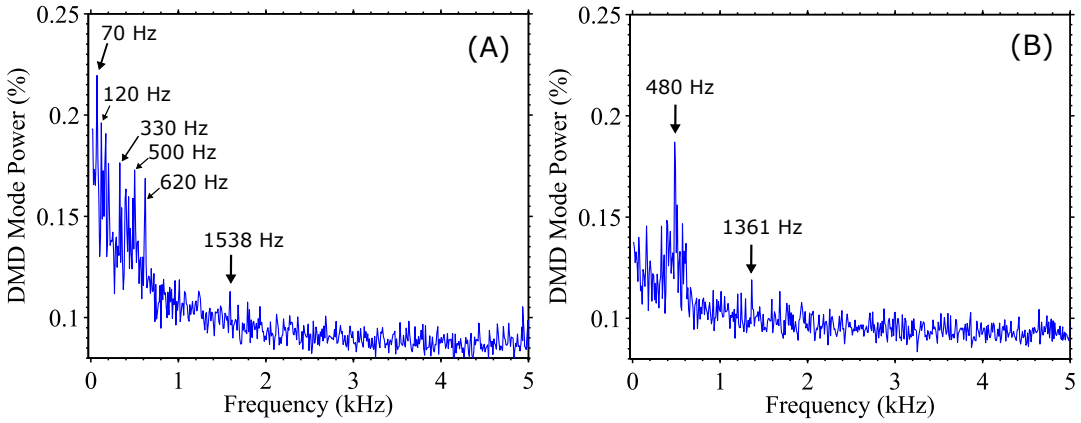

Figure 6.4.. Spectra from a DMD on (A) u_x and (B) u_y.

Figure 6.4 shows the spectral characteristics of a DMD performed separately on u_x and u_y. Similar to the POD, the DMD results in mostly energetic frequencies below 1 kHz. The DMD u_x spectra contains many spectral peaks between 70 Hz and 620 Hz, while the DMD u_y shows a dominant 480 Hz mode. The DMD of u_x also shows a 480 Hz peak wide enough also encompassing 490 Hz. First consider the frequency 480 Hz. Figure 6.5 shows time instances in the evolution of the DMD spatial structure corresponding to a combination of the 480 Hz and 490 Hz modes. At t=0 ms, a clockwise rotating vortex is located directly behind the jet orifice and centered near $(X/D, Y/D)$=(1.5,0). Also note two smaller oppositely rotating vortex structures centered at $(X/D, Y/D)$=(2.75,1.5) and $(X/D, Y/D)$=(3.5,-1). At t=0.5 ms, the largest vortex is convected downstream to $(X/D, Y/D)$=(2.25,0) and shows signs of distortion (compressing in X/D and stretching in Y/D). The bottom smaller vortex appears to convect to $(X/D, Y/D)$=(4.75,0). Between t = 0.5 ms and 1.1 ms, the large vortex structure distortion gradually increases and the coherence of the vortex dissipates. As this is ending at t = 1.1 ms, a new oppositely rotating vortex at $(X/D, Y/D)$=(1.75,0) is being generated directly behind the jet orifice, and

two smaller oppositely rotating vortices are located at $(X/D, Y/D)$=(3.75,1.25) and $(X/D, Y/D)$=(3,1.5).

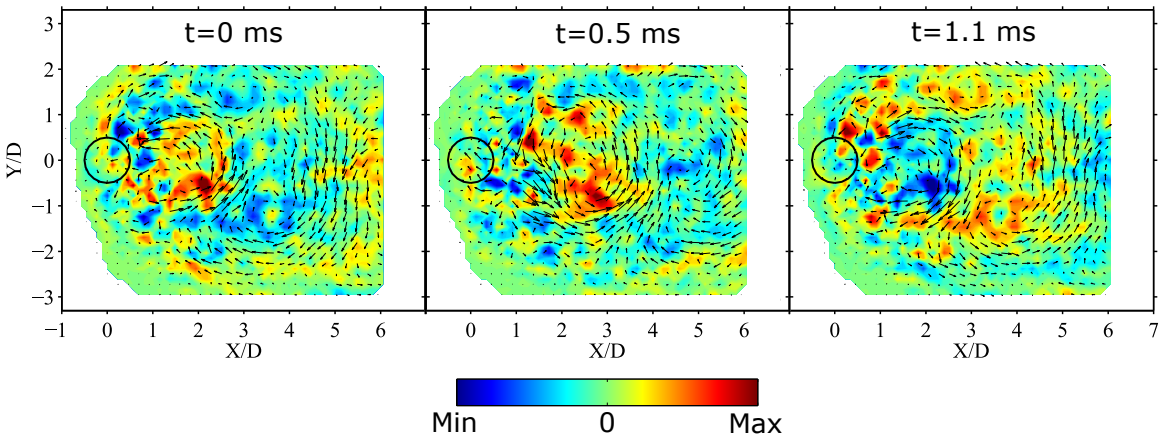

Figure 6.5.. DMD 480 Hz modal evolution showing the vortex evolution. False colored background is ω_z.

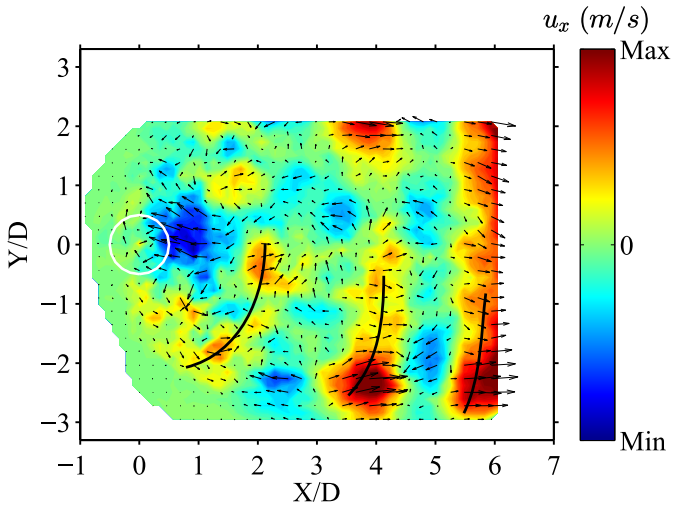

Figure 6.6.. DMD spatial mode for 620 Hz. False colored background is u_x. Three thick black curves are drawn in to indicate the streamwise velocity undulations.

Further analysis of the DMD results shows that all frequency content between 300 Hz and 500 Hz is associated with rotating structures in and near the wake of the jet that appear to be wake vortices. Consider the accumulation of energy in the spectral band centered around 480 Hz in the DMD of u_y. The 480 Hz frequency in terms of a Strouhal number is $St_{cf} = (480Hz)D_j/(26m/s) = 0.11$. This Strouhal number agrees well with reported JICF wake dynamics. This also agrees with the POD spatial modes shapes describing oscillatory motions directly behind the jet orifice in the jet wake, and with the spectral energy accumulation in POD modes 1 and 3 around the region of 400 Hz. Therefore, these dynamics are likely the jet wake hydrodynamics.

For the remaining dominant DMD modes, the 70 Hz frequency resembles a linear combination of POD modes 2, 3 and 4. The 120 Hz DMD frequency resembles POD mode 1 except without the vortex centered on Y/D=0. Analysis of the DMD frequencies between 70 Hz and 200 Hz shows that these are dominantly associated with the jet shear layer. In fact, each mode appears to describe similar behavior but at a different frequency: shear layer velocity pulsations, swaying of the jet shear layer in the Y/D direction, and convection of high velocity pockets of fluid starting close to the jet orifice and traveling down along the shear layer. Interestingly, the 330 Hz frequency DMD modal evolution describes a mixed feature: a combination of the wake vortex features and shear layer dynamics described.

One other feature is worth noting. The 620 Hz DMD frequency mode does not directly resemble a POD mode and is shown in Figure 6.6. This mode is characterized with predominantly streamwise velocity fluctuations clustered in alternating undulations. Three of the undulations are partially indicated by thick black curves in Figure 6.6 and gradually become less curved as they stretch and progress away from the jet orifice. These are not static structures. As the DMD temporal mode progress, half a period later the positive undulations become negative and vice versa.

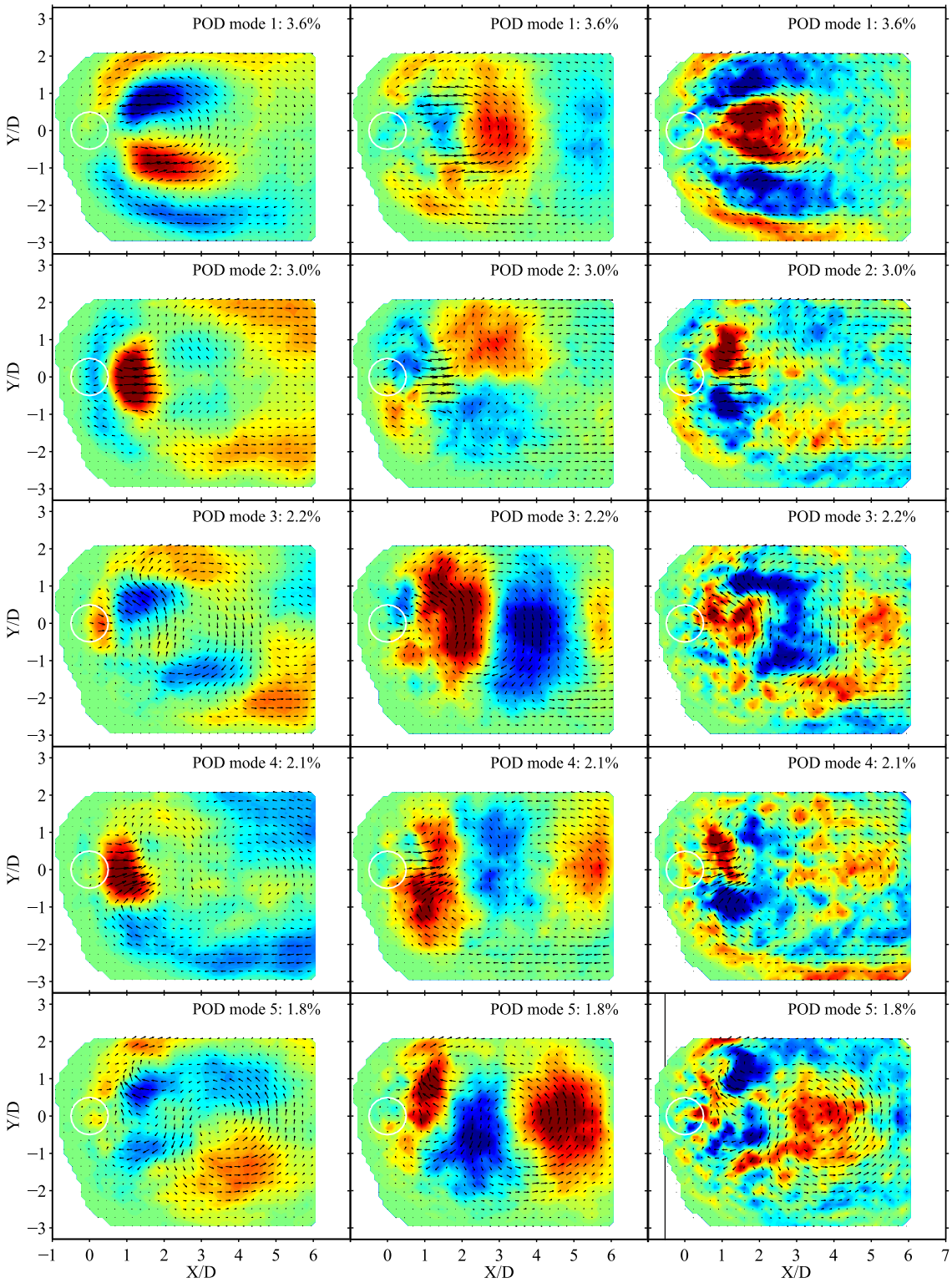

Figure 6.7.. Normalized spatial POD modes 1-3 showing u_x (left), u_y (middle) and ω_z (right).

7. Reacting H_2/N_2 Jet In a Vitiated Oscillating Crossflow at Plane Z/D = 1.0

To begin, the JICF flowfield is described at the plane Z/D = 1.0 for both medium and low amplitude unsteady crossflow conditions, case 3 and case 4, respectively, in Table 4.2. The test operating conditions for case 3 were such that the crossflow $2L$ amplitude spontaneously decreased during the OH-PLIF/PIV measurements for a short duration. This short low amplitude duration is case 4. The crossflow and jet operating conditions were fixed throughout. At this plane, the raw PIV scattering measurements show the jet fluid continuously occupying most of the PIV FOV. For case 3, a 0.1 s duration of data is presented corresponding to 1000 instantaneous calculated PIV vector fields. For case 4, a 0.06 s duration of data is presented corresponding to 606 instantaneous calculated PIV vector fields.

Figure 7.1 shows the crossflow and injector pressure behavior for case 3. Three pressure measurement locations are shown: the crossflow P1 at the combustion chamber exit, the crossflow P5 directly upstream of transverse jet, and P10 inside the jet injector. The dominant acoustic at the location P1 is the chamber $2L$ at 198 Hz. This location is a good measure of the p' amplitude of the resonant chamber acoustics, including the $2L$ p' mode. Harmonics of the $2L$ and additional higher frequencies are typically present under reacting crossflow conditions since the crossflow in general always contain low amplitude unsteadiness at the chamber resonant acoustics due to the self-excited nature of the dump combustor.

Many of the frequency peaks are highlighted in Figure 7.1. The injector P10 PSD shows three peaks at 390 Hz, 445 Hz, and 774 Hz, all of which are also measured at P1 and P5. These are the crossflow acoustic frequencies and signifies that that the injector is responding to the fluctuating local injection flowfield. The 390 Hz peak in

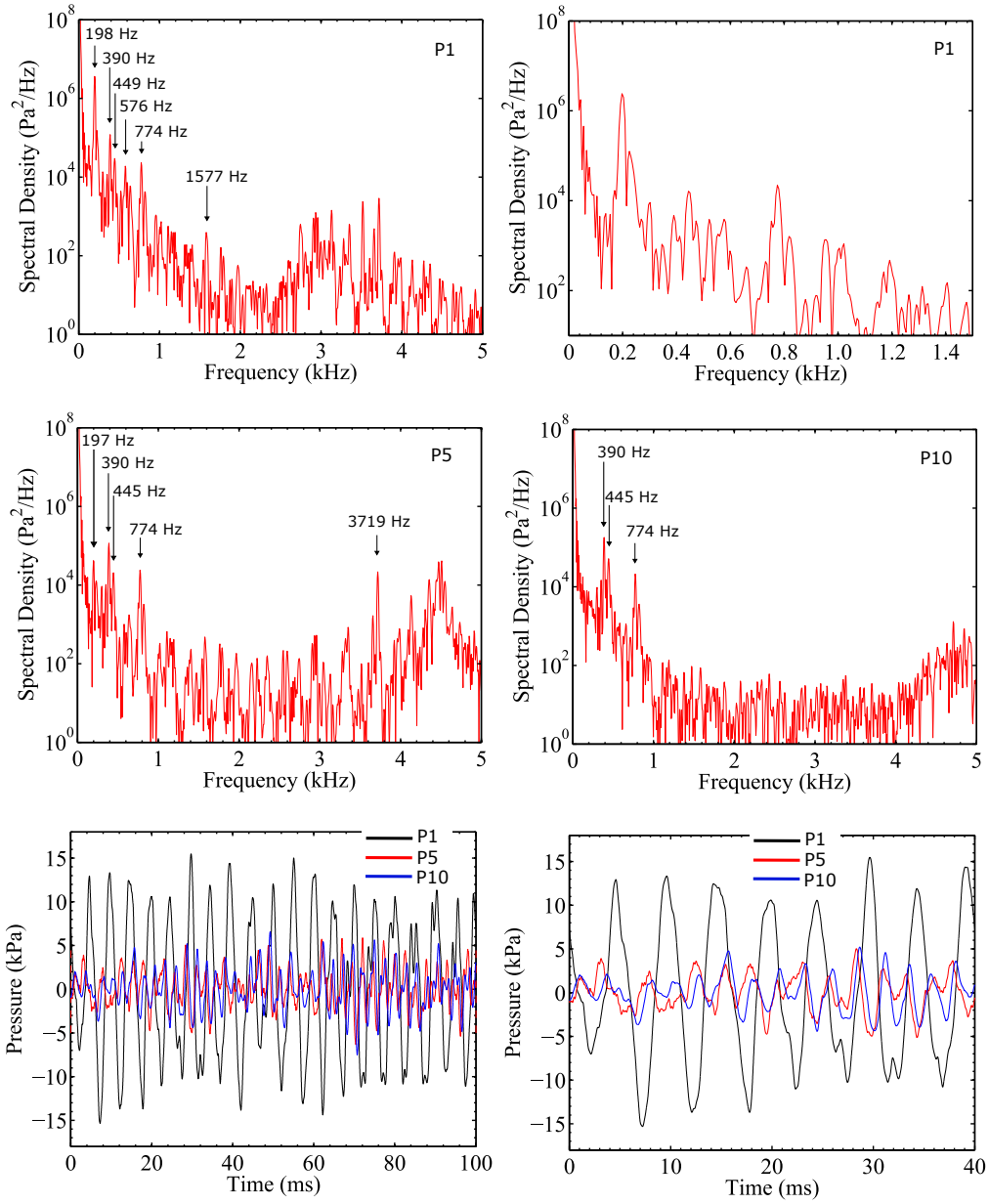

Figure 7.1.. Pressure behavior for case 3. PSD shown for the locations P1, P5 and P10, with P1 shown twice to highlight low frequency content. Also shown are the 20 Hz-2000 Hz bandpass filtered pressures from P1, P5, and P10. This trace is plotted again from 0 s to 40 s to highlight the shape of the waveforms.

P1 and P5 have a similar magnitude, which agrees with the $4L$ near 400 Hz having a p' anti-node near the jet injection point (near P5) and at the combustion chamber exit nozzle (near P1). The 774 Hz frequency is the chamber $8L$, a harmonic of the $2L$. The fact that P10 does not have a 190 Hz peak further supports that the only jet interaction with the chamber $2L$ is through crossflow velocity oscillations as the jet is located at the $2L$ p' node. Figure 7.1 also shows the pressure traces for P1, P5, and P10. The pressure was bandpass filtered between 20 Hz and 2000 Hz to highlight the the dominant dynamics and to remove the pressure port bias. Up until 70 ms, the dominant chamber fluctuation is the 198 Hz $2L$ with a relatively clean sinusoid wave. The fluctuations at P5 and P10 are smaller, but still contain a finite amplitude. After 70 ms, the P1 oscillation shows double peaks and double troughs, and the P5 and P10 fluctuations become larger. After 70 ms, the chamber 390 Hz and 774 Hz frequencies strengthen, but not by much. A PSD of P10 (not shown) from 0 ms to 60 ms shows significantly reduced PSD peaks at both 390 Hz and 774 Hz.

Figure 7.2 shows the crossflow and injector pressure behavior for case 4. The pressure locations P1 and P5 show no significant frequency content in the crossflow below 2 kHz. Also, there's minimal frequency content in the injector P10. In fact, the P10 PSD below 1 kHz resembles a PSD of P10 (not shown) for case 3 from 0 ms to 60 ms in Figure 7.1. The pressure traces for P1, P5, and P10 in Figure 7.2 are bandpass filtered between 20 Hz and 2000 Hz and are considered quasi-steady for the rig operating conditions. Case 4 is used as a reference to compare with the larger and more coherent dynamics of case 3. Figure 7.3 compares the P1 pressure trace for case 3 and case 4 highlighting that case 3 contains organized large amplitude crossflow acsoutics as opposed to the case 4 lower amplitude non-coherent crossflow acoustics.

The corresponding time averaged velocity fields are shown in Figure 7.4. Shown are the 2-component velocity magnitude $|\vec{u}| = \sqrt{u_x^2 + u_y^2}$, the z component of vorticity $\omega_z = \left(\frac{\partial u_y}{\partial x} - \frac{\partial u_x}{\partial y}\right)\vec{e}_z$, and the mean computed streamlines. Also shown is a thick black curve demarcating the jet unburned fluid region calculated from a time average of the simultaneous OH-PLIF measurements. This is analyzed later.

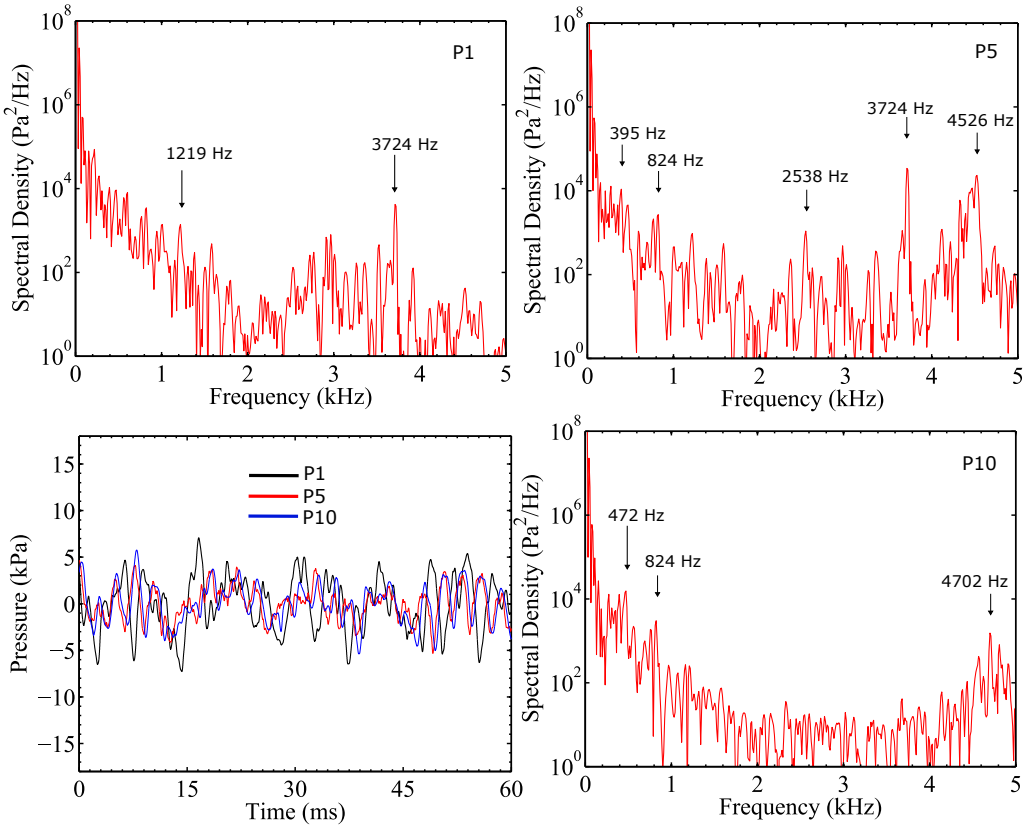

Figure 7.2.. Pressure behavior for case 4. PSD shown for the locations P1, P5 and P10. Also shown are the 20 Hz-2000 Hz bandpass filtered pressures from P1, P5, and P10.

Characteristic JICF features are present in both of these fields. A low velocity wake region downstream of the jet orifice coincides with symmetrical counter rotating vortices. This wake region exists as a consequence of the jet acting as a flow obstruction to the incoming crossflow. The wake begins to end as the crossflow fluid closes in around the leeward side of the jet (observed in the the streamlines closing in toward $Y/D = 0$ near $X/D = 3$). Over a crossflow acoustic cycle, the contents of this aft wake region vary between predominantly unburned jet fluid, burned products and flame front. The jet also displays high velocity shear layers along the jet-crossflow interface (e.g. $Y/D \pm 1.3$) which monotonically decrease in velocity with increasing X/D. This is a consequence of the the jet bending into the crossflow, volumetric en-

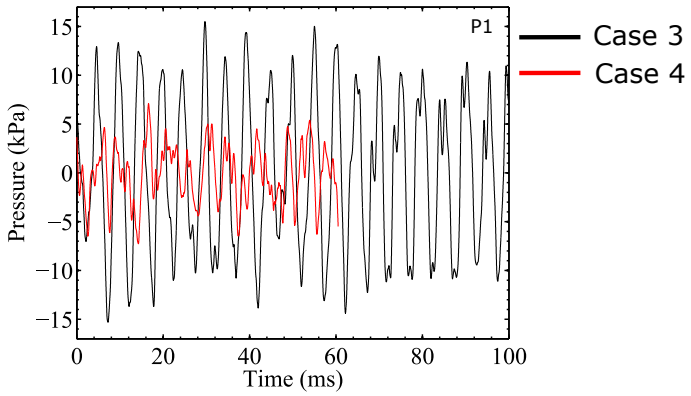

Figure 7.3.. Bandpass filtered P1 pressure (20 Hz-2000 Hz) for case 3 and case 4. This plot shows that case 3 contains organized large amplitude crossflow acsoutics, while case 4 contains lower amplitude non-coherent crossflow acoustics.

trainment of crossflow fluid, and the jet fluid tending toward the local bulk crossflow velocity. Also observe the location and size of the counter rotating ω_z pair, each centered at $(X/D, Y/D) = (1, \pm 1)$. This is a high shear region between the fast moving jet shear layer and the low velocity wake region, and an area with active transport of vitiated crossflow into the interior of the jet. At this plane Z/D=1, these larger magnitude ω_z locations are compact, beginning immediately downstream of the jet lateral edges and extending to X/D=2.5. After approximately X/D=4, the vorticity field is becoming much more homogeneous corresponding to a velocity field oriented predominantly in the streamwise $+X/D$ direction.

Most notable between case 3 and case 4 is the qualitative spatial similarity of the time averaged velocity quantities. Figure 7.5 shows a comparison of the cross sectional profiles of u_x and u_y for case 3 and case 4 as the jet progresses downstream. Four streamwise locations are shown: X/D=1, 2, 3, and 4. It's observed that u_x for case 3 is in general larger for $X/D \leq 3$, which is most pronounced in the shear layer at $X/D = 1$ and the wake at $X/D = 1 - 2$. Note that Raud et al observed decreased penetration for the jet in time varying crossflow [23]. For case 4, the larger crossflow acoustic amplitudes generate larger velocity fluctuation amplitudes at the

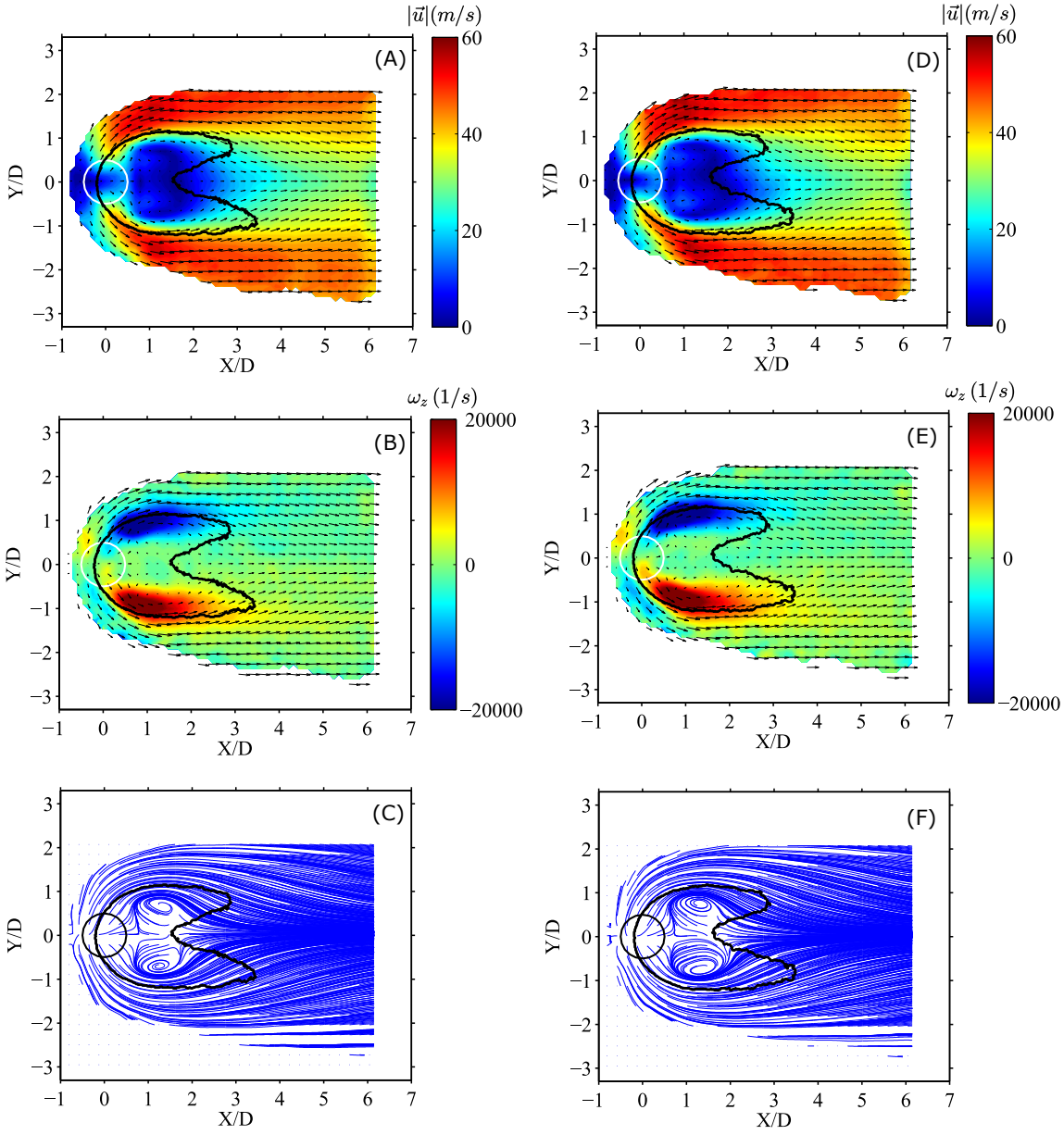

Figure 7.4.. Time averaged velocity for case 3 (A,B,C) and case 4 (D,E,F). Top row: $|\vec{u}|$. Middle row: ω_z. Bottom row: streamlines.

jet. As the crossflow velocity increases during the acoustic cycle, the jet penetration ostensibly decreases causing a larger x and y component of the 3-component velocity to be in plane. Lastly, note the wake asymmetry for u_x about Y/D=0 which is most pronounced for case 3.

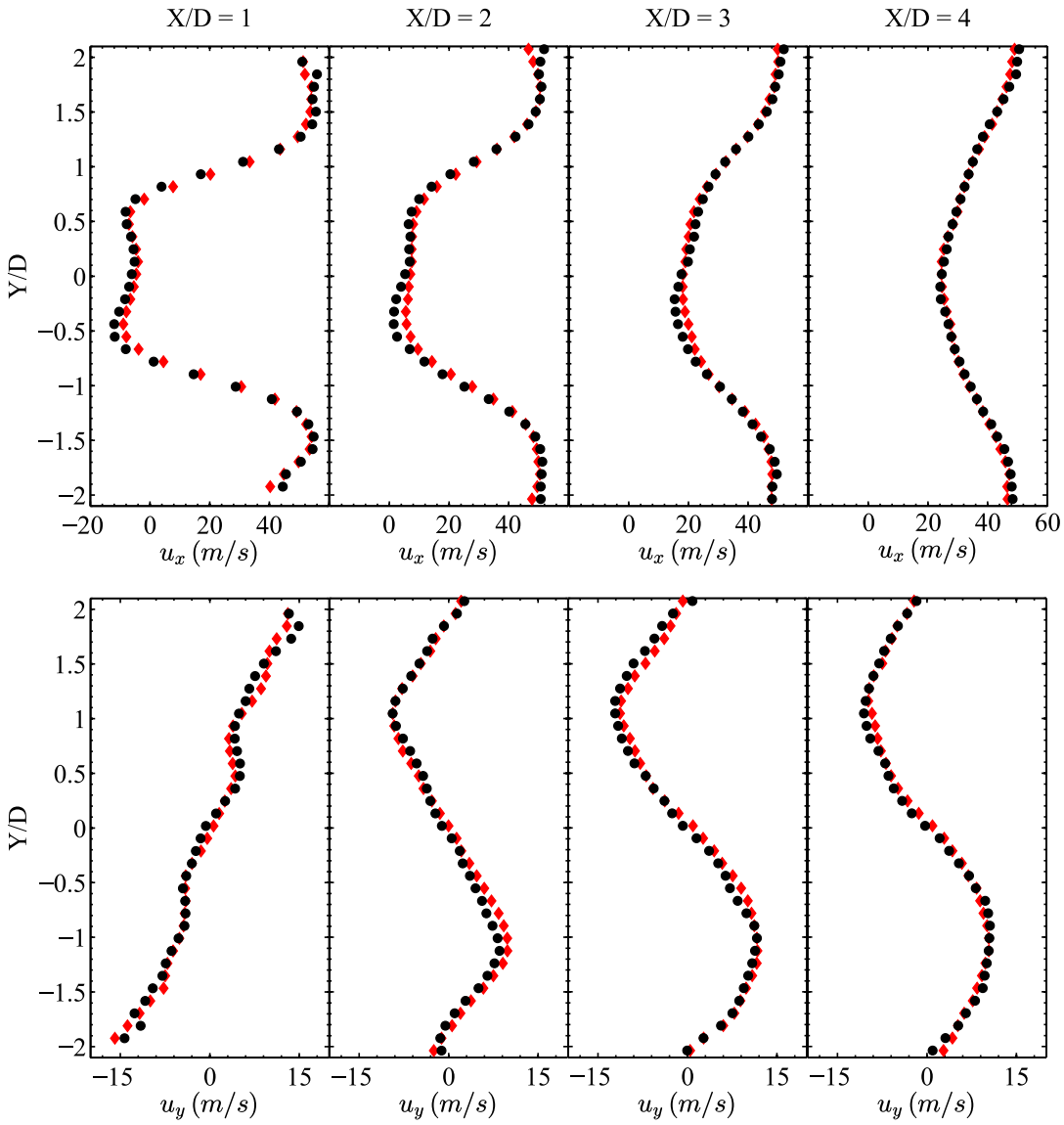

Figure 7.5.. Variation of the time averaged u_x (top row) and u_y (bottom row) at discrete X/D. Case 3 is shown with diamonds (red) and case 4 is shown with circles (black).

The momentum flux ratio influences the jet trajectory and nearfield dynamics. For the time varying crossflow, the instantaneous J is a function of the phase of the crossflow acoustic cycle. Correctly interpreting the jet behavior requires resolving the jet velocity with respect to the phase of the crossflow oscillation. For this, a phase

angle is defined. A linear representation of the acoustic phase of one cycle of the oscillatory crossflow is shown in Figure 7.6. A sinusoidal shape is assumed for this definition. The phase in the crossflow oscillation is determined from the pressure transducer P1 directly upstream of the dump combustor chamber exit nozzle. Over a crossflow cycle, a p' pressure maximum at P1 is defined as 0^o, where p' is determined from bandpass filtering the raw pressure at the $2L$ frequency peak as determined from a PSD. A total of eight locations in the cycle are focused on from 0^o to 315^o in increments of 45^o.

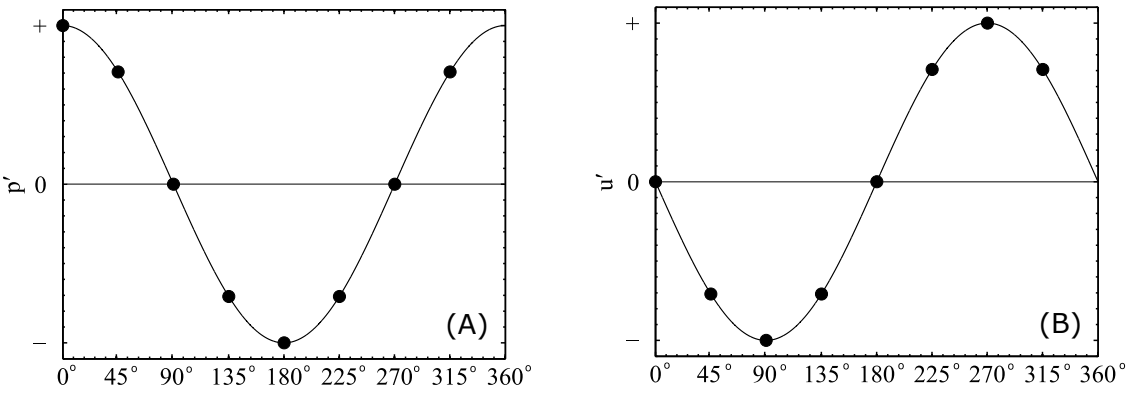

Figure 7.6.. Phase angle definition. (A) p' located at combustion chamber exit pressure anti-node (near P1). (B) Corresponding 1D linear u'_{cf} at jet injection location. Note that this definition is consistent with figure 3.7

As p' at P1 fluctuates, the crossflow velocity chamber modeshape varies accordingly with a $\pi/2$ phase delay assuming a 1D linear acoustic analogy. Over a crossflow acoustic cycle at the jet injection location, the local jet flowfield p' at the $2L$ frequency is negligible (since a 2L p' node) while the crossflow velocity u_{cf} varies about a mean value $\overline{u}_{cf}$ according to $u_{cf} = \overline{u}_{cf} + u'_{cf}$. The unsteady component u'_{cf} at the jet follows the chamber exit nozzle p', but with the $\pi/2$ delay. Following Figure 7.6 and Figure 3.7, $p' = 0$ moving from a compression ($p' > 0$) to rarefaction ($p' < 0$) corresponds with a maximum negative u'_{cf} (and thus a minimum in u_{cf} at the jet), while a $p' = 0$ moving from a rarefaction to compression corresponds with a maximum positive u'_{cf}

(and thus a maximum in u_{cf} at the jet). Figure 7.6 shows u'_{cf} at the jet injection location over this cycle. Note that u_{cf} is always >0 for the unsteady amplitudes under consideration.

Figure 7.7 and Figure 7.8 shows the phase averaged $|\vec{u}|$ and the phase averaged ω_z, respectively, for case 3. For each phase, the calculation is based on two images per cycle to decrease mean biasing with a smaller sample population, resulting in a phase average based on a value $\pm 5^o$ about the designated phase in the upper right hand corner of each image. Also shown is a thick black curve demarcating the jet unburned fluid region as calculated from a time average of the OH-PLIF measurements. This is discussed later. Most apparent from the phase averaged sequence is the difference in velocity for the first half of the cycle (0^o to 135^o) and the back half of the cycle (180^o to 315^o). The strongest velocity field exists at a phase of 270^o, which corresponds to a maximum in u'_{cf} (and thus u_{cf}), and the weakest velocity field exists at 90^o, which corresponds to a minimum in u_{cf}. The strengths and size of the counter rotating recirculating region also follows a pattern seemingly synchronized to the crossflow cycle (see Figure 7.8). Near the minimum in u_{cf}, the counter rotating wake vortex structures show a contraction toward the jet orifice and a weakening of magnitude, while near the u_{cf} maximum these zones extend further downstream and increase in magnitude. The contraction and lengthening of these regions coincides with a shrinking and enlarging low velocity wake region, respectively (see Figure 7.7).

This observed synchronization between the jet velocity and the surrounding local flowfield u_{cf} suggests that the jet fluid mechanics are closely tied with the unsteady crossflow. This is not unexpected, although the mechanisms driving the phase averaged velocity and vorticity phase differences are not yet conclusive. These difference could be attributed to two mechanisms which are in fact not necessarily independent of one another: (1) a varying J driven entirely by the varying crossflow, and (2) the closed flow around the jet of the crossflow varying with the crossflow cycle. First consider the effect of an unsteady crossflow on jet injection at a p' node. The ratio of

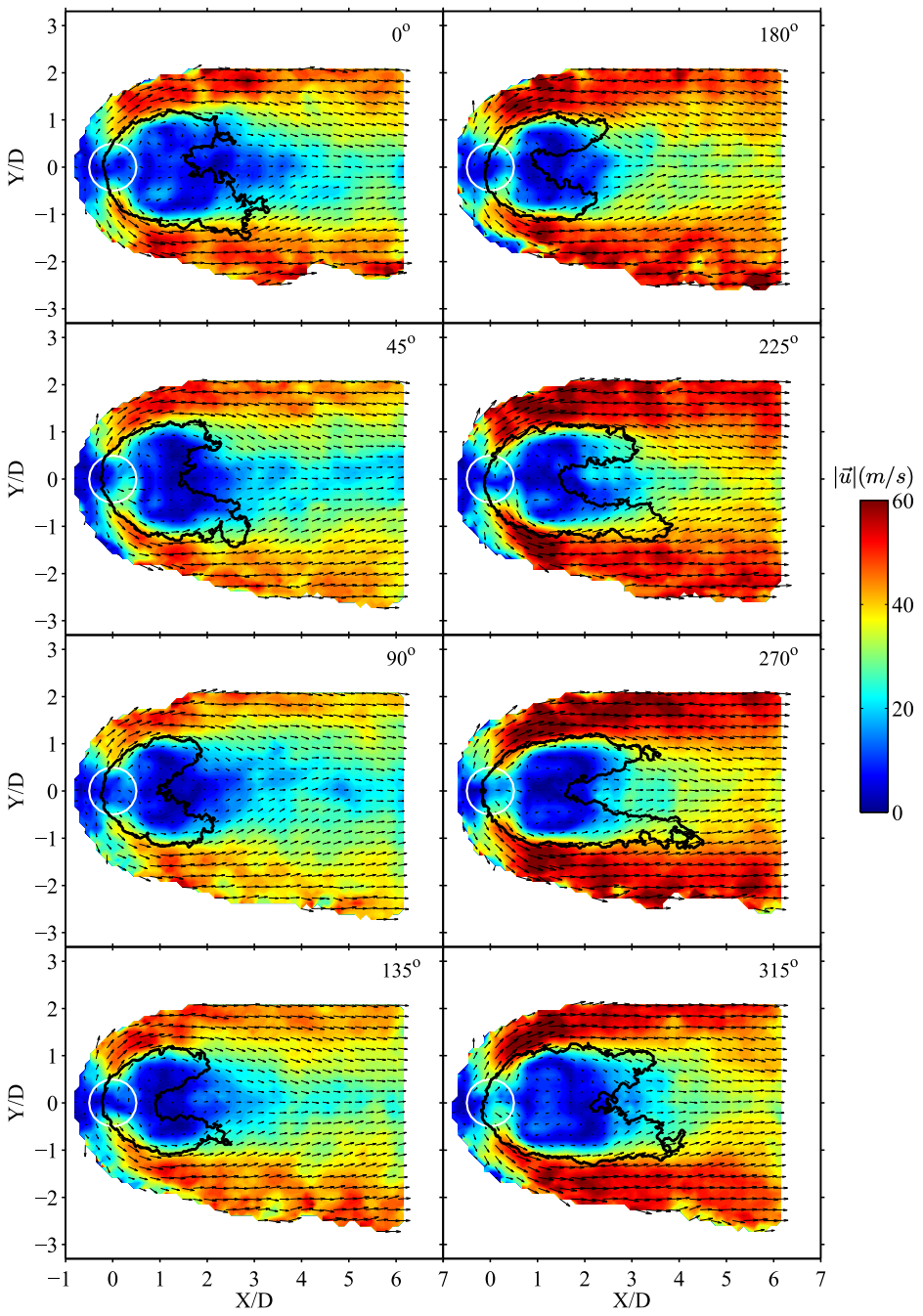

Figure 7.7.. Phase averaged velocity for case 3. Phase corresponds to figure 7.6 definition. The false colored background is the velocity magnitude. The thick black line represents the phase averaged OH-PLIF horseshoe structure.

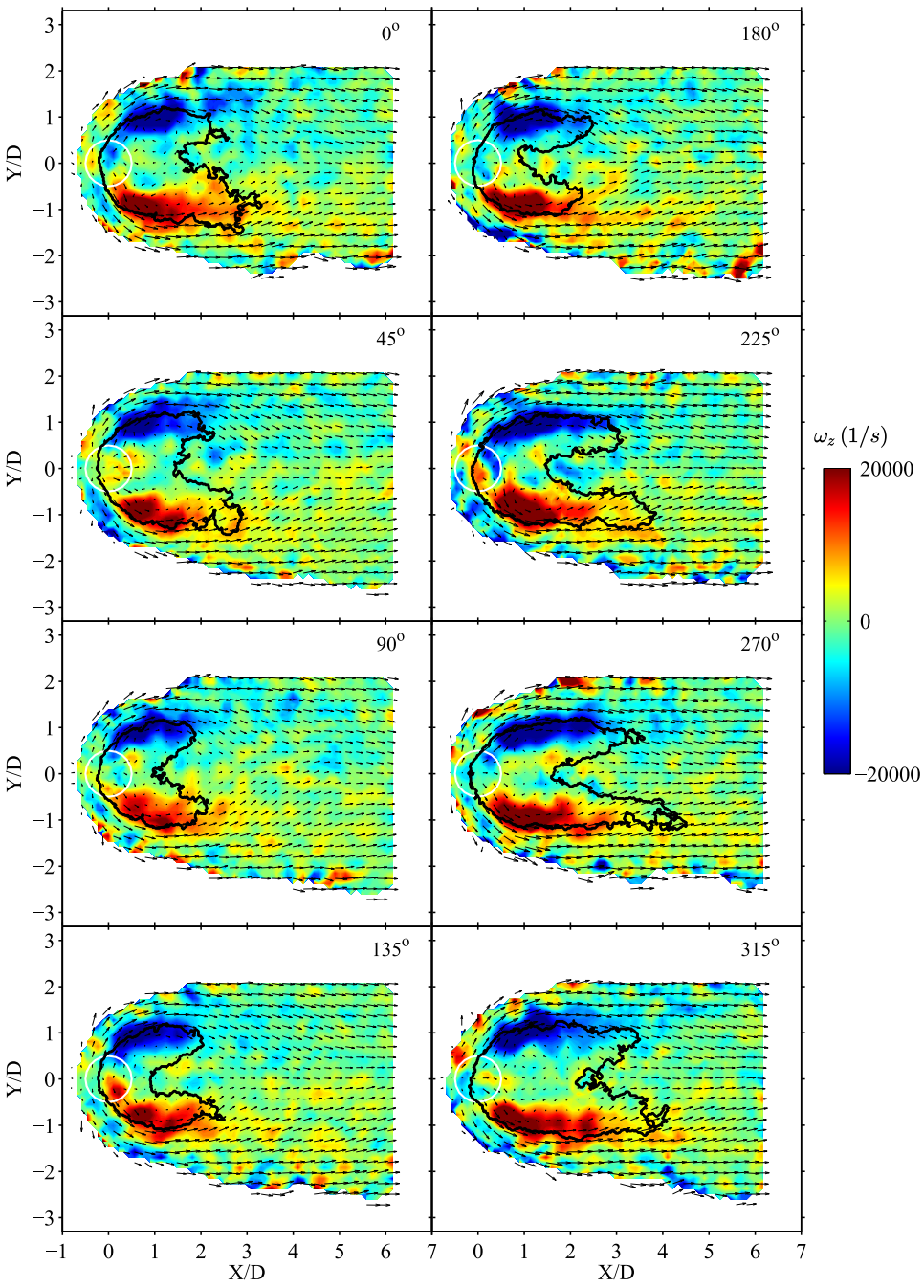

Figure 7.8.. Phase averaged vorticity for case 3. Phase corresponds to figure 7.6 definition. The false colored background is ω_z. The thick black line represents the phase averaged OH-PLIF horseshoe structure.

the instantaneous J at 90^o, defined as J_{max}, to the instantaneous J at 270^o, defined as J_{min} can be reduced to a function of $\overline{u}_{cf}$ and u'_{cf}

$$\frac{J_{max}}{J_{min}} = \frac{\left[\frac{\rho_j u_j^2}{\rho_{cf} u_{cf}^2}\right]_{max}}{\left[\frac{\rho_j u_j^2}{\rho_{cf} u_{cf}^2}\right]_{min}} = \frac{u_{cf,min}^2}{u_{cf,max}^2} = \left(\frac{\overline{u}_{cf} - u'_{cf}}{\overline{u}_{cf} + u'_{cf}}\right)^2 = \left(\frac{1 - \frac{u'_{cf}}{\overline{u}_{cf}}}{1 + \frac{u'_{cf}}{\overline{u}_{cf}}}\right)^2 \tag{7.1}$$

where it is assumed that the change in densities of the crossflow and jet between J_{min} and J_{max} is negligible, the difference in crossflow velocity at the min and max is $\pm u'_{cf}$ about the mean, and the substitution $u_{cf} = \overline{u}_{cf} + u'_{cf}$ has been made. For a fixed $\overline{u}_{cf}$, the instantaneous change in J with a fluctuating u'_{cf} can be quite significant. Consider case 3. Many of the cycles in Figure 7.1 have fluctuating pressure amplitudes near 10-12 kPa. Consider an amplitude of 12 kPa at the mean chamber pressure 945 kPa. This corresponds to a $p'/\overline{p}$=1.3%. The mean crossflow velocity and mach number are small. Linearization of the mass and momentum equations leads to the well known 1D acoustic relations in which the pressure oscillation amplitude and the velocity oscillation amplitude are related by

$$u' = \pm \frac{p'}{\overline{\rho} \overline{a}} \tag{7.2}$$

where $\overline{\rho}$ and $\overline{a}$ are the mean undisturbed gas density and sound speed, respectively, p' is the pressure pertubation amplitude and u' the corresponding velocity perturbation amplitude [64]. Equation 7.2 is a general form which does not account for the phase difference or spatial variation in u' or p'. Such differences are recovered with the appropriate application of boundary conditions. Treating the combustion chamber as a simple 1D pipe of length L with closed ends at the combustor dump plane and the combustor exit nozzle (pressure anti-nodes or velocity nodes), no heat input, isentropic, inviscid, and with negligible mean flow, application of the linearized acoustic equations results in the following well known space and time variation of u' and p' for a closed 1D pipe

$$p'(x,t) = |p'| cos(n\pi x/L) cos(2\pi f t) \tag{7.3}$$

$$u'(x,t) = -j\frac{|p'|}{\overline{\rho a}} sin(n\pi x/L) sin(2\pi f t) \tag{7.4}$$

where $|p'|$ is the maximum cycle pressure at the pressure anti-node location, n =1, 2, 3,... corresponding to the fundamental, first harmonic and second harmonic, respectively, f is the frequency and is equal to $n\overline{a}/(2L)$, t is time and x is space, varying between 0 and L. Note that equation 7.4 is imaginary and consequently $u'(x,t)$ and $p'(x,t)$ differ by a phase of $\pi/2$. Also note that the magnitude of 7.4 is equal to 7.2 as it should. For the crossflow conditions in Table 4.2 for case 3, $\overline{\rho} = 1.58$ kg/m^3 and $\overline{a}$=865 m/s. Since the jet is near the pressure node (velocity antinode), equation 7.2 gives a $u' = 8.8$ m/s, resulting in $\frac{u'_{cf}}{\overline{u}_{cf}} = 19\%$. Such a large u' for a small p' is not surprising. Stated another way, equation 7.2 can be combined with the ideal gas law to show that a relatively small $p'/\overline{p}$ can generate large u'

$$\frac{p'}{\overline{p}} = \frac{\overline{\rho a} u'}{\overline{\rho} R \overline{T}} = \frac{\gamma u'}{\overline{a}} \tag{7.5}$$

where R is the specific gas constant and $\overline{T}$ is the mean gas temperature. Finally, applying equation 7.1 and a similar relation for J_{max}/J_{mean}, where $J_{mean} = 5.6$, the result is J varies from a minimum J_{min}= 3.8 to a maximum J_{max}= 8.8 over the course of a crossflow acoustic cycle. Referring back to the phase averaged velocity, it's observed then that the strengthening on the shear layer with the $|\vec{u}|$ increase at 270^o corresponds with a decrease in J to J_{min}. This lends support of the observed velocity difference to a larger fraction of in plane velocity as the bending force on the jet increases (i.e. less out of plane velocity motion at Z/D=1), and the increase in the crossflow velocity itself which at 270^o would be >50 m/s assuming the linear result above is reasonably accurate. Note that this is a 1st order approximation with significant simplifications of the flowfield being made, e.g. by not considering the local effect of heat release on the crossflow, and any effect of an impedance mismatch directly upstream and downstream of the jet on account of the heat release, temperature and gas composition change.

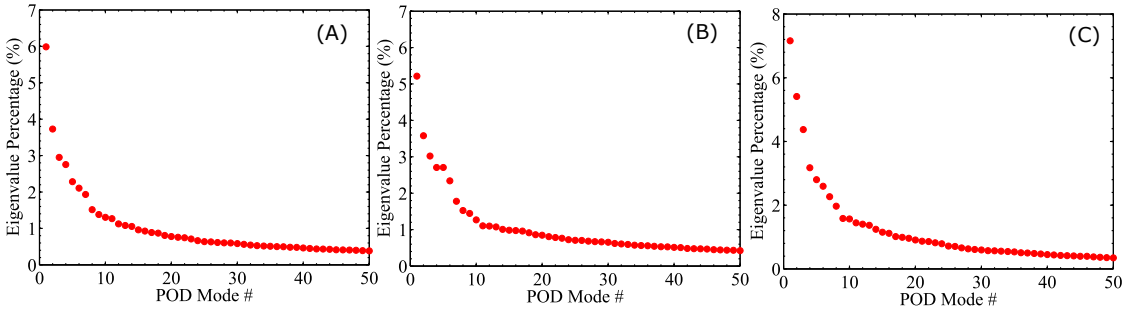

Figure 7.9.. POD eigenvalue percentage for modes 1-50. (A) Case 3. (B) Case 4. (C) Case 1 for comparison. Note that the y-axes for case 1 is different.

A POD analysis is now performed. For the POD analysis, the 5% threshold is not applied as it is understood that the most descriptive features of the flowfield as determined by the most energetic modes will sort these low quantity calculable vector energies accordingly. Figure 7.9 shows the relative value as a percentage of the first 50 POD eigenvalues λ_i for case 3 and case 4. For case 3, the first eight POD modes contain 23% of the total kinetic energy for case 3, with λ_1 and λ_2 containing nearly 10%. Similarly, for case 4 the first eight POD modes contain 22% of the total kinetic energy with λ_1 and λ_2 containing nearly 9%. For comparison, note that case 1 contains 12% for modes 1 and 2 combined and 30% for modes 1-9. This suggests that using the POD energy distribution is not a good measure for comparison alone.

Figure 7.10 and Figure 7.11 shows the normalized POD modes 1-4 and 5-8, respectively, for case 3. Each POD mode vector field is plotted three times overlaid on the false colored background for u_x (left column), u_y (middle column), and ω_z (right column). Unlike case 1 and case 2, POD modes 1-3 for case 3 do not show large clear in-plane vortical structures. POD mode 1 containing the largest percentage of energy is predominantly a streamwise X/D mode with a large portion of the mode concentrated as a u_x fluctuation in the jet shear layers ($Y/D = \pm 1.5$) and a smaller portion concentrated in the jet wake ($-1 < Y/D < 1$ and $-0.5 < X/D < 3$). Multiplying mode 1 by a negative coefficient changes the direction of both fluctuations.

POD modes 2 and 3 are concentrated near the jet shear layer regions mostly outside of the jet wake, but start much closer to the jet at the lateral edges of the projected jet orifice. Multiplying mode 2 by a negative coefficient bears resemblance to a mirrored image of mode 3 about $Y/D = 0$. In fact, a POD reconstruction separately using only mode 2 or mode 3 shows that for certain time instances the mode shapes are symmetric about $Y/D = 0$. At other time instances, these reconstructed mode shapes display an asymmetry about $Y/D = 0$ similar to each respective normalized spatial mode in Figure 7.10).

POD modes 4-8 differ from POD modes 1-3 in that the POD velocity fields are no longer oriented predominantly in the X/D streamwise direction or show a high degree of contiguity. POD modes 4-8 show clear in-plane vortical structures. These can be identified in the POD u_y contours. For example, POD mode 5 shows 3 alternating bands of positive and negative velocity u_y: a negative band centered at $X/D \approx 1.5$, a positive band centered at $X/D \approx 3$, and a negative band centered at $X/D \approx 5.25$. The vortices are centered at the interfaces between two bands, for mode 5 $(X/D, Y/D) = (2,0)$ and $(X/D, Y/D) = (4.25,0.5)$. These vortices are also recognizable in ω_z. These vortex structures are not static. The POD requires multiple modes to accurately track convecting structures. Additionally, POD mode 8 shows a vortex structure located off of the $Y/D = 0$ centerline and located at $(X/D, Y/D) = (2.75,1)$. The fact that the POD modes captures vortex structures either on or off of the $Y/D = 0$ centerline and at different X/D locations suggests convecting vortex structures and an irregularity in their generation relative to a specific spatial location due to a highly turbulent and unsteady flow.

The largest fluctuation locations for the first three modes correspond principally to the jet shear layer, and the remaining POD modes appear highly active around the wake region. Spectral analysis of the POD temporal coefficients reveals that the first few POD modes contain dominant frequency content coinciding with the unsteady crossflow. Figure 7.12 shows the spectral content of the first eight POD modes. Well defined frequencies are highlighted. POD modes 1-3 show dominant 195

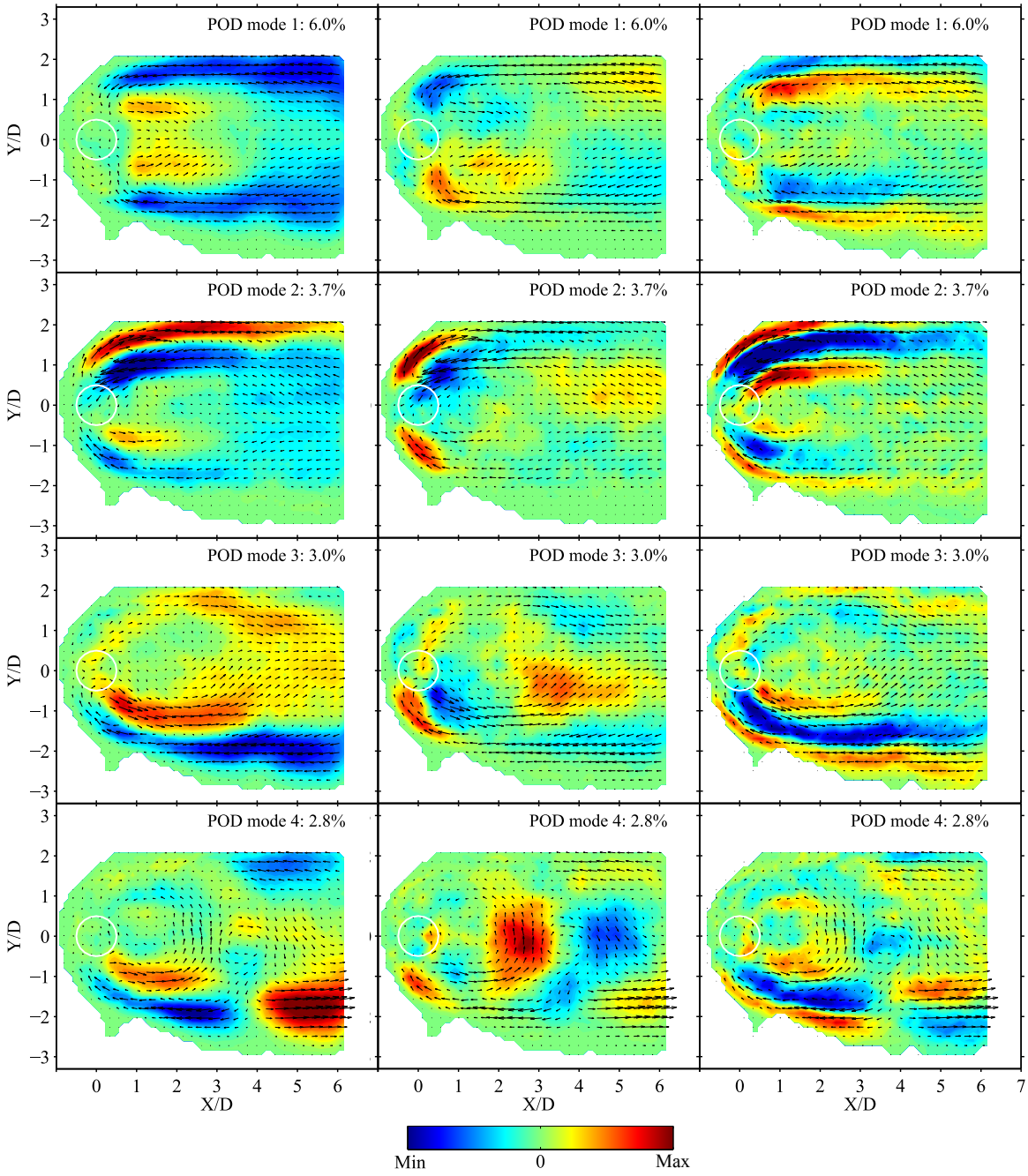

Figure 7.10.. Normalized spatial POD modes 1-4 for case 3 showing u_x (left), u_y (middle) and ω_z (right).

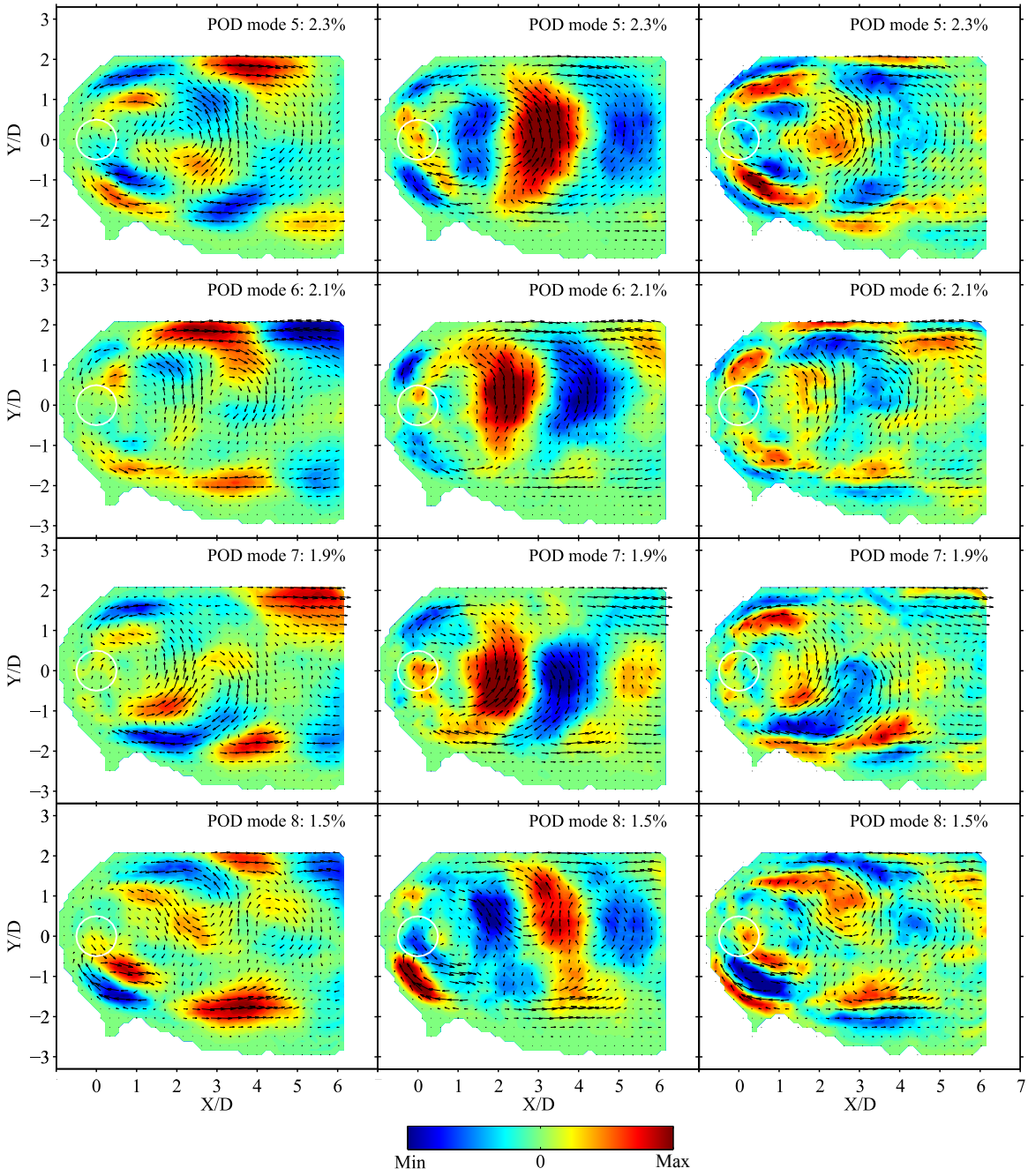

Figure 7.11.. Normalized spatial POD modes 5-8 for case 3 showing u_x (left), u_y (middle) and ω_z (right).

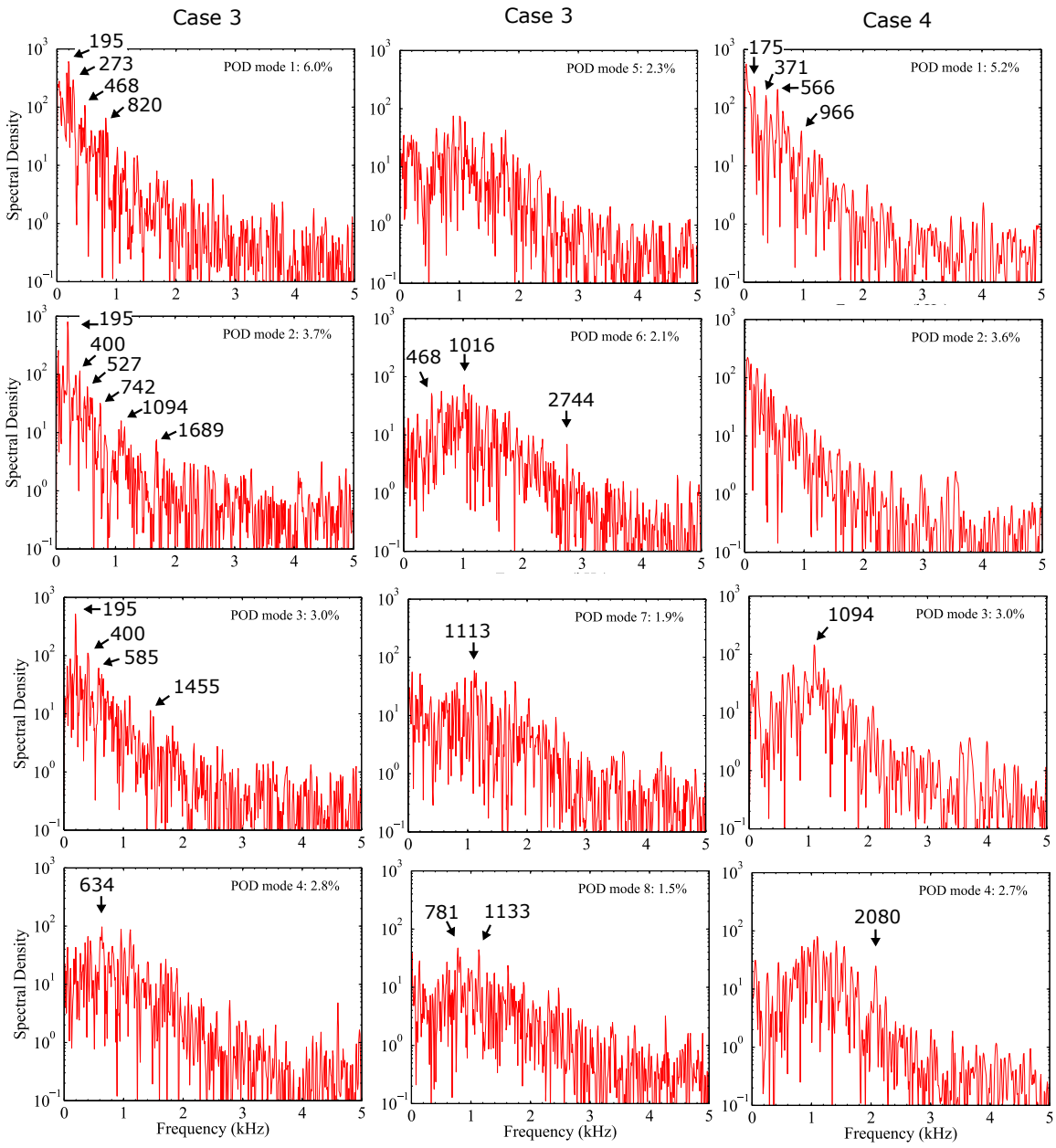

Figure 7.12.. Spectral content of POD temporal coefficients for case 3 POD modes 1-8 (left and center column) and case 4 POD modes 1-4 (right column).

Hz peaks corresponding with the crossflow 2L frequency. The 195 Hz frequency is spread out amongst the first three modes suggesting the jet response to this frequency

is not static. POD mode 1 being the most energetic contains well defined peaks with shorter time scales than 195 Hz. The 820 Hz peak coincides with a minor peak in the crossflow at P1 and P5, and in the injector P10. The 820 Hz peak is likely a jet velocity response to low level chamber acoustics. The 273 Hz peak is not present in the crossflow or the injector pressure spectra. However, note that the addition of 273 Hz and 195 Hz results in exactly 468 Hz suggesting that the 273 Hz peak is a beat frequency response between 195 Hz and 468 Hz. The closeness of 468 Hz to the 445 Hz present in the crossflow pressure spectra and to a limited extent the injector spectra obscures the origin of this frequency. The 400 Hz, 585 Hz, and 742 Hz frequencies are close enough to pressure peaks in the crossflow that these are also likely the jet responding minimally to the lower amplitude crossflow acoustics.

The remaining POD modes 4-8 show less coherent, wider and weaker peaks, but with a distinct wide spectral band centered around $\approx$ 1 kHz. In terms of a Strouhal number, a 1 kHz frequency corresponds to $St_{cf} = fD/\overline{u}_{cf} = 0.13$. Reported St_{cf} for the JICF wake region typically lie between 0.12-0.15 and resemble alternating counter rotating vortex structures generated near the jet exit and subsequently convecting downstream [13, 19]. Convection in a POD is split across modes [60] and thus the vortex structures of POD modes 4-8 for case 3 in Figure 7.10 are indeed largely describing canonical JICF vortex structures concentrated near to the jet wake.

Consider now case 4. Figure 7.13 shows the normalized POD modes 1-4 for case 4. Each POD mode vector field is plotted three times overlaid on the false colored background for u_x (left column), u_y (middle column), and ω_z (right column). The POD mode 1 contains a predominantly streamwise X/D oriented velocity field mostly in the jet shear layer and partly in the jet wake. This is similar to POD mode 1 for case 3. Unlike case 3 POD mode 1, though, there is no dominant crossflow 195 Hz frequency in the crossflow pressure. Figure 7.12 shows the temporal coefficient spectra for case 4 POD modes 1-4. POD mode 1 contains several $<$ 1 kHz frequencies. Comparing with the crossflow pressure spectra, all are within 30 Hz of a low level chamber acoustic. Case 4 POD mode 2 contains both active jet shear layer fluctu-

ations and a large clockwise rotating wake structure directly behind the jet orifice centered at $(X/D, Y/D) = (1.5,0)$. POD mode 2 resembles a combination of case 3 mode 2 (or mode 3) and mode 4. Case 4 POD modes 3 and 4 both contain predominantly wake related vortex structures, both resembling the structures in POD modes 4-8 for case 3. In fact, case 4 POD modes 3 and 4 appear to be describing the same vortex shedding and convection process. Multiplying mode 3 by a negative coefficient produces a counter clockwise vortex centered at $(X/D, Y/D) = (4,0)$. Mode 4 shows a counter clockwise vortex centered at $(X/D, Y/D) = (3.25,0)$ followed by a clockwise distorted vortex centered at $(X/D, Y/D) = (1.5,0)$. The POD modes 5-8 describe subtle features of the convection and in the irregularity of the turbulent process. The spectra for case 4 POD modes 3 and 4 show distinct broad peaks near 1 kHz. This supports the observation that the modes appear connected to the jet wake vortex processes. Note that POD mode 3 contains a dominant and sharp peak at 1094 Hz. Case 3 modes 5-8 only contain broad peaks around 1 kHz, e.g. 1016 Hz in mode 6 and 1113 in mode 7, at a relatively low energy.

A DMD analysis was also performed for the case 3 and case 4 velocity. For case 3, the DMD spectral results describes a dominant 200 Hz jet velocity response that is primarily in the streamwise u_x direction and to a large degree concentrated outside of the jet wake region. This was observed in the POD. In fact, the DMD 200 Hz mode resembles a combination of POD modes 1-3, but with increased small scale vector irregularity. This is expected since the DMD mode is sorting all of the 200 Hz into one mode, whereas the POD sorts this across modes with the smaller scale features placed in the higher number and less energetic POD modes. The case 3 DMD u_y identifies a 1001 Hz mode. A similar frequency is observed in the POD, but these peaks are broad and spread out among many POD modes. The DMD 1001 Hz mode describes wake vortices in the jet wake quite similar to a combination of POD modes 4-8. The 1001 Hz mode for case 4, however, contains relatively low energy. This is consistent with the POD sorting the broad peaks into POD modes 4-8. For case 3, a sharp 1256 Hz is identified. This frequency was not specifically found in

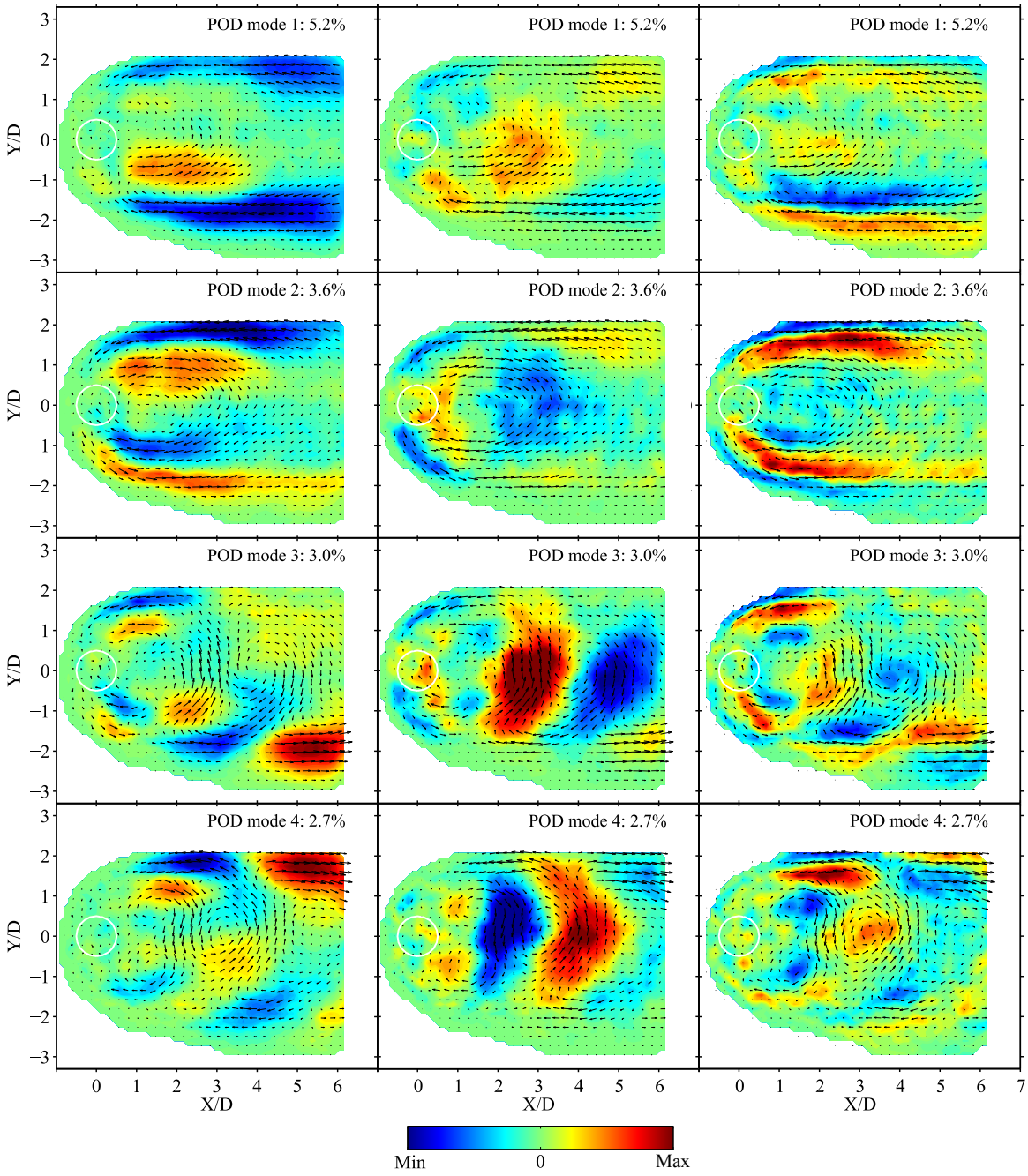

Figure 7.13.. Normalized spatial POD modes 5-8 for case 4 showing u_x (left), u_y (middle) and ω_z (right).

the POD. The DMD describes this frequency as traveling wake vortices generated directly behind the jet and convecting downstream. The distinct 562 Hz for case 4 u_x describes strong shear layer fluctuations predominantly in the streamwise direction that begin near X/D=1 and travel downstream on both shear layers. In this regard, the DMD 562 Hz resembles a combination of case 4 POD mode 1-4 in the shear layer region alone.

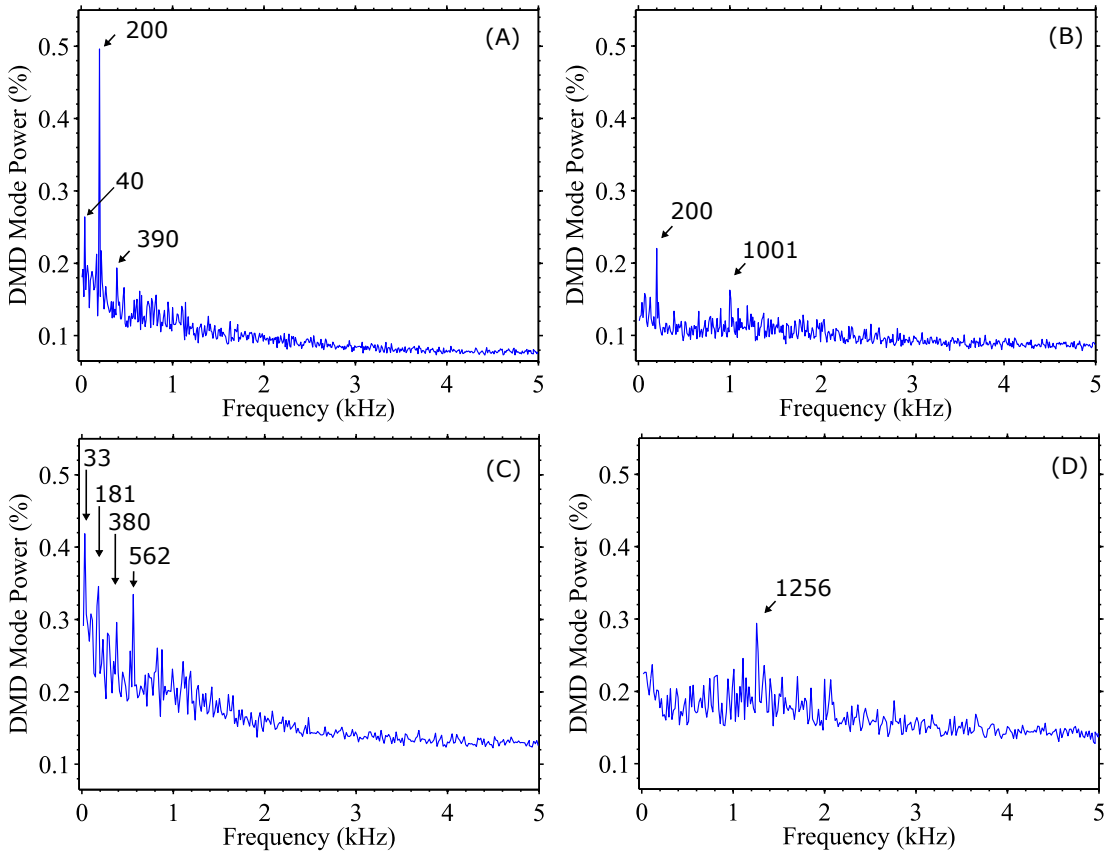

Figure 7.14.. DMD spectra performed on (A) case 3 u_x, (B) case 3 u_y, (C) case 4 u_x (D) case 4 u_y

Following the description of the jet velocity field, the simultaneously recorded OH-PLIF measurements are now presented. A sequence of corrected OH-PLIF measurements from case 3 is shown in Figure 7.15. These have been corrected for distortion, scaled to engineering units, brightfield and background corrected, and a sheet in-

tensity normalization applied using the Fourier transform correction procedure. The crossflow is from left to right. The dark region (low OH signal) downstream of the jet orifice represents mostly unburned fresh reactants. The highest OH-PLIF signals are attributed to the super equilibrium concentrations of OH formed at the reaction front and the larger gradients in the OH signal can help to qualitatively identify the flame front locations. Three sources of the lower intensity post flame equilibrium OH exist: the surrounding vitiated crossflow from the dump combustor flame, and the in-plane and out-of-plane jet flame front products. The region containing the mostly unburned jet fluid consistently displays the lowest intensity in the FOV.

The instantaneous OH-PLIF measurements show a highly corrugated reaction front with a range of contoured structure sizes. The structures tend to grow in size further from the jet exit, with the jet flame width (in Y/D) increasing in the X/D direction as the jet volumetrically expands traveling downstream. Several islands of OH exist. The origin of these is not clear, whether they are due to isolated auto-ignition pockets or a flame front spanning beyond the Z/D interrogation plane. Also note the leading edge of the jet flame. For many single shot measurements, the leading edge reaction front signal is difficult to identify, while in others there is a strong gradient. In general, the OH signal and gradient is seen to be stronger on the jet lateral edges. Also note the vitiated crossflow OH signal, e.g. $(X/D, Y/D) = (0, 2)$. The true vitiated crossflow OH is typically quite strong, in particular for $+Y/D$ where the sheet enters the test article.

The Figure 7.15 images have been corrected to remove a significant portion of the vitiated background OH. A complete background removal is not performed here to highlight the differences with the jet edges, jet flame products, and in particular certain low OH gradient regions relative to the background. Also note the central high intensity OH region centered on Y/D=0, e.g. with a leading edge at $X/D = 2.5$ at t = 0.2 ms and t = 0.3 ms. This is a characteristic feature at the plane Z/D=1 that gives the instantaneous and time average OH-PLIF a horseshoe (or kidney) shape. The leading edge and Y/D width of the central OH wake vary considerably, but in

general there is a periodicity about this leading edge fluctuating between $X/D = 0.5$ and beyond the FOV ($X/D > 7$).

At this plane, the jet column is likely still very much intact. This is supported by the observation that in general the leading edge reaction front is very near to $X/D = 0$. As the crossflow fluid closes in around the backside of the jet, the crossflow fluid is then driven upward in the $+Z/D$ direction into the jet providing fresh hot crossflow [15]. Simultaneously, the jet cross section is deforming into a kidney shaped structure with the jet trailing edge moving closer to the leading edge of the jet [16]. This combination creates what appears as the central OH wake region. As the jet flaps or penetration changes, the fixed laser sheet interrogation plane bisects the jet at different locations in the spatial-temporal evolution of the jet. This gives rise to a seemingly periodic central OH region.

Despite the high 10 kHz repetition rate, the single shot measurements are temporally uncorrelated at the smaller flame front length scales. Consider the mean jet exit velocity of 70 m/s. At 10 kHz, a fluid parcel will move 1.2 jet diameters from one frame to the next. Scaling with a 50 m/s mean crossflow velocity decreases this to $0.82D_j$. These distances are large relative to the size and apparent evolution of the small flame front length scales. This is further complicated by out-of-plane motions carrying features into and out of the plane from one frame to the next. Therefore, it's not expected to resolve local flame extinction or flowfield-flame interactions driving behavior such as flame stretching [58]. The resolution in velocity is not available anyways to study the flow-flame at these scales. Qualitatively, then, structure sizes on the order of the jet diameter and larger are of most interest here for reasonably accurate temporal correlation.

Figure 7.15 also shows for comparison the shot to shot flame edge detection results. The curve captures the largest OH gradient edges as well as the lower OH gradients contours (defined with a threshold). The curve also captures the islands of OH. Note that the lower OH gradients may in fact result from equilibrium OH (resulting from out-of-plane motions or recirculated in-plane flame product) inter-

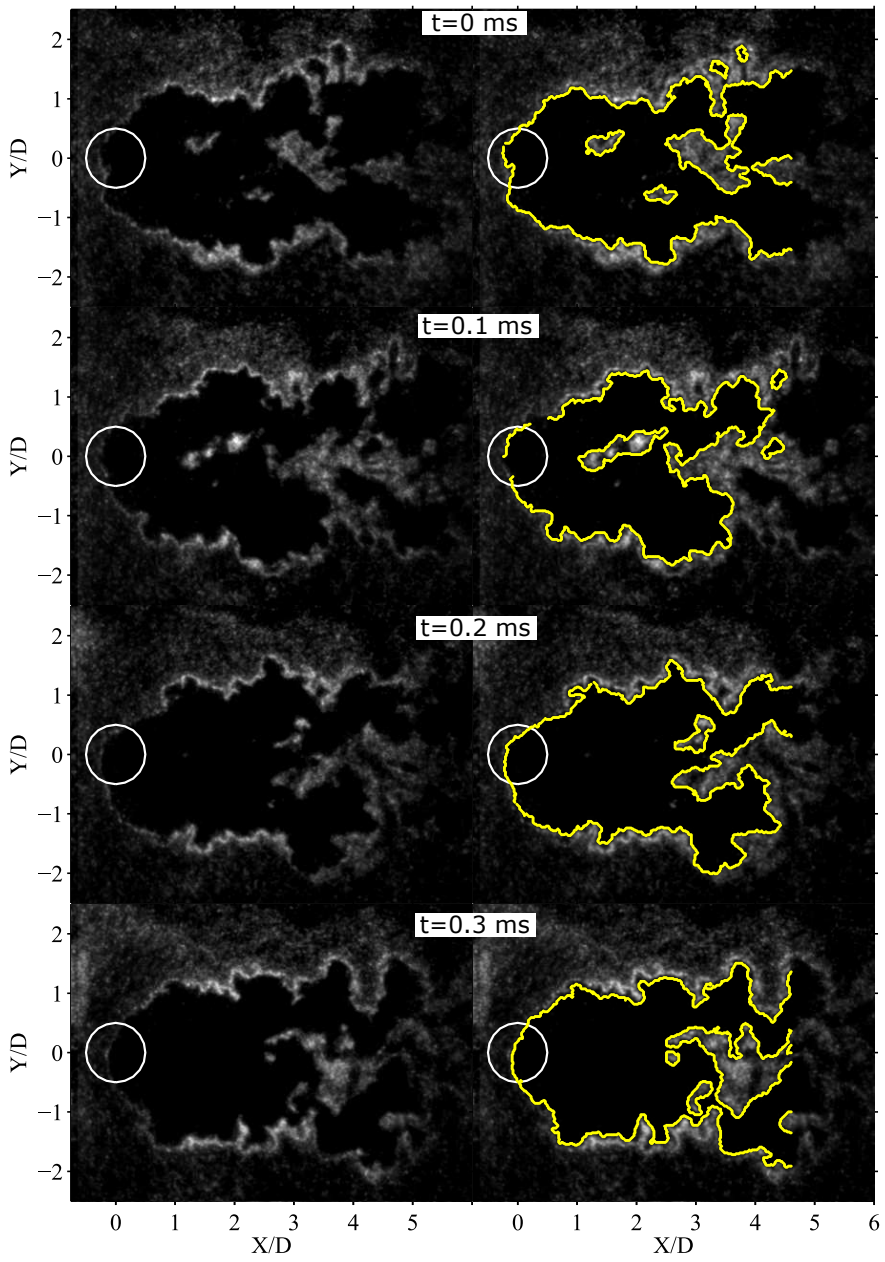

Figure 7.15.. A sequence of corrected OH-PLIF measurements showing corresponding reaction front curve. Measurements taken at 10 kHz. The right column shows the corresponding flame front result.

acting with the mostly unburned jet fluid. The objective of the current study is to

generate a qualitative boundary of the possible reaction front to correlate with the simultaneously measured velocity and the time varying crossflow.

Figure 7.16 shows the corrected time-averaged OH-PLIF for case 3. Directly behind the jet orifice, the low intensity region represents the mean location of the mostly unburned jet fluid. This region resembles a semi-symmetric horseshoe (kidney) structure about $Y/D = 0$. The structure windward and lateral edges show increased OH signal (relative to the mean vitiated crossflow) and in general coincide with the large OH gradients in the instantaneous jet lateral edge reaction fronts. The leading edge reaction front is located upstream of X/D=0. Since the jet is highly dynamic (hydrodynamically and due to the unsteady crossflow) the diffuse intensity region past $X/D \approx 3$ is largely due to a mix of reaction front, hot products, and unburned jet fluid.

A curve delineating the darker OH central region in the time-average resembling the horseshoe structure is also shown in Figure 7.16. The edge was calculated by relaxing the thresholds in the flame front tracking algorithm to demarcate the horseshoe structure. The asymmetry about Y/D=0 is likely due to the algorithm that corrects and then extracts the curve. The curve permits a qualitative comparison with the mean velocity field and is shown together with the velocity in Figure 7.4. The horseshoe feature coincides with the low velocity wake region, in fact appearing to encompass most of the wake and the counter rotating vortex structures immediately downstream of the orifice. The upstream and lateral portions of the horseshoe structure delineates the edge of the most intense OH signal, which is presumably a region of significant jet-crossflow interactions. Figure 7.17 compares the time averaged OH-PLIF for case 3 and case 4. The time-average is qualitatively indistinguishable. This is consistent with the similarity of the time average velocity fields for case 3 and case 4 in Figure 7.4.

Presumably as the jet penetration dynamics lock in to the crossflow cycle dynamics, the fixed OH-PLIF interrogation plane will bisect the jet at different cross sectional slices throughout the temporal-spatial evolution of the jet. The calculated

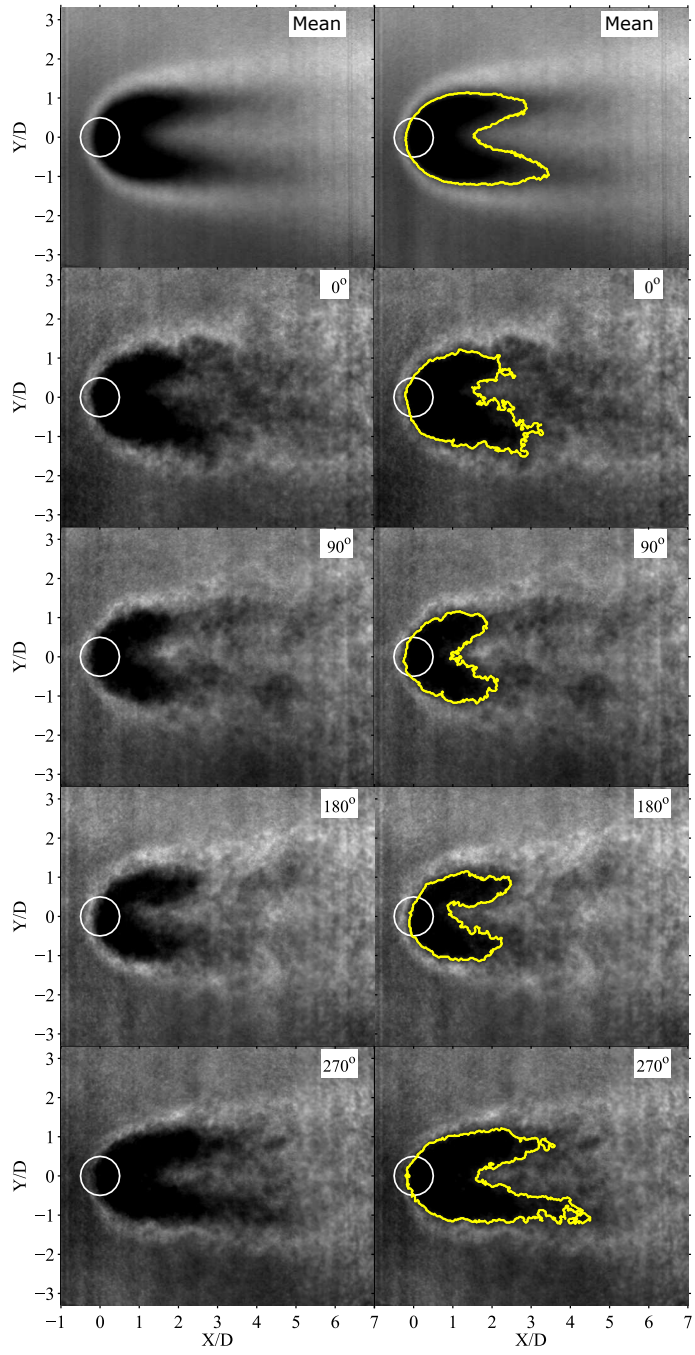

Figure 7.16.. Case 4 OH-PLIF time averaged (top row) and phase averaged at four points in the cycle. These images corresponds identically to the time and phase average of velocity previously.

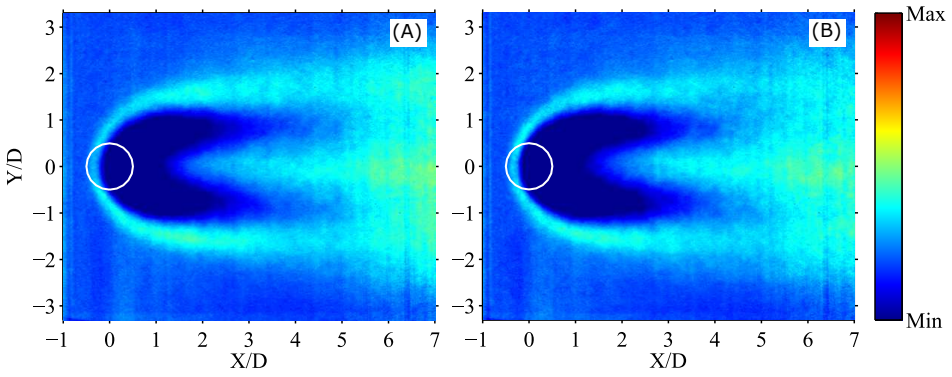

Figure 7.17.. Time averaged OH-PLIF for (A) case 3 and (B) case 4.

flame front length should then capture this. Figure 7.18 shows an FFT performed on the flame front length for case 3. The length scale in millimeters was calculated by multiplying the FFT coefficient magnitudes by the spatial resolution. The result shows multiple well defined frequencies. The frequency corresponding to the crossflow $2L$ is present, but significantly smaller than other frequencies. A dominant 405 Hz is present. Recall that a 400 Hz frequency is observed in POD modes 2 and 3, and a minor 390 Hz acoustic mode is present in the crossflow. A well-defined 1990 Hz frequency is also present, which is not an integer multiple of any of the other flame front frequencies. A closer look at the velocity POD results reveals a frequency near 1990 Hz. This is shown in Figure 7.19 along with the corresponding POD mode. Note the alternating pattern of vorticity most pronounced for $-Y/D$ that begins at the jet orifice and stretches out with increasing X/D (arrows highlight these alternating structures). From the close spatial proximity, scaling the spatial wavelength of $\approx$ 2D in the downstream portions of the jet with u_j=70 m/s would put the frequency above 6 kHz and if scaled with the u_{cf}=46 m/s would put them near 4 kHz.

The PLIF measurements are then phase averaged according to the same time instances as the phase averaged PIV results for case 3. Figure 7.16 highlights four of these phases. The phase is defined following Figure 7.6. A 4x4 kernel denoising Wiener filter was applied to $X/D > 5$ to mitigate artificially introduced noise from

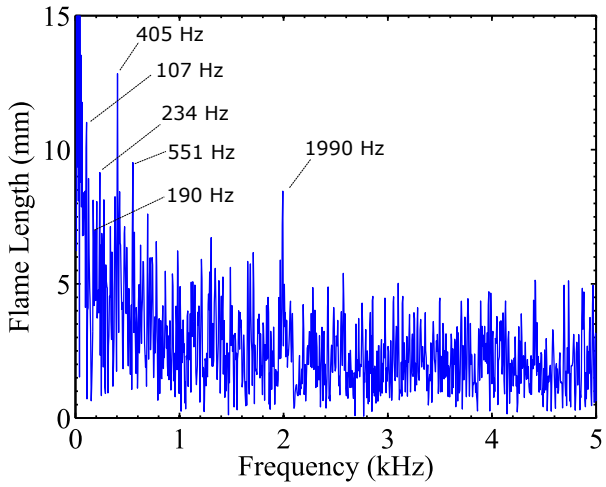

Figure 7.18.. FFT of the calculated flame length for case 3.

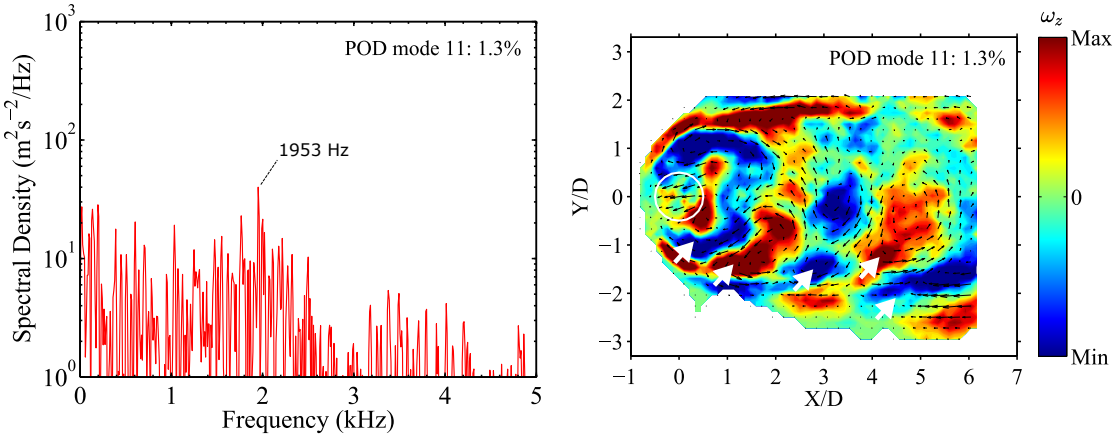

Figure 7.19.. Case 3 POD mode 11 spectral content and normalized spatial mode.

the sheet intensity correction procedure (per Figure 4.2) in the $X/D > 5$ lower intensity LIF region. The most prominent feature at all phases is the horseshoe structure representing the mostly unburned jet fluid region. At a phase of 90^o, the structure is contracted toward the jet orifice and at 270^o a lengthening occurs of the horseshoe arms. A curve is drawn to qualitatively represent the interface between the OH intensity jet fluid horseshoe structure and the higher OH intensity flame front

locations (similar to the OH-PLIF mean curve procedure). Recall that in the average, the portion of the curve intersecting with significant wake region contains a diffuse signal intensity due to averaging unburned jet fluid, flame front, and OH product. Therefore, the thresholds on the flame front tracking algorithm are relaxed to capture the closed kidney shaped curve.

The phase averaged PLIF calculated horseshoe structures are shown on the phase averaged velocity results in Figure 7.7 and Figure 7.8. First note that trend in the OH-PLIF is similar to the jet velocity: the horseshoe curve contracts and lengthens in X/D with a decreasing and increasing $|\vec{u}|$, respectively. The extension and contraction also follow the trend in the strong vorticity region directly behind the jet orifice. Moreover, the counter-rotating vorticity features are nearly encompassed by the curve. With the appearance of the jet flame wake growth synchronized to the crossflow cycle, it's interesting to find that the leading edge of the horseshoe structure (and the higher OH signal immediately preceding this) shows little movement in X/D. This is also observed in the instantaneous PLIF. This gives the appearance of a strong jet core at $Z/D = 1$, while the portions of the jet further along the trajectory and within the wake region are more susceptible to a fluctuating velocity crossflow.

A DMD analysis of the OH-PLIF measurements is presented. DMD is used to qualitatively compare the OH-PLIF dynamics with the simultaneously measured jet velocity and crossflow pressure. Figure 7.20 shows the DMD mode power as a function of frequency for case 3 and case 4.

The DMD was performed on a reduced region of the FOV, specifically $-2 < Y/D < 2$ and $-0.5 < X/D < 5.5$. This was done to minimize biasing of the DMD by the crossflow OH signal following the experimental observation of a pulsating crossflow LIF at the dominant crossflow acoustics. The dump combustor flame dynamics coupled with the chamber 2L ostensibly generate a time-varying OH crossflow concentration. This leads to misinterpretation of the transverse jet flame dynamics from the OH-PLIF data by biasing a jet flame 200 Hz response.

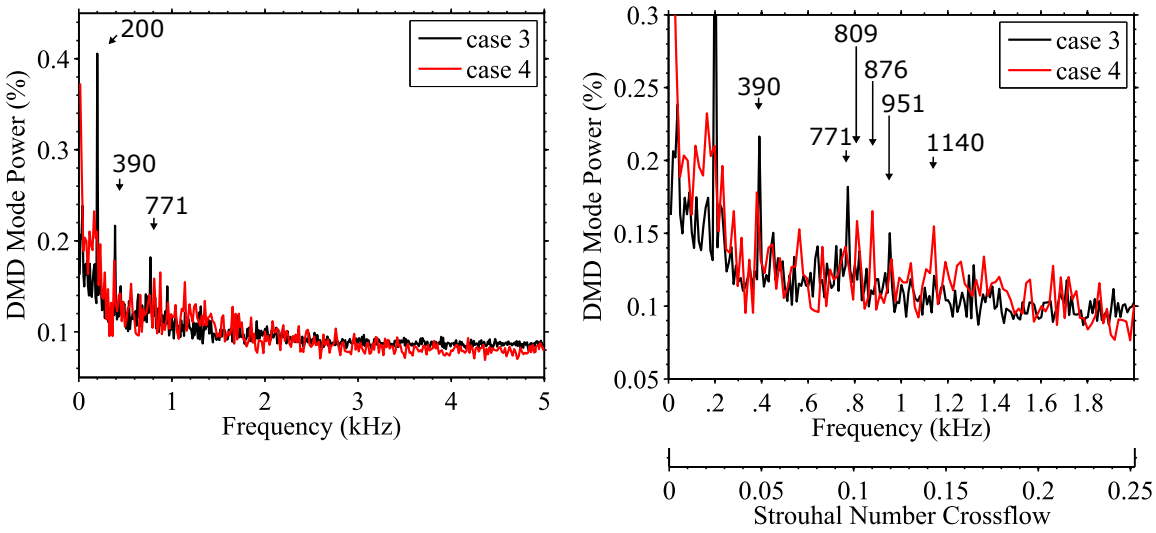

Figure 7.20.. DMD spectra from case 3 and case 4 OH-PLIF. The figure on the right is a zoomed in view of the left figure. The left figure is also plotted against the Strouahl number based on the mean crossflow velocity.

First note the discrepancy between the frequencies from the flame length FFT (Figure 7.18) and the DMD of the case 3 OH-PLIF. The flame length 234 Hz and 405 Hz are close to the 200 Hz and 390 Hz DMD spectra, but relative magnitudes are reversed. The shift in flame length frequencies may be due to a poor algorithm extraction of the flame length, which introduces significant noise into the true two-dimensional flame length.

For case 3, the DMD 200 Hz corresponds to the dominant crossflow $2L$, which is also the dominant frequency in the velocity POD results. Figure 7.21 shows the DMD 200 Hz modal evolution at six different time instances. Each image corresponds to a time in one cycle of the crossflow 2L cycle in Figure 7.24. The DMD modal evolution at 200 Hz describes a pulsating intensity in the jet shear layer and wake. When the crossflow velocity at the jet is near its minimum at time 2, the intensity fluctuation is high in the jet wake, and the leading edge flame front is furthest upstream. When the crossflow velocity is a maximum near time 4 and time 5, the only area with a locally high intensity fluctuation is the leading edge flame front which has moved down-

stream by about 0.25D. This DMD mode describes what was already observed in the phase average results, namely a contracting and lengthening of the flame front with minor leading edge flame front movements as the jet bending ostensibly fluctuates throughout the crossflow cycle.

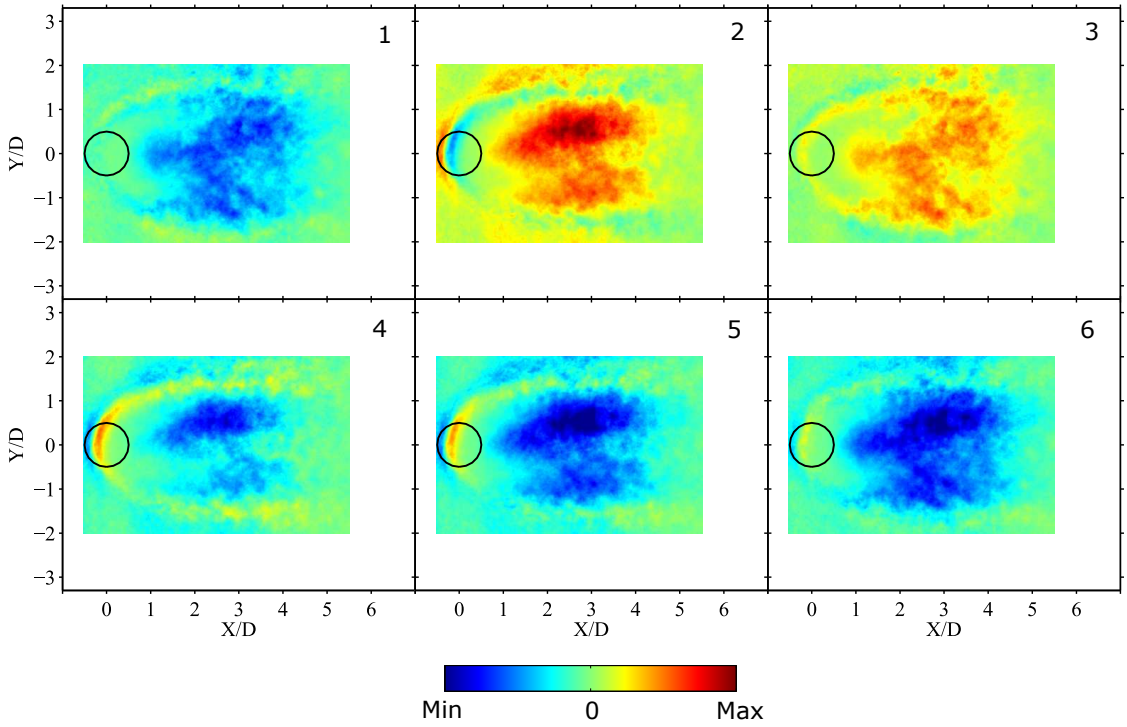

Figure 7.21.. One cycle of the DMD 200 Hz mode for case 3. The images are false colored. The number in the top right of each image corresponds to a location in the crossflow pressure cycle in Figure 7.24.

The case 3 DMD 390 Hz and 771 Hz are lower amplitude acoustics in the crossflow pressure and are also observed in the velocity spectra. For case 4, there is not a dominant OH-PLIF DMD frequency. Instead, there are a number of low amplitude (relative to case 3) responses. Many of these responses are near to low amplitude crossflow acoustic frequencies, e.g. near 200 Hz and 390 Hz.

Consider these frequencies in terms of a Strouhal number. Using the mean crosflow velocity of 46 m/s, the frequencies up to 2 kHz are shown as a Strouhal number St_{cf} in Figure 7.20. For case 4, there are a number of frequency peaks for $0.1 < St_{cf} <$

0.15. Note that in the crossflow pressure spectra, there is nothing to indicate there should be an abundance of OH-PLIF response peaks in this range as compared to any other range. The crossflow pressure spectra contains a multitude of low amplitude frequencies. Consider the 876 Hz frequency in Figure 7.20. The closest crossflow pressure frequency is 52 Hz away. The 876 Hz frequency in terms of a Strouhal number is $St_{cf} = (876Hz)D_j/(46m/s) = 0.11$, which falls within reported JICF wake dynamics.

The DMD 876 Hz modal evolution for one cycle is shown in Figure 7.22. The time instances in Figure 7.22 do not correspond to the time in Figure 7.24. At t = 0 ms, a region of high intensity along the jet shear layer is initiated near $(X/D, Y/D) = (1.5, 1.5)$. As time progresses, this high intensity fluctuation travels along the upper shear layer, moving in toward the centerline Y/D=0, and eventually dissipating.

Figure 7.23 shows the growth of a flame front inflection point along the upper shear layer for case 4. While these inflection points are also observed in case 3, analysis suggests that the DMD 876 Hz modal evolution describes a reaction front inflection point initiation, growth and and convection. This suggests that the inflection point behavior becomes tied into frequency bands that corresponds to, coincidentally, Strouhal numbers correlated with wake dynamics.

A cycle analysis is now performed focusing on the jet behavior from the instantaneous measurements over a crossflow acoustic cycle. Figure 7.24 shows the two cycles that will be examined. The case 3 cycle shows a clean period of the crossflow $2L$ with an amplitude of 13 kPa and corresponds to the cycle starting at approximately 10 ms in Figure 7.1. The low amplitude case does not contain a coherent resonant crossflow acoustic. To compare case 4 with case 3, a similar interval of points are analyzed. First consider case 3. For a 200 Hz cycle, there are approximately 50 measurement snapshots at the 10 kHz imaging repetition rate. Specific points have been marked in the cycle. These were carefully chosen to highlight the unsteady jet behavior. The cycle at time 1 starts with a high pressure (i.e., p' near a maximum) at the combustor chamber exit. This corresponds approximately to the defined phase 0^o.

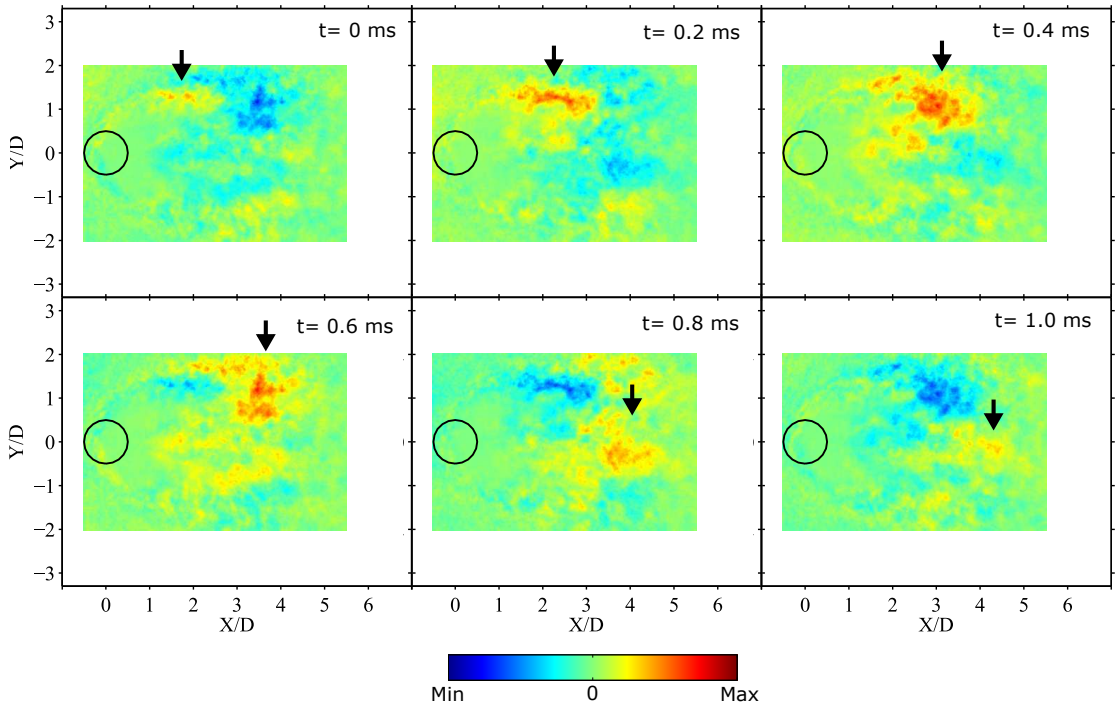

Figure 7.22.. OH-PLIF DMD 876 Hz modal evolution. Six time instances are shown in the top right of each image covering approximately one period of the 876 Hz frequency. Arrows indicate salient feature.

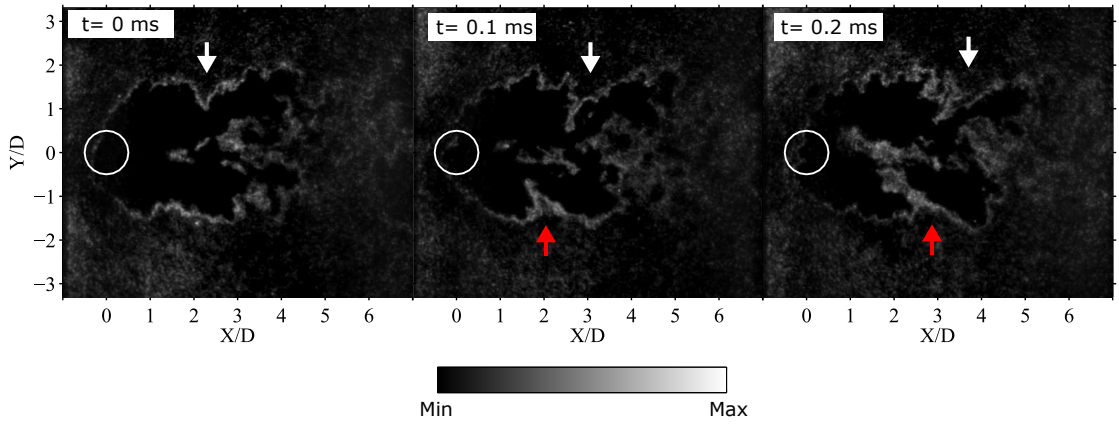

Figure 7.23.. Case 4 raw OH-PLIF highlighting the growth of flame front inflection points. White arrows ($+Y/D$) locate these points on the top edge, and the red arrows ($-Y/D$) locate these points on the bottom edge.

Figure 7.25 and 7.26 shows the corrected instantaneous OH-PLIF measurements and the instantaneous velocity field for the time points in Figure 7.24 for case 3. It was observed that much of the jet OH-PLIF dynamics could best be represented with the instantaneous snapshots as opposed to either the POD or DMD results. The calculated reaction front curve is overlaid on the corresponding velocity fields. Also, note that the instantaneous velocity fields occupy only a portion of the PIV FOV. Vector generation can only occur in regions with relatively good seed density, i.e. regions with jet fluid. Recall that the crossflow is not seeded. The jet rolling and flapping through this Z/D plane transports the calculated vectors accordingly. Therefore, velocity data in the instantaneous snapshots is only available in locations with jet fluid.

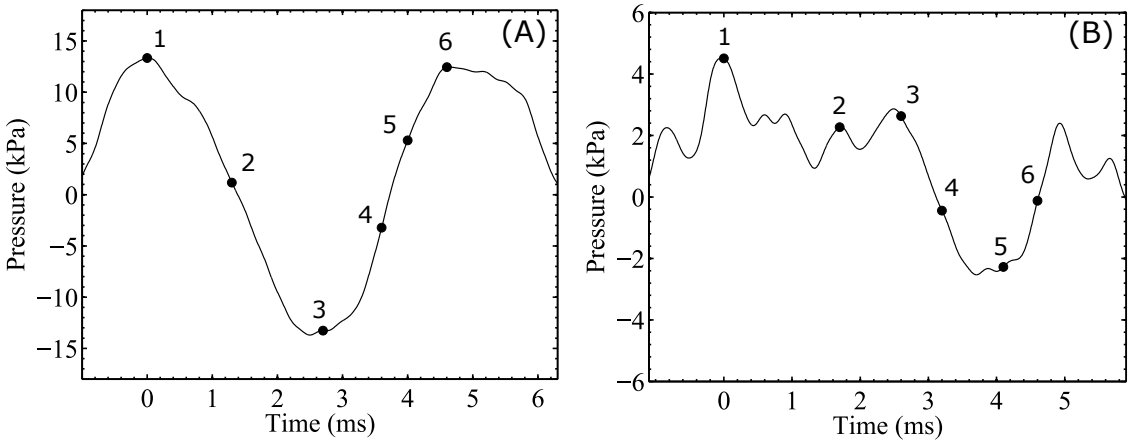

Figure 7.24.. Unsteady pressure plots for (A)case 3 and (B) case 4. Pressure bandpass-filtered between 20 Hz and 2000 Hz. Note that pressure scales are different for each figure. Pressure shown is from P1.

Starting at time 1, the cycle has just begun and the pressure at the chamber exit is just beginning to decrease from its maximum value. The crossflow velocity at the point of jet injection is decelerating below its mean value. The OH gradients identifying the reaction front extend upstream to the projected jet orifice. The flame front is fairly corrugated. An island of isolated OH signal suggests out of plane

reaction front structure piercing into this plane. The OH signal enclosed in the calculated flame front curve is typically lower than the crossflow vitiated LIF or the jet flame products OH signal. This internal region is predominantly unburned jet fluid. At this time, most of the unburned jet fluid has a relatively low streamwise u_x velocity component, with the lowest amplitude region closest to the jet orifice coinciding with the time averaged wake location. The y-component of velocity displays strong vertical bands of alternating u_y at X/D=0.5 (u_y is negative), at X/D=2.5 (u_y is positive), and at X/D=4.5 (u_y is negative). These bands resemble an alternating wake structure behind a bluff body. From the POD analysis, the interface between bands indicate the center of a vortex structure. In fact, a POD reconstruction using only modes 4-8 (not shown) shows an incipient vortex forming immediately before time 1, and at time 1 the vortex is well formed and centered at $(X/D, Y/D) = (1.5, 0)$. Also at time 1, the POD mode 4-8 reconstruction shows a distorted vortex located at $(X/D, Y/D) = (4, 0.5)$, which coincides with an interface between u_y two bands. Also note the flame front inflection point at $(X/D, Y/D) = (3, -1)$. This area corresponds with a large $+u_y$ that pinches the flame front inward toward Y/D=0, creating the start of a flame front structure that engulfs and transports crossflow fluid into the interior of the jet.

As the cycle progresses to time 2, the compression at the chamber nozzle is gone and the crossflow acoustic pertubation causes the true crossflow velocity to decrease to near its minimum cycle value. Jet penetration is near the cycle maximum. Recall that the jet is injected at the $2L$ pressure node and thus the jet exit momentum flux is relatively unchanged over a crossflow cycle. The penetration, however, ostensibly changes due to the fluctuating instantaneous crossflow momentum flux. The reaction front contracts toward the jet orifice. Occasional bursts of flame front are observed to pinch off from close to the jet orifice and convect downstream. The reaction front structure centered at $(X/D, Y/D) = (3, 1.5)$ is this structure. The y velocity at $(X/D, Y/D) = (2, 1)$ is relatively large and suggests that in addition to pinching off, the structure is swinging inward toward the jet centerline $Y/D = 0$. This highlights an important feature observed in the flowfield: the instantaneous asymmetry in the

OH-PLIF and velocity fields. Also, the velocity field as a whole is low agreeing with the phase average. The low velocity wake u_x is narrow along the centerline Y/D=0 extending to X/D=4. Finally, note that the leading edge reaction front is upstream of the jet orifice ($Y/D < 0.5$). At the plane Z/D=1, with the crossflow velocity low the jet core is expected to be even stronger than at other points in the cycle. This strong core displays bending to a lesser degree at Z/D=1 and anchors the flame front even further upstream.

At time 3, the chamber exit is beginning to move away from a rarefaction and the chamber dump plane is moving away from a compression. At this time, the crossflow is just beginning to accelerate and increase speed at the jet location. The leading edge reaction front location is relatively unchanged from time 1. In fact, the leading edge reaction front is relatively insensitive from cycle to cycle except for the time instant 2 period when the crossflow speed is near its lowest value. Most notable from the LIF are two elongated arms separated by a region that is either burned OH gases or out of plane reaction front. Instantaneously, the arm lengths are uneven. This is typically observed. Between time 2 and time 3, these arms begin as short arms near time 2 that resemble the kidney shaped horseshoe structure observed in the phase averaged OH-PLIF at 90^o. As the arms lengthen, the jet shear layer streamwise velocity increases. The u_y again displays alternating bands of strong velocity in the wake of the jet at $X/D = 2$ and $X/D = 3$. A POD reconstruction using only modes 4-8 (not shown) shows an incipient vortex forming immediately before time 3 at $(X/D, Y/D) = (1.5, 0.5)$, and at time 3 the vortex is well formed and centered at $(X/D, Y/D) = (1.5, 0)$ (the approximate interface location for the between the bands at $X/D = 2$ and $X/D = 3$). Also at time 3, the POD mode 4-8 reconstruction shows an additional coherent vortex located at $(X/D, Y/D) = (5, 0.5)$, which appears to coincide with the u_y band at $X/D = 3$ and another band which may be located at $X/D = 4.5$, but a large pocket of missing vectors makes this difficult to determine.

At time 4, the chamber exit pressure is near its mean value and the flowfield acoustic energy is instantaneously stored in the crossflow velocity which is now near

it maximum cycle value. This is supported by the increase in u_x in the lateral shear layers where a strong shear exists between the jet and crossflow. The leading edge reaction front location has not changed. The central OH wake region has aligned itself along the centerline $Y/D = 0$ and grown in width relative to time 3. This is consistent with a jet trajectory closer to the injection wall and fixed sheet interrogation plane bisecting the jet at different jet-based cross sections as the jet trajectory changes as a function of the crossflow velocity. The POD modes 1-3 similarly capture the cycle maximum velocity concentrated predominantly in the jet shear layers. The POD reconstructed modes 4-8 shows a large, but weak distorted vortex centered near $(X/D, Y/D) = (3, 0)$, which closely coincides with two small alternating direction u_y bands at $(X/D, Y/D) = (2.25, -0.5)$ and $(X/D, Y/D) = (4, -1)$. The vortex center coincides with a low u_x.

At time 5, the chamber exit pressure is just beginning to become positive again, but is low enough that the crossflow velocity is still high relative to the mean. The crossflow is beginning to decelerate back toward its mean value. The u_x in the jet shear layer remains high. Times 4 and 5 are close enough to the p'=0 crossing that it's expected that the crossflow velocity in both cases is similar, with the difference being time 4 involves a crossflow acceleration and time 5 a deceleration. The leading edge reaction front is unchanged, but the leading central wake OH has moved downstream from X/D=0.5 at time 3 and time 4 to X/D=2 at time 5. The low velocity wake behind the jet orifice observed in u_x has lengthened relative to time 4. The fact that the leading central OH is now further downstream suggests the jet penetration is even less compared to time 4. This also suggests the that jet inertia (as the crossflow forces on it changes) continues moving the jet toward the injection wall even after the crossflow starts decelerating. A POD reconstruction of modes 4-8 shows a large and weak central votex centered at $(X/D, Y/D) = (2, 0)$ and a weak distorted vortex following it centered at $(X/D, Y/D) = (4, 0)$. The POD mode 1-3 reconstruction continues to shows an above average velocity jet shear layer.

At time 6, the cycle is near complete and the chamber exit pressure is moving back to its largest value. The leading edge reaction front is unchanged. Relative to time 4 and time 5, the OH-PLIF and velocity fields show a reduced jet width in Y/D, and the central wake OH signal is now even further downstream. The movement of this central wake OH region itself indicates jet flapping at the crossflow frequency from the time varying crossflow velocity. The u_y shows the alternaing bands again, but a POD mode 4-8 reconstruction shows that the vortex at time 6 is relatively weak as compared to time 1 or time 3. However, the measurement immediately preceding and following time 6 shows high cycle strength vortex structures in the jet wake.

A cycle analysis for the quasi steady case 4 in Figure 7.24 is now performed. This time slice was chosen because of the low crossflow pressure oscillations and provides a reference with which to compare case 3 under similar crossflow and jet operating conditions. A true dominant acoustic period at any one frequency does not exist for case 4 and is verified with a PSD of the crossflow pressure. The crossflow is in a quasi steady state relative to the nominal case 3 chamber acoustics. Six points are marked over a period of 4.6 μs that highlight the jet behavior. This period is approximately the same as the case 3 cycle analysis and allows a direct comparison.

Starting a time 1, a narrow and elongated jet reaction front encloses a central OH region extending upstream to X/D=2. The leading edge reaction front is above the jet orifice similar to case 3. Note an inward pinching of the flame front at $(X/D, Y/D) = (3, -1)$, which corresponds to a region of large $+u_y$. Immediately upstream of this large $+u_y$ location exists a continuous band of $-u_y$. These interface between alternating u_y often indicates vortex centers. Indeed, a POD reconstruction using modes 3-7 show two vortex structures, one centered at $(X/D, Y/D) = (2, -0.5)$ and another at $(X/D, Y/D) = (4, 0)$. Also note the magnitude of the lateral shear layers. Although the crossflow does not contain large coherent acoustics, similar shear layer values are observed. This indicates there are two separate sources of velocity increase being observed in the shear layer. One source due to the actual crossflow itself increasing in speed and the second source due to more of the three dimensional

velocity is in-plane (i.e. less u_z, which is not possible to measure using the current PIV technique).

At time 2, the leading edge reaction front is still above the jet orifice. Also note a similar (but temporally uncorrelated) structure as in time 1 of the flame front pinching in from the lateral edges. This structure coincides with low u_x and large u_y. The instantaneous OH-PLIF measurements leading up to time 2 (not shown) show a flame edge gradually moving inward back toward the jet orifice. Before this structure begins moving inwards, the jet is qualitatively similar to time 1. The velocity field is actively engulfing and transporting the hot crossflow fluid into the interior of the jet. Large areas of alternating u_y indicate multiple vortex structures. A POD reconstruction of modes 3-7 show at least 3 distinct vortex structures centered at $(X/D, Y/D) = (4.25, 0)$ (counterclockwise rotation), $(X/D, Y/D) = (2.25, 0)$ (clockwise), and $(X/D, Y/D) = (1, 0)$ (counterclockwise).

At time 3, there's a significant increase in width of the flame front structure. The leading edge flame front is still above the jet orifice. For the wider jet, the low velocity u_x wake region widens as well. Note u_y and the proportion of the wake region with in the $-Y$ direction as opposed to the two smaller regions of $+u_y$. The POD reconstruction of modes 3-7 show multiple large vortex structures spanning the enlarged jet wake, e.g. a distorted vortex at $(X/D, Y/D) = (3.25, 0)$ (clockwise rotation) and an incipient vortex at $(X/D, Y/D) = (1.5, 0.25)$ (counterclockwise). The flame front structure relative to the other times is highly convoluted and multiple islands of OH signal are present. Further downstream at $(X/D, Y/D) = (5, 1)$, there's a flame front pinching inward from the jet lateral edge toward Y/D=0 but also traveling in the upstream direction. Overall, the velocity field is qualitatively similar to time 1 and 2.

Times 4, 5, and 6 all shows qualitatively similar behavior to times 1-3. Times 4-6 shows the progression of flame edge structures progressing inward form both lateral sides of the jet giving the nearfield impression of a contracted flame front. The leading edge flame fronts are still above the jet orifice. Multiple in-plane vortical structures

are present at each time with centers coinciding with the interfaces between bands of alternating u_y. Also, there are no observable trends in u_x in the jet shear layer as there were for case 3.

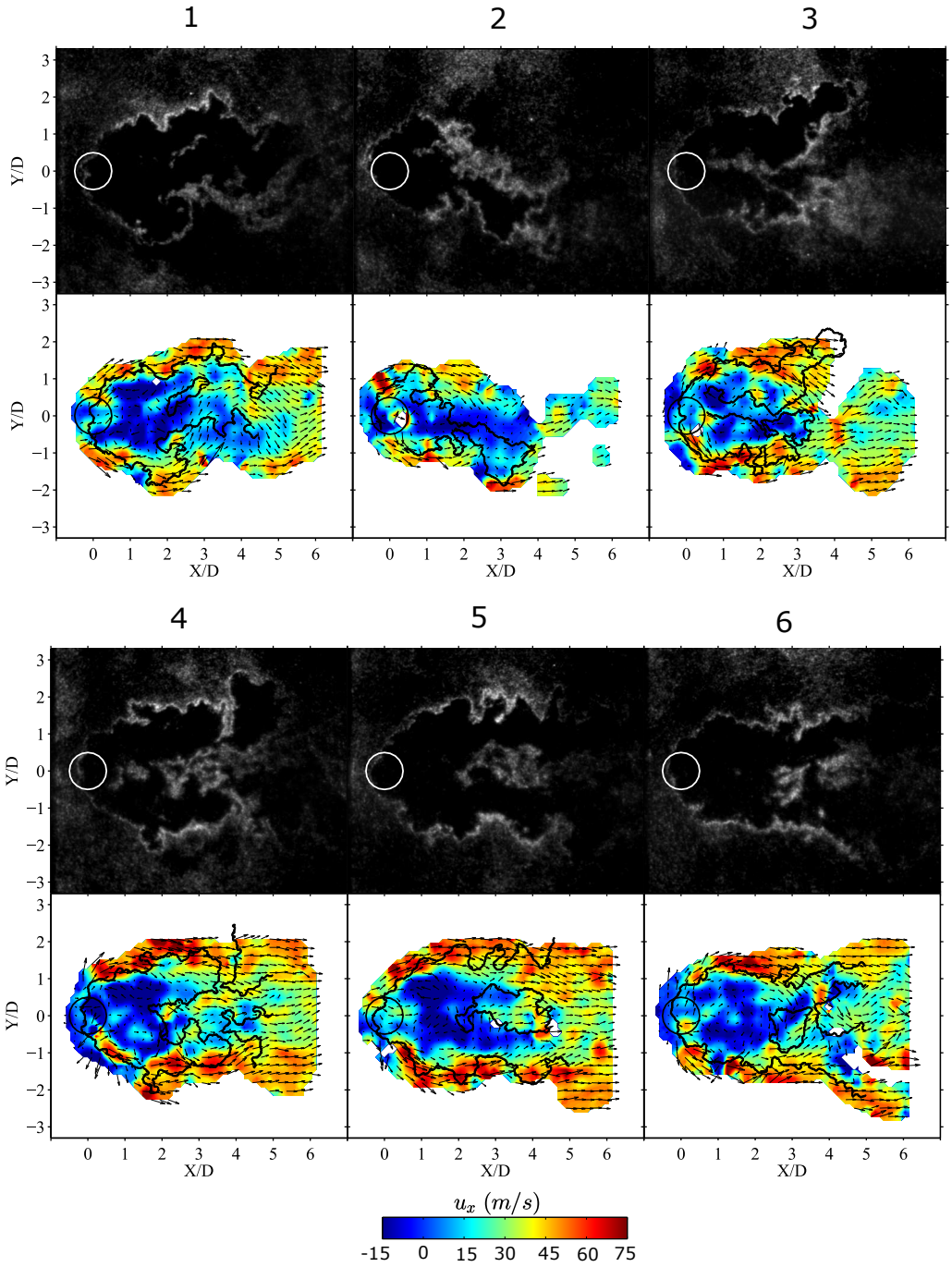

Figure 7.25.. Cycle snapshots for case 3 at $Z/D = 1$. Top rows are corrected OH-PLIF. Bottom rows are the instantaneous velocity fields with a u_x false colored background. The black curve overlaid on the velocity field is the corresponding OH-PLIF calculated flame front curve.

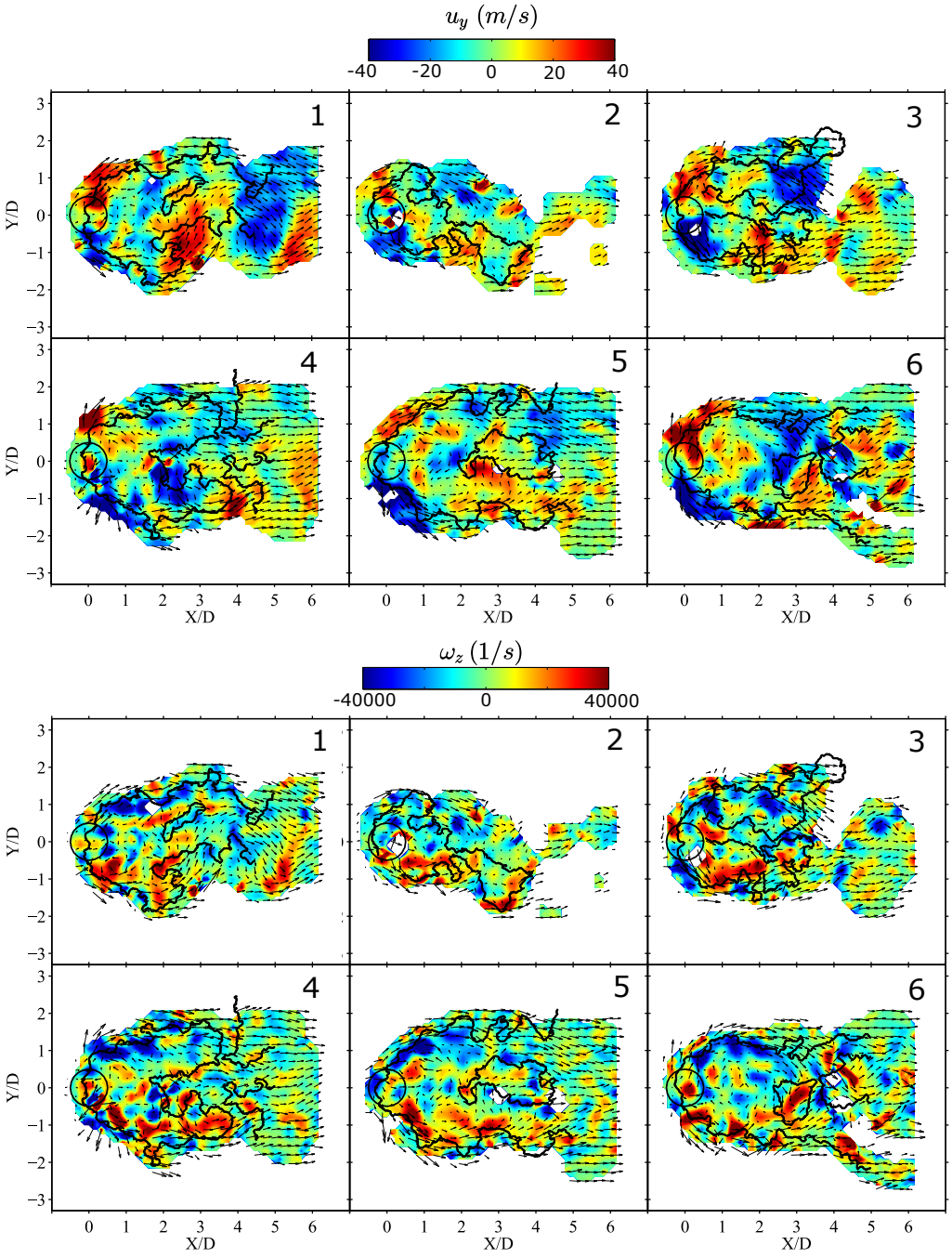

Figure 7.26.. Cycle snapshots of the instantaneous velocity for case 3 at $Z/D = 1$. Top two rows show u_y background color and bottom two rows show a ω_z background color. The black curve overlaid on the velocity field is the corresponding OH-PLIF calculated flame front curve.

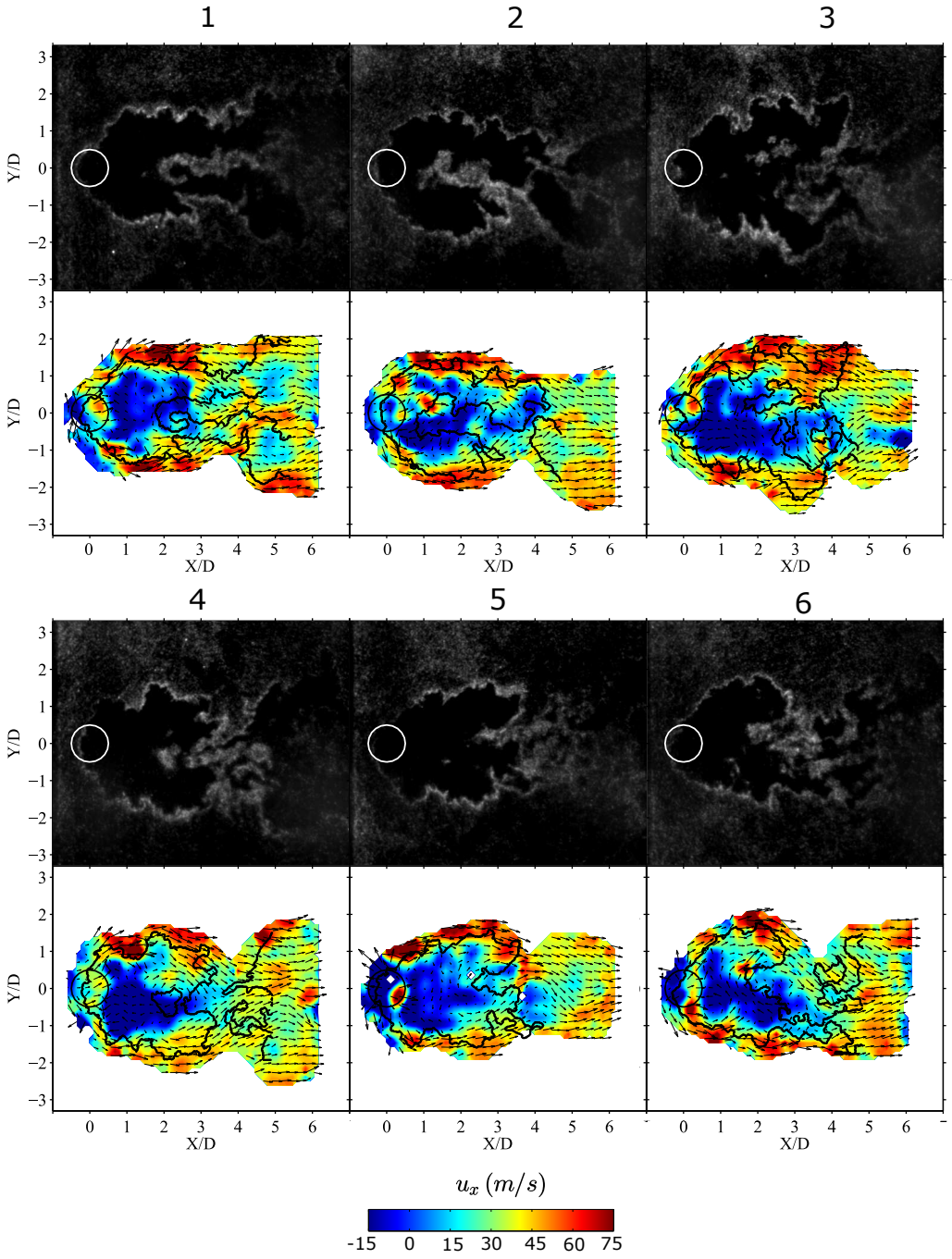

Figure 7.27.. Cycle snapshots for case 4 at $Z/D = 1$. Top rows are corrected OH-PLIF. Bottom rows are the instantaneous veloicty fields with u_x false colored background. The black curve overlaid on the velocity field is the corresponding OH-PLIF calculated flame front curve.

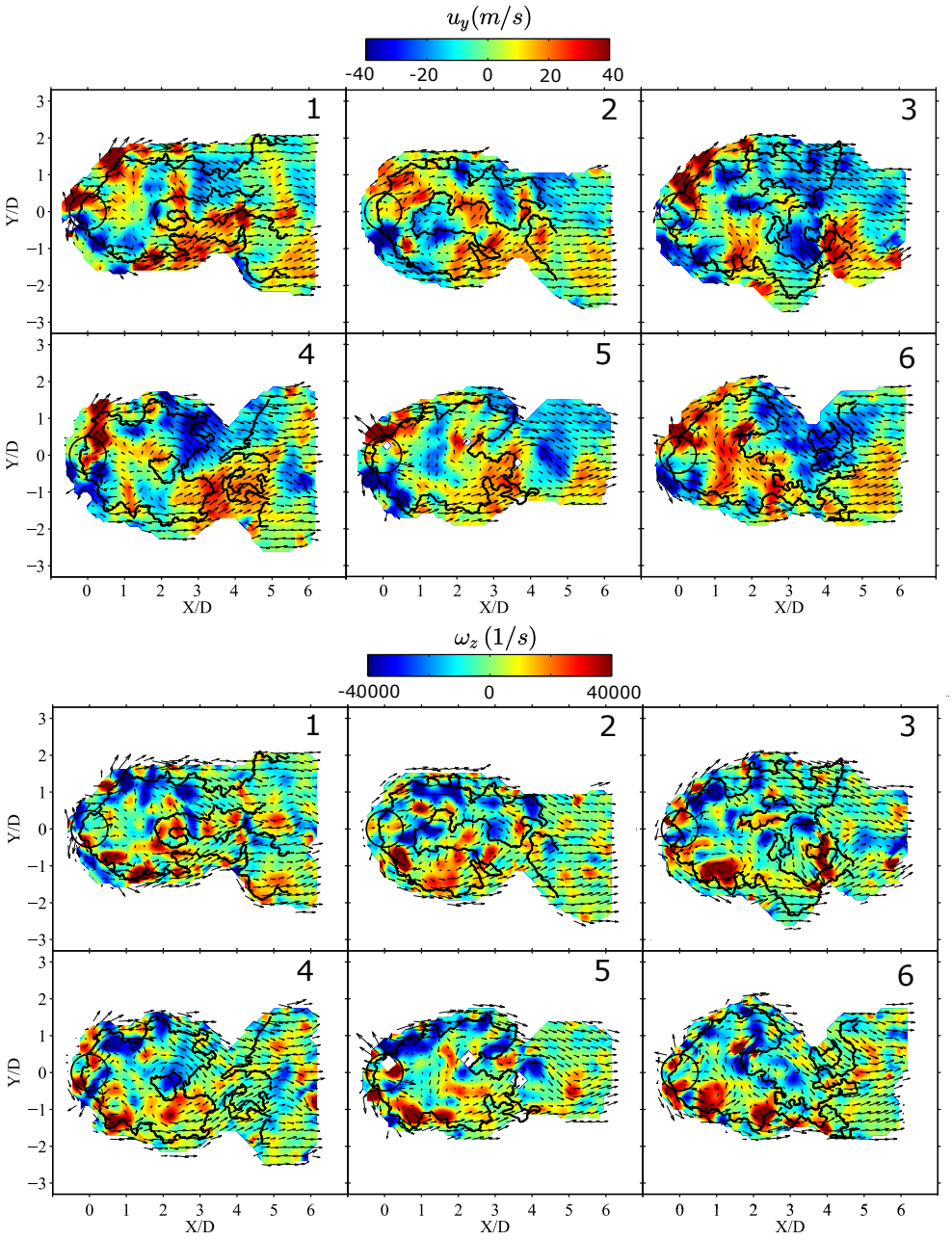

Figure 7.28.. Cycle snapshots of the instantaneous velocity for case 4 at $Z/D = 1$. Top two rows show a u_y false colored background and bottom two rows show a ω_z false colored background. The black curve overlaid on the velocity field is the corresponding OH-PLIF calculated flame front curve.

8. Reacting H_2/N_2 Jet In a Vitiated Oscillating Crossflow at Plane Z/D = 2.7

The JICF flowfield is now described at the plane $Z/D = 2.7$. This is case 5 in Table 4.2. This corresponds to a 0.1 s time slice and 1001 images. At this plane, the raw PIV scattering measurements show the jet fluid intermittently moving in and out of the plane. This suggests a high degree of jet flapping. The OH-PLIF measurements also show this.

Figure 8.1 shows the crossflow and injector pressure behavior for case 5. Three pressure measurement locations are shown: the crossflow P1 at the combustion chamber exit, the crossflow P5 directly upstream of transverse jet, and P10 inside the jet injector. The dominant acoustic at the location P1 is the chamber $2L$ at 198 Hz. Recall, this location is a good measure of the p' amplitude of the $2L'$ resonant chamber acoustic. Harmonics of the $2L$ and additional higher frequencies are typically present under reacting crossflow conditions. The crossflow in general always contain low amplitude unsteadiness at the chamber resonant acoustics due to the self-excited nature of the dump combustor.

Many of the frequency peaks are highlighted in Figure 8.1. The injector P10 PSD shows three peaks at 401 Hz, 455 Hz, and 829 Hz, all of which are also measured at P1 and P5 suggesting these are the crossflow acoustics and that the injector is responding to the fluctuating local injection flowfield. The 401 Hz peak in P1 and P5 have a similar magnitude, which agrees with the $4L$ near 400 Hz having a p' anti-node near the jet injection point (near P5) and at the combustion chamber exit nozzle (near P1). The 830 Hz frequency is likely the chamber $8L$, a harmonic of the $4L$. The fact that P10 does not have a 190 Hz peak further supports that the only jet interaction with the chamber $2L$ is through crossflow velocity oscillations (since the

jet is located at the $2L$ p' node). Figure 8.1 also shows the pressure traces for P1, P5, and P10. The pressure was bandpass filtered between 20 Hz and 2000 Hz to highlight the fluctuations of the the dominant dynamics and to remove pressure port bias. There is a clear dominant chamber fluctuation at the 198 Hz $2L$. The fluctuations at P5 and P10 are smaller, but still contain a finite amplitude. For a few cycles of the $2L$, the P1 oscillation shows double peaks and double troughs, indicating some contribution from the lower amplitude chamber crossflow 401 Hz or 582 Hz. In the following analysis, velocity and OH-PLIF results do indeed show a 400 Hz frequency, ostensibly from the crossflow $4L$. For OH-PLIF measurements, the 400 Hz frequency is an order of magnitude lower than the most dominant spectral dynamics. For PIV, the 400 Hz is a more distinct spectral peak, but is still orders of magnitude lower than the dominant dynamics. The POD and DMD will prove useful in sorting these dynamics.

Figure 8.2 shows the time averaged velocity quantities $|\vec{u}|$, ω_z, u_y, and the streamlines. The thick black curve, calculated from a time average of the OH-PLIF measurements, marks the interface between the qualitative flame front and the jet unburned fluid region. At this plane, the jet is showing signs of bending into the crossflow. A larger fraction of the calculated velocity exists for $X/D > 1$ (recall, vector generation only occurs in regions with jet fluid since only the jet was seeded). This is also evident by the absence of a mean concentrated wake region immediately downstream of the projected jet orifice as was observed at plane Z/D=1 for case 3 and case 4. Instead, there exists a nearly continuous high velocity distribution from one side of the jet shear layer (e.g. $Y/D = 1.5$) to the other along the upstream edge. Also, the shear layer $|\vec{u}|$ is lower than in case 3 or case 4 indicating the jet fluid is moving toward realizing a velocity near the mean bulk crossflow fluid. The lower velocity wake region continues further downstream and resides entirely within the mean OH-PLIF curve. The z-vorticity shows two oppositely oriented vorticity regions directly above and below the Y/D centerline and also residing predominantly within the OH-PLIF mean curve. The length of these has increased substantially relative to the plane $Z/D = 1$.

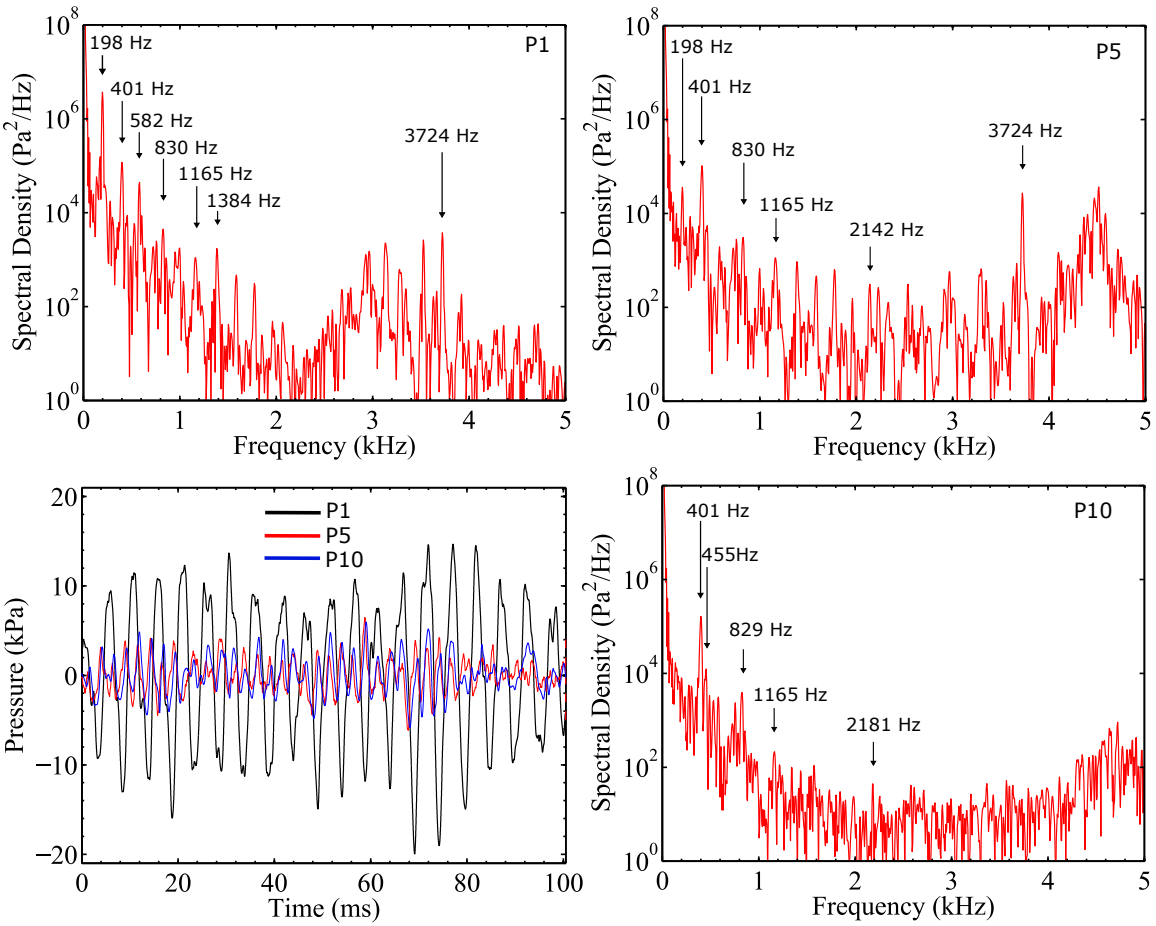

Figure 8.1.. Pressure behavior for case 5. PSD shown for the locations P1, P5 and P10. Also shown are the 20 Hz-2000 Hz bandpass filtered pressures from P1, P5, and P10.

Finally, the streamlines do not indicate any mean vortex structures and instead show an initial jet shear layer outward expansion for $X/D < 3$ followed by a streamwise oriented velocity field for $X/D > 3$. This is also evident in u_y. The fact that there are two large ω_z regions, but no corresponding streamline vortices, indicates that this is predominantly shear induced vortictiy and not due to actual mean vortex structures.

Figure 8.3 and 8.4 shows the phase averaged $|\vec{u}|$ and ω_z, respectively. Eight phase locations are shown. For each phase, the calculation is based on two images per cycle to decrease mean biasing with a smaller sample population, resulting in a phase

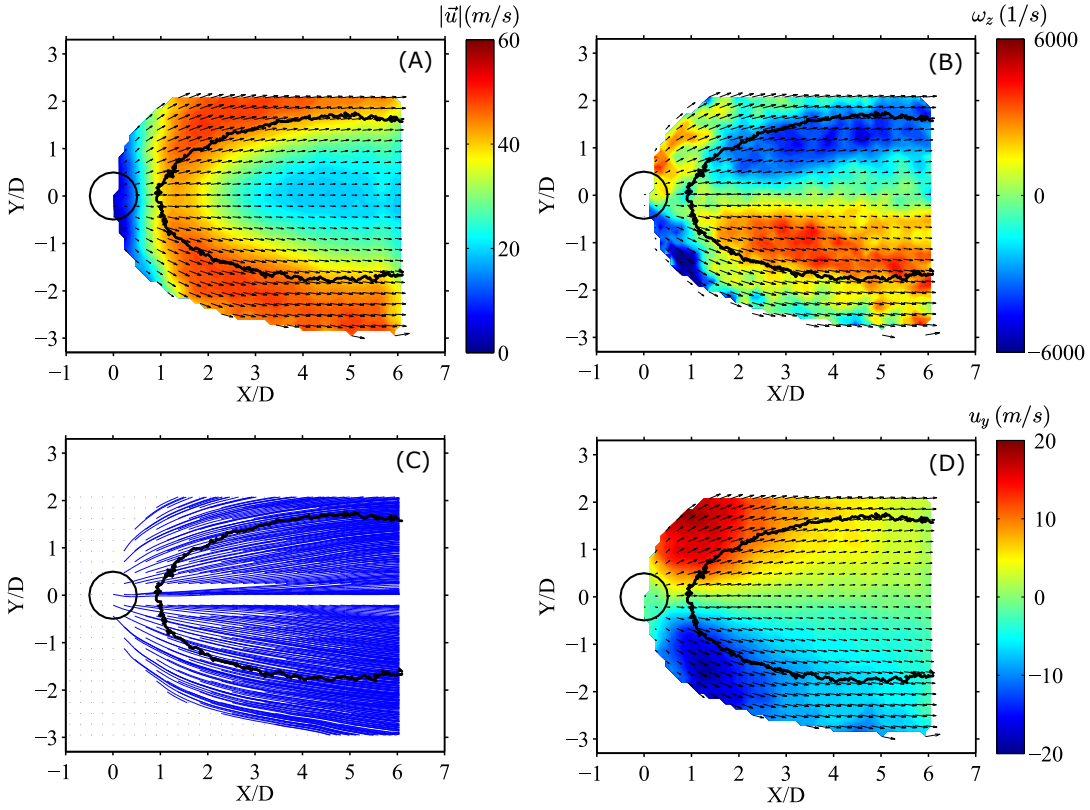

Figure 8.2.. Time average velocity for case 5. (A) $|\vec{u}|$. (B) ω_z. (C) streamlines. (D) u_y.

average based on a value $\pm 5^o$ about the designated phase in the upper right hand corner of each image. A 20% vector cutoff threshold was placed on the field at each phase to remove locations with infrequent vector population. This was necessary to reduce a time-average biasing at a given location due regions with intermittent seed and vector generation from the apparent large degree of jet flapping in and out of the plane. Unlike the $Z/D = 1$ plane, a phase averaged OH-PLIF curve is not shown for each phase. At this plane Z/D=2.7, the high degree of flame front motion resulted in a diffuse and less informative OH-PLIF average.

Most apparent from the phase averaged sequence is the difference in velocity between a time of low crossflow velocity (45^o to 135^o) and high crossflow velocity(225^o to 315^o). At 0^o the local jet crossflow velocity is near its mean and the chamber exit

pressure P1 is at a compression. The jet shear layer and lower velocity wake resemble the time-average. At 45^o, the pressure at P1 starts to drop and the local jet crossflow velocity begins to decrease. The jet shear layer and wake velocity both decrease, and the low velocity jet wake increases in size and now extends further upstream. At 90^o, the crossflow velocity is near its cycle minimum. This is consistent with the jet shear layer velocity displaying the lowest cycle shear layer velocity, and the lowest velocity portion of the jet wake at its cycle maximum in size. At 135^o, the crossflow is beginning to accelerate toward its mean value and the shear layer and wake $|\vec{u}|$ is increasing again. At 180^o, u_{cf} is back near its mean cycle value. Notice that $|\vec{u}|$ at 0^o and 180^o are qualitatively similar. In the crossflow cycle, 0^o and 180^o are both near the $\overline{u}_{cf}$ with the difference being the former coincides with an decelerating crossflow and the latter an accelerating crossflow.

At 225^o, u_{cf} is above the mean and approaching its maximum cycle value. This is consistent with the jet shear layer and wake $|\vec{u}|$ increasing. At 270^o, u_{cf} is near its maximum cycle velocity. The jet shear layer is strongest in the cycle and the jet wake is considerably reduced in size. The wake size reduction is indicative of the jet penetration instantaneously at a minimum. As u_{cf} is high, the jet bending is increased for the approximately fixed jet momentum flux at the $2L$ p' node location. The jet width at 270^o also suggests that this phase coincides with the most bottom portions of the jet plume as the jet trajectory decreases. At 315^o, u_{cf} is still high relative to the mean. The jet shear layer is strong and similar to 225^o, but the start of the lower velocity wake region is not as far upstream as at 225^o. This also indicates jet flapping at the crossflow $2L$ frequency. Now refer to Figure 8.4. The vorticity field displays a dichotomy of either a fine scale turbulent distribution or large coherent wake vorticity. At 45^o to 135^o, regions of coherent counter rotating vorticty coincides with the large wake regions in the phase average $|\vec{u}|$. The finer turbulent distribution at the other phases coincides with a strengthened shear layer and a reduced low velocity wake. With the jet seemingly flapping at the crossflow $2L$, the POD and DMD techniques will prove critical in identifying and sorting the wake dynamics.

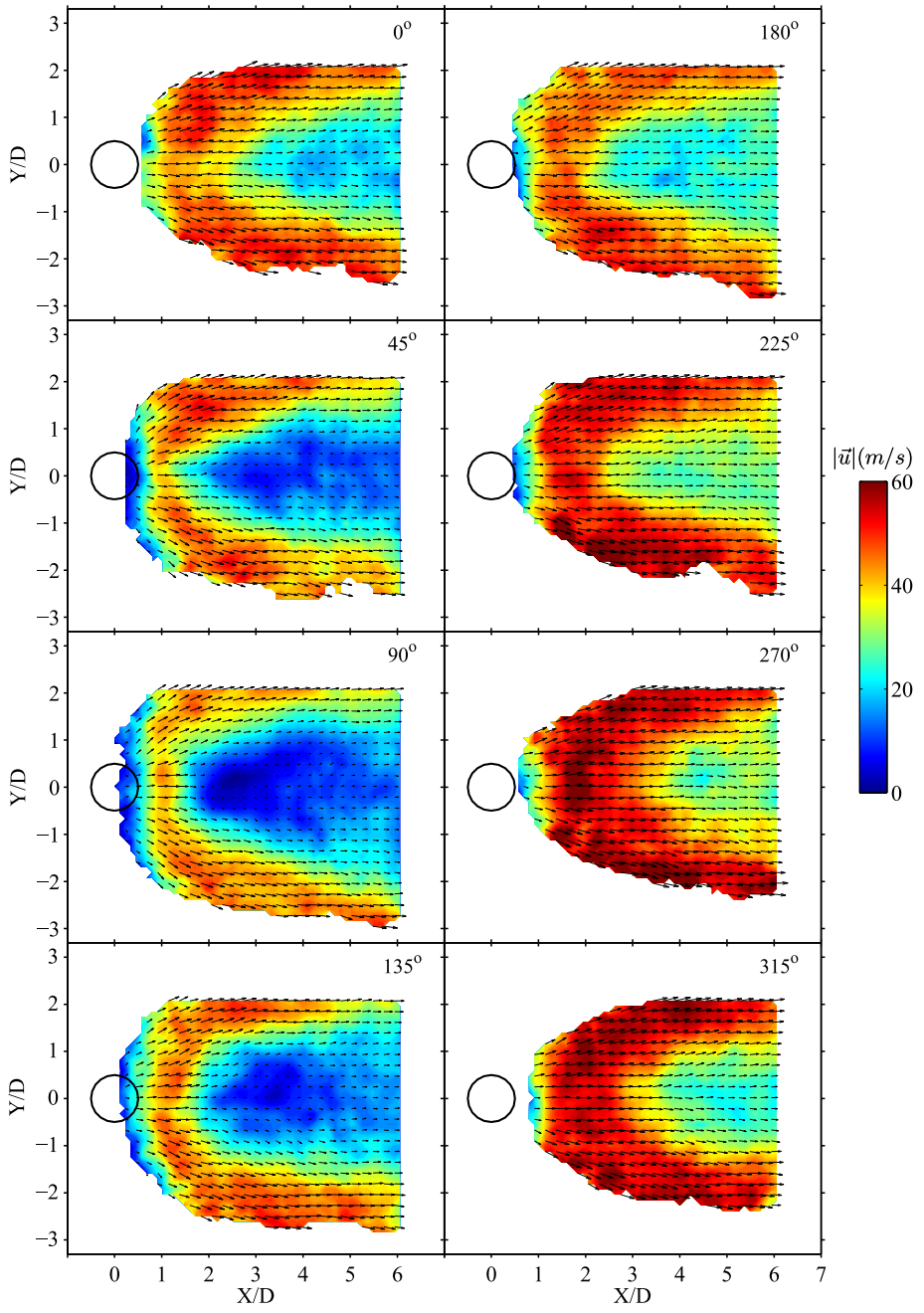

Figure 8.3.. Phase averaged velocity magnitude $|\vec{u}|$ for case 5. Eight phases are shown relative to the crossflow acoustic cycle per the definition in Figure 7.6. Note that this definition is consistent with Figure 3.7.

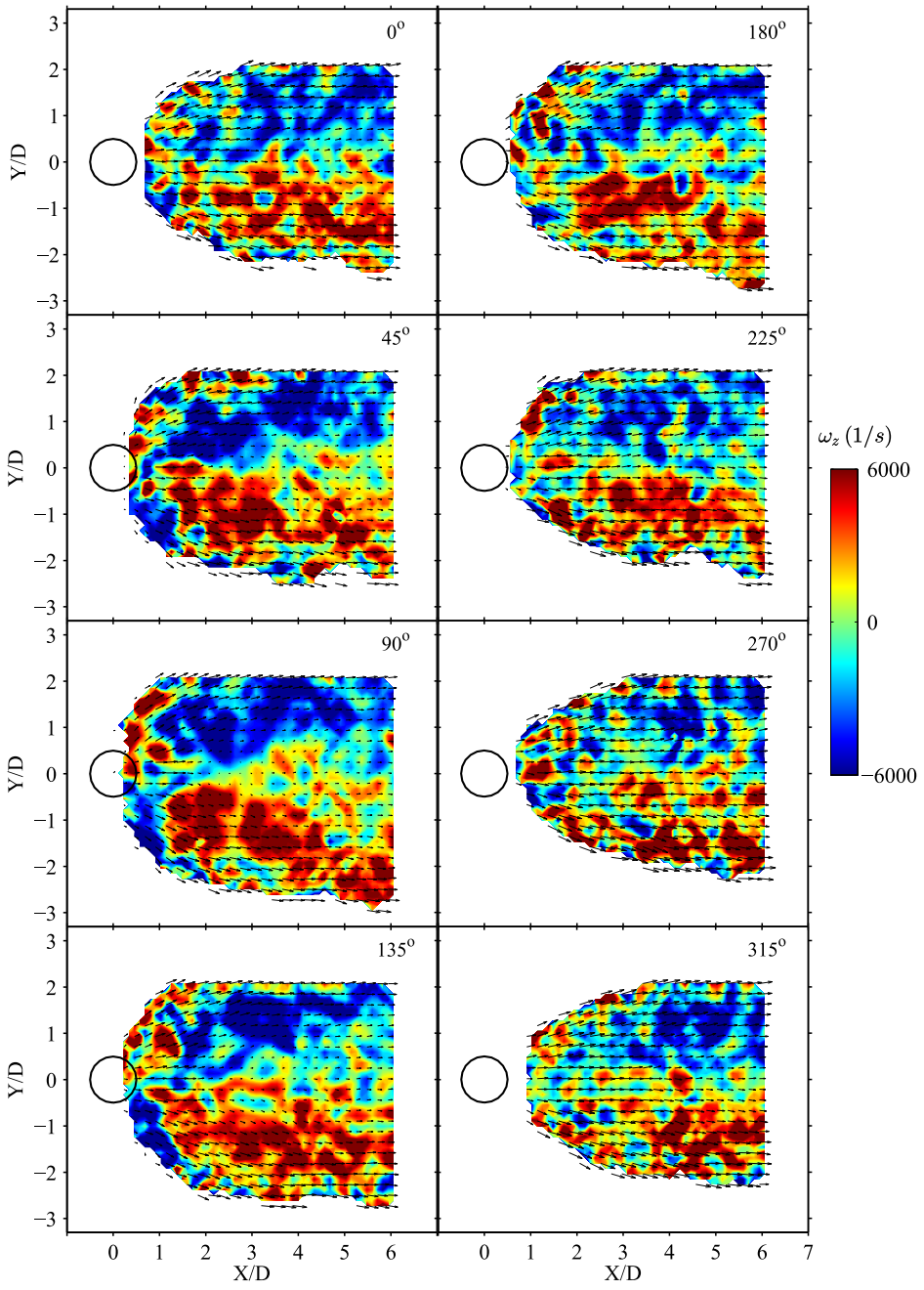

Figure 8.4.. Phase averaged vorticity ω_z magnitude for case 5. Eight phases are shown relative to the crossflow acoustic cycle per the definition in Figure 7.6. Note that this definition is consistent with Figure 3.7.

The time and phase averaged OH-PLIF are shown in Figure 8.5 and 8.6, respectively. At this plane, sharp gradients of high mean OH don't exist. A high degree of flame front motion results in a more diffuse OH-PLIF average as compared to plane Z/D=1. The largest OH gradients exist at the interfaces with predominantly jet unburned fluid. The upstream most portion of the mean jet flame front is no longer above the projected jet exit like it was at the plane Z/D=1. The yellow curve extending to X/D=7 denotes a threshold boundary marking the interface between the flame front and the mostly unburned jet fluid. The kindey shaped (horseshoe) mean OH-PLIF structure from plane Z/D=1 is also shown for reference. This highlights the quick evolution of the jet in less than 2 jet diameters in Z as it bends into the crossflow. The average OH-PLIF is also wider than at Z/D=1, consistent with volumetric expansion of the jet plume as entrainment occurs and the jet density drops.

The phase average OH-PLIF shows a periodic movement of the leading upstream edge. This coincides with the phase averaged jet velocity fluctuations. At 90^o the leading edge is furthest upstream (pointed out with an arrow) and is wide (in Y/D) relative to other phases. The crossflow u_{cf} is at a cycle minimum at this phase, jet penetration is ostensibly high, and the leading edge reaction front is as far upstream as the jet fluid takes it. At 270^o the leading edge has moved further downstream (pointed out with an arrow) and the OH-PLIF as a whole is much more diffuse as compared to the large low OH signal at 90^0 for $1 < X/D < 6$ and $-1.5 < Y/D < 1.5$. The crossflow u_{cf} is at a cycle maximum at this phase, jet penetration is ostensibly low, and the leading edge reaction front is further downstream. The width of the low OH signal at 315^o (denoted by a double sided arrow) is also low relative to either 0^0 or 90^0, and also to 225^0. At 225^0 and 315^0, u_{cf} is similar, except the former involves a crossflow acceleration and the latter a crossflow deceleration. This is also seen in the phase average velocity. The low velocity wake at 315^o is wider, but shortened relative to 225^0 where it is narrower, but longer. The initial jet injected density is

higher than the incoming crossflow suggesting inertia effects of the jet are at play, i.e. once the crossflow begins decelerating, the jet momentarily continues forward.

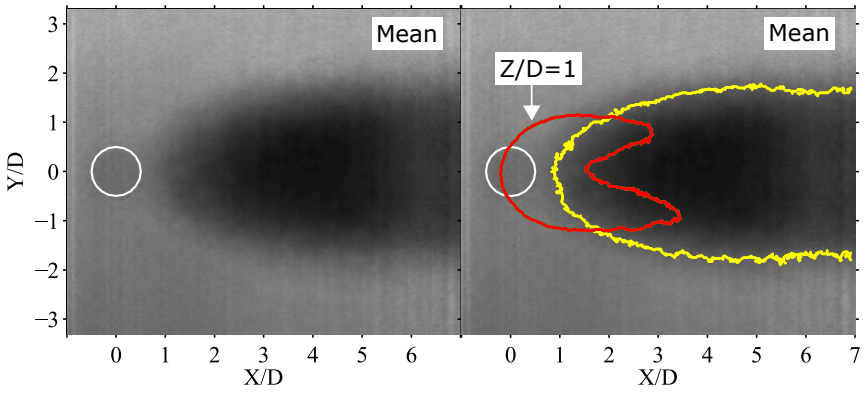

Figure 8.5.. Time average OH-PLIF for case 5. The plane is Z/D=2.7. The yellow curve extending to X/D=7 denotes a threshold boundary for the low OH intensity central region. For reference, the kidney shaped (horseshoe) structure from the time average OH-PLIF at plane Z/D=1 is also drawn on the same plot.

The phase averaged velocity and OH-PLIF clearly shows temporally correlated dynamics with the fluctuating crossflow. As the local crossflow velocity increases toward its cycle maximum, the jet velocity field intensifies in phase with a downstream displacement of the the mean upstream flame front. The relatively large reaction front downstream movement was not observed at the plane Z/D =1 suggesting the jet core momentum at Z/D=1 is still large enough to resist a relatively significant X/D displacement. Further along the jet trajectory at Z/D=2.7, the jet is now bending more. The volumetrically larger jet plume with a decreased jet momentum as the jet moves toward the crossflow velocity, in combination with a decreased jet density due to entrainment and combustion, would make the jet plume more susceptible to flowfield fluctuations.

A POD and DMD analysis is now performed. Figure 8.7 shows the spectral content of the first eight POD temporal coefficients. POD mode 1 contains nearly 16% of the total fluctuating kinetic energy in the flowfield. The dominant peak at

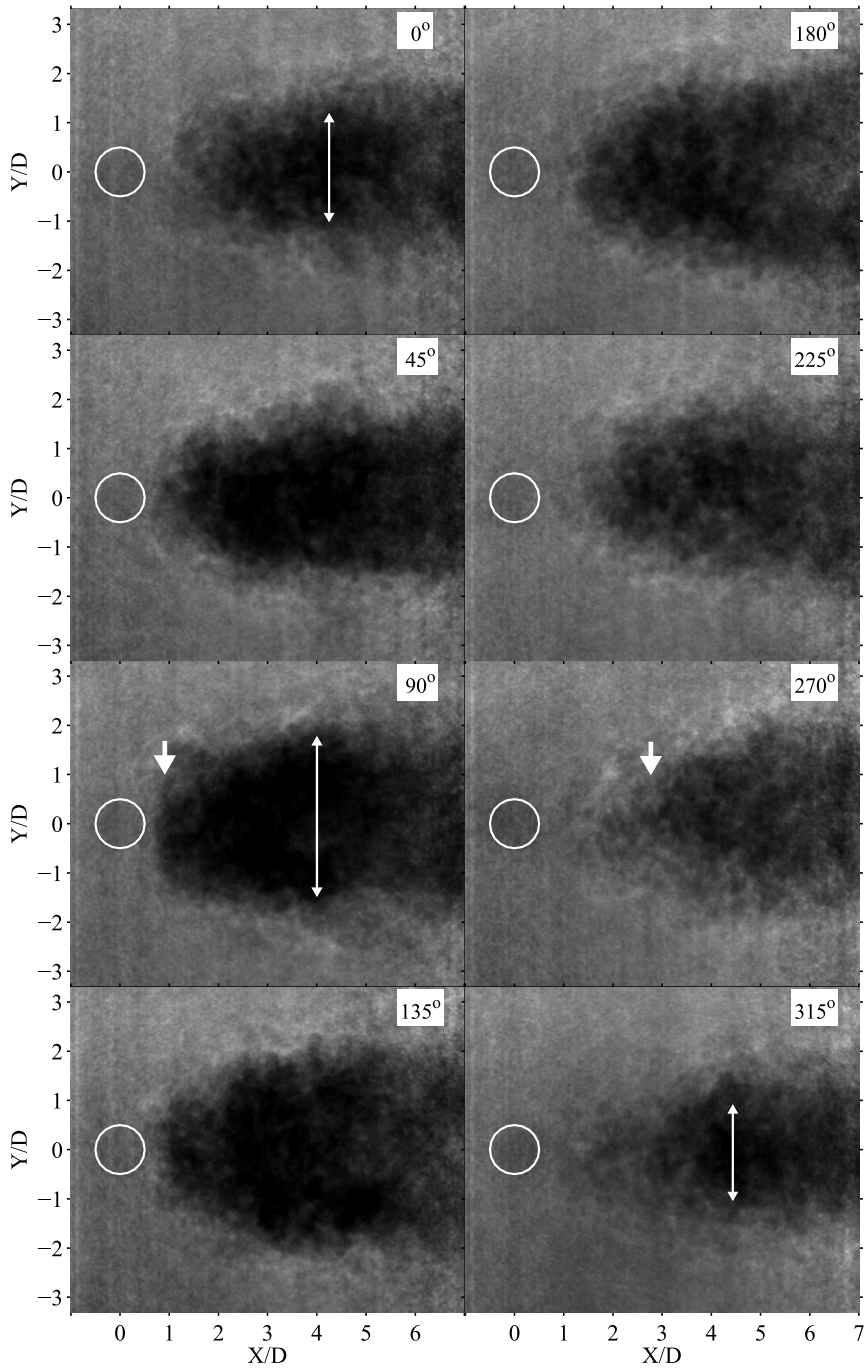

Figure 8.6.. Phase averaged OH-PLIF for case 5. Eight phases are shown relative to the crossflow acoustic cycle per the definition in Figure 7.6. Note that this definition is consistent with Figure 3.7.

195 Hz corresponds with the dominant crossflow frequency 198 Hz. Interestingly, the remaining seven spectra don't contain strong peaks at 195 Hz. This suggests the jet response to the crossflow $2L$ at the plane Z/D=2.7 is different from the response at Z/D=1 in so far that the spatial fluctuations at 195 Hz are spatially simple to describe. A peak at 395 Hz in POD mode 1 and mode 2, and 410 Hz in POD mode 4 are ostensibly due to the low amplitude crossflow $4L$. The pressure spectra during case 5 contains low level crossflow acoustic behavior at the chamber $4L$. Similarly, the injector pressure contains a 401 Hz frequency and thus it's expected that this frequency is present in the jet velocity. Higher frequency content at 820 Hz is also likely the jet responding to low level crossflow acoustics. A few modes contain low frequency peaks above 1 kHz, but these are near to the small amplitude crossflow acoustic frequencies.

Figure 8.8 and 8.9 shows the normalized POD modes 1-4 and 5-8, respectively, for case 5. Each POD mode vector field is plotted three times overlaid on the false colored background for u_x (left column), u_y (middle column), and ω_z (right column). POD mode 1 with the largest percentage of energy shows a spatial mode shape that resembles the time and phase average velocity. Beginning directly behind the projected jet orifice at $(X/D, Y/D) = (0.5, 0)$, there's an arc of $-u_x$ extending from $Y/D = 2$ to $Y/D = -2$. This is the upstream jet shear layer. Multiplying mode 1 by a negative coefficient shows u_x in the $+X$ direction and u_y expanding outward from the $Y/D = 0$ centerline. Downstream of this, a region of $+u_x$ with little u_y is of opposite direction relative to the jet shear layer.

The phase average velocity indicates that the whole velocity field (jet shear layer and wake) increases together and decreases together. The POD mode 1 spatially splits the wake and jet shear layer and suggests they are out of phase. Consider POD modes 2-3 which are concentrated in the jet shear layer. A POD reconstruction using POD modes 1-3 (not shown) captures a bulk streamwise fluctuating velocity. It appears then that the POD mode 1 upstream jet shear layer out of phase with the downstream wake is a consequence of the jet fluid physically being displaced further

downstream in X/D as jet penetration decreases under elevated crossflow velocity. This is consistent with the strength of the POD mode 1 wake region vector magnitude as compared to the much smaller POD mode 1 jet shear layer.

POD modes 1-5 all indicate fluctuations oriented predominantly in the X/D direction linked to a fluctuating jet in response to the oscillating crossflow velocity. POD modes 1-5 do not contain clear in-plane vortex structures. POD modes 6-8 show organized alternating bands of u_y with the interfaces between two bands identifying a vortex center. This was also observed at the plane Z/D=1. Consider POD mode 7. There are 6 alternating bands resulting in 4 interfaces and 4 vortices. Bands of u_y are located at $(X/D, Y/D) = (1, \pm 1)$, $(X/D, Y/D) = (3, \pm 1.25)$, and $(X/D, Y/D) = (5.25, \pm 1.5)$, with corresponding vortices centered at $(X/D, Y/D) = (2, \pm 1)$, $(X/D, Y/D) = (4.25, 1)$, and $(X/D, Y/D) = (4, 1.5)$. The vorticity field also shows the vortices. Note that the streamwise X/D position of two vortices is similar and that they are oppositely oriented.

This suggests a periodic counter rotating vortex pair being generated closer to the jet orifice and convecting downstream. The distance between the two consecutive counter rotating vortex structures in POD mode 6 is $\approx$ 2.25D. Scaling with a mean crossflow velocity 50 m/s, this results in a shedding frequency 3800 Hz, which is near to a 3984 Hz peak in POD mode 6. Multiple POD modes would be necessary to capture the convection, and POD modes 6 and 8 show vortex structures shifted in space relative to POD mode 7. The spectral content of these wake structures, however, is not highly energetic at a single frequency. The frequency content of POD modes 6-8 in Figure 8.7 do not show well defined and strong peaks. Instead, multiple low amplitude peaks above 1 kHz are present in each mode, e.g. POD mode 6 shows a 3984 Hz peak and POD mode 8 shows a 1250 Hz. This is likely due to different vortex generation sources present, pairing processes creating lower frequency subharmonics, and the irregularity of the processes on account of an unsteady flowfield.

A DMD was also performed on the x and y components of velocity. The capability of DMD to extract modes based on frequency unlike POD modes allows the

interactions between the crossflow acoustics and jet dynamics to be viewed as individual modes. Figure 8.7 shows the DMD spectra for u_x and u_y. The spectral content obtained from a DMD on u_x is qualitatively similar to a DMD on u_y. The spectra both display a dominant 200 Hz frequency that coincides with the crossflow $2L$ and both show a frequency close to the chamber $4L$. The remaining frequencies are also qualitatively similar to the POD spectra. The DMD spatial dynamics at 200 Hz resemble a combination a POD modes 1-3. The strongest jet velocity response to the oscillating crossflow is at the crossflow frequency. Similarly, the DMD 390 Hz and 410 Hz resemble a combination of POD modes 1-4. The DMD 710 Hz and 970 Hz describe in-plane vortices. The 710 Hz frequency describes counter rotating vortices which begin directly behind the jet orifice, convect downstream, grow in size, and eventually dissipate. The 970 Hz describes elongated and distorted counter rotating vortices generated behind the jet and followed by a downstream convection and subsequent dissipation. Note that for both the POD and DMD, the dominant description of the flowfield is the jet response at the dominant crossflow frequencies. Unsteady wake structures are present and identifiable, but display low relative amplitudes in the flow.

A POD and DMD is then performed on the OH-PLIF measurements. The POD and DMD OH-PLIF spectral content is shown in Figure 8.11. The POD modes 1, 2, and 6 all contain a dominant 195 Hz. This is the crossflow acoustic frequency. Unlike DMD, the frequency content is spread out among multiple modes. Comparison of the DMD 200 Hz spatial mode shape mode with the POD mode 1 (or a POD reconstruction using POD modes 1, 2, and 6) shows that they capture reasonably well the same dominant response as was captured in the phase averaged OH-PLIF. Figure 8.12 shows two snapshots of the DMD 200 Hz separated by 2.6 ms, which is approximately 1/2 the 200 Hz period. At (A) in the cycle, there is a minimum in OH intensity over most of the jet region except at the upstream edge of the jet shear layer. Half a period later at (B), the high OH intensity has moved downstream and organized itself into a horseshoe pattern. The arrows highlight this movement. This

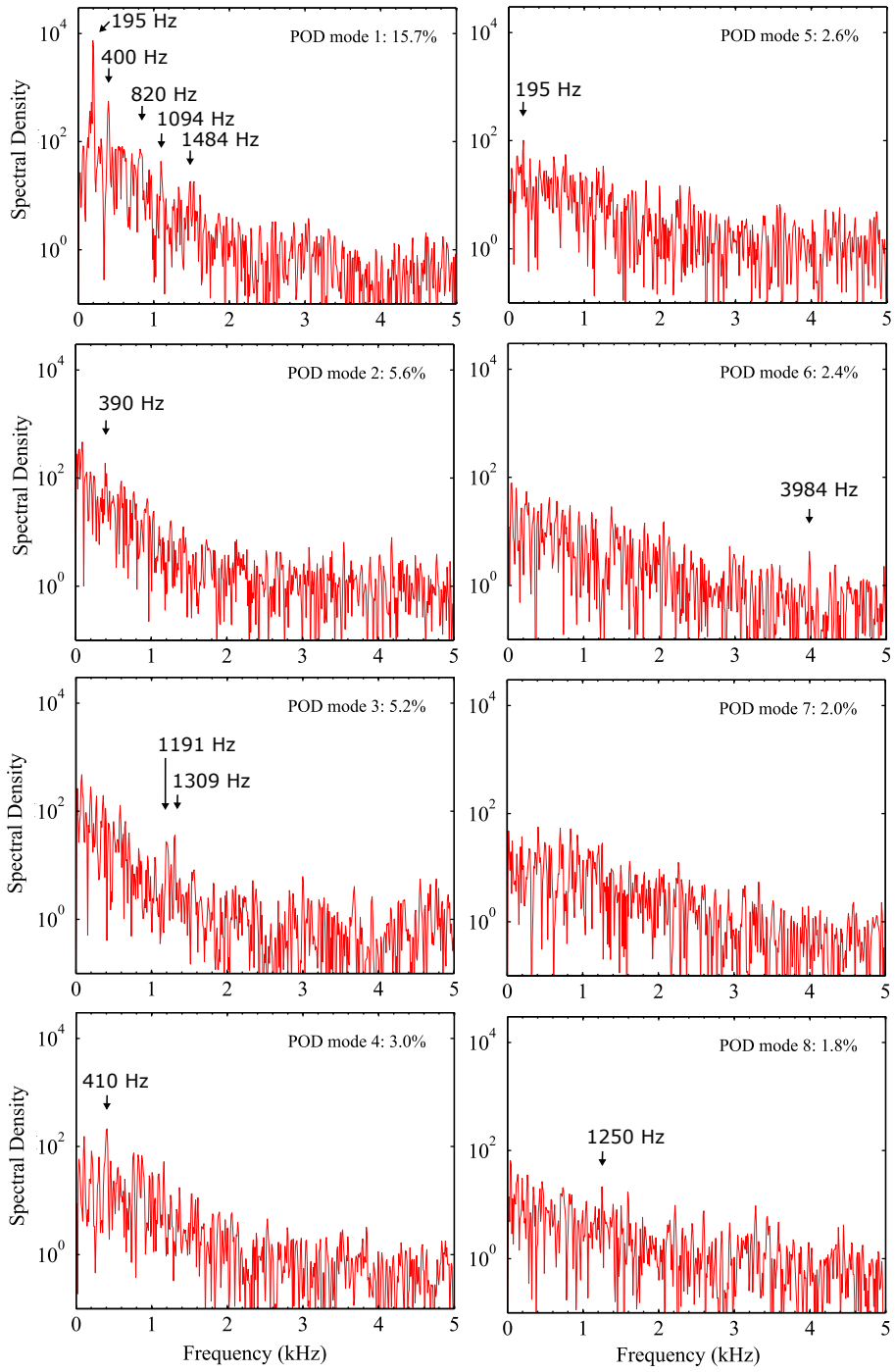

Figure 8.7.. PSD of the POD temporal coefficients for modes 1-8 for case 5.

movement occurs as the jet crossflow velocity increases and jet penetration decreases. Note that the DMD spatial modes are diffuse, obscure, and appear to lose most of the underlying thin flame front dynamics. In fact, the use of POD or DMD of OH-PLIF data beyond a power spectra has not proven reasonably beneficial in describing the dynamics as compared to a careful approach using a combination of the phase average and instantaneous measurements.

Higher frequency content is also present in Figure 8.11 such as 1201 Hz in POD mode 1, or 1191 Hz and 1812 Hz in DMD. These were observed at $Z/D = 1$. A closer examination of the crossflow acoustics shows that a 1200 Hz and 1780 Hz frequency is present in the combustion chamber, both with a low amplitude and likely harmonics of the dominant crossflow 200 Hz. When scaled with the crossflow velocity, the closeness of these frequencies to reported JICF wake dynamics (e.g. St_{cf} $0.1 - 0.15$) suggests the experimental apparatus is inadvertently biasing the response of the reacting JICF to the dominant crossflow acoustic modes, at least in the predominantly wake region. A 300 Hz frequency, and minor 260 Hz, is also observed in this plane. The jet velocity does not contain these frequencies. The plane $Z/D = 1$ also displayed a 300 Hz peak. A closer examination of the crossflow pressure spectra shows very low amplitude 277 Hz and 299 Hz present throughout the combustion chamber. This is verified with a close examination of the DMD 300 Hz mode shape revealing that its behavior in the PLIF FOV is mostly outside the region of the jet. The DMD 620 Hz is close to a crossflow pressure acoustic, but not identically. Figure 8.12 shows four snapshots of the DMD 620 Hz. This frequency describes a local region of high OH beginning directly behind the jet orifice and subsequently convecting downstream along the inner jet shear layer edge. The process is not symmetric about Y/D=0, but could be explained by the fact that this mode is relatively weak and the laser sheet enters from the $+Y$ direction. This may cause a bias in measuring structures using the OH signal within the $-Y$ jet shear layer.

A cycle analysis is now performed focusing on the behavior over a single crossflow acoustic cycle. Figure 8.13 shows the cycle that will be examined. The start of this

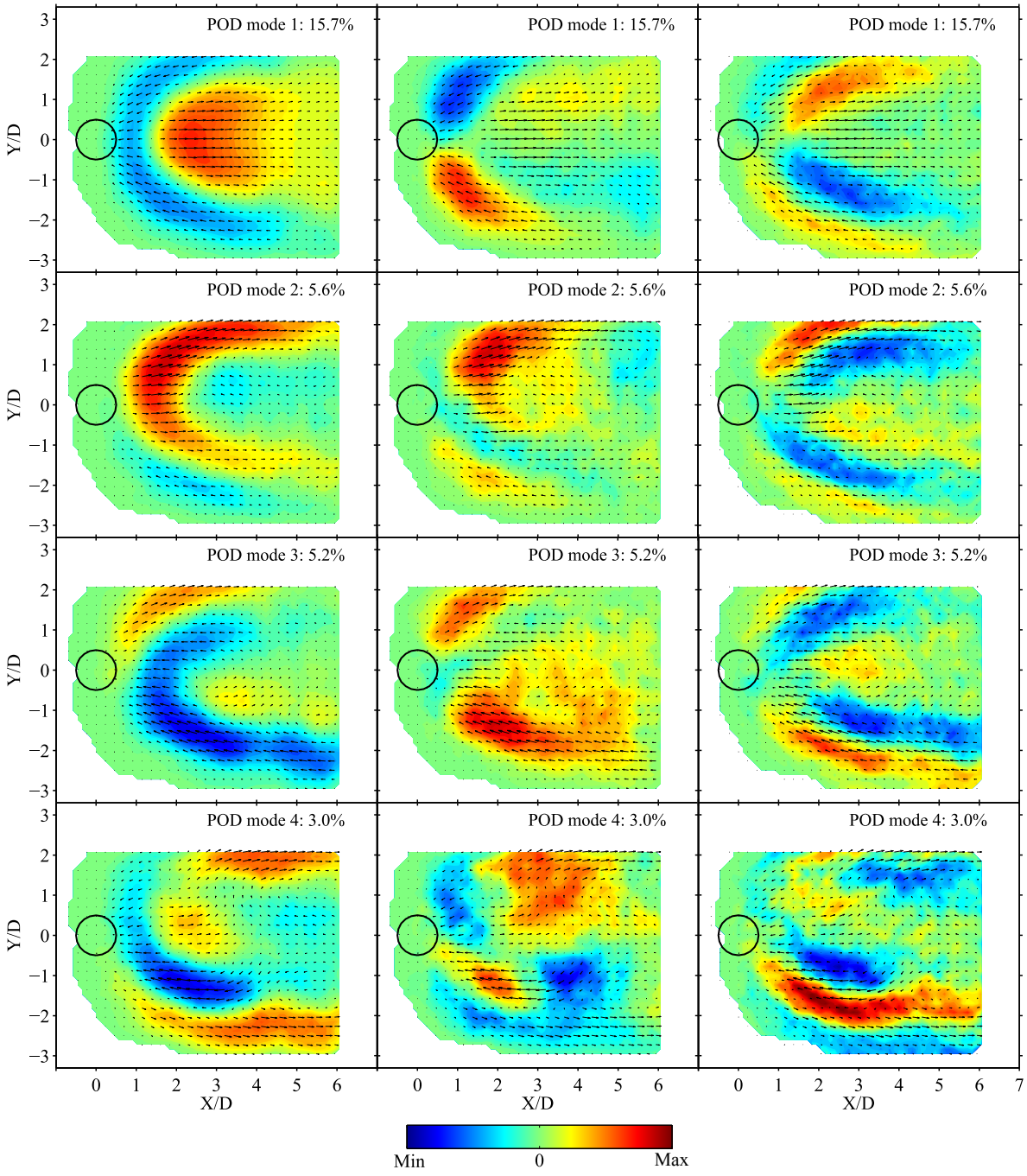

Figure 8.8.. Normalized spatial POD modes 1-4 for case 5 showing u_x (left), u_y (middle) and ω_z (right).

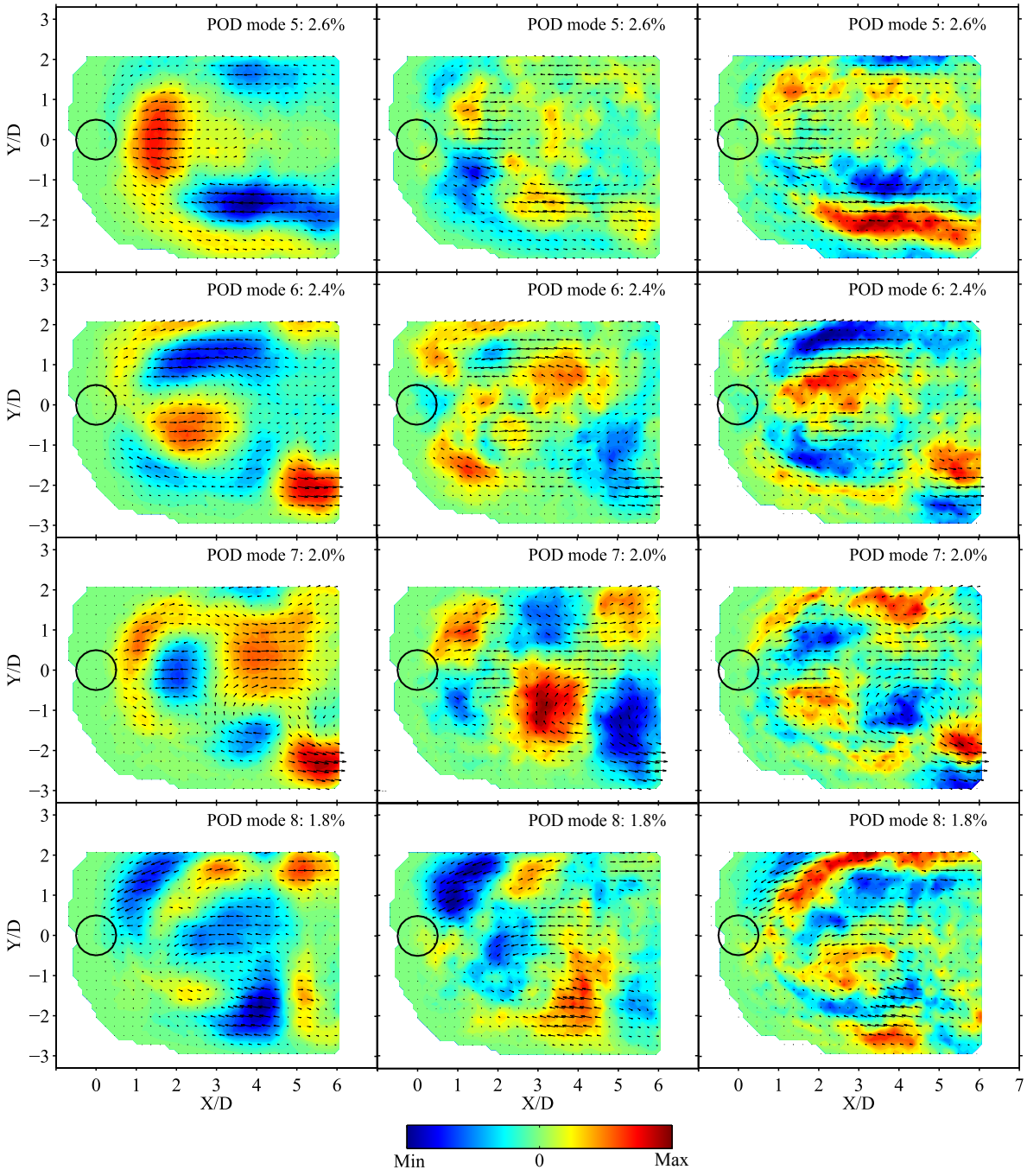

Figure 8.9.. Normalized spatial POD modes 5-8 for case 5 showing u_x (left), u_y (middle) and ω_z (right).

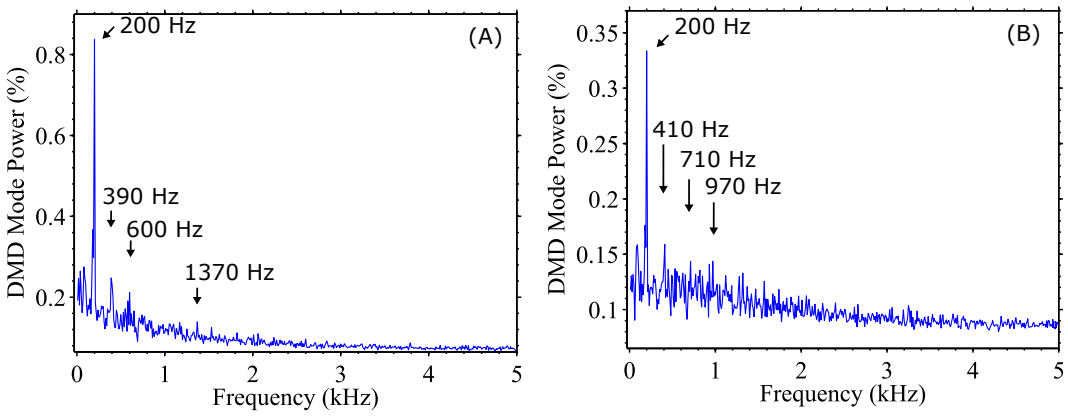

Figure 8.10.. DMD spectra for (A) u_x and (B) u_y. Note that the scales are different.

cycle corresponds to the time 77 ms in Figure 8.1 and was chosen since it displayed low amplitude acoustics at P5 and P10 with a clean crossflow $2L$. The cycle starts with high pressure p' at the combustor chamber exit. This corresponds to approximately the defined phase 0^o in Figures 3.7 and 7.6. Specific points have been marked in the cycle. These were carefully chosen to highlight the unsteady jet behavior. Note that the waveform in Figure 8.13 has a period near 5 ms, the period of the crossflow $2L$. Figures 8.14 and 8.15 shows a series of instantaneous measurements for the time points in Figure 8.13. Shown are the corrected OH-PLIF and instantaneous u_x, u_y, and ω_z. At this plane, strong jet flapping is apparent from the raw measurements where only portions of the FOV contain jet seed available for vector generation or flame front. With an unseeded crossflow, the available spatial data is limited for certain periods of the cycle.

Starting at time 1, the cycle has just begun and the pressure at the chamber exit is just beginning to decrease from its maximum value. The relatively large OH gradients demarcating the reaction front extend upstream to the projected jet orifice, and the lateral reaction fronts are very near to mean OH curve in Figure 8.6. At this instant, the velocity is near its mean value since the crossflow acoustic energy is momentarily stored in the compression. The velocity wake region is small in width,

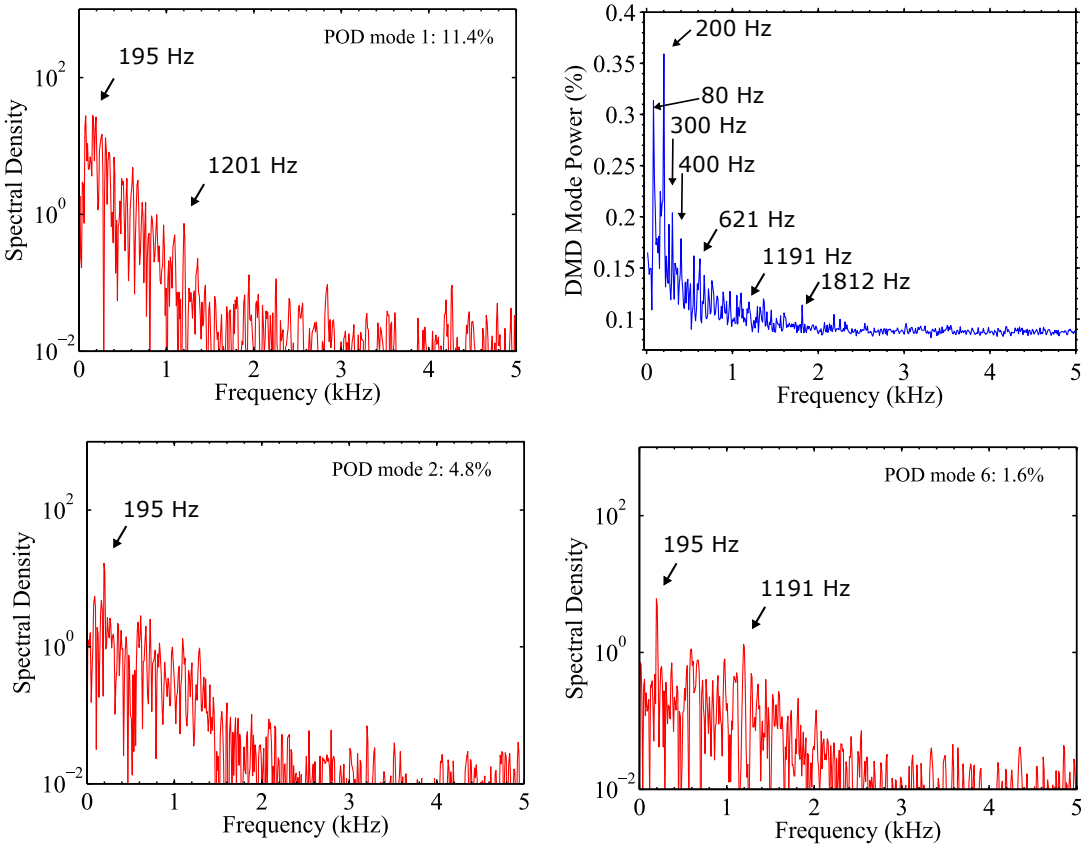

Figure 8.11.. Spectra from a POD and DMD performed on case 5 OH-PLIF. POD modes 1, 2 and 6 are shown. The DMD spectra is at top right.

but is elongated to the end of the FOV at X/D=6. A low velocity wake with this length and width was not observed at Z/D=1. Also note u_y and ω_z. Near $X/D = 2$, the velocity field is strongly curling in the $-Y$ direction and immediately preceding this the velocity is curling upward in $+Y$. A POD reconstruction using modes 4-8 identifies two vortices present at time 1. A counter-clockwise vortex centered at $(X/D, Y/D) = (3, -1)$ and a clockwise vortex centered at $(X/D, Y/D) = (2.25, 1)$. This is observable in the instantaneous ω_z field, but challenging due to a mean base flow.

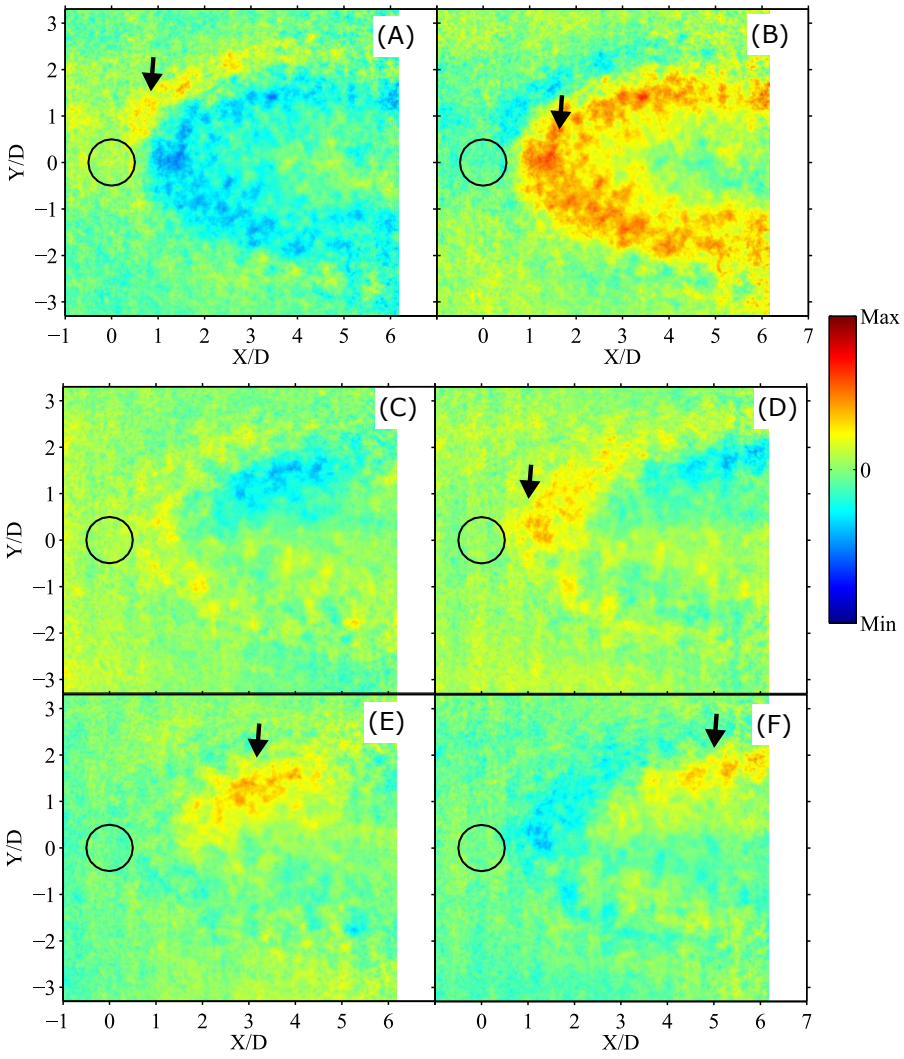

Figure 8.12.. DMD of case 5 OH-PLIF. Top row is the DMD 200 Hz mode. The time separation between (A) and (B) is 2.6 ms ($\approx 1/2$ of the 200 Hz period). Middle and bottom row is a sequence for 620 Hz. Relative to the time at (C), the time at (D), (E), and (F) is 0.3 ms, 0.7 ms, and 1.1 ms, respectively.

As the cycle progresses to time 2, the compression at the chamber nozzle is gone and the crossflow acoustic pertubation causes the actual crossflow velocity to decrease near its minimum cycle value and driving jet penetration up. The OH-PLIF shows a widening in Y/D of the mostly unburned jet fluid (dark OH signal) pushing the lateral

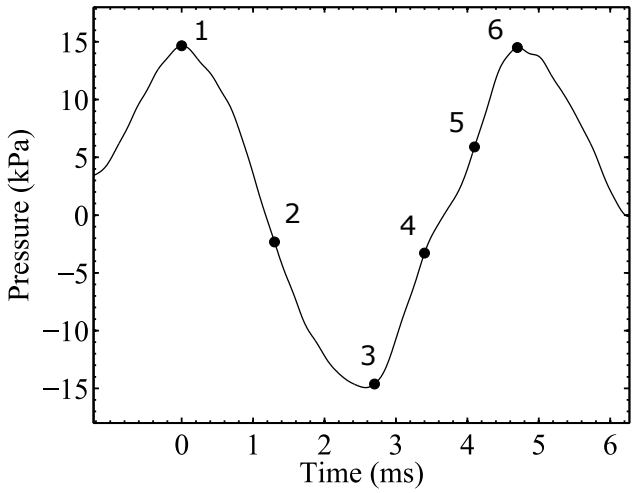

Figure 8.13.. Unsteady pressure plot for case 5 with six points highlighted. Pressure bandpass-filtered between 20 Hz and 2000 Hz. Pressure shown is from P1.

reaction fronts out as well. Accordingly, jet seeding occurs further out in Y/D, and thus vectors are observed over a larger portion of the PIV FOV. The higher velocity upstream shear layer expands outward and the low velocity wake region grows in size. This suggests that the jet penetration is increased relative to time 1. The jet at Z/D=2.7 has volumetrically expanded due to entertainment and combustion lowering its initially high injected density. Also note the relative insensitivity of the upstream reaction front between time 1 and 2. It appears the jet plume dynamics are more sensitive to a crossflow deceleration than the upstream jet edge, which is closer to the jet core and should still contain a higher momentum. Also note u_y and ω_z. The jet wake is now at its cycle maximum in size and the y-velocity and vorticity suggests rotating structures. A POD reconstruction using modes 4-8 identifies two vortices present at time 2. A clockwise vortex centered at $(X/D, Y/D) = (3, -1)$ and a counter-clockwise vortex centered at $(X/D, Y/D) = (2.25, 1)$. While this isn't too unexpected considering the same POD modes were used in a reconstruction as in time 1, the structures phases coinciding between time 1 and 2 suggest these are large scale three dimensional jet interior dynamics being measured in two dimensions.

At time 3, the chamber exit is now moving away from a rarefaction (pressure minimum) and the chamber dump plane is moving away from a compression. At this time, the crossflow is beginning to accelerate and increase in speed. The leading reaction front is now further dowmstream at X/D 1.5 and the jet plume width is inbetween time 1 and time 2. This is the first observation of a significant displacement in the leading edge reaction front (it was not observed at plane Z/D=1 for either case 3 or case 4). The jet velocity shifts downstream accordingly and strengthens. A low velocity wake region like at time 1 and time 2 no longer exists. Directly behind the leading edge of the flame front curve, a POD reconstruction shows two weak and small counter rotating vortex structures at $(X/D, Y/D) = (2, \pm 1)$. These are considerably weaker than at times 1 or 2.

At time 4, the crossflow cycle velocity is near a maximum. The leading edge reaction front is further downstream indicating decrease jet penetration. The reaction front discontinuities in the darker OH jet fluid region signify structures from out of plane piercing through the $Z/D = 2.7$ plane. The high velocity region in a kidney shape at time 4 has contracted toward the $Y/D = 0$ centerline. Since there are no structures upstream of X/D 1.5 in the OH-PLIF field or vectors generated either, it appears the $Z/D = 2.7$ plane is now skirting portions of the windward bottom edges of the jet, where the jet wake region on the leeward topside of the jet is located closer to the injection wall. A POD reconstruction of modes 4-8 do not show in-plane vortical structures at time 4. At time 5, the chamber exit pressure is beginning to increase again, but is low enough that the crossflow velocity is still high relative to the mean. Very little reaction front is found in this plane. Smaller discontinuous structures suggest the bulk of the jet is still at a plane closer to the injection wall. The velocity is still high locally in the reaction front locations. The higher jet velocity has now fully contracted and is predominantly in the X direction (note the direction of the vector arrows). At time 6, the cycle is near complete with the chamber exit pressure moving back to its largest value. The reaction front has moved back toward the jet orifice and the jet shear layer is re stabilizing back to its value at time 1. A POD

reconstruction using modes 4-8 identifies two vortices present at time 6. A clockwise vortex centered at $(X/D, Y/D) = (3.5, -1.5)$ and a counter-clockwise vortex centered at $(X/D, Y/D) = (4, 1.5)$. As the cycle finishes, the flowfield relaxes back to a state similar to time 1 with a leading edge reaction front at the projected jet orifice and a velocity field with a thin shear layer surrounding a narrow and long low velocity wake.

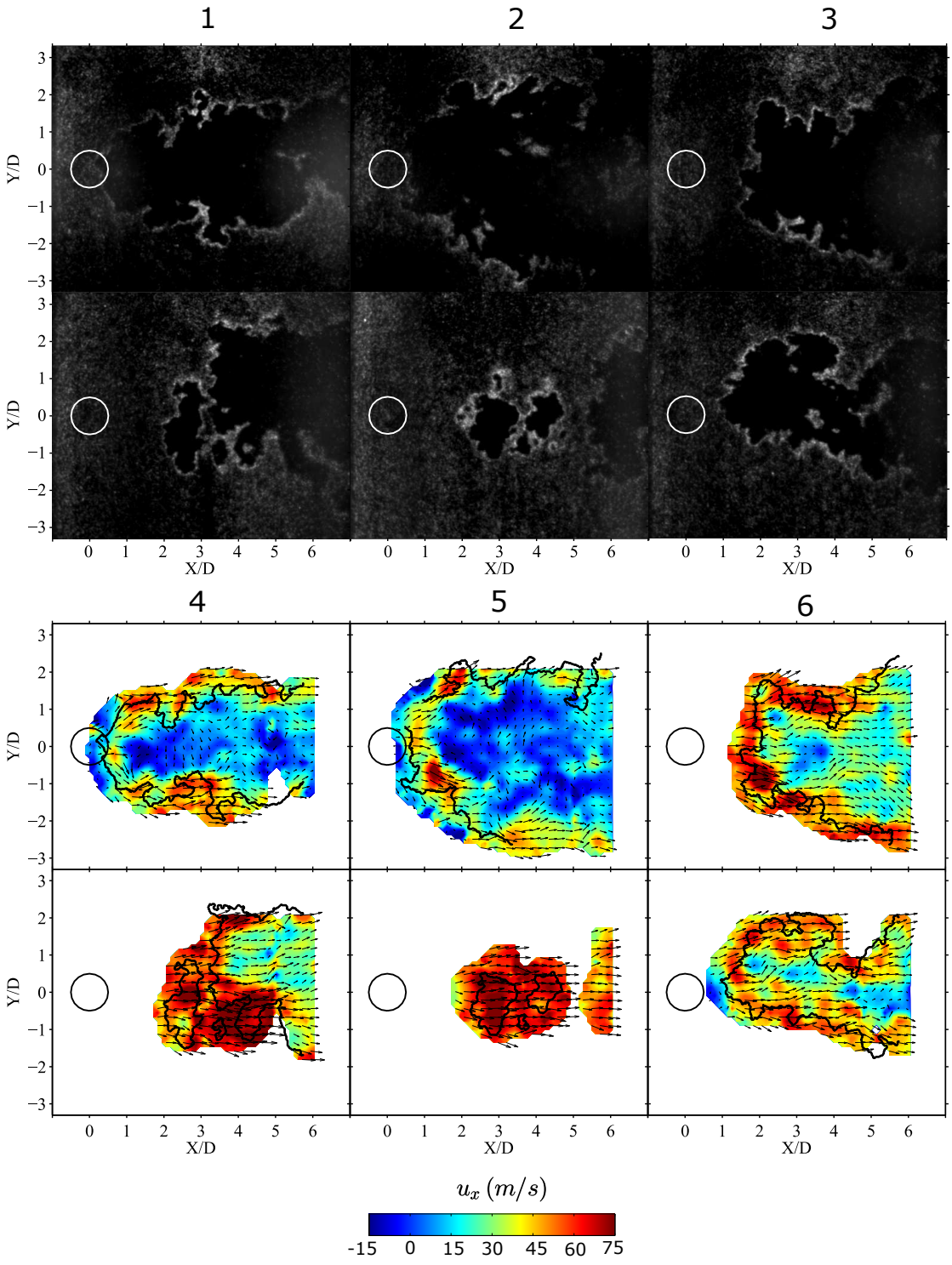

Figure 8.14.. Cycle snapshots for case 5 at $Z/D = 2.7$. Top rows are corrected OH-PLIF. Bottom rows are the instantaneous velocity fields with u_x false colored background. The black curve overlaid on the velocity field is the corresponding OH-PLIF calculated flame front curve.

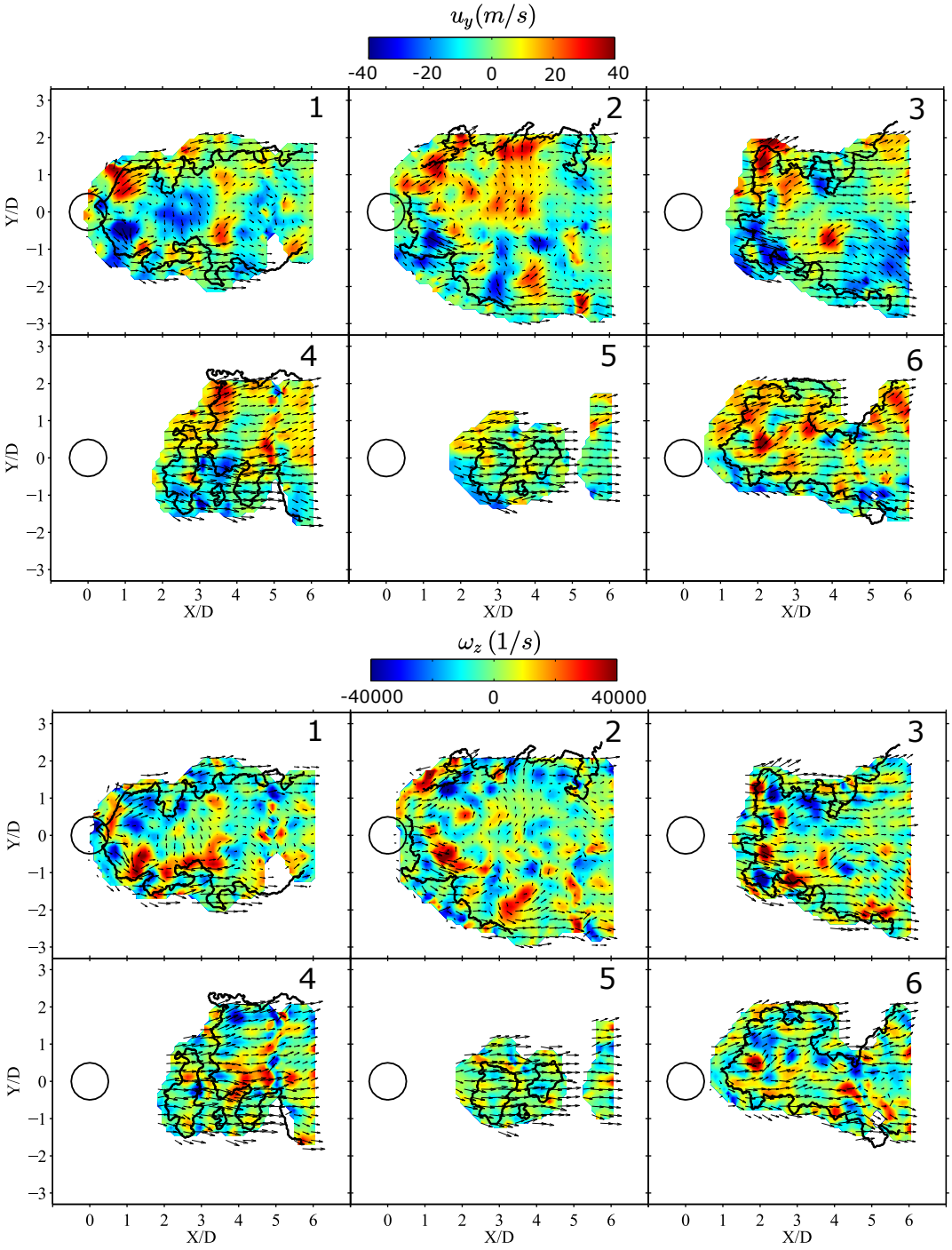

Figure 8.15.. Cycle snapshots for case 5 at $Z/D = 2.7$. The top two rows are the instantaneous velocity fields with u_y false colored background. The bottom two rows are the instantaneous velocity fields with ω_z false colored background. The black curve overlaid on the velocity field is the corresponding OH-PLIF calculated flame front curve.

9. Summary

To characterize the coupling of a jet in unsteady crossflow, the effects of an unsteady pressure flowfield and an unsteady velocity flowfield are separately investigated. A resonant combustion chamber is used to create an acoustic standing wave that is superimposed on a mean flow. This is the unsteady crossflow. The location of jet injection corresponds to one of two locations, where one location is the pressure node and the other location the pressure anti-node of the resonant chamber acoustic mode. The injection location is optically accessible, and the dynamic interactions between the transverse jet flow and the 1st and 2nd axial combustor modes are measured using 10 kHz OH PLIF and 2D PIV.

The design and operation of the experimental rig for generating an unsteady vitiated crossflow at elevated operating conditions was described. The choice of dominant resonant crossflow acoustics is driven by the dump combustor length and operating conditions. A polynomial contoured jet injector was chosen with a preheated H_2/N_2 jet mixture. The injector dimensions and mixture gas temperature were carefully chosen to strategically avoid overlap of the natural injector resonances with either the dominant chamber crossflow acoustics or the jet hydrodynamics.

This thesis presented results for jet injection near the pressure node of the 1st axial combustor mode. This is 1.11 m downstream of the combustor dump plane. At this injection location, the dominant crossflow unsteadiness is a time varying crossflow velocity about the mean. Five test cases were presented: two non-reacting jet cases and three reacting jet cases.

For a non-reacting H_2/N_2 jet in a heated air crossflow, the interrogation planes analyzed were at a distance of Z/D=1.0 and 2.7 from the jet injection wall. For the non-reacting operating conditions, the resultant jet-to-crossflow momentum flux ratio is 19. The resonant crossflow chamber acoustics are not excited, however the

crossflow still contains low amplitude and multi-spectral unsteadiness within 0.5 kPa. The time average velocity for planes $Z/D = 1$ and 2.7 displays characteristic JICF features for this cross sectional plane. These include a high velocity jet shear layer and a low velocity jet wake. The time average velocity structures grow in size further away from the jet injection wall consistent with a jet bending into the crossflow and crossflow fluid entrainment.

The dynamics of the non-reacting transverse jet were extracted by performing a proper orthogonal decomposition and dynamic mode decomposition on the velocity field. At the plane $Z/D = 1$, the dominant dynamics were identified as unsteady wake structures directly behind the jet orifice with wake Strouhal numbers (based on the mean crossflow velocity) corresponding to well reported non-reacting JICF wake Strouhal numbers. At the plane $Z/D = 2.7$, two ranges of frequencies were identified. The first range is a band between 40 Hz and 250 Hz that is mostly concentrated in the jet shear layer. The second range centered around 400 Hz - 480 Hz is mostly concentrated in the lower velocity jet wake region. The POD and DMD modal decomposition at both cross sectional planes shows organized and strong wake dynamics manifested as vortex structure initiation, growth, convection and dissipation.

For a reacting H_2/N_2 jet in a unsteady vitiated crossflow, the interrogation planes analyzed were at a distance of Z/D=1.0 and 2.7 from the jet injection wall. For the reacting operating conditions, the resultant jet-to-crossflow momentum flux ratio is 6. At the plane $Z/D = 1$, two reacting cases were compared with the same crossflow and jet operating conditions. The first contained low amplitude and multi-spectral crossflow unsteadiness below 5 kPa. The second contained coherent fluctuating crossflow pressure amplitudes up to 15 kPa at the 1st axial combustor mode. At the plane Z/D=2.7, one reacting case was analyzed with a crossflow fluctuating pressure amplitude up to 14 kPa at the 1st axial combustor mode.

At the plane $Z/D = 1$, the low and high amplitude crossflow cases showed similar time average velocity and OH-PLIF structures. A phase average of the high amplitude crossflow case showed a jet shear layer locked into the crossflow velocity

oscillations: the jet shear layer velocity increased with an increase in crossflow velocity, and decreased with a decrease in crossflow velocity. Similarly, the extracted OH-PLIF reaction front is observed to lengthen with an increase in crossflow velocity and decrease with a decreasing crossflow velocity, but with a small phase delay relative to the jet shear layer velocity pulsations.

A POD and DMD on the velocity and OH-PLIF fields shows that the dominant velocity and OH-PLIF oscillations occur at the dominant unsteady crossflow frequency for the large amplitude unsteady crossflow case. When the unsteady crossflow amplitude is decreased at the plane $Z/D = 1$, there is an increase in the spectral sharpness and strength for frequencies around 1 kHz to 1.3 kHz. This frequency range corresponds to JICF wake dynamic Strouhal numbers (based on the mean crossflow velocity) reported under non-reacting and reacting conditions. The dominance of the velocity wake frequencies in all of the reacting test cases is not as great, however, as for the non-reacting jet cases considered.

10. Conclusions

Conclusions are made based on the experience of designing and operating the unsteady experimental apparatus for transverse jet injection studies. Also, based on the five test cases analyzed, conclusions are made for jet injection at the pressure node of the 1st axial combustor mode.

1. A resonant combustion chamber is a robust approach to characterize the coupling of a jet in an unsteady crossflow at elevated operating conditions. A range of crossflow unsteady amplitudes can be generated at the 1st and 2nd axial combustor modes. These frequencies can be changed by discretely varying the combustor length. By varying the dump combustor operating conditions, the effects of an unsteady pressure flowfield and an unsteady velocity flowfield can be separately investigated.

2. Two dimensional laser diagnostic measurements on a reacting unsteady jet provides relevant, but restrictive information on the jet-crossflow coupling. By focusing on the XY cross section which bisects the jet core and wake, information is lost regarding the out-of-plane three dimensionality of the jet flame, which is ostensibly flapping out-of-plane at the unsteady crossflow frequency. At a minimum, the highly three dimensional jet flame should be probed with 3D diagnostics such as stereo or tomographic PIV and PLIF, or line-of-sight integrated chemiluminescence imaging.

3. For the non-reacting jet cases, the time average velocity field is highly symmetric along the Y/D=0 centerline. Also, the low velocity jet wake dynamics show distinct and strong spectral peaks for frequencies corresponding to Strouhal numbers consistent with unsteady JICF wake dynamics reported in literature.

4. At a distance of 1 and 2.7 jet diameters from the jet injection wall, the amplitude of the crossflow unsteadiness has a clear influence on the jet velocity and OH-PLIF dynamics. For the larger amplitude unsteady crossflow case at Z/D=1 and unsteady case at Z/D=2.7, the jet velocity and reaction front lock into the crossflow acoustic frequency. The jet shear layer is in phase with the crossflow velocity. The reaction front near to the Y/D=0 centerline shows a small phase shift with the crossflow velocity.

5. The amplitude of crossflow unsteadiness appears to play a role in the sharpness of the wake dynamics as determined by a POD and DMD on the velocity and OH-PLIF fields. For the non-reacting cases, the wake dynamics are strong and dominant spectral features in the flowfield. For the reacting cases, the larger unsteady crossflow amplitude appears to suppress the spectral sharpness in the frequency range corresponding to wake Strouhal numbers.

6. The leading edge reaction front at $Z/D = 1$ is consistently anchored directly above the jet orifice despite the elevated magnitude of crossflow velocity oscillations. The leading edge front is displaced no more than $0.25D_j$ in the axial direction under large crossflow velocity oscillations at the 1st combustor axial mode. At the plane $Z/D = 2.7$, the leading edge front is highly variable and is displaced as much as $2D_j$ axially downstream for positive velocity oscillations. The displacement at both cross sectional planes is interpreted in the context of a time-varying jet penetration. Since the jet is located at approximately a pressure node of the 1st axial combustor mode, the time varying crossflow velocity drives a time varying jet-to-cross momentum flux ratio. This results in decreased jet penetration as the crossflow velocity increases (and the upstream flame front moves downstream) and increased jet penetration as the crossflow velocity decreases (and the upstream flame front moves upstream).

11. Recommendations

Recommendations are made based on the experience of obtaining, processing and analyzing the velocity and OH-PLIF measurements.

1. Seed both the crossflow and jet fluid with the Titanium Dioxide particles for the PIV diagnostic. Seeding only the jet as was done in this thesis offers a limited view of the flowfield since vector generation can only occur in areas with good seeding density. Seeding both fluid streams will decrease velocity calculation uncertainty and permit visualization of the crossflow velocity flowfield surrounding the jet.

2. Determine the degree of flapping in the Z direction to better interpret the XY cross-sectional plane dynamics. For jet injection at a pressure node, the jet is ostensibly flapping in the Z direction at the unsteady crossflow frequency. In the XY two-dimensional plane, this maps to a lengthening and contraction of the reaction front and low velocity wake region. Performing stereo PIV would at least give the out-of-plane z-velocity component. Similarly, investigate the jet trajectory cross sections XZ by performing PIV and OH-PLIF. Alternately, perform chemiluminescence imaging of the XZ cross section simultaneously with OH-PLIF of the XY cross section to aid in interpreting to three dimensionality of the jet flame.

3. Perform non-reacting jet and heated air crossflow test cases for J=6. These would provide a more robust baseline dataset with which to compare the reacting J=6 analyzed test cases as compared to the J=19 analyzed non-reacting jet.

LIST OF REFERENCES

LIST OF REFERENCES

[1] T.C. Lieuwen and V. Yang. *Combustion Instabilities in Gas Turbine Engines: Operational Experience, Fundamental Mechanisms, and Modeling*. AIAA, 2005.

[2] T. Lieuwen, M. Chang, and A. Amato. Stationary gas turbine combustion: Technology needs and policy considerations. *Combustion and Flame*, 160(8):1311–1314, 2013.

[3] Thierry Poinsot and Denis Veynante. *Theoretical and Numerical Combustion*. Third edition.

[4] A.R. Karagozian. Transverse jets and their control. *Progress in Energy and Combustion Science*, 36(5):531–553, 2010.

[5] S. Hayashi and Hideshi Yamada. Nox emissions in combustion of lean premixed mixtures injected into hot burned gas. *Proceedings of the Combustion Institute*, 28(2):2443–2449, 2000.

[6] W.G. Lamont, M. Roa, S.E. Meyer, and R.P. Lucht. Emission measurements and ch* chemiluminescence of a staged combustion rig for stationary gas turbine applications. *Journal of Gas Turbine and Engineering*, 134(8), 2012.

[7] F. Nicoud and T. Poinsot. Thermoacoustic instabilities: Should the rayleigh criterion be extended to include entropy changes? *Combustion and Flame*, 142(1):153–159, 2005.

[8] Jared M. Pent. *Combustion Instability Mechanism of a Reacting Jet in Cross Flow at Gas Turbine Operating Conditions*. PhD thesis, University of Central Florida, 2014.

[9] S.R. Shapiri, J.M. King, M'Closkey R.T., and A.R. Karagozian. Optimization of controlled jets in crossflow. *AIAA Journal*, 44(6):1292–1298, 2006.

[10] S. Megerian, J. Davitian, L.S.DE B. Alves, and A.R. Karagozian. Transverse-jet shear-layer instabilities. part 1. experimental studies. *Journal of Fluid Mechanics*, 593:93–129, 2007.

[11] M.P. Juniper, L.K.B. Li, and J.W. Nichols. Forcing of self-excited round jet diffusion flames. *Proceedings of the Combustion Institute*, 32:1191–1198, 2009.

[12] J.D. Holdeman and R.E. Walker. Mixing of a row of jets with a confined crossflow. *AIAA*, 15(2):243–249, 1977.

[13] T.F. Fric and A. Roshko. Vortical structures in the wake of a transverse jet. *Journal of Fluid Mechanics*, 271:1–47, 1994.

[14] R. Kelso and A. Smits. Horseshoe vortex systems resulting from the interaction between a laminar boundary layer and a transverse jet. *Physics of Fluids*, 7(1):153–158, 1995.

[15] S. Muppidi and K. Mahesh. Direct numerical simulation of passive scalar transport in transverse jets. *Journal of Fluid Mechanics*, 598:335–360, 2008.

[16] S. Muppidi and K. Mahesh. Two-dimensional model problem to explain counter-rotating vortex pair formation in a transverse jet. *Physics of Fluids*, 18(8), 2006.

[17] L. Cortelezzi and A.R. Karagozian. On the formation of the counter-rotating vortex pair in transverse jets. *Journal of Fluid Mechanics*, 446:347–373, 2001.

[18] S.H. Smith and M.G. Mungal. Mixing, structure and scaling of the jet in crossflow. *Journal of Fluid Mechanics*, 357:83–122, 1998.

[19] P.P. Panda, M. Roa, P. Szedlacsek, W.R. Laster, and R.P. Lucht. Structure and dynamics of the wake of a reacting jet injected into a swirling, vitiated crossflow in a staged combustion system. *Experiments in Fluids*, 56(21):1–20, 2015.

[20] S. Narayanan, P. Barooah, and J.N. Cohen. Dynamics and control of an isolated jet in crossflow. *AIAA*, 41(12):2316–2330, 2003.

[21] K.C. Marr, N.T. Clemens, and O.A. Ezekoye. Mixing characteristics and emissions of strongly-forced and non-premixed and partially-premixed jet flames in crossflow. *Combustion and Flame*, 159(2):707–721, 2013.

[22] G. Bidan and D.E. Nikitopoulos. On steady and pulsed low-blowing-ratio transverse jets. *Journal of Fluid Mechanics*, 714:393–433, 2013.

[23] N. Raud, Y. Bury, R. Bazile, J. Boree, and G. Charnay. Experimental study of the behavior of confined variable density jets in a time varying crossflow. *Journal of Fluids Engineering*, 121:65–72, 1999.

[24] L.M. Xia and K.M. Lam. Unsteady effluent dispersion in a round jet interacting with an oscillating cross-flow. *Journal of Hydraulic Engineering*, 130(7):667–677, 2004.

[25] Liwei Zhang. *Flow Dynamics and Scalar Mixing of Transverse Jets into Crossflows*. PhD thesis, The Pennsylvania State University, 2011.

[26] D.D. Kremer, M.T. am Ende, J.G. Mustakis, and D.J. am Ende. A numerical investigation of a jet in oscillating crossflow. *Physics of Fluids*, 19(9), 2007.

[27] R.T. M'closkey and A.R. Karagaozian. The actively controlled jet in crossflow. *Journal of Fluid Mechanics*, 452:325–335, 2002.

[28] R.E. El Behery, A.A. Mohamad, and M.M. Kamal. Combustion enhancement of a gas flare using acoustical excitation. *Combustion Science and Technology*, 177(9):1627–1659, 1992.

[29] P.J. Vermeulen, V. Ramesh, B. Sanders, and J. Odgers. Acoustic control of combustor primary zone air-jet mixing. *Journal of Propulsion and Power*, 11(2):261–267, 1995.

[30] H. Johari. Scaling of fully pulsed jets in crossflow. *AIAA Journal*, 44(11):2719–2725, 2006.

[31] D.R. Getsinger, C. Hendrickson, and A.R. Karagozian. Shear layer instabilities in low-density transverse jets. *Journal of Fluid Mechanics*, 53:783–801, 2012.

[32] P.A. Monkewitz, D.W. Bechert, B. Barsikow, and B. Lehmann. Self-excited oscillations and mixing in a heated round jet. *Journal of Fluid Mechanics*, 213:611–639, 1990.

[33] L.L. Yuan and R.L. Street. Trajectory and entrainment of a round jet in crossflow. *Physics of Fluids*, 10(9):2323–2335, 1998.

[34] K.C. Schadow and E. Gutmark. Coombustion instability related to vortex shedding in dump combustors and their passive control. *Progress in Energy and Combustion Science*, 18(2):117–132, 1992.

[35] A.T. Ganji and R.F. Sawyer. Turbulence, combustion, pollutant, and stability characterization of a premixed, step combustor. Technical Report Contractor Report 3230, NASA, 1980.

[36] Duane A. Smith. *An Experimental Study of Acoustically Excited, Vortex Driven, Combustion Instability Within a Rearward Facing Step Combustor*. PhD thesis, California Institute of Technology, 1985.

[37] A.F. Ghoniem, S. Park, A. Wachsman, A. Annaswamy, D. Wee, and H.M. Altay. Mechanism of combustion dynamics in a backward-facing step stabilized premixed flame. *Proceedings of the Combustion Institute*, 30(2):1783–1790, 2005.

[38] T.J. Poinsot, A.C. Trouve, D.P. Veynante, S.M. Candel, and E.J. Esposito. Vortex-driven acoustically coupled combustion instabilities. *Journal of Fluid Mechanics*, 177:265–292, 1987.

[39] Yen Ching Yu. *Experimental and Analytical Investigations of Longitudinal Combustion Instability in a Continuously Variable Resonance Combustor (CVRC)*. PhD thesis, Purdue University, 2009.

[40] K.H. Yu, A. Trouve, and J.W. Daily. Low-frequency pressure oscillations in a model ramjet combustor. *Journal of Fluid Mechanics*, 232:47–72, 1991.

[41] P.A. Hield, M.J. Brear, and S.H. Jin. Thermoacoustic limit cycles in a premixed laboratory combustor with open and choked exits. *Combustion and Flame*, 156(9), 2009.

[42] F. Boudy, D. Durox, T. Schuller, and S. Candel. Nonlinear mode triggering in a multiple flame combustor. *Proceedings of the Combustion Institute*, 33(1):1121–1128, 2011.

[43] Panhandle Energy. panhandleenergy.com.

[44] Warren G. Lamont. *Experimental Study of a Staged Combustion System for Stationary Gas Turbine Applications*. PhD thesis, Purdue Univeristy, 2012.

[45] M.B. Standing and D.L. Katz. Density of natural gases. *Trans. AIME*, 146(91942):140–149, 1942.

[46] A.M. Elsharkawy, Y.S.K.S. Hashem, and A.A. Alikhan. Compressibility factor for gas condensates. *Energy and Fuels*, 15(4):807–816, 2001.

[47] B Guo and A Ghalambor. *Natural gas engineering handbook*. Gulf Pub. Co, 2005.

[48] P. Dranchuk and H. Abou-Kassem. Calculation of z factors for natural gases using equations of state. *Journal of Canadian Petroleum Technology*, 14(3), 1975.

[49] A. Lyra, B. Wilde, H. Kolla, J.M. Seitzman, T.C. Lieuwen, and J.H. Chen. Structure of hydrogen-rich transverse jets in a vitiated crossflow. *Combustion and Flame*, 162, 2015.

[50] W. Fey, M. Konig, and H. Eckelmann. A new strouhal-reynolds-number relationship for the circular cylinder in the range 47¡re¡105. *Physics of Fluids*, 10(7):1547–1549, 1998.

[51] Lawrence Kinsler, Austin Frey, Alan Coppens, and James Sanders. *Fundamentals of Acoustics*. John Wiley and Sons, New York, 2000.

[52] Mark Hamilton and David Blackstock. *Nonlinear Acoustics*. Academic Press, San Diego, 1990.

[53] V. Yang and W. Anderon. *Liquid Rocket Engine Combustion Instability*. AIAA, 1995.

[54] U. Ingard and H. Ising. Acoustic nonlinearity of an orifice. *The Journal of Acoustical Society of America*, 42(1):6–17, 1967.

[55] B.J. McBride and S. Gordon. Computer program for calculation of complex chemical equilibrium compositions and applications. Technical Report NASA Reference Publication 1311, NASA, 1996.

[56] E.W. Lemmon, M.L. Huber, and M.O. McLinden. *NIST Reference Fluid Thermodynamic and Transport Properties - REFPROP*. U.S. Secretary of Commerce, Boulder, Colorado, 2013.

[57] A.M. Steinberg, I. Boxx, M. Stohr, C.D. Carter, and W. Meier. Flow-flame interactions causing acoustically coupled heat release fluctuatins in a thermoacoustically unstable gas turbine combustor. *Combustion and Flame*, 157(12):2250–2266, 2010.

[58] W. Meier, I. Boxx, M. Stohr, and Carter C.D. Laser-based investigations in gas turbine model combustors. *Experiments in Fluids*, 49:865–882, 2010.

[59] L. Sirovich. Turbulence and the dyanmics of coherent structures part i: Coherent structures. *Quarterly of Applied Mathematics*, XLV(3):561–571, 1987.

[60] K. Meyer, J. Pedersen, and O. Ozcan. A turbulent jet in crossflow analyzed with proper orthogonal decomposition. *Journal of Fluid Mechanics*, 583, 2007.

[61] M.E. Harvazinksi, C. Huang, V. Sankaran, T.W. Feldman, Anderson. W.E., C.L. Merkle, and D.G. Talley. Coupling between hydrodynamics, acoustics, and heat release in a self-excited unstable combustor. *Physics of Fluids*, 27, 2015.

[62] Schmid P.J. Dynamic mode decomposition of numerical and experimental data. *Journal of Fluid Mechanics*, 656:5–28, 2010.

[63] C. Huang, Anderson. W.E., M.E. Harvazinksi, and V. Sankaran. Analysis of self-excited combustion instabilities using decomposition techniques. *51st AIAA Aerospace Sciences Meeting*, 2013.

[64] John D. Anderson. *Modern Compressible Flow.* McGraw Hill, New York, 2003.

APPENDICES

A. Plumbing and Instrumentation Diagram (P&ID)

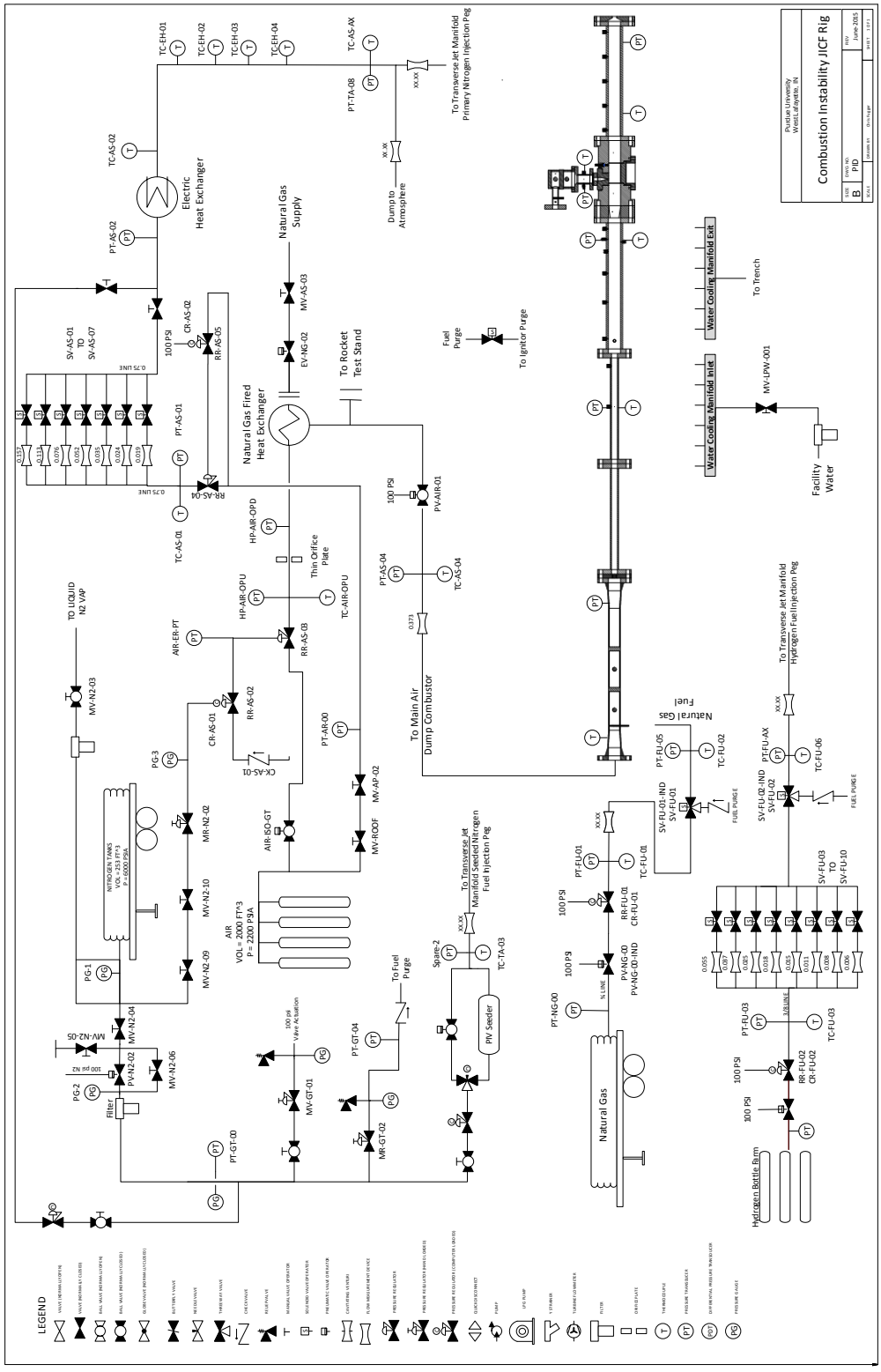

Figure A.1.. Plumbing and instrumentation diagram (P&ID) for the unsteady dump combustor transverse jet injection test rig.

B. Hardware and Setup

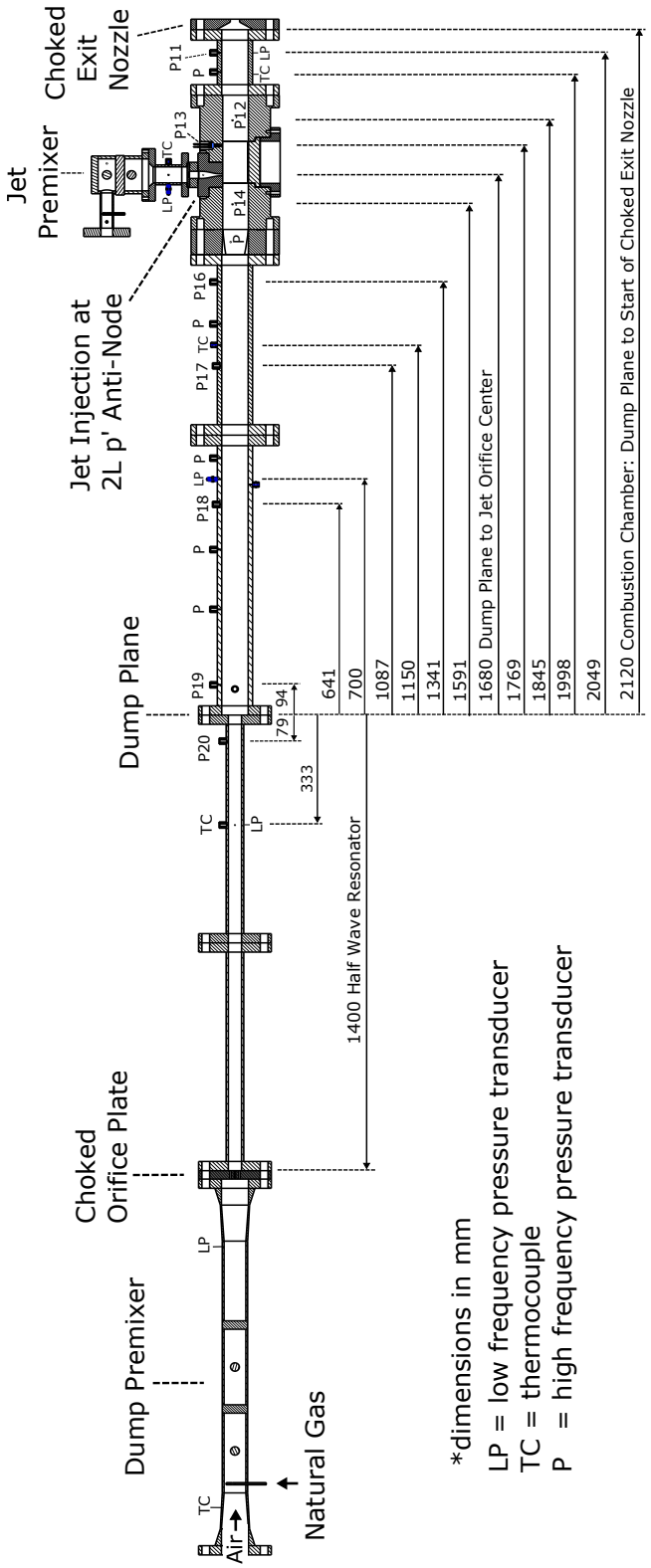

Figure B.1.. Schematic of the unsteady transverse jet test rig with jet injection location 1.68 m downstream of the dump combustor dump plane.

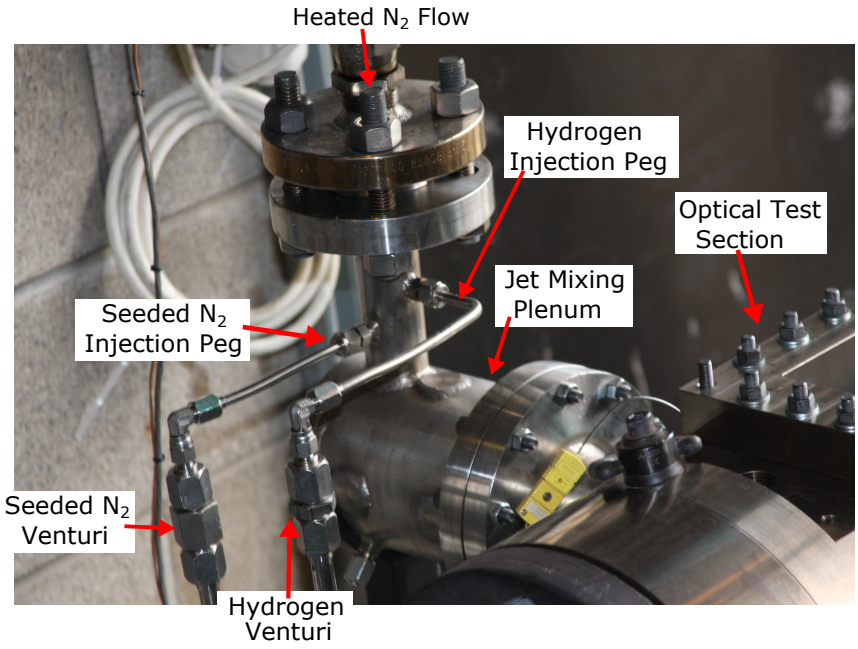

Figure B.2.. Transverse jet manifold hardware mounted on one side of the combustion chamber optical test section. The transverse jet is fed using three separately metered and controlled propellant lines: a heated nitrogen line, a hydrogen line, and a seeded nitrogen line.

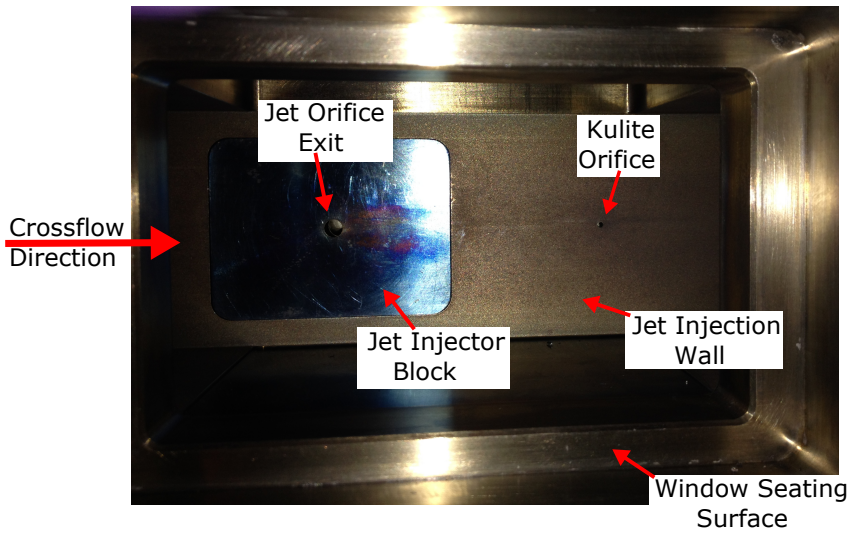

Figure B.3.. View of the transverse jet orifice exit and injection wall taken from the window port opposite of the injector.

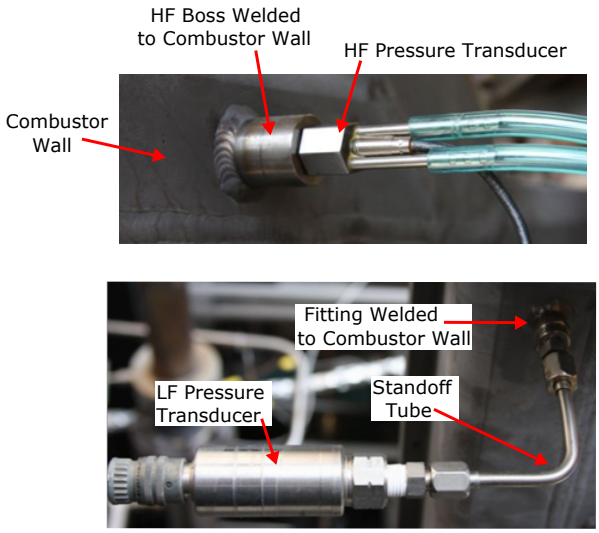

Figure B.4.. Top: High frequency (HF) pressure transducer mounted on the combustor wall. Bottom: Low frequency (LF) pressure transducer mounted on the combustor wall using a 6 mm O.D. standoff tube

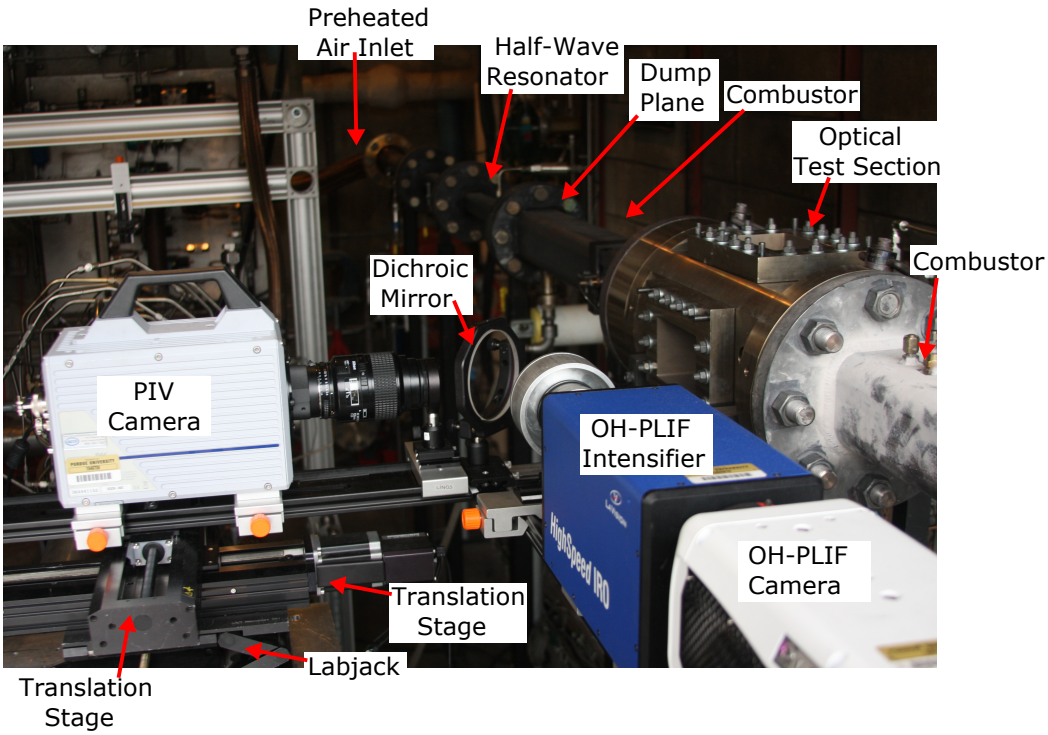

Figure B.5.. View of the dump combustor, optical test section, and imaging systems hardware.

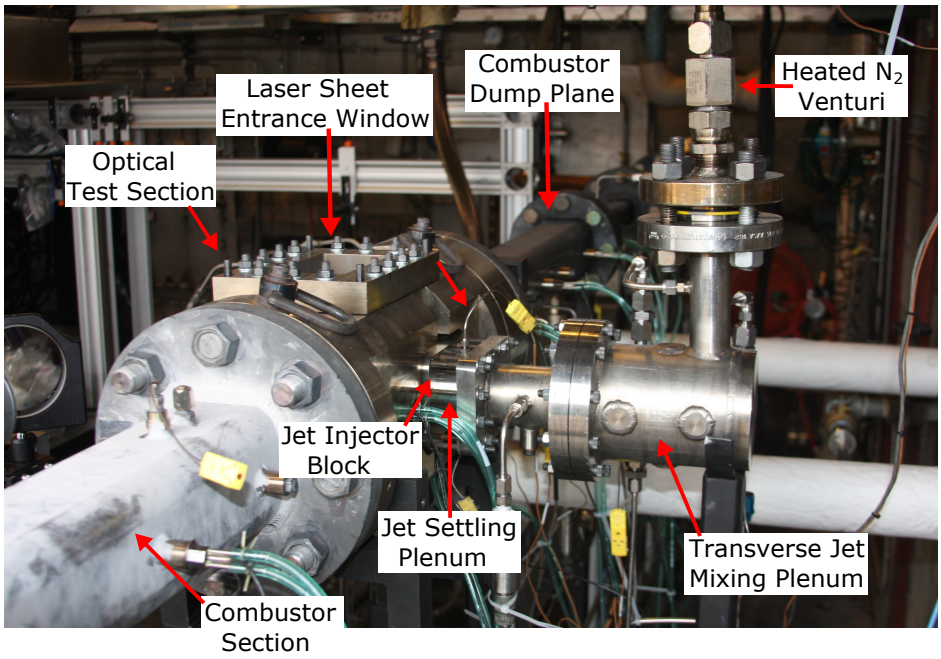

Figure B.6.. View of the dump combustor, optical test section, and the transverse jet injection assembly hardware.

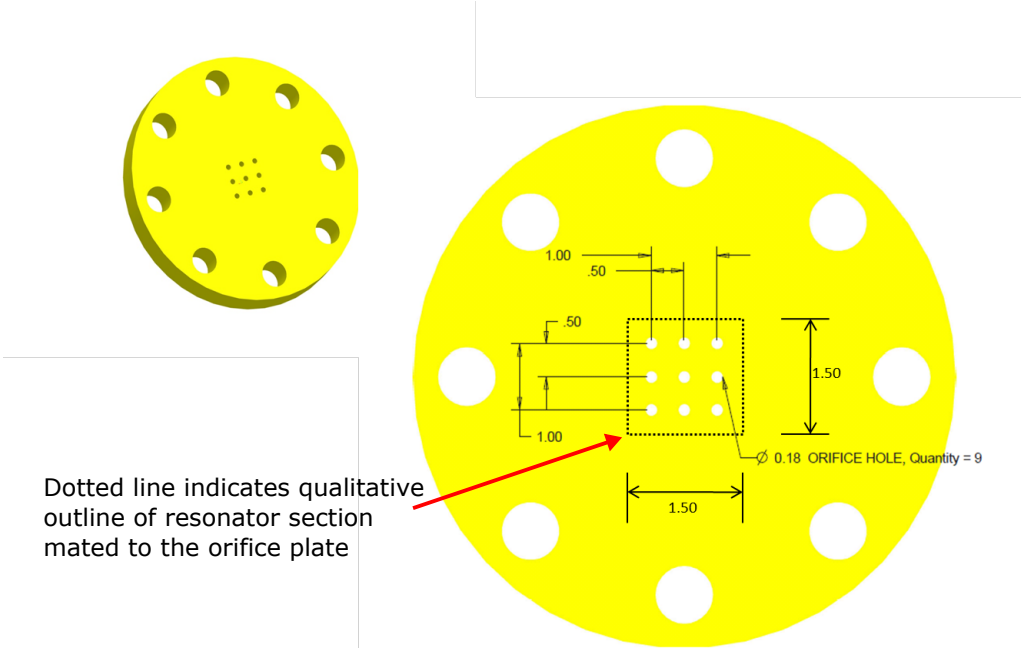

Figure B.7.. Dump combustor choked orifice plate located between the premixed air-natural gas premixer and the half-wave inlet resonator.

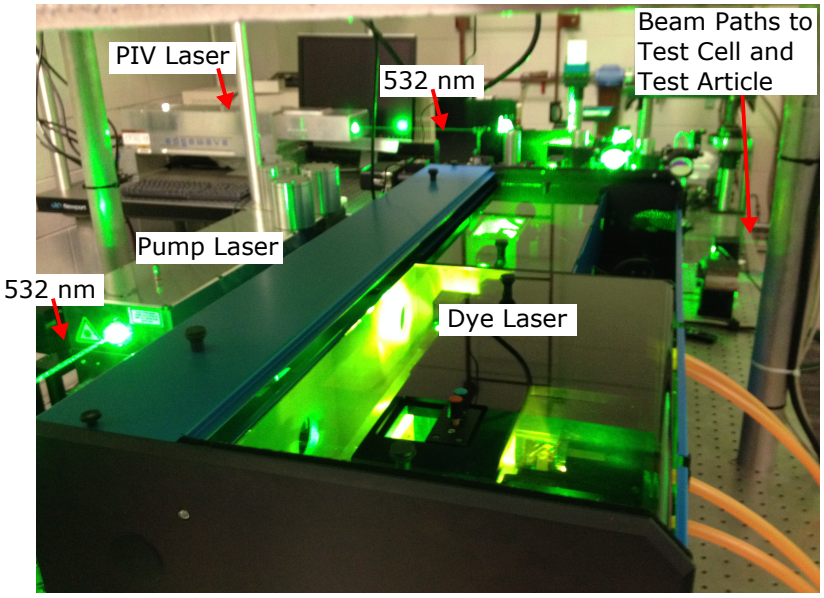

Figure B.8.. View of the laser lab located directly behind the test cell. All lasers are in operation. The dual-head PIV laser is shown in the back. The pump laser and the dye laser for OH-PLIF is shown in the foreground.

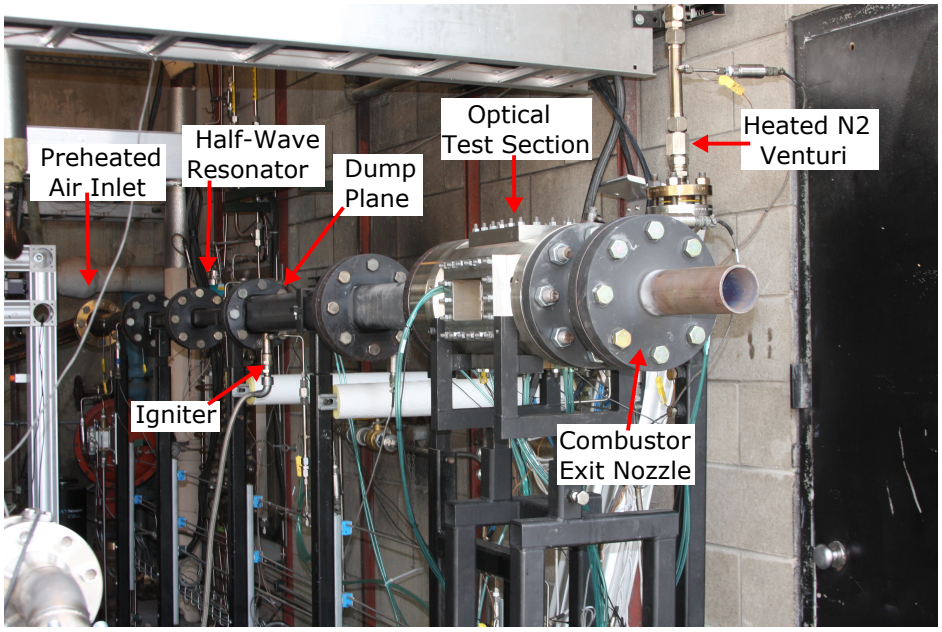

Figure B.9.. View of the dump combustor and optical test section hardware for transverse jet injection near the pressure anti-node of the 1st axial combustor mode. Note that the optical rail structure surrounding the optical section has not yet been assembled.

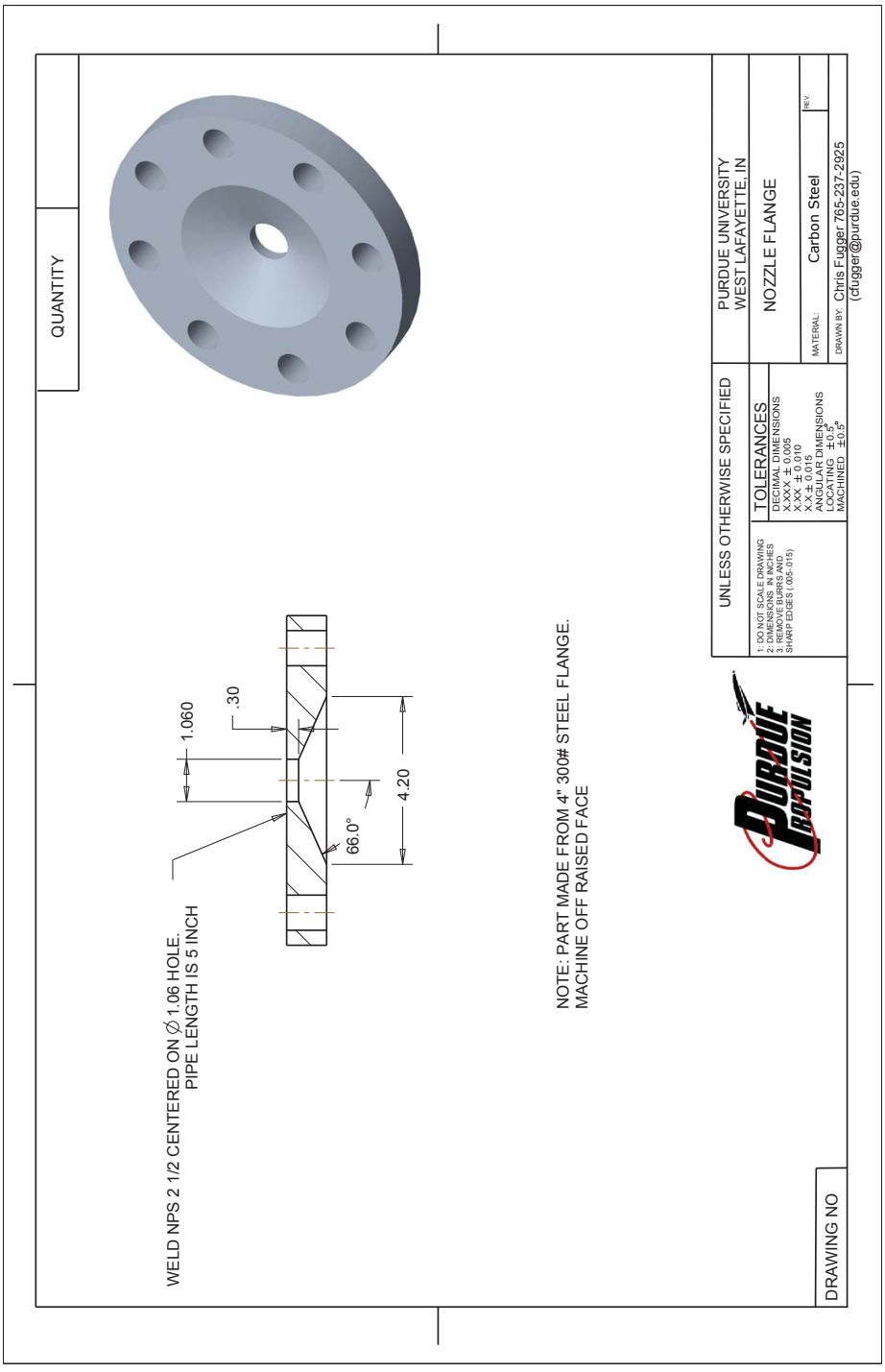

Figure B.10.. Machine drawing of the dump combustor exit nozzle.

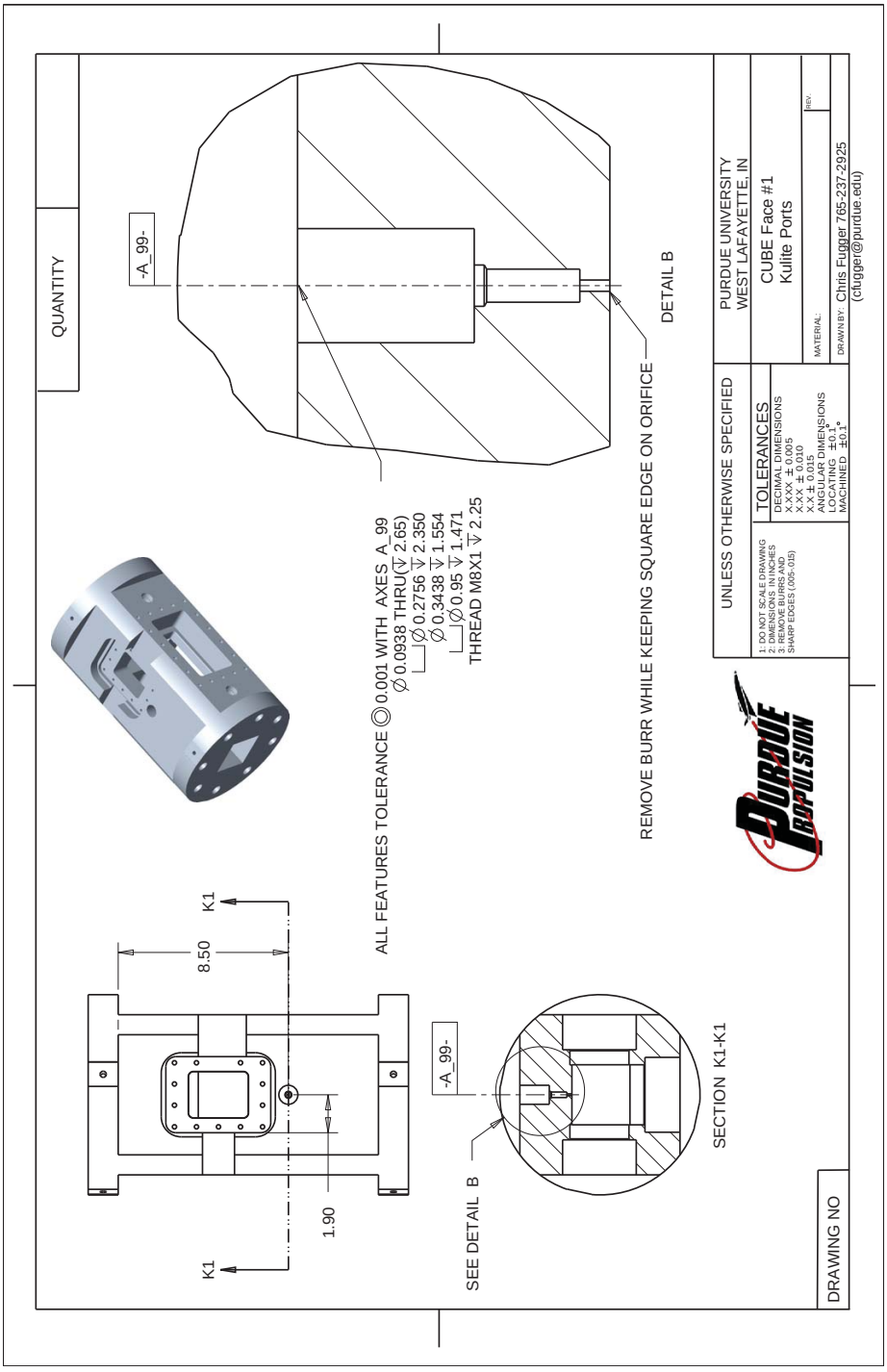

Figure B.11.. Machine drawing of the high frequency pressure transducer port on the combustor optical test section.

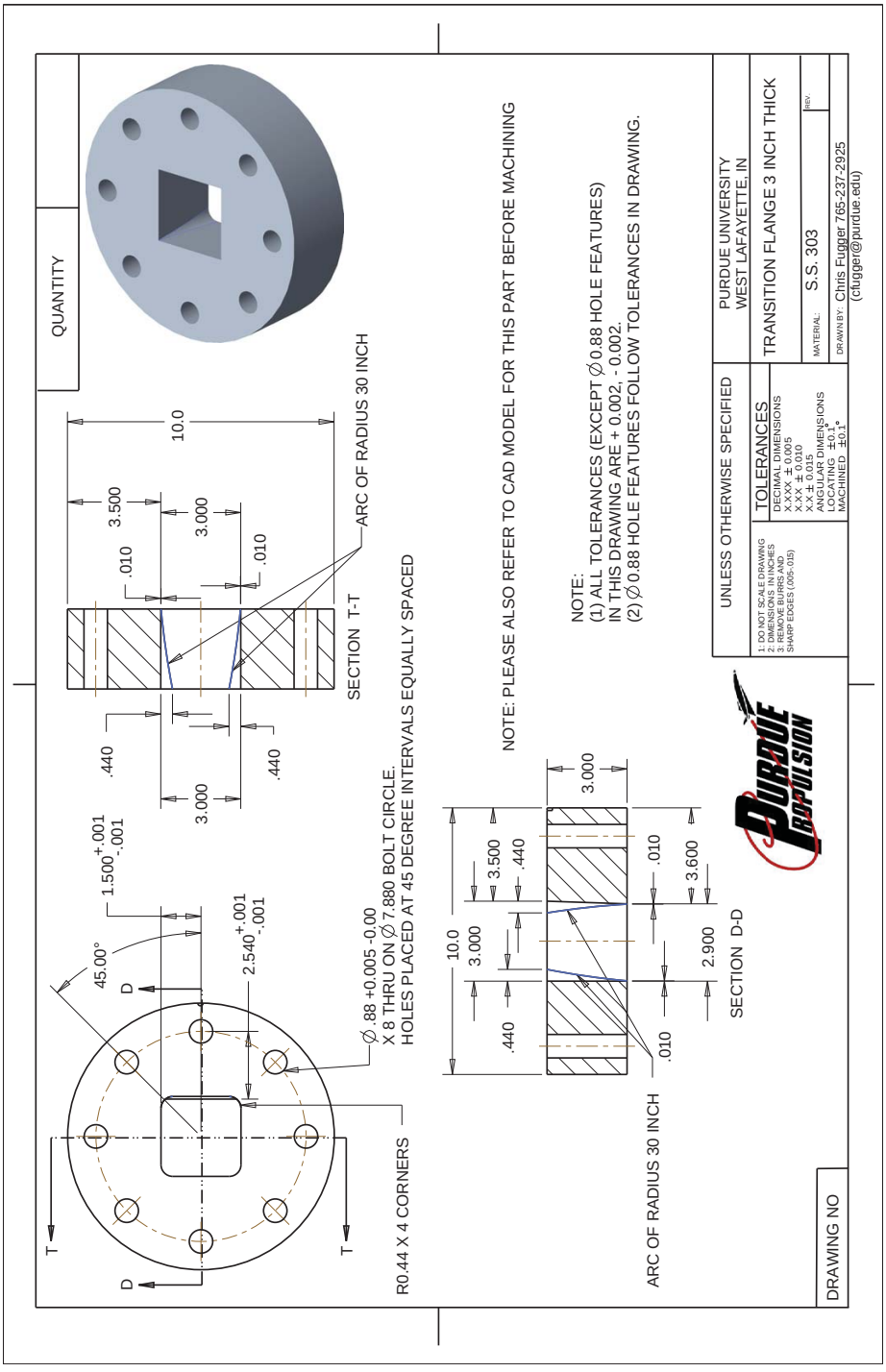

Figure B.12.. Machine drawing of the crossflow transition section located directly upstream of the combustor optical test section.

VITA

VITA

Christopher A. Fugger was born on October 10, 1983. He earned his Bachelor of Science in Physics from Loyola University in Chicago in 2006. He moved to Purdue University in 2008 to start a Master of Science in Aerospace Engineering. In 2010, he completed his Masters and began his doctorate. He has been conducting research on combustion dynamics and transverse jet flames since that time. Chris is married to Adrienne R. Fugger and recently became a father to Lucille M. Fugger.